HIGHWAY RESEARCH RECORD

Number 39

Stresses in Soils and Layered Systems

9 Reports

Presented at the
42nd ANNUAL MEETING
January 7-11, 1963

HIGHWAY RESEARCH BOARD
of the
Division of Engineering and Industrial Research
National Academy of Sciences—
National Research Council
Washington, D. C.
1963

Department of Soils, Geology and Foundations

Eldon J. Yoder, Chairman
Joint Highway Research Project, Purdue University
Lafayette, Indiana

COMMITTEE ON STRESS DISTRIBUTION IN EARTH MASSES

H. Bolton Seed, Chairman
Department of Civil Engineering
University of California, Berkeley

Richard G. Ahlvin, Chief Engineer, Special Projects Section, Waterways Experiment Station, Vicksburg, Mississippi

E. S. Barber, Consulting Engineer, Soil Mechanics and Foundations, Arlington, Virginia

B. F. Colley, Portland Cement Association, Skokie, Illinois

Melvin T. Davisson, University of Illinois, Urbana

Lawrence A. DuBose, Testing Service Corporation, Lombard, Illinois

Austin H. Emery, Associate Soils Engineer, Bureau of Soil Mechanics, New York State Department of Public Works, Albany

Jacob Feld, Consulting Engineer, New York, N. Y.

F. N. Finn, Technical Director, Products Engineering, Golden Bear Oil Company, Bakersfield, California

Hamilton Gray, Chairman, Department of Civil Engineering, Ohio State University, Columbus

Milton E. Harr, Associate Professor of Soil Mechanics, School of Civil Engineering, Purdue University, Lafayette, Indiana

R. G. Hennes, Department of Civil Engineering, University of Washington, Seattle

W. S. Housel, University of Michigan, Ann Arbor

T. F. McMahon, U. S. Bureau of Public Roads, Washington, D. C.

Robert L. McNeill, Supervisor, Soil Dynamics, Shock Tube Laboratory, University Station, Albuquerque, New Mexico

Carl L. Monismith, University of California, Berkeley

J. O. Osterberg, Civil Engineering Department, Northwestern University, Evanston, Illinois

F. E. Richart, University of Michigan, Ann Arbor

Robert L. Schiffman, Soil Engineering Division, Massachusetts Institute of Technology, Cambridge

Werner E. Schmid, Assistant Professor, Department of Civil Engineering, Princeton University, Princeton, New Jersey

F. H. Scrivner, Pavement Research Engineer, Texas Transportation Institute, A & M College of Texas, College Station

Department of Design

T. E. Shelburne, Chairman
Director of Research, Virginia Department of Highways
Charlottesville

Harold Allen, Chief, Division of Physical Research, Office of Research, U.S. Bureau of Public Roads, Washington, D.C.
Glenn, Anschutz, Engineer of Aerial Surveys and Photogrammetry Section, Kansas State Highway Commission, Topeka
Robert F. Baker, Director, Office of Research and Development, U.S. Bureau of Public Roads, Washington, D.C.
Joseph Barnett, Deputy Director of Engineering, U.S. Bureau of Public Roads, Washington, D.C.
A.C. Benkelman, Altamonte Springs, Florida
Phillip P. Brown, Consultant, Soils, Mechanics and Paving, Bureau of Yards and Docks, Department of the Navy, Washington, D.C.
J.N. Clary, Engineer of Bridges, Virginia Department of Highways, Richmond
C.N. Conner, Hollywood, Florida
Eric L. Erickson, Chief, Bridge Division, Office of Engineering, U.S. Bureau of Public Roads, Washington, D.C.
Wilbur J. Garmhausen, Chief Landscape Architect, Ohio Department of Highways, Columbus
A.T. Goldbeck, Chevy Chase, Maryland
John M. Griffith, Director of Research and Development, The Asphalt Institute, University of Maryland, College Park
Carl F. Izzard, Chief, Office of Research and Development, Hydraulic Research Division, U.S. Bureau of Public Roads, Washington, D.C.
R.E. Livingston, Planning and Research Engineer, Colorado State Highway Department, Denver
D.W. Loutzenheiser, Chief, Highway Standards and Design Division, U.S. Bureau of Public Roads, Washington, D.C.
Ralph A. Moyer, Research Engineer, Institute of Transportation and Traffic Engineering, University of California, Berkeley
Ernest T. Perkins, Executive Director, East Hudson Parkway Authority, Pleasantville, New York
Thomas B. Pringle, Chief, Civil Engineering Branch, Engineering Division, Military Construction, Office Chief of Engineers, Department of the Army, Washington, D.C.
Gordon K. Ray, Manager, Paving Bureau, Portland Cement Association, Chicago, Illinois
K.A. Stonex, Assistant Engineer-in-Charge, General Motors Corporation, Warren, Michigan
William, Van Breemen, Research Engineer, Engineering Research, New Jersey State Highway Department, Trenton
Eldon J. Yoder, Joint Highway Research Project, Purdue University, Lafayette, Indiana

COMMITTEE ON FLEXIBLE PAVEMENT DESIGN

R. E. Livingston, Chairman
Planning and Research Engineer
Colorado State Highway Department, Denver

Stuart Williams, Secretary
Supervisory Highway Research Engineer
U. S. Bureau of Public Roads, Washington, D. C.

A. C. Benkelman, Altamonte Springs, Florida
John A. Bishop, Director, Soils and Pavement Division, U.S. Naval Civil Engineering Laboratory, Port Hueneme, California
Thomas L. Bransford, Engineer of Research and In-Service Training, Florida State Road Department, Gainesville
W. H. Campen, Manager, Omaha Testing Laboratories, Nebraska
George H. Dent, Benjamin E. Beavin Company, Baltimore, Maryland
James M. Desmond, Assistant State Materials Engineer, Wyoming State Highway Department, Cheyenne
T. V. Fahnestock, Bituminous Engineer, North Carolina State Highway Commission, Raleigh
Charles R. Foster, Coordinator of Research, National Bituminous Concrete Association, Texas A & M College, College Station
F. H. Gardner, Transportation Engineer Office, Transportation Research Command, Fort Eustis, Virginia
J. E. Gray, Engineering Director, National Crushed Stone Association, Washington, D. C.
John M. Griffith, Director of Research & Development, The Asphalt Institute, University of Maryland, College Park
R. A. Helmer, Research Engineer, Oklahoma Department of Highways, Oklahoma City
Frank B. Hennion, Assistant Chief, Civil Engineering Branch, Engineering Division, Military Construction, Office Chief of Engineers, Department of the Army, Washington, D. C.
Raymond C. Herner, Consulting Engineer, Indianapolis, Indiana
W. S. Housel, University of Michigan, Ann Arbor
F. N. Hveem, Materials and Research Engineer, California Division of Highways, Sacramento
Charles W. Johnson, Engineer of Construction, New Mexico State Highway Department, Santa Fe
Henry J. Lichtefeld, Federal Aviation Agency, Airports Division, Washington, D. C.
Wallace J. Liddle, Chief Materials Engineer, Materials Testing Laboratory, Utah State Department of Highways, Salt Lake City
Chester McDowell, Supervising Soils Engineer, Texas Highway Department, Austin
Alfred W. Maner, Staff Engineer, The Asphalt Institute, University of Maryland, College Park
C. E. Minor, Materials and Research Engineer, Washington Department of Highways, Olympia
Carl L. Monismith, University of California, Berkeley
A. O. Neiser, Assistant State Highway Engineer, Kentucky Department of Highways, Frankfort
Frank P. Nichols, Jr., Highway Research Engineer, Virginia Department of Highways, Charlottesville
R. L. Peyton, Assistant State Highway Engineer, State Highway Commission of Kansas, Topeka
E. G. Robbins, Portland Cement Association, Chicago, Illinois
Rollin J. Smith, Engineer—Manager, Asphalt Department, Skelly Oil Company, Kansas City, Missouri
Fred Sternberg, Senior Highway Engineer—Research, Connecticut State Highway Department, Hartford
John H. Swanberg, Chief Engineer, Minnesota Department of Highways, St. Paul
B. A. Vallerga, Vice President, Golden Bear Oil Company, Bakersfield, California

Contents

Analysis of Dynamic Behavior of Roads Subject to Longitudinally Moving Loads

WILLIAM E. THOMPSON, Cornell Aeronautical Laboratory, Buffalo, New York

The flexural motion of a long road pavement of unit width, viscously damped and uniformly supported by an elastic subgrade, was found for the case of a steady, normal, concentrated load moving longitudinally at constant velocity. Deflections of the pavement were written in terms of the roots of the characteristic equation associated with the equation of motion of the pavement. A detailed study of the roots demonstrated that the solutions for the deflections fall into three distinct regimes distinguished by the value of the discriminant of the fourth order characteristic equation. In terms of the concepts of (1) subgrade damping ratio, ζ (ratio of subgrade damping coefficient to subgrade critical damping), and (2) the velocity ratio, θ (ratio of the load velocity to the propagation velocity of a transverse-displacement wave along a freely vibrating, elastically supported plate of unit width with zero damping), it is found that for light damping in the subgrade ($\zeta < 0.7$), an increase in the velocity of the load up to the vicinity of a velocity ratio of unity produces an increase in the dynamic value of the maximum pavement deflection. For heavy damping in the subgrade ($\zeta \geq 0.7$) and increasing load velocity, the maximum deflection decreases from the corresponding static value. The latter result is observed to be in accordance with measurements that have been obtained by others.

•THE present work arises in an endeavor to devise theoretical techniques, amply verified experimentally, for establishing the relative influence of dynamic and static loading on the deflections and stresses induced by a vehicle in the pavement of a road structure. It was shown by Fabian, Clark and Hutchinson (8) that the peak axle loadings of the pavement beneath a moving vehicle can be somewhat in excess of the static axle loads that are exerted by a stationary vehicle because of the dynamic excitation of suspension resonances by road surface irregularities. Further work by Clark (3) demonstrated that the road structure is itself a dynamical system, forced by the vehicle, and capable of magnification of pavement deflections and stresses through the action of energy transfer between the potential energy stored in subgrade compression and pavement bending, and the kinetic energy of a moving pavement mass. Thus, the simple static analyses of pavement stress and deflection heretofore considered adequate to describe the road response to vehicle loading forces are shown to be only special cases of the more general dynamical analyses introduced in these studies. Further, Clark (3) noted that, because of the distributed nature of the elements of a road structure, a dynamic loading of the pavement results from the action of a moving load, as well as time-varying load. Using the model of the road structure devised by Clark, the present work continues the road dynamics study by imposing a concentrated, steady, normal load moving along the road at constant velocity.

The mathematical model of the road-subgrade structure is oriented within the linear theory of elasticity and with respect to beams and plates as structural elements. A

Paper Sponsored by Committee on Stress Distribution in Earth Masses.

longitudinally moving load produces transverse vibrations of a beam or plate. Note that the motion of the freely-vibrating, simple (unsupported) beam was formulated by Euler (7) and Bernoulli (2) in the following equation:

$$EIw_{\bar{x}\bar{x}\bar{x}\bar{x}} + \rho A w_{\bar{t}\bar{t}} = 0 \text{ (lb/in.)} \tag{1}$$

in which the subscripts denote partial derivatives. Further, if this simple beam is supported by an elastic subgrade possessing viscous damping, the equation of motion for the transverse vibrations of the beam becomes

$$EIw_{\bar{x}\bar{x}\bar{x}\bar{x}} + \rho A w_{\bar{t}\bar{t}} + c' w_{\bar{t}} + k' w = 0 \text{ (lb/in.)} \tag{2}$$

In comparison, the free transverse vibrations of a free plate are described by

$$D\left(w_{\bar{x}\bar{x}\bar{x}\bar{x}} + 2w_{\bar{x}\bar{x}\bar{y}\bar{y}} + w_{\bar{y}\bar{y}\bar{y}\bar{y}}\right) + \rho h w_{\bar{t}\bar{t}} = 0 \left(\frac{\text{lb/in.}}{\text{in.}}\right) \tag{3}$$

in which D is the flexural rigidity of the plate and is analogous to EI for the beam. Rayleigh (18) and Lamb (11) first studied plate dynamics in connection with seismic wave phenomena and devised suitable forcing functions, q″, for the right hand side of Eq. 3.

If one should choose to characterize the motion of a long ribbon of road pavement by the plate model (i.e., Eq. 3), a further simplification is possible. Assume that the displacement of the plate is constant in the lateral ($\bar{y}$-axis) direction, that is, constant across the width of the road, and varies only in the longitudinal ($\bar{x}$-axis) and transverse ($\bar{z}$-axis) directions. This assumption may be expressed as $( )_{\bar{y}} = ( )_{\bar{y}\bar{y}} = w_{\bar{y}\bar{y}\bar{y}\bar{y}} = 0$. Applying these conditions to Eq. 3 and incorporating the damping and elastic reaction effects, one obtains

$$Dw_{\bar{x}\bar{x}\bar{x}\bar{x}} + \rho h w_{\bar{t}\bar{t}} + c'' w_{\bar{t}} + k'' w = 0 \left(\frac{\text{lb/in.}}{\text{in.}}\right) \tag{4}$$

which is the mathematical model of the road adopted by Clark (3). (It is important to note that the assumption of uniform deflection in the $\bar{y}$-direction is equivalent to zero deformation of the plate cross-section in the $\bar{y}\bar{z}$-plane. Hence, strain is confined to the $\bar{x}\bar{z}$-plane and is zero in the $\bar{y}\bar{z}$-plane. Such a problem is then one of "plane strain," a familiar approach in the two-dimensional theory of elasticity.)

In the derivation of the above forms of the equation of motion of the road pavement, the effects of rotatory inertia and shear deformation are neglected. Timoshenko (21, 22) and Mindlin (15) incorporate these effects into simple beam and simple plate theory, respectively, and subsequently show that inclusion of at least shear deformation is required if physically satisfactory results are to be obtained at high vibrational frequencies or short wave lengths. Neither of these effects has been included either in the work previously reported or in the present investigation, although Crandall (5) finds that their inclusion gives rise to several conditions of critical velocity of the moving load as compared with the single critical condition (at which displacement instability occurs) predicted by the simple plate theory employed in this study.

When Eqs. 2 and 4 are compared, they are identical except for constants, and it clearly becomes possible to apply techniques for solving the equation of motion of the beam to the solution of the road-vibration problem. Both Kenney (10) and Mathews (14) report parts of the solution of the beam problem in connection with the vibrations induced by a load moving along a rail. Mathews utilizes Fourier transforms in treating Eq. 2, but his results are incomplete for present purposes. On the other hand, Kenney

effects a transformation of Eq. 2 and then adopts the elementary method of undetermined coefficients in the solution of the resulting equation. However, many typographical errors make his work unreliable. Hopefully, then, it is intended that the present work will both clarify and complete the solution of the problem of beam (or road) vibrations where the structure is subjected to a concentrated vertical load moving longitudinally at constant velocity.

It should be noted that an important simplification of Eq. 4 can be made by transforming the independent variables from a set $(\bar{x}, \bar{z}, \bar{t})$ fixed with respect to the road to a set (x, z) fixed with respect to the moving load by means of the following relations which are illustrated in the sketch.

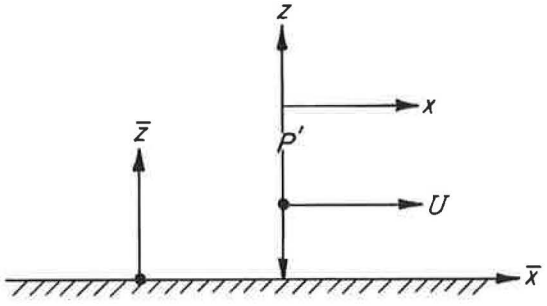

SKETCH

$$x = \bar{x} - U\bar{t} \tag{5a}$$

$$z = \bar{z} \tag{5b}$$

Under this transformation, the derivatives in Eq. 4 become

$$w_{\bar{x}\bar{x}\bar{x}\bar{x}} = w_{xxxx}, \; w_{\bar{t}\bar{t}} = U^2 w_{xx}, \; w_{\bar{t}} = -U w_x$$

and upon substitution in Eq. 4, one obtains

$$D w_{xxxx} + \rho h U^2 w_{xx} - c'' U w_x + k'' w = 0 \tag{6a}$$

Thus, in the moving coordinate system the displacement of the plate is independent of time after all the transient vibrations have disappeared and the motion of the plate is said to be "steady." Eqs. 5a and 5b define a Galilean transformation which has been used to advantage in a number of recent studies by Cole and Huth (4), Eringen and Samuels (6) and Mann-Nachbar (13) in addition to the work of Kenney (10).

Since the vertical displacement is now a function of x only, Eq. 6a may be rewritten in terms of ordinary derivatives

$$\frac{d^4 w}{dx^4} + \frac{\rho h U^2}{D} \frac{d^2 w}{dx^2} - \frac{c'' U}{D} \frac{dw}{dx} + \frac{k''}{D} w = 0 \tag{6b}$$

The main effort in this investigation has been devoted to (a) solving Eq. 6b for the deflection w, and (b) obtaining numerical solutions for the deflection of the road pavement in a general, nondimensional form.

For convenience, an alphabetical list of terms used, with their definitions, is given in the Appendix.

FORMULATION OF ROAD DEFLECTIONS

Characteristic Equation

Further study of Eq. 6b will be greatly helped by introducing the following defined quantities:

1. $\beta = (k'' / 4D)^{\frac{1}{4}}$, wave number (reciprocal of the wave length) for the case of a single, concentrated static load on an elastically supported plate;

2. $c''_{cr} = 2(k'' \rho h)^{\frac{1}{2}}$, critical value of the subgrade damping coefficient;

3. $U_{cr} = \left[(4k'' D)/(\rho h)^2\right]^{\frac{1}{4}}$, propagation velocity of a transverse displacement wave along a freely vibrating, elastically supported plate of unit width with zero damping;

4. $\theta = U/U_{cr}$, the velocity ratio; $\zeta = c''/c''_{cr}$, the damping ratio.

In terms of the definitions, the coefficients in Eq. 6b become

$$(\rho h U^2)/D = 4\theta^2 \beta^2$$

$$(c'' U)/D = 8\zeta \theta \beta^3$$

$$k''/D = 4\beta^4$$

and on substitution in Eq. 6b

$$\frac{d^4 w}{dx^4} + 4\theta^2 \beta^2 \frac{d^2 w}{dx^2} - 8\zeta\theta\beta^3 \frac{dw}{dx} + 4\beta^4 w = 0 \qquad (7)$$

In a fashion similar to Kenney (10), the elementary method of undetermined coefficients will be used to find the several particular solutions of this ordinary, fourth-order, homogeneous differential equation.

Assuming the solution to be of the form $w = Ce^{mx}$, derivatives of w may be calculated and substituted in Eq. 7 leading to the auxiliary or characteristic equation

$$m^4 + 4\theta^2\beta^2 m^2 - 8\zeta\theta\beta^3 m + 4\beta^4 = 0 \qquad (8)$$

The four roots (m_1, m_2, m_3, m_4) of Eq. 8 can be designated formally by stating that

$$(m - m_1)(m - m_2)(m - m_3)(m - m_4) = 0$$

where the next section is devoted to establishing the nature of the roots, m_i, for all physically acceptable values of ζ and θ.

The substitution $m = \hat{m}\beta$ in Eq. 8 achieves a further simplification:

$$\beta^4 (\hat{m}^4 + 4\theta^2 \hat{m}^2 - 8\theta\zeta\hat{m} + 4) = 0 \qquad (9a)$$

or

$$\hat{m}^4 + 4\theta^2 \hat{m}^2 - 8\theta\zeta\hat{m} + 4 = 0 \qquad (9b)$$

where it is seen that β plays the role of a scale factor and has been removed from the problem of specifying the roots $\hat{m}_i$.

From the definition of θ and ζ, for all possible physical cases of the road-vehicle system:

$$\theta \geq 0, \quad \zeta \geq 0 \tag{10a}$$

If $\theta = 0$, regardless of the value of ζ, Eq. 7 becomes the deflection equation for the road under static loading. If $\theta > 0$ and $\zeta = 0$, the case of undamped vibrations of the road due to a moving load is obtained.[1] However, the present investigation will be limited to

$$\theta > 0, \quad \zeta > 0 \tag{10b}$$

which correspond to a moving load and subgrade damping, in accordance with the assumed road-vehicle system. In view of Eq. 10b, the coefficients of Eq. 9 can be abbreviated as

$$4\theta^2 \equiv a > 0, \quad 8\theta\zeta \equiv b > 0 \tag{10c}$$

and the characteristic equation can finally be recorded as

$$\hat{m}^4 + a\hat{m}^2 - b\hat{m} + 4 = 0 \tag{11}$$

Regimes of Pavement Motion

In developing the solution of Eq. 7 in the form, $w = Ce^{mx}$, two steps must be taken. The first step sufficies to establish the nature of the roots m_i of the characteristic equation; the second serves to determine the constants of integration from the boundary conditions. The results of the study of the roots of the characteristic equation are presented first, followed by a presentation of the values of the constants of integration, together with the completed equations for the pavement deflections.[2]

The nature of the roots m_i, for all physically acceptable values of ζ and θ may be deduced by the systematic application of four algebraic theorems. The first of these, Routh's criterion, was used to ascertain the location of the roots in the complex variable plane.[3] The results are summarized in the following conclusions:

1. The real parts of two of the roots of Eq. 11 are positive and appear in the RHP.
2. There are no roots located in radial symmetry about the origin; in particular, there are no imaginary roots of Eq. 11.
3. Since Eq. 11 has precisely four roots, two of which have positive real parts and none of which is imaginary, the remaining two roots can have only negative real parts.

It is clear that the roots in both half-planes may be either real and/or complex-conjugate pairs and that further information is necessary to more clearly define the roots. For this purpose the discriminant of Eq. 11 was calculated from which there

---

[1] The undamped motion has been studied by both Kenney (10) and Mathews (14).

[2] Details of the processes for finding the roots and evaluating the constants are given in Appendices A and B of the report by Thompson (20).

[3] The roots $\hat{m}_i$ of Eq. 11 may be real, imaginary and/or complex. As such they may be plotted in a plane with the real parts of the roots taken along the abscissa and the imaginary parts along the ordinate. A customary way of designating the location of the roots is then to describe roots with positive real parts as appearing in the right half of the plane (RHP), etc.

follows information which not only helps to specify the roots but also establishes that there are three distinct solutions of the equation of motion of the assumed road model as a function of θ and ζ.

In terms of its coefficients, the discriminant of Eq. 11 becomes

$$\Delta = \frac{1}{256}\left[(16,384 - 2,048a^2 + 64a^4) + (576a - 4a^3)b^2 - 27b^4\right] \qquad (12)$$

and upon converting a and b to the parameters θ and ζ

$$\Delta = 16\left[4(1 - \zeta^2)\theta^3 - (8 - 36\zeta^2 + 27\zeta^4)\theta^4 + 4\right] \qquad (13)$$

According to the properties of the discriminant [given, for example, by Routh (19, paragraph 285)], the nature of the roots changes with the value of Δ, an important boundary being $\Delta = 0$. A plot of the locus of ζ and θ making $\Delta = 0$ is shown in Figure 1, together with information identifying the regions of the figure where $\Delta > 0$ and $\Delta < 0$. In terms of Δ then, further conclusions regarding the nature of the roots can be stated:

4. For $\Delta > 0$, Eq. 11 has two pairs of complex-conjugate roots.
   For $\Delta = 0$, Eq. 11 has two equal real roots and one complex-conjugate pair.
   For $\Delta < 0$, Eq. 11 has two unequal real roots and one complex-conjugate pair.

The three separate solutions of Eq. 7 then follow from adopting, in turn, each of the three sets of roots associated with $\Delta \gtrless 0$.

Despite the conclusions which have been obtained so far regarding the roots of Eq. 11, an ambiguity exists in placing the roots in the correct half-plane. This may be removed by ascertaining the location of the real roots for each case $\Delta \gtrless 0$, using

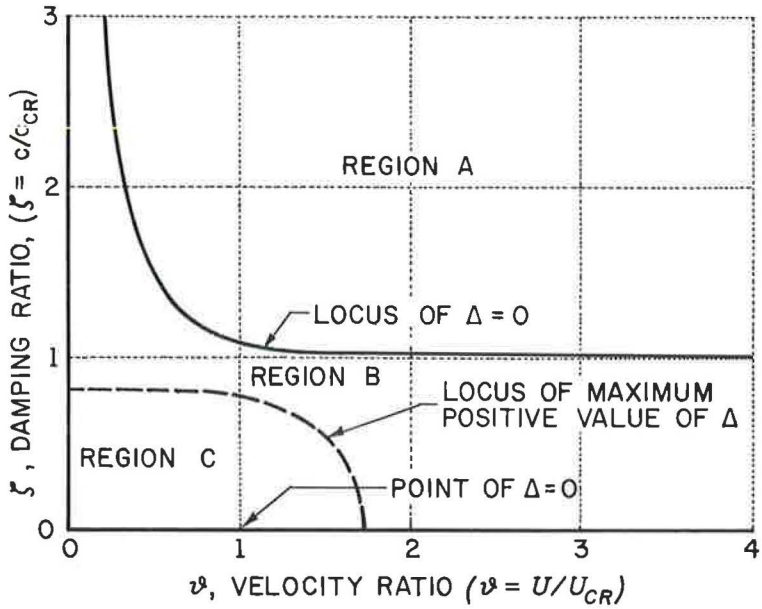

Figure 1. Portrait of $\Delta(\theta, \zeta) = 0$. Δ is the discriminant of the quartic characteristic equation associated with the transformed equation of motion of the road. For $\Delta = 0$, there are two real, equal and one complex conjugate pair of roots. For $\Delta < 0$, $\partial\Delta/\partial\zeta < 0$ (Region A), there are two real, unequal and one complex conjugate pair of roots. For $\Delta > 0$, $\partial\Delta/\partial\zeta < 0$ (Region B) and for $\Delta > 0$, $\partial\Delta/\partial\zeta > 0$) (Region C), there are two complex, conjugate pairs of roots.

Sturm's theorem. Although the theorem is commonly used to locate roots of polynomials between specified values of the independent variable, here it will be used only to check for the location of real roots in the left half-plane ($-\infty \leq \hat{m} \leq -\epsilon$) and the right half-plane ($+\epsilon \leq \hat{m} \leq +\infty$). A series of polynomials, called Sturm's functions, which begin with the original $f(\hat{m})$, i.e., Eq. 11, is evaluated at the extremes of each of the given intervals. Interpreting the numbers of sign changes (the function passes through $\hat{m} = 0$) which occur in the intervals, one draws the following conclusion relating to the position of the real roots:

5. For $\Delta > 0$, there are no real roots in either half-plane.
   For $\Delta = 0$, there is one, real, double root in the right half-plane.
   For $\Delta < 0$, there are two, real, unequal roots in the right half-plane.

From the conclusions 1-5, it is now possible to summarize the form of the roots of Eq. 8. Here one reverts to the roots m_i which are given by $m_i = \hat{m}_i \beta$, inasmuch as conclusions regarding $\hat{m}_i$ will not be affected by multiplying by the constant β. As a function of the sign of Δ, finally, for

$$\Delta > 0: \quad \left.\begin{aligned} m_1 &= A_1 + iB_1, \; m_3 = -A_2 + iB_2 \\ m_2 &= A_1 - iB_1, \; m_4 = -A_2 - iB_2 \end{aligned}\right\} \tag{14a}$$

$$\Delta = 0: \quad \left.\begin{aligned} m_1 &= -A_3 + iB_3, \; m_3 = A_4 \\ m_2 &= -A_3 - iB_3, \; m_4 = A_4 \end{aligned}\right\} \tag{14b}$$

$$\Delta < 0: \quad \left.\begin{aligned} m_1 &= A_6, \; m_3 = -A_5 + iB_5 \\ m_2 &= A_7, \; m_4 = -A_5 - iB_5 \end{aligned}\right\} \tag{14c}$$

Without requiring any information on the road-vehicle system beyond that already introduced, expressions for the real and imaginary parts of the roots may be determined in terms of the parameters θ, ζ, and β. Depending upon a further theorem from the theory of equations (which relates the coefficients of Eq. 8 to sums of the products of the roots) for this calculation, it is found that the constants defined by Eq. 14 are yielded by the following equations, grouped as a function of Δ.

$$\Delta > 0: \quad A_1^6 + 2\theta^2\beta^2 A_1^4 + \beta^4(\theta^4 - 1)A_1^2 - \theta^2\zeta^2\beta^6 = 0 \tag{15a}$$

$$A_2 = A_1 \tag{15b}$$

$$B_1^2 = \beta^2\left[2\theta^2 + A_1^2/\beta^2 - (2\theta\zeta\beta)/A_1\right] \tag{15c}$$

$$B_2^2 = \beta^2\left[2\theta^2 + A_1^2/\beta^2 + (2\theta\zeta\beta)/A_1\right] \tag{15d}$$

$$\Delta = 0: \quad A_3^3 + 2\theta^2\beta^2 A_3 - 2\theta\zeta\beta^3 = 0 \tag{16a}$$

$$A_4 = A_3 \tag{16b}$$

$$B_3^2 = 2\beta^2\left[2\theta^2 + A_3^2/\beta^2\right] \tag{16c}$$

$$\Delta < 0: \quad A_5^6 + 2\theta^2\beta^2 A_5^4 + \beta^4(\theta^4 - 1)A_5^2 - \theta^2\zeta^2\beta^6 = 0 \tag{17a}$$

$$A_6 = A_5 + \left[(2\theta\zeta\beta^3)/A_5 - 2\theta^2\beta^2 - A_5^2\right]^{\frac{1}{2}} \tag{17b}$$

$$A_7 = A_5 - \left[(2\theta\zeta\beta^3)/A_5 - 2\theta^2\beta^2 - A_5^2\right]^{\frac{1}{2}} \tag{17c}$$

$$B_5 = \left[(2\theta\zeta\beta^3)/A_5 + 2\theta^2\beta^2 + A_5^2\right]^{\frac{1}{2}} \tag{17d}$$

In practice it will be necessary to solve the implicit expressions for A_1, A_3 and A_5 before the calculation can proceed. It is clear from Eq. 14 as well that only real positive values of the A's are physically acceptable. Hence, Eqs. 15a, 16a and 17a were checked with Descartes' rule of signs by which it was found that each of these expressions possesses only one, real, positive root. These roots are adopted for the A's and all the others are considered superfluous.

Deflections Due to Longitudinally Moving Load

The solution of the equation of motion of the road-subgrade model, Eq. 7, for each of the three situations, $\Delta \gtrless 0$, may now be completed. Information in the form of boundary conditions at large distances from the load and compatibility conditions under the load will be needed to evaluate the constants of integration in the general solution in order to obtain particular results for each case.

1. When $\Delta > 0$

The general solution of Eq. 7 in terms of the roots m_i may be written immediately as

$$w = D_1 e^{m_1 x} + E_1 e^{m_2 x} + F_1 e^{m_3 x} + G_1 e^{m_4 x} \tag{18a}$$

On substituting the expressions for the roots, Eqs. 14a and 15b, into Eq. 18, and utilizing the relationships

$$e^{iB_1 x} = \cos B_1 x + i \sin B_1 x \tag{19a}$$

$$e^{-iB_1 x} = \cos B_1 x - i \sin B_1 x, \text{ etc.} \tag{19b}$$

it is found that

$$w = e^{-A_1 x}\left[C_1 \sin B_2 x + C_2 \cos B_2 x\right] + e^{A_1 x}\left[C_3 \sin B_1 x + C_4 \cos B_1 x\right] \tag{18b}$$

where C_1, C_2, C_3 and C_4 are to be found from the boundary conditions.

At $x = \pm \infty$, both the deflection of the road surface w and the slope of the surface, dw/dx are zero. Inasmuch as A_1 is always positive and real, for negative x, $C_1 = C_2 = 0$; and for positive x, $C_3 = C_4 = 0$, in order to meet the deflection and slope conditions. The solution may then be written in two parts,

$$w = e^{-A_1 x}\left[C_1 \sin B_2 x + C_2 \cos B_2 x\right] \quad \text{for } x > 0 \tag{20a}$$

$$w = e^{A_1 x}\left[C_3 \sin B_1 x + C_4 \cos B_1 x\right] \quad \text{for } x < 0 \tag{20b}$$

The remaining conditions for finding the C's are given by the compatibility of the deflection, slope and bending moment of the pavement under the load and by the formulation of the discontinuity in the shear load. Algebraic details involved in satisfying the boundary conditions, thereby determining the C's, are given by Thompson (20) and only the results are presented here.

$$C_2 = C_4 = \frac{-P' A_1}{D\left[A_1^2 (4A_1^2 + B_2^2 + 3B_1^2) + \frac{(B_2^2 - B_1^2)(4A_1^2 - B_1^2 + B_2^2)}{4}\right]} \tag{21a}$$

$$C_1 = \left[(B_1^2 - B_2^2 + 4A_1^2)/(4A_1 B_2)\right] C_2 \tag{21b}$$

$$C_3 = \left[(B_1^2 - B_2^2 - 4A_1^2)/(4A_1 B_1)\right] C_2 \tag{21c}$$

The final expressions for the deflection of the pavement can now be found by substituting Eq. 21 into Eq. 20 with the result

$$\frac{w}{w_0} = -8\beta^3 \left[\frac{e^{-A_1 x}}{B_2}\right]\left[\frac{4A_1 B_2 \cos B_2 x + (4A_1^2 + B_1^2 - B_2^2)\sin B_2 x}{16A_1^2 B_2^2 + (4A_1^2 - B_2^2 + B_1^2)^2}\right] \quad \text{for } x > 0 \tag{22a}$$

$$\frac{w}{w_0} = -8\beta^3 \left[\frac{e^{A_1 x}}{B_1}\right]\left[\frac{4A_1 B_1 \cos B_1 x - (4A_1^2 + B_2^2 - B_1^2)\sin B_1 x}{16A_1^2 B_1^2 + (4A_1^2 + B_2^2 - B_1^2)^2}\right] \quad \text{for } x < 0 \tag{22b}$$

which is in the form given by Mathews (14). The nondimensional form of the deflection, perhaps more accurately called the "dynamic-deflection amplification," is obtained by normalizing the deflection under dynamic conditions by the deflection under a static load, given by Clark (3, Eq. 8b) as

$$w_0 = (P'\beta)/(2k'')$$

The ratio w/w_0 is then an indication of the magnitude of the deflection under dynamic conditions relative to that under static conditions. The negative sign in Eq. 22 will occur in all the deflection formulas calculated in this investigation and arises from the fact that deflections under the load are deflections in the negative z-direction when viewed in the right-hand coordinate system shown in the previous sketch.

Although the first form of the solution given by Eq. 22 is very convenient for numerical work because A_1, B_1, B_2 are useful abbreviations, the solution may be expressed directly in terms of the parameters θ, ζ, β of the problem by utilizing Eq. 15 and the further abbreviations $A_1/\beta = \eta$ or $A_1 = \beta\eta$.

$$w = -\frac{P'\beta}{2k''}\left[\frac{\eta e^{-\beta\eta x}}{\eta^4 + \theta^2\eta^2 + \frac{1}{2}(\theta\zeta/\eta)^2}\right]\left[\frac{-(\theta\zeta/\eta - \eta^2)}{\eta(2\theta^2 + \eta^2 + 2\theta\zeta/\eta)^{\frac{1}{2}}} \times \right.$$

$$\left. \sin(2\theta^2 + \eta^2 + 2\theta\zeta/\eta)^{\frac{1}{2}}\beta x + \cos(2\theta^2 + \eta^2 + 2\theta\zeta/\eta)^{\frac{1}{2}}\beta x\right] \quad \text{for } x > 0 \tag{23a}$$

$$w = -\frac{P'\beta}{2k''}\left[\frac{\eta e^{\beta\eta x}}{\eta^4 + \theta^2\eta^2 + \frac{1}{2}(\theta\zeta/\eta)^2}\right]\left[\frac{-(\theta\zeta/\eta + \eta^2)}{\eta(2\theta^2 + \eta^2 - 2\theta\zeta/\eta)^{\frac{1}{2}}} \times \right.$$

$$\left. \sin(2\theta^2 + \eta^2 - 2\theta\zeta/\eta)^{\frac{1}{2}}\beta x + \cos(2\theta^2 + \eta^2 - 2\theta\zeta/\eta)^{\frac{1}{2}}\beta x\right] \quad \text{for } x < 0 \tag{23b}$$

which are in a form given by Kenney (10). Note that the above equations may be nondimensionalized by dividing by w_0.

2. When $\Delta = 0$

The general solution of Eq. 7 may be written again as

$$w = D_2 e^{m_1 x} + E_2 e^{m_2 x} + F_2 e^{m_3 x} + x G_2 e^{m_3 x} \tag{24}$$

where the multiple root m_3 is accommodated. Upon substituting the roots, Eqs. 14b and 16b, and simplifying

$$w = e^{-A_3 x}\left[C_5 \sin B_3 x + C_6 \cos B_3 x\right] + e^{A_3 x}\left[C_7 + C_8 x\right] \qquad (25)$$

Again the C_5, C_6, C_7, and C_8 are evaluated in two steps from the boundary conditions using the same process as for the condition $\Delta > 0$. The results of the work show that

$$C_6 = C_7 = \frac{-P' A_3}{D\left[A_3^2 (4A_3^2 + B_3^2) + \frac{B_3^2 (4A_3^2 + B_3^2)}{4}\right]} \qquad (26a)$$

$$C_5 = \left[(4A_3^2 - B_3^2)/(4A_3 B_3)\right] C_6 \qquad (26b)$$

$$C_8 = -\left[(4A_3^2 + B_3^2)/(4A_3)\right] C_6 \qquad (26c)$$

The deflection of the pavement is then found by using the separated form of Eq. 25 valid in front of and behind the load, and by further substituting Eq. 26 thus obtaining expressions in terms of A_3 and B_3,

$$\frac{w}{w_0} = -8\beta^3 \left[\frac{e^{-A_3 x}}{B_3}\right]\left[\frac{4A_3 B_3 \cos B_3 x + (4A_3^2 - B_3^2)}{(4A_3^2 + B_3^2)^2} \sin B_3 x\right] \quad \text{for } x > 0 \qquad (27a)$$

$$\frac{w}{w_0} = -8\beta^3 \left[e^{A_3 x}\right]\left[\frac{4A_3 - (4A_3^2 + B_3^2)x}{(4A_3^2 + B_3^2)^2}\right] \quad \text{for } x < 0 \qquad (27b)$$

which have the form of the results of Mathews (14).

In terms of the physical parameters θ, ζ, and β, Eq. 27 may be converted to equations of Kenney's form. Adopting Eq. 16 and making the abbreviations $A_3/\beta = \eta$ or $A_3 = \eta\beta$, Eq. 27 becomes

$$w = -\frac{P'\beta}{2k''}\left[\frac{e^{-\eta\beta x}}{9\eta^4 + 12\eta^2\theta^2 + 4\theta^4}\right]\left[\frac{4(\eta^2 - 2\theta^2)}{(4\theta^2 + 2\eta^2)^{\frac{1}{2}}} \times \right.$$

$$\left. \sin (4\theta^2 + 2\eta^2)^{\frac{1}{2}}\beta x + 8\eta \cos (4\theta^2 + 2\eta^2)^{\frac{1}{2}}\beta x\right] \quad \text{for } x > 0 \qquad (28a)$$

$$w = -\frac{P'\beta}{2k''}\left[\frac{e^{\eta\beta x}}{9\eta^4 + 12\eta^2\theta^2 + 4\theta^4}\right]\left[8\eta - 2(6\eta^2 + 4\theta^2)\beta x\right] \quad \text{for } x < 0 \qquad (28b)$$

These results may also be easily nondimensionalized by dividing by w_0.

3. When $\Delta < 0$

In the development of the final part of the solution of Eq. 7, one begins again with

$$w = D_3 e^{m_1 x} + E_3 e^{m_2 x} + F_3 e^{m_3 x} + G_3 e^{m_4 x} \qquad (29)$$

Since for this case, the roots m_i cannot be simplified, they are substituted directly from Eq. 14c. After collecting terms,

$$w = C_9 e^{A_6 x} + C_{10} e^{A_7 x} + e^{-A_5 x}\left[C_{11} \sin B_5 x + C_{12} \cos B_5 x\right] \qquad (30)$$

Finally the development of the constants C_9, C_{10}, C_{11} and C_{12} from the boundary conditions yields the results,

$$C_9 = P'\Big/\left\{D\left[(A_5 + A_6)^2 + B_5^2\right](A_6 - A_7)\right\} \qquad (31a)$$

$$C_{10} = -P'\Big/\left\{D\left[(A_5 + A_7)^2 + B_5^2\right](A_6 - A_7)\right\} \qquad (31b)$$

$$C_{11} = \frac{P'}{D}\left\{\frac{\left[B_5^2 - (A_5 + A_6)(A_5 + A_7)\right]}{B_5\left[(A_5 + A_6)^2 + B_5^2\right]\left[(A_5 + A_7^2) + B_5^2\right]}\right\} \qquad (31c)$$

$$C_{12} = -\frac{P'}{D}\left\{\frac{(2A_5 + A_6 + A_7)}{\left[(A_5 + A_6)^2 + B_5^2\right]\left[(A_5 + A_7)^2 + B_5^2\right]}\right\} \qquad (31d)$$

Mathew's form of the deflection equations is now found by using the separated form of Eq. 30, and substituting Eq. 31.

$$\frac{w}{w_0} = -8\beta^3\left\{\frac{e^{-A_5 x}}{B_5}\right\} \times$$

$$\left\{\frac{B_5(2A_5 + A_6 + A_7)\cos B_5 x - \left[B_5^2 - (A_5 + A_6)(A_5 + A_7)\right]\sin B_5 x}{\left[(A_5 + A_6)^2 + B_5^2\right]\left[(A_5 + A_7)^2 + B_5^2\right]}\right\} \quad \text{for } x > 0 \qquad (32a)$$

$$\frac{w}{w_0} = -8\beta^3\left\{-\frac{e^{A_6 x}}{\left[(A_5 + A_6)^2 + B_5^2\right](A_6 - A_7)} + \frac{e^{A_7 x}}{\left[(A_5 + A_7)^2 + B_5^2\right](A_6 - A_7)}\right\}$$

$$\text{for } x < 0 \qquad (32b)$$

As a last calculation, it is valuable to obtain the deflections in terms of the parameters θ, ζ, β for the present case, $\Delta < 0$. Eq. 17 facilitates the conversion and, after introducing the abbreviation $A_5/\beta = \eta$ or $A_5 = \eta\beta$, one obtains

$$w = -\frac{P'\beta}{2k''}\left[\frac{\eta e^{-\eta\beta x}}{\eta^4 + \theta^2\eta^2 + \frac{1}{2}(\theta\zeta/\eta)^2}\right]\left[\frac{-(\theta\zeta/\eta - \eta^2)}{\eta(2\theta\zeta/\eta + 2\theta^2 + \eta^2)^{\frac{1}{2}}} \times\right.$$

$$\left.\sin(2\theta\zeta/\eta + 2\theta^2 + \eta^2)^{\frac{1}{2}}\beta x + \cos(2\theta\zeta/\eta + 2\theta^2 + \eta^2)^{\frac{1}{2}}\beta x\right] \quad \text{for } x > 0 \qquad (33a)$$

$$w = -\frac{P'\beta}{2k''}\left\{\eta e^{\eta\beta x}\right\}\left\{\frac{e^{-(2\theta\zeta/\eta - 2\theta^2 - \eta^2)^{\frac{1}{2}}\beta x}}{\eta\left[(\theta\zeta/\eta + \eta^2)(2\theta\zeta/\eta - 2\theta^2 - \eta^2)^{\frac{1}{2}} - \eta(2\theta\zeta/\eta - 2\theta^2 - \eta^2)\right]} -\right.$$

$$\left.\frac{e^{(2\theta\zeta/\eta - 2\theta^2 - \eta^2)^{\frac{1}{2}}\beta x}}{\eta\left[(\theta\zeta/\eta + \eta^2)(2\theta\zeta/\eta - 2\theta^2 - \eta^2)^{\frac{1}{2}} + \eta(2\theta\zeta/\eta - 2\theta^2 - \eta^2)\right]}\right\}$$

$$\text{for } x < 0 \qquad (33b)$$

The exponential quantities may be expressed in terms of hyperbolic functions, and on so doing Eq. 33b takes on an appearance quite similar to Eq. 23b. In terms of obvious abbreviations, the second bracket in Eq. 33b may be written as

$$\left(\frac{e^{-u}}{a-b} - \frac{e^{u}}{a+b}\right) = \left(\frac{2b}{a^2 - b^2}\right)\left(-\frac{a}{b}\sinh u + \cosh u\right)$$

After working out the new functions of the parameters θ, ζ, β, an alternative form of Eq. 33b becomes

$$w = -\frac{P'\beta}{2k''}\left\{\frac{\eta e^{\eta\beta x}}{\eta^4 + \theta^2\eta^2 + \frac{1}{2}(\theta\zeta/\eta)^2}\right\}\left\{\frac{-(\theta\zeta/\eta + \eta^2)}{\eta(2\theta\zeta/\eta - 2\theta^2 - \eta^2)^{\frac{1}{2}}}\right\} \times$$

$$\left\{\sinh(2\theta\zeta/\eta - 2\theta^2 - \eta^2)^{\frac{1}{2}}\beta x + \cosh(2\theta\zeta/\eta - 2\theta^2 - \eta^2)^{\frac{1}{2}}\beta x\right\} \quad \text{for } x < 0 \qquad (33c)$$

Eq. 33 may be nondimensionalized as before.

Referring to Figure 1, an immediate conclusion regarding the solutions of the fourth-order road system characterized by Eq. 7 is evident. On recalling that the solution of a second-order dynamic system is described as underdamped, critically damped, or overdamped depending upon whether $\zeta \lessgtr 1$, it is now seen that at small velocities of the moving load (small θ), a single solution is valid for the damping ratio $\zeta \lessgtr 1$. Thus, for the fourth-order road system, the concept of critical damping can no longer be associated with $\zeta = 1$, inasmuch as the nature of the solutions is separated by the condition $\Delta = 0$. The relation of ζ to the $\Delta = 0$ condition is expressed in Eq. 13 and clearly is no simple relationship. However, the series of equations which have just been presented can be utilized to examine the role of the discriminant Δ as it bears on the form of the solutions to the assumed fourth-order road system.

An important feature of the road vibrations that occur because of a moving load is that the deflections are not symmetrical about the load. While the wavy profile of the pavement does propagate along the road with the same velocity as the load, the waves ahead of the load ($x > 0$) have a shorter wave length and smaller amplitude, in general, than the waves behind the load ($x < 0$). Referring to Eqs. 22a, 27a, and 32a for the deflections in front of the load in the three instances, $\Delta \lessgtr 0$, respectively, all three of the results are similar (i.e., damped, superposed sine and cosine wave forms). It is concluded that regardless of Δ, the road motion in front of the load exhibits a typically "underdamped" behavior. Behind the load, Eqs. 22b, 27b, and 32b describe the deflections. For $\Delta > 0$, Eq. 22b has a superposed sine and cosine waveform multiplied by an exponential decay, which in a second-order system would be characteristic of damping less than critical. For $\Delta \leqslant 0$, both Eqs. 27b and 32b show an exponential decay of the deflection with distance behind the load without the presence of an oscillatory wave form. This latter result could be arbitrarily described as a wave-form typical of overdamped, second-order systems.

In each set of the three solutions, nondimensional forms of the deflections are given as w/w_0. The resulting amplification factors are presumably calculated at specific dimensional distances from the load. Inspection of Eqs. 23, 28, and 33 shows, however, that x and β always appear as a product and, in fact, βx becomes a most suitable nondimensional distance. Therefore, by interpreting βx as a nondimensional distance, the results give normalized deflections at normalized distances from the load, both of which may be particularized to any specific case of axle load and road-subgrade configuration.

GENERALIZED DEFLECTION COMPUTATIONS

Nondimensional Profiles

In order to compute the deflection w, or its normalized form w/w_0, from Eqs. 22, 27 and 32 in an efficient manner, an iterative program for machine calculations using an IBM 704 electronic data processing machine was written in Fortran II (formula translation) language. A sample of the resulting numerical solutions has been plotted for presentation in this paper. The scope of the present investigation and paper limits the presentation of numerical results to a discriminating sample of the many possibilities. Besides physical limitations, it would be misleading to present, somewhat in the form of a handbook, a vast compilation of deflection profiles, etc., that have not been substantiated by experiment and that have arisen from a first experience in solving the equation of motion of an assumed road-subgrade system subjected to a moving load.

For a given road construction or pavement-subgrade configuration, one matter of concern is how the deflections or vibrations of the road will change with an increase in velocity of the moving load. Figures 2 and 3 show the effects of load velocity as predicted by the present study. Several conditions are common to both figures. At static conditions, $\theta = 0$, (not shown in the figures) the maximum deflection w_0 occurs under the load (at $\beta x = 0$) with the deflection curve being symmetrical about the position $\beta x = 0$ (3, Fig. 6). As the velocity increases (i.e., $\theta > 0$), the point of maximum deflection falls behind the load; thus the load appears to be imposed on the inclined side of the trough. All profiles computed in this work show the trend of maximum deflection falling behind the loads as speed increases. To the extent of the present calculations, however, the point of load application never rises above the level of the undeflected pavement surface in "climbing out" of the trough with increasing speed.

It should be noted that positive (upward) deflections occur in front of the load for all values of Δ and occur behind the load for $\Delta > 0$. Behind the load for $\Delta < 0$, one expects

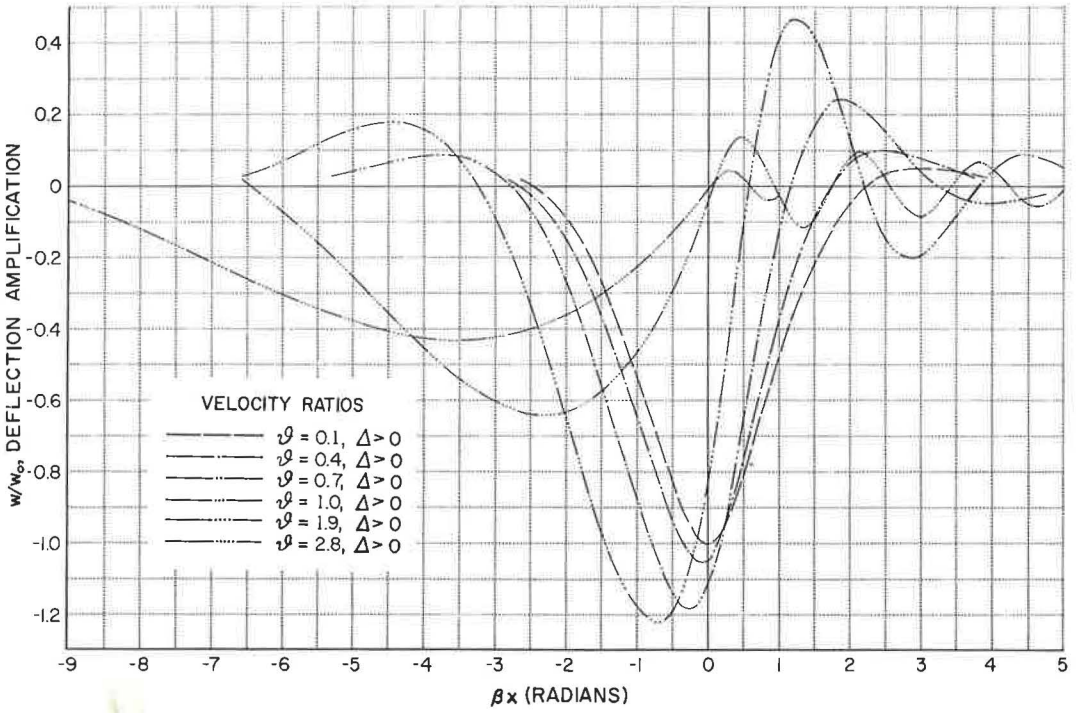

Figure 2. General nondimensional surface displacements; variation of surface displacement with velocity of the moving load for a case of light damping, $\zeta = 0.4$.

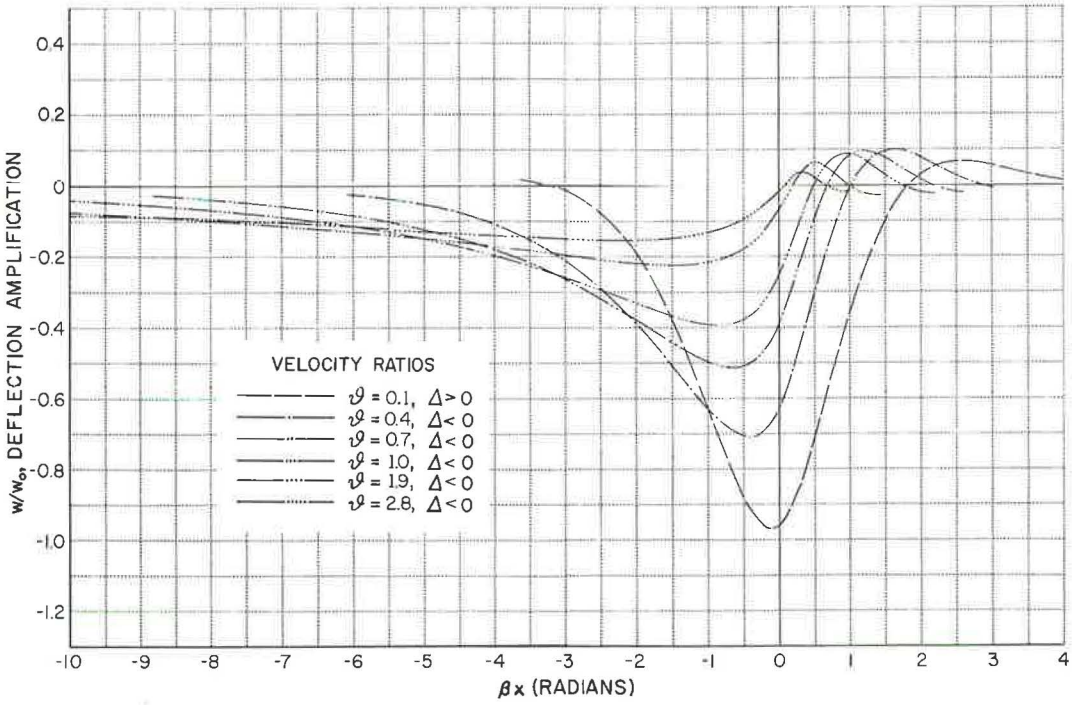

Figure 3. General nondimensional surface displacements; variation of surface displacement with velocity of the moving load for a case of heavy damping, $\zeta = 2.0$.

the deflections to approach $w/w_0 = 0$ at distances far away from the load but to never become positive. Again, beginning with the symmetrical condition at zero speed, ahead of the load the wavelength becomes shorter with increasing speed; behind the load the wavelength becomes extended to where, at $\Delta < 0$, no oscillatory waveform will ever be obtained. This pattern appears to be a kind of "Doppler" effect. Indeed, the point may be carried one step further by noting, from a point of view often taken in compressible fluid mechanics, that the medium (elastic pavement material) before the load has been advised of the approaching load by signals (elastic waves) propagated at sonic velocity[4] in the medium. As the load speed increases, the distance ahead of the load to which the signals penetrate before the load passes becomes shorter and shorter, thus the distance ahead of the load affected by vibrations becomes shorter. When the load travels at sonic speed, the load and information about its presence move together and when the load speed exceeds sonic speed, a shock wave condition exists in the medium at and behind the load. At and above sonic speed for the moving load, no vibrations are expected in the plate ahead of the load. However, this discussion does not completely define the matter, because in elastic solids there are two conditions of sonic speed[5] corresponding to the propagation velocities of longitudinal, compression and tension waves and of transverse shear waves. Wave interactions then tend to obscure a simple phenomenological picture.

The essential difference between Figures 2 and 3 is the damping in the subgrade, where light damping, characterized by $\zeta = 0.4$, is assumed in Figure 2 and heavy

---

[4] Sonic velocity referred to here is not to be confused with U_{cr}, the flexural wave velocity for the freely vibrating, elastically supported plate.

[5] In a solid, two sonic velocities exist corresponding to the propagation velocity, c_1 of longitudinal or normal stress waves and to the propagation velocity c_2 of transverse or shear stress waves. By way of illustration for conditions of the numerical given example, $c_1 = 3{,}290$ ft/sec, $c_2 = 2{,}105$ ft/sec, whereas $U_{cr} = 244$ ft/sec.

damping, $\zeta = 2.0$, is assumed in Figure 3. In each figure, pavement profiles both ahead of ($\beta x > 0$) and behind ($\beta < 0$) the load are drawn for several values of θ. The important difference in the deflections due to the difference in the damping is that at light damping and with speeds increasing up to the vicinity of U_{cr} ($\theta = 1$), the maximum deflection behind the load increases beyond its static value, whereas for heavy damping the maximum deflection behind the load decreases from the static value. If the linear damping of a subgrade is equivalent to values of ζ less than "critical," maximum deflections under dynamic conditions of moving loads should be expected to be more severe than the static deflections and to increase to a maximum as the speed increases to the vicinity of the critical velocity. If, however, road subgrades exhibit heavy damping characteristics, the expectation is that the maximum deflection occurs under a static load and decreases without exception as the load velocity increases.

An alternate way of viewing the results obtained in the computational study is shown in Figures 4 and 5, called stability diagrams. The maximum deflection amplification factors at positions fore and aft of the load through the range of the velocity ratio have been plotted for values of constant damping ratio. Figure 5 shows that maximum deflections behind the load develop from the negative static deflection under the load. However, the maximum deflection ahead of the load occurs in the region of positive deflection where it may be normalized by the corresponding static value resulting in a very similar plot. The positive deflection ahead of the load may also be arbitrarily normalized by w_0, resulting in Figure 4.

The appearance of Figure 5 is quite similar to steady-state resonance diagrams displayed, for example, by second-order systems subjected to a constant amplitude, sinusoidal forcing function. When the damping is small and the frequency of the forcing function approaches the natural frequency of the system, the displacements exhibit ex-

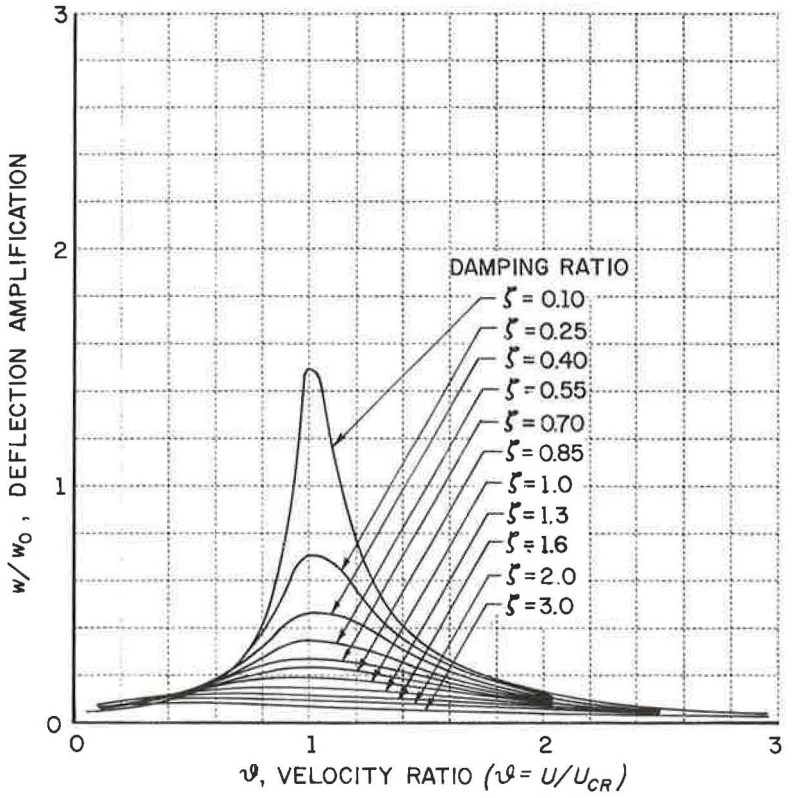

Figure 4. Stability diagram for surface displacements ahead of the load; maximum deflection amplification ahead of the load is normalized to the static deflection under the load.

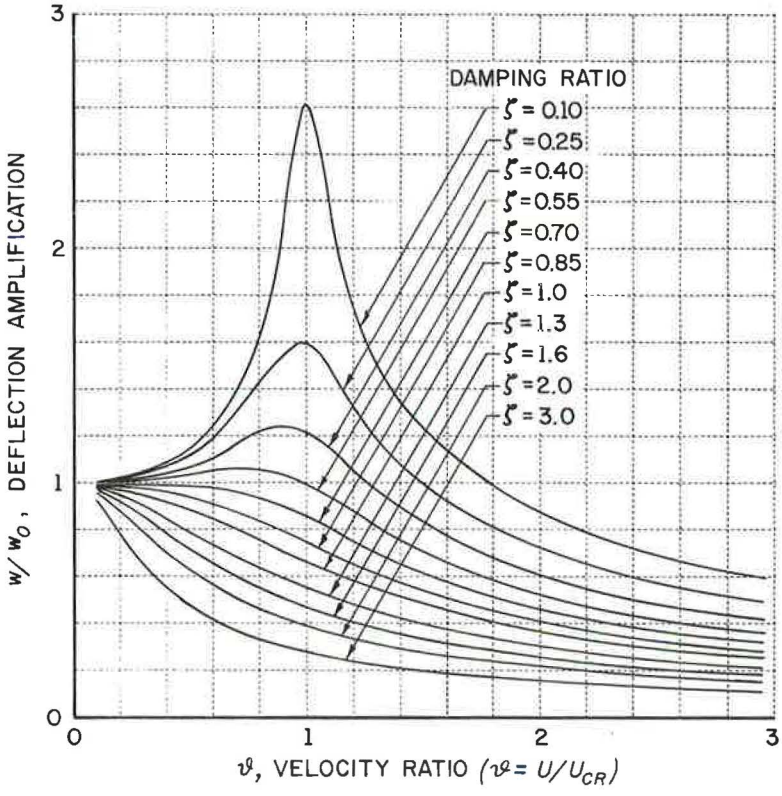

Figure 5. Stability diagram for surface displacements behind the load; maximum deflection amplification behind the load is normalized to the static deflection under the load.

cursions to very large values because of conditions of resonance. In the assumed fourth-order road system, such excursions in the deflections due to a steady, moving load occur when the velocity of the moving load approaches the critical value given by the propagation velocity of transverse flexure waves of the freely vibrating road structure. However, no forcing function containing a circular frequency is involved. Because of this difference then, the example of Piszczek (17) and others is followed and the conditions of maximum road deflection near $\theta = 1$ are termed instability rather than resonance.

The conditions of deflection amplification greater than unity at light damping and less than unity at heavy damping are shown most clearly in the stability diagrams. For $\zeta < 0.7$ (approximately), the deflection behind the load always exceeds the static deflection in the range of low values of the velocity (Fig. 5). As in the second-order system, the numerical results obtained herein indicate that the $\zeta = 0.7$ curve has a maximum value at zero speed, and is the value of the damping ratio at and beyond which the deflections always decrease with increasing speed.

Example of Deflection Derived from General Results

It is desirable to show the relation between the above general, nondimensional results and a specific choice of load and road parameters that are possibly typical of actual road constructions. In order to implement this comparison, Figures 6 through 10 were drawn for values of θ, corresponding to realistic velocities of road vehicles. Because of the uncertainty of the values of damping ratio ζ that would be exhibited by typical road-subgrade systems, a range of damping ratios was used. The information is the same as in Figures 2 and 3, except that the roles of θ and ζ have been inter-

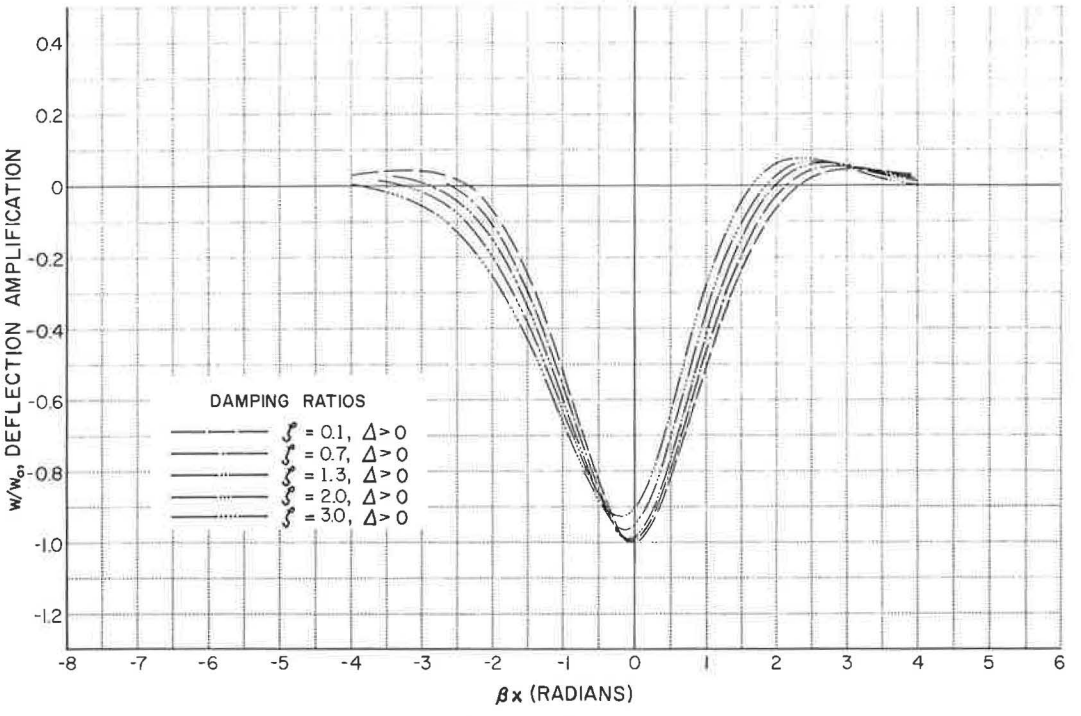

Figure 6. General nondimensional surface displacements; variation of surface displacement with the subgrade damping characteristic for the velocity of the moving load, θ = 0.10.

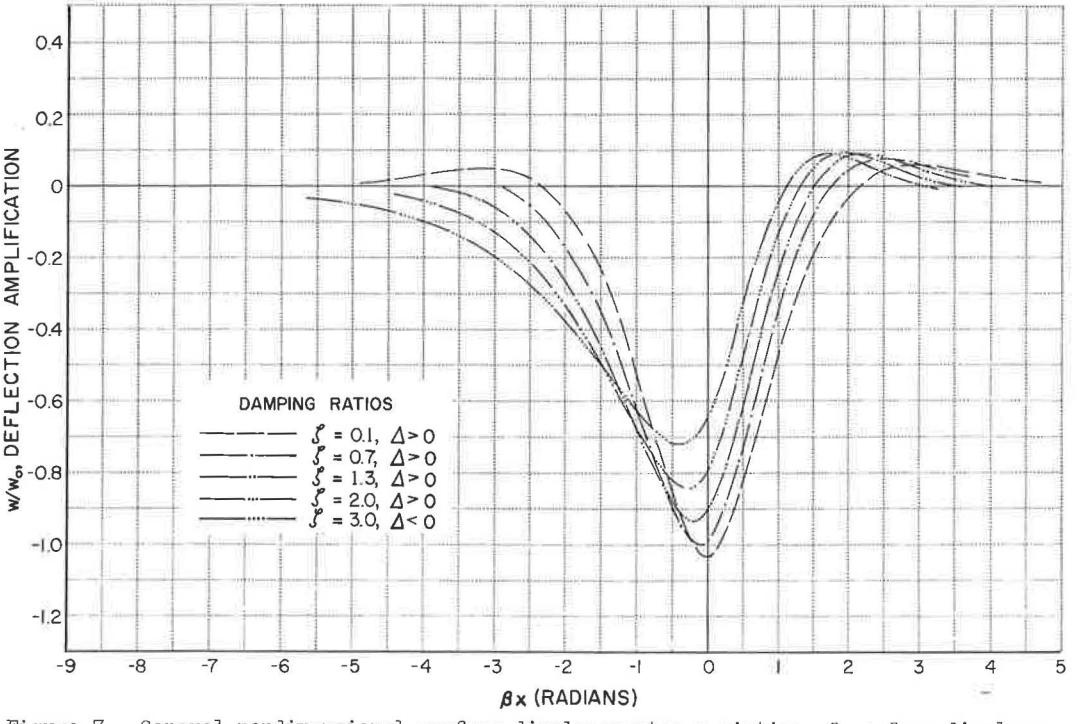

Figure 7. General nondimensional surface displacements; variation of surface displacement with the subgrade damping characteristic for the velocity of the moving load, θ = 0.25.

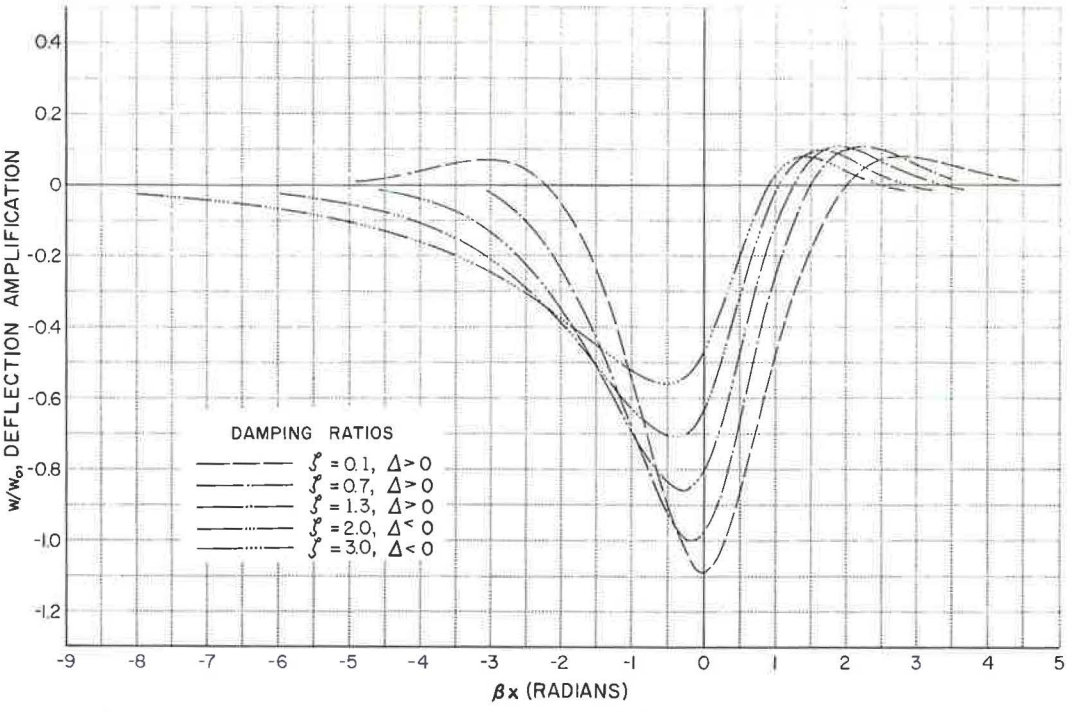

Figure 8. General nondimensional surface displacements; variation of surface displacement with the subgrade damping characteristic for the velocity of the moving load, $\theta = 0.40$.

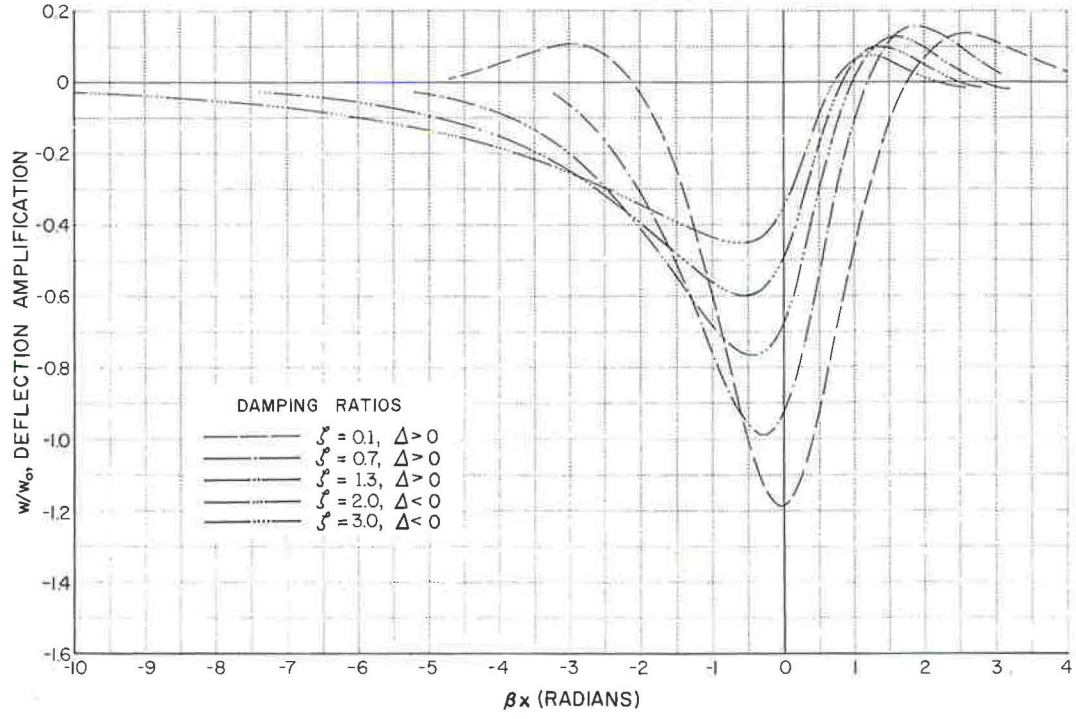

Figure 9. General nondimensional surface displacements; variation of surface displacement with the subgrade damping characteristic for the velocity of the moving load, $\theta = 0.55$.

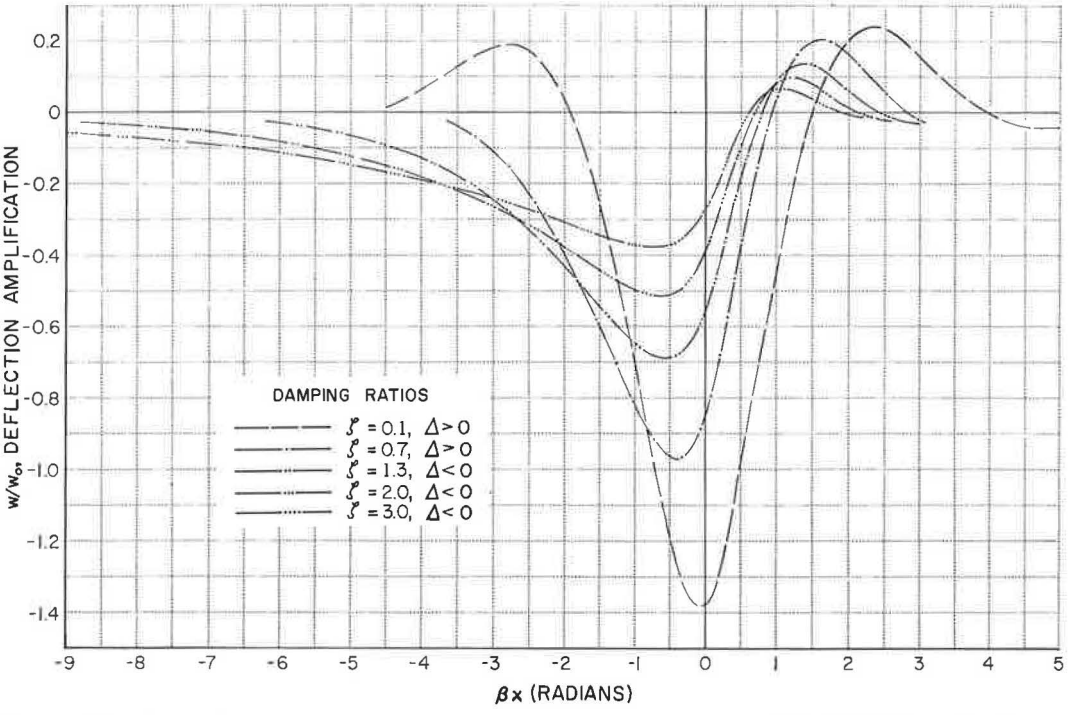

Figure 10. General nondimensional surface displacements; variation of surface displacement with the subgrade damping characteristic for the velocity of the moving load, θ = 0.70.

changed. It should be noted that use of ζ as a variable parameter, because of its uncertainty, does not imply certainty in the value of θ by any means. In the definition of U_{cr}, the parameter used to normalize the velocity of the moving load, the spring constant k'' of the elastic subgrade, is required. Clark (3) assumed a value of 50 pci, while Livesley (12) illustrates the airport runway problem with a value of 750 pci. Many values between these extremes have been noted in the literature. Values of k'' ascertained experimentally on the AASHO Road Test were not available in time for use in this study.

Because of the large variation in values of k'' that have been quoted, it was not practical to prepare Figures 6 through 10 for such specific values of the velocity of the moving load as 20 mph, 60 mph, 120 mph, etc. Instead, a range of low values of θ are presented; that is, θ = 0.1, 0.25, 0.40, 0.55, and 0.70.

In the following example, values of the parameters and physical properties of a load and a road configuration are first specified, the static deflection is computed and, by means of Figures 6 through 10, various aspects of the deflection profiles due to the moving load are found.

On specifying[6]:

$E = 4 \times 10^6$ lbf/in.^{2},

[6] E for concrete was found based on the suggestion of Grinter (9) and Norris, et al (16) that $E = 1{,}000\, f'_c$. An average value of f'_c reported by the AASHO Staff (1) was 3,966 psi for all pavements where h > 5 in. Poisson's ratio, ν, was measured by the AASHO Staff, is contained in their Data Systems, but was not given in the test reports. The value used here is a very coarse handbook value. The AASHO Staff (1) also reported the average density listed above for payments where h > 5 in. The thickness and road width represent a typical cross section.

$\nu = 0.15$,

$\rho = 150.9$ lbm/ft^3 $= 0.271 \times 10^{-2}$ lb-sec^2/in.^{4},

$k'' = 50$ pci,

$h = 8$ in., road width $= 12$ ft,

Axle load $= 18,000$ lb; thus

$P' = 125$ lb/in.

one obtains:

$$D = (Eh^3)/12(1 - \nu^2) = 1.7460 \times 10^6 \text{ psi/in.},$$

$$\beta = (k''/4D)^{\frac{1}{4}} = 1.6358 \times 10^{-2} \text{ rad/in.},$$

$$w_o = (P'\beta)/(2k'') = 2.0447 \times 10^{-2} \text{ in.; and}$$

$$U_{cr} = \left[(4k'' D)/(\rho h)^2\right]^{\frac{1}{4}} = 244 \text{ ft/sec} = 166.8 \text{ mph.}$$

Using the above value of U_{cr}, the velocity of the moving load represented by each of the five figures is

Fig.	6	7	8	9	10
U (mph)	16.7	41.7	66.6	91.7	116.8

The deflections and positions of the maximum deflection fore and aft of the load can then be found as follows: At $\theta = 0.40$ (66.6 mph) and $\zeta = 2.0$, from Figure 8 the maximum negative and positive deflection behind and in front of the load together with the distance from the load are

$$(w/w_o)_{-max} = -0.709 \qquad w_{-max} = -0.709 \times 0.02045 = -0.0145 \text{ in.}$$

$$(w/w_o)_{+max} = +0.0997 \qquad w_{+max} = +0.0997 \times 0.02045 = +0.00204 \text{ in.}$$

$$(\beta x)_{-max} = -0.400 \qquad x_{-max} = -0.400/0.01636 = -24.4 \text{ in.}$$

$$(\beta x)_{+max} = +1.60 \qquad x_{+max} = +1.60/0.01636 = 97.8 \text{ in.}$$

Similarly, a large number of such conversions will suffice to construct an entire profile for the assumed example. The dimensional profiles will, of course, be a critical function of the road design variables that determine the nondimensional parameters, θ and ζ.

CONCLUSIONS

1. The equation of motion of a long, narrow, elastic pavement, viscously damped and uniformly supported by an elastic subgrade, was formulated. Since the pavement model is subjected to a steady, normal, concentrated load moving longitudinally at constant velocity, transformation from a coordinate system fixed with respect to the pavement to one fixed with respect to the moving load is possible. The resulting ordinary differential equation which describes the dynamic road system is then amenable to solution by elementary techniques, the method of undetermined coefficients being used here following the suggestion of Kenney.

2. The roots of the characteristic equation, associated with the transformed equation of motion of the road-vehicle system, divide the solution for the pavement deflection into three parts for all physically acceptable values of the damping ratio ζ and the velocity ratio θ. The value of the discriminant of the characteristic equation is indicative of the three regimes of the solution.

3. Contrary to the conditions wherein $\zeta \lessgtr 1$ characterizes the underdamped, critically damped, and overdamped motions, respectively, of a second-order dynamic system, no simple, single value or function of ζ separates the solutions of the fourth-order, road-vehicle system. The conditions $\Delta \gtrless 0$ do distinguish the solutions mathematically, but the separate solutions for the motion of the pavement in front of and behind the load obscure this distinction.

4. In satisfying the boundary conditions in the solution of the equation of motion of the pavement, separate formulations are obtained for the deflection in front of and behind the load. Irrespective of the value of Δ, the pavement vibrations in front of the load exhibit a typically underdamped behavior. Behind the load an underdamped motion again appears when $\Delta > 0$, while for $\Delta \leq 0$, the vibrations decay with distance behind the load without ever achieving an oscillatory waveform.

5. The deflection of the pavement surface proves to be a function of the nondimensional product βx. Since the deflection equations may be normalized by a reference deflection, such as w_o, the results of this investigation may be cast into a general nondimensional form which can then be adapted to any load and road configuration consistent with the assumed road model.

6. The pavement profile computations demonstrate that the position of maximum deflection of the pavement falls behind the load as velocity of the load increases. The point of load application occurs on the forward side of the deflection trough but, to the extent of the calculations made in this investigation, never reaches a vertical position corresponding to the undeflected surface. As the velocity of the load increases, the wavelength of the vibrations in front of the load decreases; behind the load, the wavelength increases. This result is obtained independent of damping.

7. An important difference in deflections due to the influence of subgrade damping is evident from the computed pavement-deflection profiles. At light damping ($\zeta < 0.7$) and with speeds increasing up to the vicinity of U_{cr} ($\theta = 1$), the maximum deflection located behind the load increases, whereas for heavy damping ($\zeta \leq 0.7$) the maximum deflection always decreases from the static value. If light damping characterizes road construction, maximum deflections under moving loads are expected to be more severe than the static deflections, and to increase as speed increases up to the vicinity of U_{cr}. If, however, heavy damping characterizes road construction, the expectation is that maximum deflection occurs under a static load and decreases as the load velocity increases.

8. It can be argued that the road model described herein is not complete to the extent that the model does not include: (a) the effects of rotatory inertia and/or shear deformation of the pavement; (b) energy losses due to pavement flexure; (c) an adequate determination of the boundary conditions that prevail with finite-length pavement slabs; (d) the transient terms associated with an unsteady load velocity and magnitude; (e) the three-dimensional effects of a finite width pavement slab; (f) the inertia of the subgrade; and (g) the dynamics of the vehicle.

It is anticipated, however, that many or all of these refinements will contribute only second-order or smaller perturbations to the present solutions, especially for the relatively low velocity ratios characteristic of contemporary or future vehicles. Accordingly, the current major requirement in the program of "road loading mechanics" research is the necessity for an experimental program to indicate the validity of the postulated, analytical model of the road-subgrade system.

ACKNOWLEDGMENT

The research effort reported in this paper was sponsored by the Office of Research, U.S. Bureau of Public Roads, under contracts CPR-11-7863 and CPR-11-7993.

REFERENCES

1. "The AASHO Road Test: Report 2—Materials and Construction." HRB Special Report 61B (1962).
2. Bernoulli, D., "Comenentarii Academiae Scientiarum Imperialis Petropolitanie." Vol. 13 (1751).

3. Clark, D.C., "On the Kinetic Behavior of Roads." HRB Proc., 40:179-204 (1961).
4. Cole, J., and Huth, J., "Stresses Produced in a Half Plane by Moving Loads." Jour. of Applied Mechanics, 25:4, 433-436 (1958).
5. Crandall, S.H., "The Timoshenko Beam on an Elastic Foundation." Proc., Third Midwestern Conf. on Solid Mech., Univ. of Michigan Press (1958).
6. Eringen, A.C., and Samuels, J.C., "Impact and Moving Loads on a Slightly Curved Elastic Half Space." Jour. of Applied Mechanics, 26E:4, 491-498 (1959).
7. Euler, L., "Methodus inveniendi lineas curvas maximi minimive proprietate gandentes." Additamentum, "De curvis elasticis." (1744).
8. Fabian, G.J., Clark, D.C., and Hutchinson, C.H., "Preliminary Analysis of Road Loading Mechanics." HRB Bull. 250, 1-19 (1960).
9. Grinter, L.E., "Elementary Structural Analysis and Design." Macmillan (1947).
10. Kenney, J.T., "Steady-State Vibrations of Beam on Elastic Foundation for Moving Load." Jour. of Applied Mechanics, 21:4, 359-364 (1954).
11. Lamb, H., "On Waves in an Elastic Plate." Proc., Royal Society of London, 93A: 114-128 (1916).
12. Livesley, R.K., "Some Notes on the Mathematical Theory of a Loaded Elastic Plate Resting on an Elastic Foundation." Quarterly Jour. of Mech. and Applied Math., Vol. 6, Pt. 1, 32-44 (1953).
13. Mann-Nachbar, P., "On the Role of Bending in the Dynamic Response of Thin Shells to Moving Discontinuous Loads." Jour. of Aerospace Sciences, 29:6, 648-657 (1962).
14. Mathews, P.M., "Vibration of a Beam on Elastic Foundation." I, II, Zeitschrift für Angewandte Mathematik und Mechanik, 38: 3/4, 105-115 (1958); 39:1/2, 13-19 (1959).
15. Mindlin, R.D., "Influence of Rotatory Inertia and Shear on Flexural Motions of Isotropic Elastic Plates." Jour. of Applied Mechanics, 18:1, 31-38 (1951).
16. Norris, C.H., Hansen, R.J., Holley, M.J., Biggs, J.M., Namyet, S., and Minami, J.K., "Structural Design for Dynamic Loads." McGraw-Hill (1959).
17. Piszczek, K., "The Possibility of Dynamic Stability Loss Under Moving Concentrated Loads." (In English) Archiwum Mechaniki Stosowanej, 10:2, 195-210 (1958).
18. Rayleigh, Lord (J.W. Strutt), "On the Free Vibrations of an Infinite Plate of Homogeneous Isotropic Elastic Matter." Proc., London Math. Soc., 20:225-234 (1889).
19. Routh, E.J., "Dynamics of a System of Rigid Bodies." Advanced part, 6th ed., Macmilan (1905). (Reprinted by Dover Publications, 1955.)
20. Thompson, W.E., "Analysis of Dynamic Behavior of Roads Subject to Longitudinally Moving Loads." Report No. VJ-1620-V-1, Cornell Aeronatical Lab. (June 1961).
21. Timoshenko, S.P., "On the Correction for Shear of the Differential Equation for Transverse Vibrations of Prismatic Bars." Philosophical Magazine, 41:245, 744-746 (1921). (See also Collected Papers, McGraw-Hill, 1953.)
22. Timoshenko, S.P., "On the Transverse Vibration of Bars of Uniform Cross-Section." Philosophical Magazine, 43:253, 125-131 (1922). (See also Collected Papers, McGraw-Hill, 1953.)

Appendix

NOMENCLATURE

A = beam or plate cross-sectional area (sq in.).

$A_1, A_2, A_3, \ldots$ = real parts of the roots of the characteristic equation.

a = an abbreviation; $a = 4\theta^2$.

$B_1, B_2, B_3, \ldots$ = imaginary parts of the roots of the characteristic equation.

b = an abbreviation; $b = 8\theta\zeta$.

$C, C_1, C_2 \ldots$ = constants of integration.

c = internal viscous damping coefficient for elastic subgrade (lb-sec/in.).

c' = damping coefficient/unit length of beam (lb-sec/in.)/(in.).

c'' = damping coefficient/unit area of plate (lb-sec/in.)/(sq in.).

c''_{cr} = critical value of the damping coefficient (lb-sec/in.)/(sq in.).

D = flexural rigidity of the plate (psi/in.).

D_1, D_2, D_3 = constants of integration.

E = modulus of elasticity (psi).

E_1, E_2, E_3 = constants of integration.

e = base of natural logarithms (e = 2.71828).

F_1, F_2, F_3 = constants of integration.

G_1, G_2, G_3 = constants of integration.

h = plate thickness taken in transverse direction (in.).

I = moment of inertia (in.^{4}).

i = the imaginary operator; $i = (-1)^{\frac{1}{2}}$.

k = spring constant for elastic subgrade (lb/in.).

k' = spring constant/unit length of beam (lb/in.)/(in.).

k'' = spring constant/unit area of plate (lb/in.)/(sq in.).

$m, m_1, m_2, \ldots$ = roots of the characteristic equation.

$\hat{m}$ = an abbreviation for the root, $m/\beta = \hat{m}$.

P' = concentrated, transverse moving load/unit width of road (lb/in.).

q = loading (lb).

q' = load intensity or force/unit length of beam (lb/in.).

q'' = load intensity/unit width or force/unit area (psi).

$\bar{t}$ = time (sec).

U = constant velocity of the moving load (in./sec).

U_{cr} = propagation velocity of a flexure wave in a freely vibrating, undamped, elastically supported plate (in./sec).

u, v, w = displacements in the x, y, z directions, respectively (in.).

w_o = deflection of road under the load for the static case where the load velocity vanishes (in.).

$\bar{x}, \bar{y}, \bar{z}$ = Cartesian coordinates (longitudinal, lateral and transverse directions, respectively) fixed with respect to the road.

x, y, z = Cartesian coordinates fixed with respect to the moving load.

β = wave number of plate vibrations—wave number is reciprocal of the wave length (rad/in.).

Δ = the discriminant of the "reduced" quartic characteristic equation.

ϵ = arbitrarily small longitudinal distance from point of load application.

ζ = damping ratio: $\zeta = c'' / c''_{cr}$.

η = an abbreviation having three similar uses: $\eta = A_1/\beta$, $\eta = A_3/\beta$, $\eta = A_5/\beta$.

θ = velocity ratio: $\theta = U/U_{cr}$.

ν = Poisson's ratio.

ρ = density (mass/unit volume) of pavement material (lb-sec^2/in.^{4}).

A Review of Soil-Pole Behavior

M. T. DAVISSON and SHAMSHER PRAKASH, respectively, Assistant Professor of Civil Engineering, University of Illinois, Urbana, and Reader in Civil Engineering, University of Roorkee, Roorkee, India

The behavior of a pole embedded in soil is reviewed in the light of modern soil mechanics. A compilation and interpretation of the available published and unpublished test results provide the background information used in a discussion of the real behavior of a soil-pole system. A theoretical analysis is presented that accounts for vertical, lateral and moment loads on the pole; the nature of the previous theoretical work available in the literature is tabulated for comparison. The proposed analytical techniques also include a simple quantitative means for determining if a flexural member is rigid enough that its deflection can be described solely as a rotation.

In application of the analytical techniques to pole designs a simple means of approximating the strength and subgrade modulus of the soil is shown to be necessary. A simple static soil penetrometer test is suggested as a practical device for field use. Other variables that must be considered in developing pole design standards are the method of construction, the loading conditions and the geometrical configuration of the poles.

• THE USES or service classifications of poles are numerous; they vary from tent stakes and fence posts to supports for the heavy signs used by many highway departments and outdoor advertising companies. Lateral loads on poles may arise from wind, guy wires and/or an alignment change on power poles. Moment loads may be due to couples, lateral loads and/or eccentric vertical loads. Vertical loads may be exerted by signs, power lines, guy wires and transformers. Additional loads of consequence can arise from earthquake motions if an appreciable mass is supported by a pole. The nature of the loading on a pole can also be of some consequence; for instance, cyclic loading is usually more serious than a static loading of equal magnitude.

The purpose of this paper is to provide a review of previous theoretical and experimental work on the soil-pole problem and to explain soil-pole behavior so that realistic pole design procedures may be developed. A critical analysis of the available experimental data will provide the basis for a physical interpretation of the interaction between a pole and the soil surrounding it. Further, a comprehensive analytical procedure will be developed that accounts for the lateral, vertical and moment loads on the pole and, in addition, provides for a wide range in soil behavior. An initial inclination of the pole is also considered in the analysis. The results of tests in typical soils will be evaluated in light of the preceding analysis and discussion of soil-pole behavior. Suggestions will be given for using the information contained herein in the development of pole design standards for different pole service classifications. Finally, it will be recommended that for practical use, the strength and subgrade modulus of different soils be correlated with a simple static penetrometer test performed in the field.

STATEMENT OF PROBLEM

Poles are considered herein as essentially rigid members whose lateral deflections under load are primarily due to rotation about a point along the embedded length of the

Paper sponsored by Committee on Stress Distribution in Earth Masses.

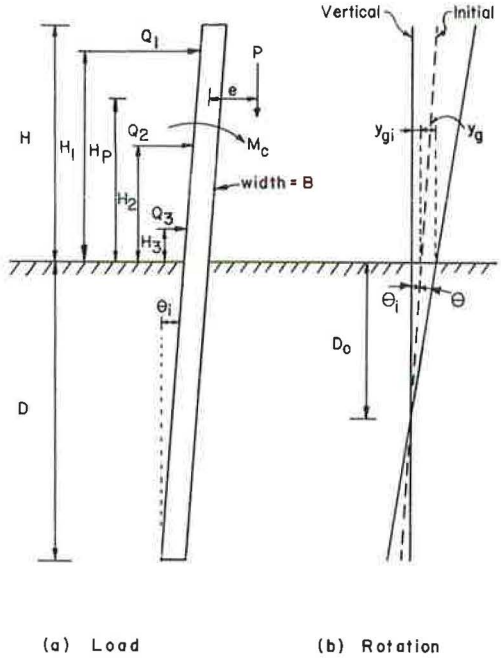

Figure 1. Loads acting on a pole.

pole. A criterion will be given for determining when the flexural member that serves as the pole is stiff enough to be considered rigid. Because the rotational resistance of a rigid pole is governed solely by the load-deformation characteristics of the soil adjacent to the embedded portion of the pole, it is the soil that controls the behavior of a laterally loaded soil-pole system.

Figure 1a shows a pole of width B (normal to the direction of loading), embedded for a length D, and subjected to a system of lateral loads Q_1, Q_2, and Q_3 at distances H_1, H_2, and H_3 above the ground surface. For generality, a couple M_c and a vertical load P acting with an eccentricity e from the pole axis are also shown. Because an initial rotation θ_i is likely to be experienced under field conditions and because it leads to additional moments when vertical loads are present, it has been included as a variable. The pole is shown in Figure 1b as rotating an angle θ about a point at a depth D_o below the ground surface; the horizontal deflections y are measured with respect to a vertical line through the point of rotation. The initial rotation θ_i causes an initial deflection y_{gi} to exist at the ground surface; an additional deflection y_g is caused by the applied loads. Soil reactions which must be in equilibrium with the applied loads are induced by the pole rotation. The nature of the soil reactions for different soil types and loading conditions is discussed subsequently.

The scope of this paper is limited to isolated, rigid, vertical or slightly inclined poles, embedded in a homogeneous soil and subjected to vertical, lateral and moment loads. Generally poles are not placed close enough to each other that group action becomes important; however, if poles are spaced at 3 diameters or less normal to the direction of the loading, and/or 6 diameters or less parallel to the loading, group action will develop. If necessary, the effects of group action may be estimated from the work of Prakash (1).

SOIL RESISTANCE

The following discussion of soil-pole interaction represents the authors' theoretical reasoning and interpretation of the available test results. The discussion will be developed by studying the soil behavior as the lateral load on a pole is increased to failure.

Pole Rotation

Figure 2a shows a pole of width B and embedment D subjected to an increasing lateral load Q at a distance H above the ground surface. As the load Q is increased, four successive rotated positions (i to iv) are shown in Figure 2b. The net soil reaction w (force/unit of depth) is plotted versus depth in Figure 2c for the successive stages of rotation. It should be noted that w is the total reaction across the width B of the pole; it is usually considered to act uniformly across the width B, whereas in reality it represents the increase in pressure on the loaded face of the pole minus the decrease in pressure on the backside of the pole plus the shear resistance along the sides of the pole. The soil reactions for three depths (B, 2B and 3B) are plotted versus the corresponding deflections in Figure 2d. As the load is increased the point of rotation shifts downward along the pole. Furthermore, the upper point of relative

Failure

As the rotation of a pole is increased to failure, three general modes of failure may be identified. A flexural failure of the pole may occur above or below the groundline depending on the flexural properties of the pole and the nature of the loading. The elimination of a flexural failure is a simple matter once the moments along the embedded portion of the pole are known; a procedure will be given subsequently for estimating the moments. Another mode of failure is excessive rotation which may or may not be due to plastic soil behavior. Finally, a complete collapse of the pole can occur when a sufficient amount of plastic soil behavior has developed. The latter behavior has been illustrated by Krynine (3) in tests wherein the point of rotation moved downward along the pole until at large rotations it shifted to the ground surface; a wedge of soil equal to the embedded length of the pole was then forced upward as shown in Figure 4a. Appleford (4) attempted to analyze this state of total collapse by bounding the wedge with a line from the bottom of the pole inclined at an angle of 60 degrees; Williams (5) performed a similar analysis using an angle of 45 degrees.

Ultimate Soil Resistance

A discussion of the ultimate soil resistance that is available to resist the rotation of a pole will aid in understanding the soil-pole behavior at loads near the collapse load. Figure 4b shows a fully plastic distribution of soil reactions along the embedded portion of a pole (solid line). In reality, for loads near the collapse load where large rotations are observed, the actual distribution of the soil reactions is more in agreement with the dotted line in Figure 4b. It may be reasoned that collapse is impending when either the upper or lower point of maximum soil reaction reaches the fully plastic condition. Therefore, if the soil reactions and the ultimate soil resistance can be predicted, the ultimate soil resistance can be divided by a factor of safety to obtain a limit to the working values of the soil reactions.

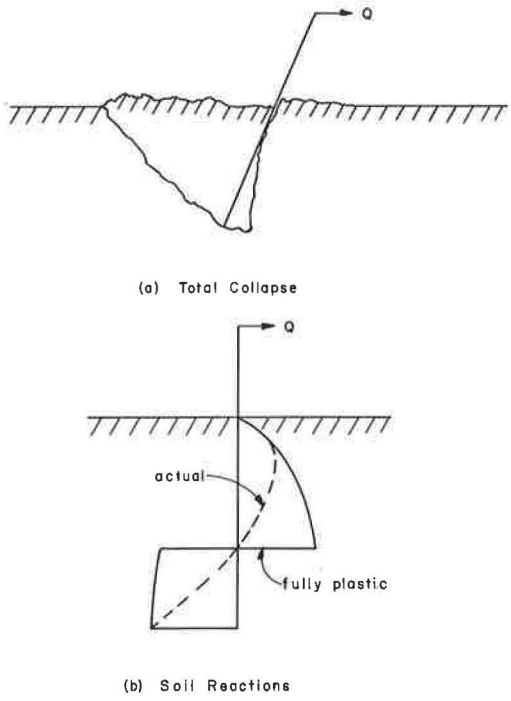

Figure 4. Collapse conditions for a pole.

If the loaded face of a pole is considered to be infinite in lateral extent it then becomes a wall; the ultimate soil resistance against a wall is the familiar two-dimensional passive pressure. Many investigators have assumed, mistakenly, that the ultimate soil resistance offered to a pole is the two-dimensional passive pressure. Actually the problem is three-dimensional because of the end effects at the edges of the pole; therefore, the ultimate soil resistance must exceed the two-dimensional passive pressure. At depth, a lateral translation of the pole will deform the soil in a mode similar to that for the bearing capacity of a deep footing. The problem then becomes that of the two-dimensional bearing capacity of a footing completely surrounded by soil. The ultimate soil resistance, therefore, varies with the depth below the ground surface even though the strength parameters φ and c are constant with respect to depth. In summary, the ultimate soil resistance is slightly in excess of the two-dimensional passive earth pressure at the ground surface; it increases with depth as it makes a transition to that given by the two-dimensional lateral bearing capacity.

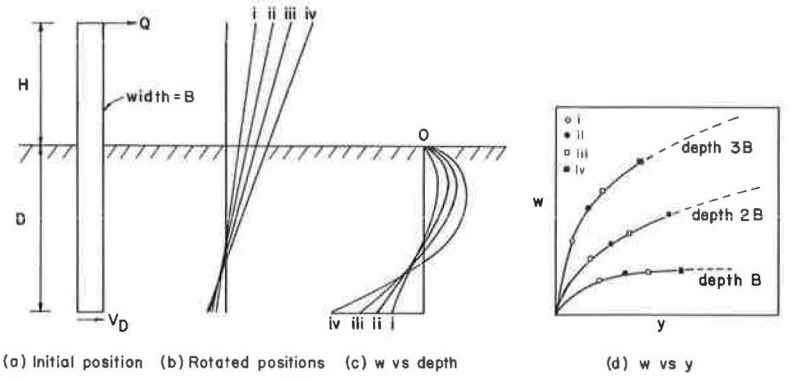

Figure 2. Pole rotation and soil reactions.

maximum soil reaction shifts downward along the pole although the same qualitative shape of the soil reaction versus depth diagram is maintained. The geometry of the pole rotation requires the largest deflections to occur at the ground surface and at the bottom of the pole; therefore, the soil resistance initially becomes plastic in these two areas before spreading downward and upwards along the pole. Generally, plastic soil resistance is observed near the ground surface even if it does not occur at the bottom of the pole. The w versus y curves in Figure 2d illustrate the foregoing discussion. At depth B plastic behavior is observed, whereas at depths 2B and 3B the soil reactions are at successively smaller percentages of the ultimate values. The ultimate soil resistance increases with depth even though the strength parameters, the cohesion c and the angle of internal friction φ, are constant with depth.

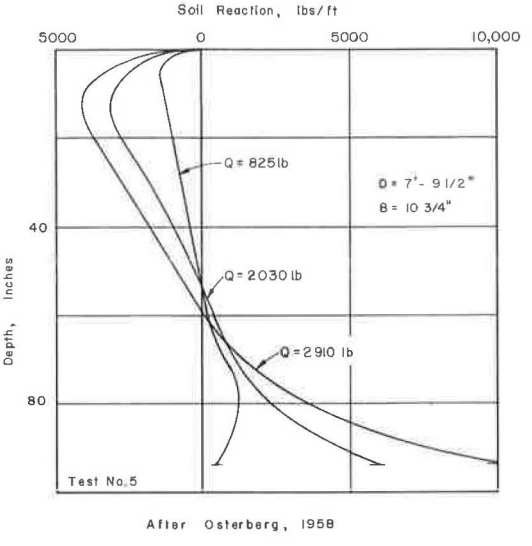

Figure 3. Soil reaction vs depth from a test in clay.

Shear on Bottom of Pole

Another element of resistance that is usually ignored in pole analyses is the sheer V_D acting along the bottom of the pole (Fig. 2a). Neglecting V_D is conservative for design purposes but the analysis of test results becomes difficult because it may or may not be present or may be present in the earlier stages of loading and practically disappears during the later stages. For laterally loaded piles V_D is ignored because piles are usually long enough that the effect of V_D cannot be detected. As the embedded length of the flexural member is decreased into the range of that for poles, V_D becomes progressively more important. Finally, for very short poles which are really block foundations, the incorporation of V_D into an analysis becomes a necessity as is also true with the vertical pressures on the bottom of the foundation. Figure 3 shows several soil reaction versus depth curves for a test on a pole in stiff clay that was reported by Osterberg (2). Under the 825-lb load, the action of V_D on the bottom of the pole is quite pronounced, whereas for higher loads its action appears negligible.

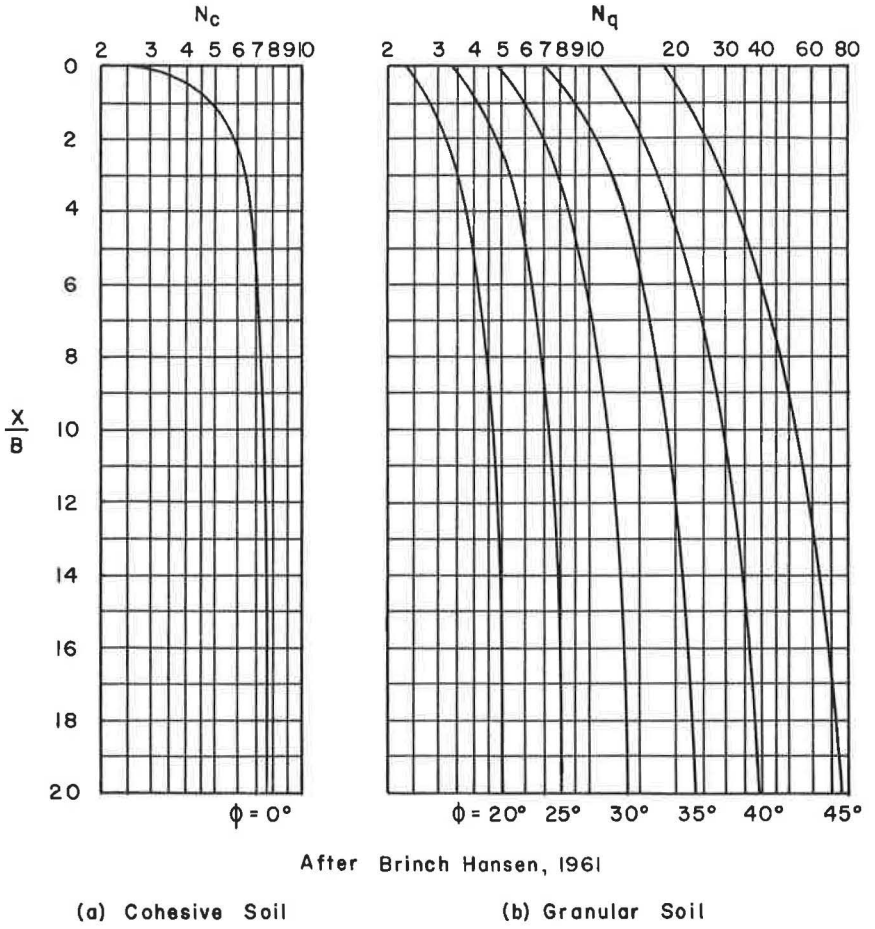

Figure 5. Bearing capacity factors vs depth.

Several authors have observed the foregoing behavior. Minikin (6) found that the ultimate soil resistance offered to poles was 2.3 to 3.4 times greater than that offered to a wall in the same soil. Krynine (7) has shown that the ultimate soil resistance was proportional to the depth for a wall and to the second power of depth for a pole. In addition, Stobie (8) measured pressures against a pole in excess of Rankine's passive pressure.

The unit lateral bearing capacity of cohesive soils ($\varphi = 0^0$ condition) can be expressed as cN_c where N_c is a dimensionless bearing capacity factor. Meyerhoff (9) has computed N_c to be as high as 11.42, whereas Brinch Hansen (10) has computed 8.14. MacKenzie's (11) tests indicate that a value between 8 and 9 is appropriate for N_c. Brinch Hansen (10), on the basis of reasonable assumptions, has computed the ultimate soil resistance against a pole as a function of depth for both cohesive and granular soils; Figure 5 shows the essential results of Hansen's theory. In this paper soils will be treated as either cohesive ($\varphi = 0^0$) or granular ($c = 0$). Correspondingly, Figure 5a shows N_c versus the depth x divided by the pole width B. The ultimate soil reaction for a cohesive soil is then expressed as

$$w_u{}^x = B c N_c{}^x \qquad (1)$$

in which the superscript x indicates that w_u corresponds to the depth x for which N_c was determined. Similarly, Figure 5b shows N_q plotted versus x/B for various values

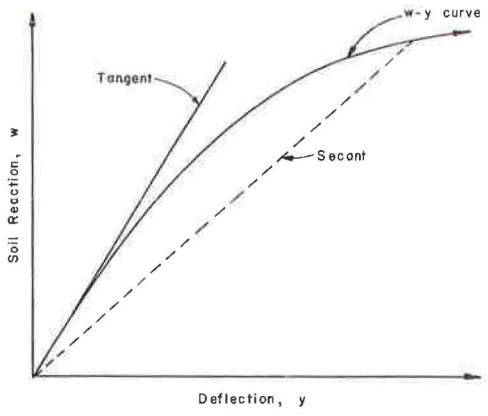

Figure 6. Soil reaction vs deflection.

of φ where N_q is a dimensionless bearing capacity factor dependent on φ. The ultimate soil reaction of a granular soil is then expressed as

$$w_u{}^x = Bq' N_q{}^x \qquad (2)$$

where q' is the vertical effective stress at the depth x.

Subgrade Modulus

To calculate the soil reactions consistent with a given rotated position of the pole, some knowledge of the soil reaction versus deflection relationship (w vs y) is required. If the soil reactions can be determined under given conditions, then they may be compared to the ultimate soil resistance for the purpose of estimating the factor of safety against a total collapse of the pole.

Figure 6 shows a typical w-y curve for soil. For soil reactions of less than one-third to one-half of the ultimate soil reaction, the w-y relationship can be expressed adequately by a tangent modulus. For larger soil reactions a secant modulus is more appropriate. Because it will generally be desirable to keep the soil reactions smaller than one-third of the ultimate soil reaction, the discussion as developed herein will be concerned with the tangent modulus k (expressed in units of force/length^2)

$$k = \frac{w}{y} \qquad (3)$$

If a reasonable variation of k with depth can be formulated, then a pole may be analyzed as a rigid member restrained by a series of infinitely closely spaced independent elastic springs. This is the concept of a subgrade modulus.

In using a subgrade modulus to define the soil stiffness it is assumed that the springs are independent, whereas in reality they are interrelated in a complex fashion. The error involved may be estimated by considering the contribution of Vesic (12) who extended Biot's (13) work concerning a flexible beam supported on an elastic half-space. For long relatively flexible members such as piles the error in the computed bending moments based on the subgrade modulus assumption was no more than a few percent when compared to the theory of elasticity solution. The error increased to as much as 14 percent for relatively short and essentially rigid beams. Therefore, the subgrade modulus concept has a reasonable theoretical foundation; it is believed to be more than adequate for the pole problem.

Several variations of the subgrade modulus with depth have been used in pole theories. The most useful variation was that developed by Miche (14), Titze (15) and later Palmer and Thompson (16); they expressed the modulus as

$$k_x = K\left(\frac{x}{D}\right)^n \qquad (4)$$

in which K is the value of k at the bottom of the pole and n is an empirical coefficient equal to or greater than zero. Figure 7 shows the variation of k with depth for various values of n. Most authors of pole theories assumed that n = 0 for clays, or that the modulus was constant with depth, and n = 1 for granular soils, or that the modulus increased directly with depth.

The theoretical reasoning of Terzaghi (17) indicates that n is approximately unity for sands and, in addition, virtually all of the test results in granular soils can be adequately analyzed with n = 1 although there are indications that an n-value of 1.5 may be more

appropriate. No conclusive test results are available for clays, but on the basis of the previous discussion concerning the w-y relationships in Figure 2d, it is likely that a value of n greater than zero is more realistic than a value of zero. A tentative value of 0.15 for n is herein suggested on the basis of the information presently available; this has the effect of including an allowance for plastic soil behavior at the ground surface. It should not be expected that a unique relationship in the form of Eq. 4 can be obtained for the variation of k with depth in clay soils because the D/B ratio, the nature of the loading, and the soil itself all affect k. However, some reasonable n-value is likely to be adequate for the majority of preloaded clays that are encountered.

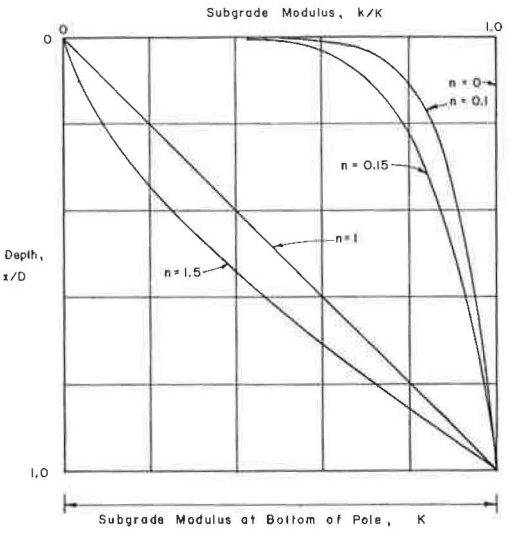

Figure 7. Variation of subgrade modulus with depth.

Terzaghi (17) has presented an extensive discussion regarding the effect of size of the loaded area on the subgrade modulus. For example, a loaded pole of width B produces soil reactions w and deflections y. If another pole of equal embedment in the same soil but of width 2B is subjected to the same loading, the soil reactions and deflections will be equal to those for the pole of width B. Although the unit soil pressures across the face of the pole with width 2B are one-half those for the pole with width B, the dimensions of the stressed volume of soil are doubled because of the size of the loaded area; therefore, the deflections at the faces of the two poles are equal. After k has been determined for a given pole its value is unchanged if the pole width B is changed.

Poles Widened at the Ground Surface

The foregoing discussion concerning the size of the loaded area was based on the assumption of linear elastic behavior for the soil. Actually, as shown in Figure 2d, plastic soil behavior is likely to develop at the ground surface. In the analysis of a pole with uniform width B this behavior will be accounted for by using an empirically predetermined elastic modulus variation with depth that really involves both the secant modulus (Fig. 6) near the ground surface and the tangent modulus at greater depths. If a pole of width B were to be widened, for example to width 2B for some depth below the ground surface, strictly elastic considerations would indicate no change in the load-deflection behavior. In actuality, the ultimate soil reaction for the enlarged portion of the pole is approximately doubled because it depends on the width, whereas the soil reaction itself is only slightly increased. This has the effect of increasing the magnitude of the secant modulus (Fig. 6) because the soil reaction is now a smaller percentage of the ultimate soil reaction than it was for an unenlarged pole section; therefore, the deflections should be reduced.

Anderson (18) and Osterberg (2) have shown large reductions in the rotation of poles that have been enlarged or otherwise stiffened at the ground surface when compared to unenlarged poles. Davisson and Gill (19) have analytically studied a similar effect for laterally loaded piles and found that reductions of 50 percent in the lateral deflection of the pile under a given load are easily obtained.

Effect of Pole Shape

Conflicting opinions have been reported in the literature on the effect of the shape of the pole on its behavior. Czerniak (20) believes that because the maximum pressure against the middle element of a circular pole is 1.57 times the average pressure on the

projected area, or on a flat surface equal in width to the pole diameter, and that because a curved surface can penetrate the soil more easily than a flat surface, the effectiveness of a round pole must be lower than that of a square pole. Shilts, Graves and Driscoll's (21) experimental evidence on model poles in sands showed that a 3-in. diameter pole moved more (approximately 33 %) under a given load than a 3-in. square section. On the other hand, Williams (5) concluded from his tests on model poles that square poles of width B could withstand only about 90 percent of the overturning moment withstood by poles with a circular section of diameter B.

Davisson (22) analyzed Nakamura's (23) tests on 6-cm wide model poles embedded in sand. The shapes studied were round, square, and diamond. The diamond-shaped poles were actually square bars loaded along the diagonal rather than along a side. According to this analysis, the shape of the pole cross-section has a negligible effect on the soil resistance and pole deflections.

Effect of Cyclic Loading

Several aspects of soil behavior may influence the strength and stiffness of the soil surrounding a pole. As an example, cyclic loading may remold an undisturbed cohesive soil by the process of repeated shearing deformations. This will reduce both its strength and stiffness. However, a rest period may produce an increase in strength and stiffness depending on the thixotropic and consolidation characteristics of the soil. Similar events can occur for poles that are driven into clay soils. Matsuo (24) has shown that the lateral load resistance of driven poles increases with time after driving because of the strength increase caused by thixotropy and consolidation under the high horizontal pressures induced by driving the pole.

Cyclic loading usually causes a permanent displacement of the soil at the ground surface, thereby leaving a gap between the soil and the pole. This has the effect of reducing the subgrade modulus k to zero, regardless of its initial value. Therefore, an n-value of zero in Eq. 4 is virtually an impossibility.

Effect of Climate and Method of Construction

The soil resistance may vary considerably according to the season. Seasonal moisture variations brought on by floods, rains, frost action, droughts or other causes may exert a controlling influence on the soil resistance. For purposes of design or research, the worst soil condition should be studied.

Construction procedures also control, to a large extent, the behavior of a soil-pole system. Poles may be placed in loose or tight fitting holes that have been hand-dug or bored; they may also be driven into place. The backfill around a pole may be loose or compact or may vary considerably in thickness (horizontally), depending on the size of the hole. Good construction practice calls for a tamped or otherwise compacted fill. If the fill is thin, the load-deformation characteristics of the undisturbed soil around the pole will control the behavior. For a thick fill, the behavior may be controlled entirely by the load-deformation characteristics of the fill.

ANALYTICAL STUDIES

In the analysis of a pole it is assumed that the pole is rigid enough that its deflected shape can be described by a rotation. As the embedment of a given pole section is increased, the greater is the possibility that this assumption will become invalid. For a flexural member embedded in an elastic medium wherein k can be assumed to be constant with respect to depth (n = 0), solutions are available that define the depth to which a pole may be assumed rigid. Grandholm (25) and later Davisson and Gill (19) have suggested the following criterion: If the depth D divided by the relative stiffness factor R (Eq. 5) is equal to or less than 2, then the pole may be considered rigid.

$$R = \sqrt[4]{\frac{EI}{K}} \qquad (5)$$

$$\frac{D}{R} \leq 2 \text{ (rigid pole)} \tag{6}$$

EI represents the flexural stiffness of the pole. It is recommended that Eqs. 5 and 6 be used to approximate the limits of a pole in cohesive soils even though n is closer to 0.15 than it is to zero.

For granular soils (n = 1) Eq. 4 reduces to

$$k_x = n_h x \tag{7}$$

where n_h is the constant of the horizontal subgrade reaction equal to K/D and with units of force/length^3. Matlock and Reese (26) and Davisson (22) have proposed a criterion, similar to that given above, for poles embedded in soils for which the subgrade modulus is directly proportional to depth. It is recommended that the following equations be used for granular soils and for any other soils for which an n-value of unity is a good approximation:

$$T = \sqrt[5]{\frac{EI}{n_h}} \tag{8}$$

$$\frac{D}{T} \leq 2 \text{ (rigid pole)} \tag{9}$$

Again, T is a relative stiffness factor.

In the following analysis the initial inclination of a pole may be of significance if a vertical load is acting on the pole. Furthermore, it is necessary that the vertical load placed on the pole does not exceed the critical vertical load P_{cr}. Because the complete analysis is facilitated if the axial load P is expressed as αP_{cr}, where α equals P/P_{cr}, the expressions for P_{cr} will be given first.

An initially vertical pole embedded for a depth D is considered to be subjected to a vertical load P at a distance H_p above the ground surface. If it is assumed that the shear V and the moment M are zero at the bottom of the pole ($V_D = M_D = 0$), and that $\sin\theta$ is approximately equal to θ, then the soil-pole system is essentially a rigid bar restrained by a moment spring. The characteristics of the moment spring are those of the soil as represented by the modulus of subgrade reaction which is considered to be governed by Eq. 4. On the basis of the foregoing assumptions Prakash (27) has derived the following equation for P_{cr}:

$$P_{cr} = \frac{KD^2}{(n+3)(n+2)^2\left(1+\frac{H_p}{D}\right)} \tag{10}$$

It is presumed that the vertical bearing capacity of the pole is sufficient to carry the imposed vertical load or that the pole is adequately designed as a pile.

Figure 8 illustrates the general conditions considered in the following pole analysis. In Figure 8a a pole of width B normal to the plane of the loading is embedded for a length D and unsupported for a length H. It is inclined at an angle θ_i before being subjected to the moment M_g and the horizontal load Q_g at the ground surface plus the vertical load P at a distance H_p above the ground surface. M_g is the resultant moment for all the horizontal loads and couples on the pole and includes the moment due to the eccentricity of the vertical load from the pole axis. Likewise, Q_g is the summation of all horizontal loads. The pole is shown rotated through the angle θ in Figure 8b; x is the depth coordinate measured from the ground surface and D_o is the depth to the point of rotation. Eq. 4 expresses the soil stiffness shown schematically in Figure 8c and

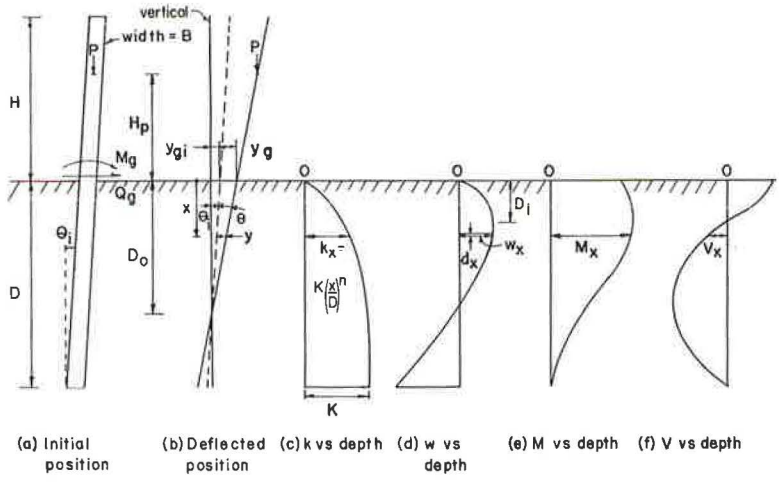

Figure 8. Variables considered in the pole analysis.

the soil reactions develop as shown in Figure 8d. The general shapes of the moment and shear diagrams versus depth are shown in Figure 8e and f, respectively. Assuming that $\sin\theta$ is approximately equal to θ and that the shear and moment are zero at the bottom of the pole ($V_D = M_D = 0$), the following expressions have been developed by Prakash (27):

$$\frac{D_o}{D} = \frac{\frac{M_g}{Q_g D} + \frac{n+2}{n+3} - \frac{\alpha}{(n+2)(n+3)} + \frac{\alpha \theta_i K D^2}{(n+3)(n+2)^2 Q_g}}{\frac{n+2}{n+1}\frac{M_g}{Q_g D} + \frac{\alpha \theta_i K D^2}{(n+1)(n+2)(n+3) Q_g} + 1} \tag{11}$$

$$y_g = \frac{(n+2) Q_g \frac{D_o}{D}}{KD\left(\frac{n+2}{n+1}\frac{D_o}{D} - 1\right)} \tag{12}$$

$$\theta = \frac{y_g}{D_o} \tag{13}$$

$$w_x = K\left(\frac{x}{D}\right)^n y_g \frac{D_o - x}{D_o} \tag{14}$$

With the foregoing equations the moments and shears along the embedded portion of the pole can be computed. To check the upper and lower points of relative maximum soil reaction against the ultimate soil resistance, an expression for the depth D_1 (Figure 8d) is needed. The upper point of maximum soil reaction occurs at

$$D_1 = \frac{n}{n+1} D_o \tag{15}$$

whereas the lower maximum is at the depth D.

It should be noted that the principle of superposition was assumed valid in the derivations. This follows directly from the assumption of linear elastic soil behavior. Because these equations are intended for use in the range of small rotations, as is desirable under working conditions, the soil behavior should be nearly elastic; therefore, the principle of superposition becomes a reasonable approximation.

For granular soils and for any other soils for which an n-value of unity is reasonable, Eqs. 10, 11, 12, and 14 reduce to the following equations on substitution of n = 1 and $K = n_h D$

$$P_{cr} = \frac{n_h D^3}{36\left(1+\frac{H_p}{D}\right)} \quad (n = 1) \tag{16}$$

$$\frac{D_o}{D} = \frac{\frac{M_g}{Q_g D} + \frac{3}{4} - \frac{\alpha}{12} + \frac{\alpha \theta_i n_h D^3}{36\, Q_g}}{\frac{3}{2}\frac{M_g}{Q_g D} + \frac{\alpha \theta_i n_h D^3}{24\, Q_g} + 1} \quad (n = 1) \tag{17}$$

$$y_g = \frac{3\, Q_g \frac{D_o}{D}}{n_h D^2\left(\frac{3}{2}\frac{D_o}{D} - 1\right)} \quad (n = 1) \tag{18}$$

$$w_x = \frac{3\, Q_g}{D\left(\frac{3}{2}\frac{D_o}{D} - 1\right)}\left(\frac{D_o}{D} - \frac{x}{D}\right)\frac{x}{D} \quad (n = 1) \tag{19}$$

On substitution of the proper depths in Eq. 19 the two maximum soil reactions may be expressed as follows:

$$w_{D1} = \frac{3\, Q_g}{D\left(\frac{3}{2}\frac{D_o}{D} - 1\right)}\left(\frac{D_o}{2D}\right)^2 \quad (n = 1) \tag{20}$$

$$w_D = \frac{3\, Q_g}{D\left(\frac{3}{2}\frac{D_o}{D} - 1\right)}\left(\frac{D_o}{D} - 1\right) \quad (n = 1) \tag{21}$$

Similarly, for preloaded cohesive soils for which an n-value of 0.15 is tentatively offered

$$P_{cr} = \frac{KD^2}{14.6\left(1+\frac{H_p}{D}\right)} \quad (n = 0.15) \tag{22}$$

$$\frac{D_o}{D} = \frac{\frac{M_g}{Q_g D} + 0.683 - \frac{\alpha}{6.78} + \frac{\alpha\theta_i K D^2}{14.6 Q_g}}{1.87\frac{M_g}{Q_g D} + \frac{\alpha\theta_i K D^2}{7.80 Q_g} + 1} \quad (n = 0.15) \tag{23}$$

$$y_g = \frac{2.15 Q_g \frac{D_o}{D}}{KD\left(1.87\frac{D_o}{D} - 1\right)} \quad (n = 0.15) \tag{24}$$

$$w_x = \frac{2.15 Q_g}{D\left(1.87\frac{D_o}{D} - 1\right)}\left(\frac{D_o}{D} - \frac{x}{D}\right)\left(\frac{x}{D}\right)^{0.15} \quad (n = 0.15) \tag{25}$$

$$w_{D1} = \frac{2.15 Q_g}{D\left(187\frac{D_o}{D} - 1\right)}\left(0.870\frac{D_o}{D}\right)\left(0.130\frac{D_o}{D}\right)^{0.15} \quad (n = 0.15) \tag{26}$$

$$w_D = \frac{2.15 Q_g}{D\left(1.87\frac{D_o}{D} - 1\right)}\left(\frac{D_o}{D} - 1\right) \quad (n = 0.15) \tag{27}$$

The preceding equations are tractable once the quantity D_o/D is determined. If θ_i is taken as zero, Eq. 11 can be solved by the use of graphs similar to Figure 9a for the solution of Eq. 17 and Figure 9b for the solution of Eq. 23. A somewhat more complicated nomograph can be developed that will account for any of the parameters that it is desired to vary. Because poles are generally considered to be subjected to some standard loading and because large quantities of similar poles are used, a nomograph can be developed for each standard pole type. This approach will greatly reduce the necessary calculations when a large number of similar poles are under consideration.

REVIEW OF THEORETICAL DEVELOPMENTS

The development of adequate pole theories has been a rather slow process. A pole foundation involves most of the uncertainties that are present in large and very important projects; these uncertainties may be grouped under the headings of soil properties and the interaction between the soil and the foundation when a load is applied. Therefore, the desire for a simple pole design procedure is analogous to the desire for a magic wand to aid in the solution of foundation engineering problems. Simple design procedures can be developed for a limited range of variables, but their development requires a broad understanding of the problem.

The earlier theories tried to predict the lateral load necessary to overturn a pole; it was usually assumed that the ultimate soil resistance was equal to the two-dimensional passive pressure. This resulted in very conservative expressions for the overturning force. Although Carpentier (28), Demogue (29) and Stobie (8) recognized the error involved in using the two-dimensional passive pressure, other authors continued to develop and publish a proliferation of erroneous theories.

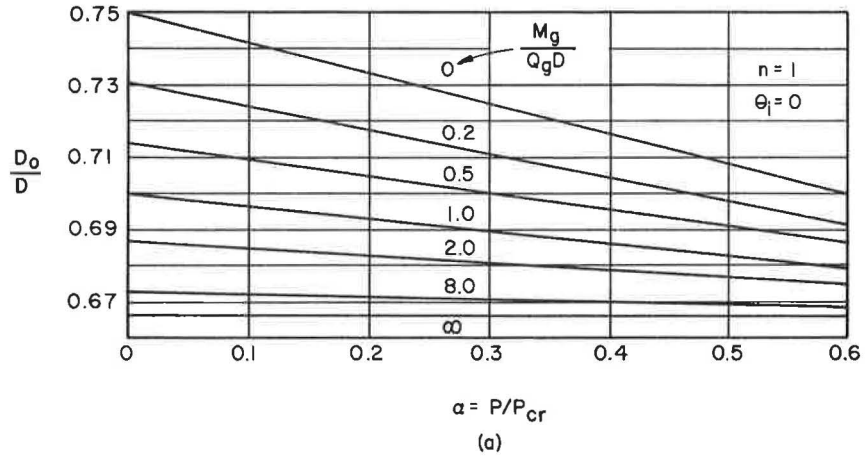

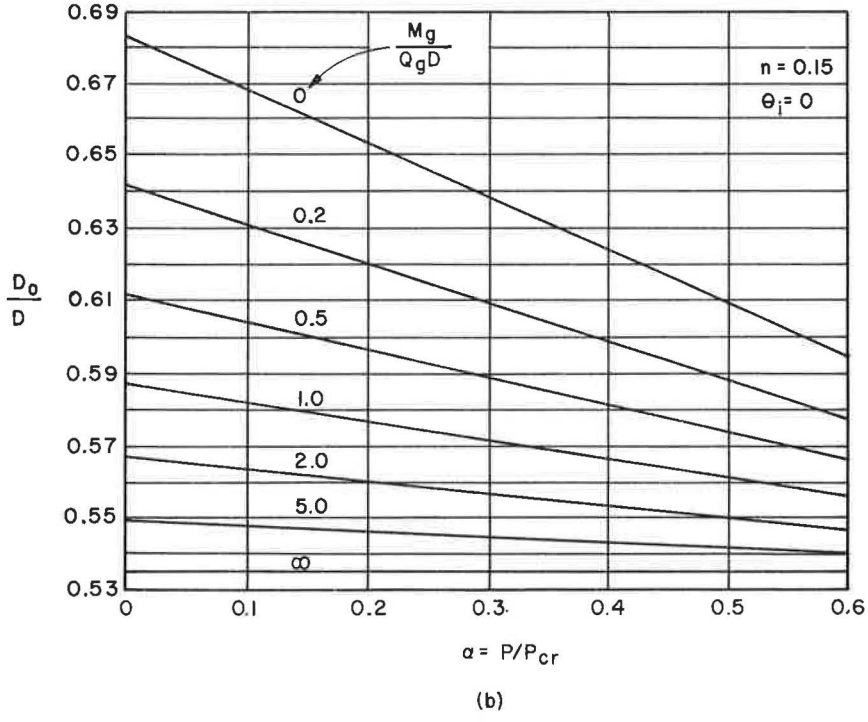

Figure 9. Chart for determining D_o/D.

More realistic analyses of the force required to overturn a pole were developed on the basis of a wedge of soil that became plastic during loading. Seiler (30) and Drucker (31) were among the earliest to use this approach. Analyses concerned with predicting the load deformation characteristics of the soil-pole system have usually been based on the assumption that the soil stiffness can be represented by a subgrade modulus. Grandholm (25) was the earliest to indicate when a flexural member is stiff enough to be considered rigid in a pole analysis. Rowe (32) was among the first to use a realistic variation of the subgrade modulus with depth, whereas Brinch Hansen (10) gave the first unified picture of the variation of the ultimate soil resistance with depth. Anderson

TABLE 1

THEORETICAL CONTRIBUTIONS

Author	Remarks
Carpentier (28)	Parabolic distribution of soil reactions assumed.
Schutz (35)	Linear variation of soil pressures.
Baldini (36)	
Stotzer (37)	
Goodrich (38)	
Grandholm (25)	Defined a pole using subgrade modulus technique.
Williams (5)	Solved for point of rotation and soil reactions.
Wilcoxen (39)	
Jager (40)	Usefulness of enlarged pole sections at ground surface noted.
Seiler (30)	Empirical adjustment of theory to fit tests.
Wolff (41)	
Drucker (31)	
Raes (42)	
Demogue (29)	
Griffith (45)	
Abbet (44)	
Minikin (45)	
O'Neil (46)	Considered non-uniform pole sections.
Fordham (47)	
Kohler (48)	
Pender (49)	
Gray (50)	
Lummis (51)	
Minikin (6)	
Terzaghi (17)	Realistic soil properties.
Rowe (32)	Realistic soil properties.
Robbins (52)	
Nelidov (53)	
Czerniak (20)	
Anderson (18)	Considers poles enlarged at the ground surface.
Matlock and Reese (26)	Define a pole. General subgrade modulus techniques.
Prakash (27)	Includes vertical load and initial rotations.
Greene (33)	Dimensional analysis techniques.
Kent (34)	Non-linear subgrade modulus.
Brinch Hansen (10)	Variation of ultimate soil resistance with depth.

(18) took into account various shapes for the loaded face of the pole; his analysis indicates that pole shapes widened at the ground surface are remarkably efficient in reducing the pole rotation under a given load. Greene (33) has used dimensional analysis techniques combined with test results to develop empirical expressions for the load versus rotation relationship, whereas Kent (34) has used a nonlinear expression for the subgrade modulus in an attempt to arrive at the same relationship.

Table 1 lists the various authors of theories applicable to poles in a generally chronological order; remarks are listed for selected pertinent references. A review of the literature indicates that pole theories are so simple that most authors develop and publish their own original work quite unaware that exactly the same thing has been done many times before.

REVIEW OF EXPERIMENTAL RESULTS

A considerable amount of experimental work has been performed on poles by a large number of authors; however, most of the test data cannot be analyzed because

the pertinent properties of the soil are unknown. In most cases, the soil is not even adequately described. Therefore, the majority of the experimental data is useful only for the aspects of soil-pole behavior that can be physically observed. This observed behavior has been used in the discussion of soil resistance previously given. Table 2 gives a summary of the experimental sources known to the authors.

Sandeman (54) performed the first set of pole-pile tests reported in the literature. Wooden poles were embedded to various depths in sand, clay and fill composed of ashes. The results indicated that the ultimate load a pole could withstand increased with embedment until a depth was reached where the structural strength of the pole limited the loading. It was not until fifty years later that Stobie (8) performed a series of tests, measuring soil reactions, that proved equally useful. Nakamura's (23) tests, besides indicating the pole shape effect previously cited, illustrated that progressively increasing deflections are observed for poles embedded in sand when subjected to repeated loads. Rifaat (59) performed tests in sands with soil reaction measurements. He found that an n-value of unity in Eq. 4 expressed the variation of subgrade modulus with depth; however, it was necessary to consider the shear V_D along the bottom of the pole in the analysis.

Matsuo (24) found that the deflections for a given lateral load on a pole decreased with the time after driving of the pole in clay. Minikin (6, 45) experimentally observed the difference in the unit ultimate soil resistance between poles and walls. He proposed coefficients for the two-dimensional passive pressure formulas to account for the three-dimensional behavior of poles. Anderson (62) experimentally demonstrated the large reduction in the deflections of a pole enlarged at the ground surface when compared to a prismatic pole.

Loos and Breth (64) presented the first test results using SR-4 gages to indicate the moments along the embedded portion of the pole. Similar techniques have been used by Wilkins (65), Walsenko (71) and Osterberg (2, 67). The bending moment diagrams may be double differentiated to obtain an approximate curve of soil reaction versus depth. Tests of this type are generally suitable for analysis if a sufficient quantity of closely spaced SR-4 gages are employed.

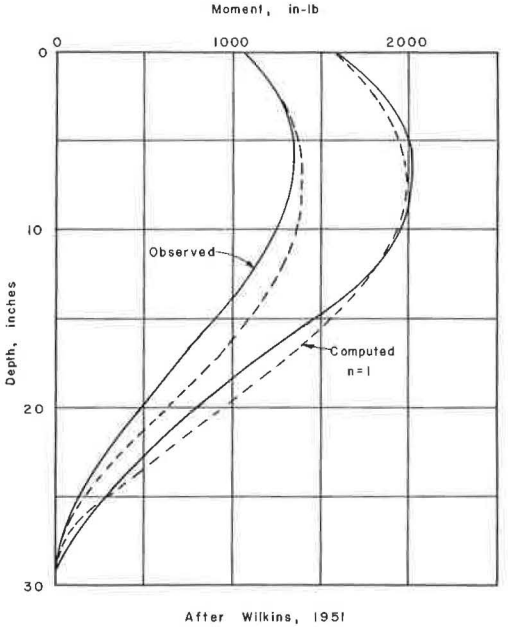

Figure 10. Moment vs depth from a test in sand.

ANALYSIS OF TEST RESULTS

Virtually all test data available for either piles or poles indicate that an n-value of unity in Eq. 4 is appropriate for granular soils and normally loaded cohesive soils. Davisson (22) and Prakash (1, 27) have collected ample evidence to support this statement. An example of the differences between the theoretically computed and the experimentally observed moments for a pole in sand is shown in Figure 10. Wilkin's (65) tests were analyzed by using the observed moment, lateral load, and deflection at the ground line in Eqs. 17 and 18 to obtain n_h. Then Eq. 19 was used in the calculation of the theoretical moments shown by the dashed lines (Fig. 10). The comparison between these observed and computed moments is typical of all test data analyzed in the foregoing manner for granular soils and normally loaded cohesive soils.

The only tests in preloaded cohesive soils suitable for analysis are those by Osterberg (2, 67). Unfortunately, these tests are obscured by variations in the

TABLE 2

EXPERIMENTAL STUDIES

Author	Soil Type	Remarks
Sandeman (54)	Sand, clay, ashes	First published tests.
Winchester (55)	Gravel, sand	
Stieves (56)		
Carpentier (28)		
Chardin (57)		
Browne and Fontaine (58)	Hard clay	
Stobie (8)	Sand, clay	First pressure measurements.
Krynine (3)	Clay	
Nakamura (23)	Sand	Effect of pole shape and repeated loads.
Rifaat (59)	Sand	Pressure measurements, effect of V_D.
Agatz (60)		
Raes (42)	Sand	
Matsuo (24)	Clay	Effect of remolding soil.
Minikin (45)	Sand, clay	Realistic appraisal of ultimate soil resistance.
Fordham (47)	Sand	
Osipovich (61)		
Gray (50)		
Schilts, Graves, and Driscoll (21)	Sand, clay	
Anderson (62)		Effect of poles enlarged at the ground surface.
Gruyter and Schieveen (63)		
Loos and Breth (64)	Sand	Moments determined from SR-4 gage measurements. Illustrated transition from rigid pole to flexible pile behavior.
Minikin (6)	Sand, clay	Realistic appraisal of ultimate soil resistance.
Wilkins (65)	Sand	Moments determined from SR-4 gage measurements.
Williams (5)	Sand	
Marjerrison (66)	Rock, pumice	
(Rutledge) Osterberg (67)	Clay	Moments determined from SR-4 gage measurements.
Caswell and Andrews (68)	Gravel, clay	Use of gravel to improve clay backfills.
Rowe (32)	Sand	Realistic appraisal of subgrade modulus.
Mors (69)		
Lazard (70)	All types	Statistical results of over 200 tests.
Steel (71)	Gelatin	Model studies to find D_O.
Walsenko (72)	Sand	Moments determined from SR-4 gage measurements.
Osterberg (2)	Clay	Moments determined from SR-4 gage measurements.
Behn (73)	Sand, clay	Short-term and long-term tests.
Kent (34)	Sand	
Greene (33)	Sand	
Christensen (74)	Sand	Concerned with ultimate load.

properties of the clay and the technique of placing the pole. The pole was a 10.75-in. diameter aluminum pipe equipped with SR-4 gages. Installation was made by augering a 2-in. oversize hole in the stiff clay soil; the pole was placed, plumbed and a sand backfill was vibrated, by tapping the pole, into the space between the pipe and the sides of the hole. Therefore, the tests do not reflect entirely the behavior of the clay, but are a combination of the behavior of sand and clay. One test was selected by the authors as being the most representative of the clay; this test was analyzed assuming various values for n and applying the same techniques used in analyzing Wilkin's tests. An n-value of 0.15 was selected as reasonable. Figure 11 shows the observed moments (solid line) compared to the calculated moments (dashed line) for n = 0.15. It is on the basis of this test combined with reasoning that a tentative value for n of 0.15 is recommended.

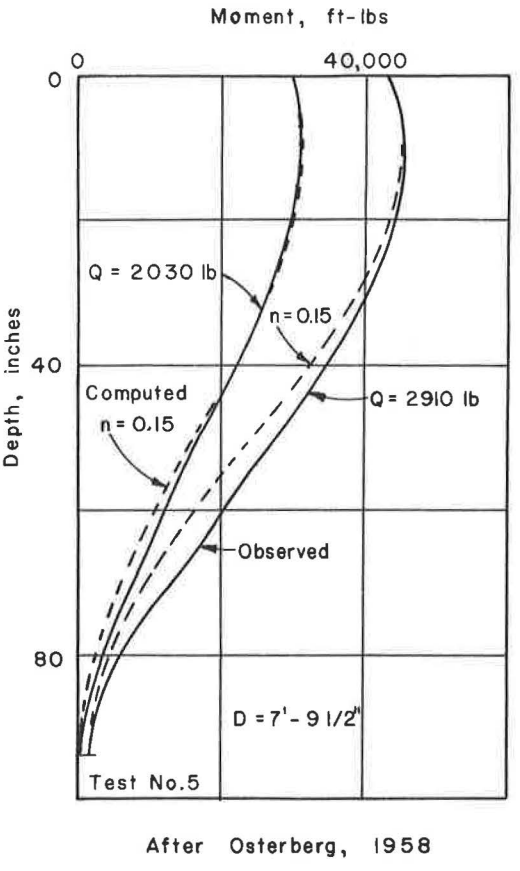

Figure 11. Moment vs depth from a test in clay.

No experimental evidence was available to verify the expression for the critical vertical load P_{cr} given in Eq. 10. To rectify this, a simple test was performed on a pole in sand for which it is known that n = 1 is a good assumption. The pole was a 0.5-in. diameter, 12-in. long steel rod embedded 3 in. A lateral load test was performed and analyzed for n_h in the same manner as Wilkin's tests. Using the n_h value determined experimentally in Eq. 16, a critical load of 16.7 lb was obtained. Three vertical load tests were performed by placing weights on top of the pole; failure occurred twice at loads of 16 lb and once at a load of 18 lb, or an average of 16.7 lb. It is not suggested that the excellent agreement obtained between test and theory is indicative of the accuracy of Eq. 10; it is only suggested that Eq. 10 is a reasonable approximation of the actual critical vertical load.

APPLICATION

Because poles are generally relatively inexpensive structures used in large quantities over wide geographical areas, there is considerable pressure for a simple design procedure that will produce answers at a glance. Economics will not allow the use of refined design procedures involving extensive soil exploration. The foregoing discussion makes it clear, however, that no panacea in the form of a rule of thumb or a chart is likely to be found. It is not the purpose of this paper to provide a specific design procedure, but rather to review the aspects of soil-pole behavior that occur and must be accounted for, and to provide an adequate theoretical framework within which design procedures may be either developed or evaluated.

There are several features concerning the use of poles that will allow simple design procedures to be developed for a specific range of working conditions. For example, in a given series of pole installations the physical characteristics of the pole (EI, H) and the loading (P, M_g, Q_g) are known and can be standardized to give constant values.

TABLE 3

RECOMMENDED VALUES OF n_h FOR SANDS

Author	n_h (pci)					
	Loose		Medium		Dense	
	Dry	Submerged	Dry	Submerged	Dry	Submerged
Terzaghi (17)	9.4	5.3	28	19	75	45
Rowe (75)	8.1	—	—	—	65	—

Furthermore, the allowable initial inclination (θ_i) can be specified. Then the theoretical expressions can be evaluated in terms of the depth of embedment (D) and the soil properties (c, ϕ, k_x). In addition, the method of construction is likely to be known and it may be predetermined if the desired soil properties will be those of the undisturbed soil, for example, as it would be with a concrete pole cast in a drilled hole, or those of the backfill. In the latter case, the soil properties can be controlled by the construction procedure. At this point two alternates are available. The soils likely to be encountered may be grouped under 4 or 5 headings, with conservative soil properties assigned to each, and the depth of embedment computed; then it is merely necessary to identify the soil at the location of any pole as belonging to one of these groups in order to obtain the depth of embedment. A more versatile but also more involved procedure involves the use of a hand-operated static penetrometer in the soil controlling the behavior of the pole at any given location. With this technique any desired number of typical soil classifications could be incorporated. The pertinent soil properties could be assigned to each group and the depth of embedment expressed as a function of the penetrometer record. Obviously, correlations would have to be developed between the penetrometer readings and the strengths and subgrade moduli of the selected soil groups. This appears to be easily accomplished in view of the success with static penetrometers in Europe.

In using the theoretical expressions a minimum factor of safety of 3, as defined earlier, is recommended to keep the pole rotations in the range where they can be predicted, and also to insure an adequate margin against failure. Repetitive loading has been shown to induce a progressively increasing rotation; this factor may be accounted for by increasing the factor of safety in the design analysis. Unfortunately, the necessary increase in the factor of safety is presently unknown.

The design approach recommended above would be greatly enhanced if the results of two or more series of carefully conducted tests in granular and preloaded cohesive soils were to become available. Each test series should be in a carefully controlled soil whose pertinent physical properties are known. One test in each series should be carried to failure. Static short-time loading and long-time loading should then be applied to a pole equipped with SR-4 gages for the purpose of determining the moments on the embedded portion of the pole. Then repetitive loading of various degrees of severity should be applied in one or more instrumented pole tests. With this information, the variation of subgrade modulus with depth in cohesive soils could be determined and the required factor of safety under repeated load service conditions expressed as a function of the severity of the repeated load.

In using the analytical procedures presented herein, some notion of the magnitude of the subgrade moduli likely to be encountered will be helpful. For granular soils Terzaghi (17) and Rowe (75) have published realistic values for n_h (Table 3). In addition, the authors have observed n_h-values for very loose submerged sands as low as 1.5 pci under repetitive loading and over 100 pci for dry, very dense sand under static loading. In soft, essentially normally loaded clays n_h-values of 2 pci under static loading and 1.0 pci under repetitive loading have been observed. For very soft, or-

TABLE 4

RECOMMENDED VALUES OF K FOR CLAYS

q_u (tons/ft^2)[a]	Range of K (psi)	Recommended K (psi)
1 - 2	463 - 926	694
2 - 4	926 - 1,390	1,390
> 4	> 1,852	2,780

[a]Unconfined compressive strength.

ganic silt n_h-values ranging from 0.4 pci to 1.0 pci have been reported by Peck and Davisson (76).

Very little information exists concerning K-values for piles and poles in preloaded clays. Terzaghi's (17) recommended values have been converted to the system used in this paper (Table 4). It should be noted that Terzaghi's recommendations are conservative and can be presumed to include an allowance for consolidation under static long time loading.

A large quantity of empirical data regarding the subgrade modulus may be obtained economically by performing pole tests in the following manner:

1. Use Tables 3 and 4 to estimate the values of n_h or K for the soils in which the tests will be performed.
2. Design the test pole to be rigid using Eqs. 5 through 9.
3. Install the pole and displace it upwards slightly to eliminate the possible effects of V_D.
4. Determine D and the height above the ground surface to the lateral load.
5. Measure the lateral load Q, and the deflection at the ground surface y_g, and the pole rotation θ.
6. Assume that Eq. 4 applies and determine n from Eq. 11 and K from Eq. 12.
7. Check step 2 to be sure that the pole is rigid.
8. Estimate or measure the soil strength parameters (c, φ) and describe the soil, preferably by the AASHO and Unified Soil Classification Systems.

This test procedure will provide the soil parameters necessary for a complete pole analysis. It can be used as a means of collecting data for developing a design procedure, either for soils in general or for a selected soil type in particular.

SUMMARY AND CONCLUSIONS

It has been shown that the behavior of a soil-pole system is governed by the properties of the soil, and therefore, by any factors affecting these properties. For example, repeated loading leads to progressively increasing deflections which indicates a reduction in the subgrade modulus. Also, seasonal changes in the moisture content of cohesive soils can greatly affect their properties. In addition, the method of construction can determine whether the pertinent soil properties are those of the backfill or those of the undisturbed soil.

The pertinent soil properties are the shear strength (φ, c) and the subgrade modulus along with its variation with respect to depth. An n-value of unity in Eq. 4 has been shown reasonable for granular soils and normally loaded cohesive soils, whereas an n-value of 0.15 has been tentatively suggested for preloaded cohesive soils. Although the soil behavior is nearly elastic in the recommended working range, the subgrade modulus has been empirically adjusted somewhat to account for the plastic soil behavior which usually occurs near the ground surface.

Expressions have been given in terms of the flexural stiffness of the pole and the soil stiffness (subgrade modulus) which determine if a pole is rigid enough to meet the assumption that the pole deflections can be described by a rotation. Furthermore, a comprehensive analytical technique is presented that accounts for the moment and shear

loads at the ground line in addition to the vertical load and any initial rotation that the pole may have. The analysis allows virtually any variation of subgrade modulus with the depth to be considered. The variation of the ultimate soil resistance with depth is also presented and a technique involving a factor of safety is recommended to insure an adequate margin against overturning; it also insures that the soil reactions are in a range where they can be expressed as a linear function of the deflections.

Recommendations have been given for the test programs necessary for furnishing the information needed to develop general design procedures within the framework of this paper. Repeated load tests in both sands and clays are recommended; it is hoped that the factor of safety used in design can be related to the severity of the repeated loading. Tests are needed in preloaded cohesive soils to help define more precisely the variation of the subgrade modulus with depth.

The reduced deflections under a given load that are observed for a pole section that is enlarged near the ground surface, when compared to an unenlarged pole, are explained. Expressions indicating the behavior of these pole types can be developed in a manner similar to the expressions given in this paper. Similarly, expressions can be developed for other imposed conditions of restraint.

Two general design approaches are outlined. Both involve grouping the soil under a selected number of headings and choosing conservative soil properties for each group. Designs can then be prepared for the different standard poles and standard loadings where the depth of embedment is a function of the soil type. The simplest procedure involves only 4 or 5 soil types with a single conservative depth of embedment for each type. A more versatile procedure would make the depth of embedment a function of the static soil penetrometer record within each soil type.

Finally, it is hoped that this paper can serve as a source of reference material on pole behavior and provide a framework within which pole design procedures can be evaluated and developed.

ACKNOWLEDGMENTS

The junior author was supported at the University of Illinois during this investigation by a scholarship granted by the International Cooperation Administration while he was on a leave of absence from the University of Roorkee, Roorkee, India. J. O. Osterberg generously permitted the authors to use his experimental data on poles in clay. Keith Robinson drafted the figures and aided in many ways during the preparation of this paper.

REFERENCES

1. Prakash, Shamsher, "Behavior of Pile Groups Subjected to Lateral Loads." Ph. D thesis, Univ. of Illinois (1962).
2. Osterberg, J. O., "Lateral Stability of Poles Embedded in a Clay Soil." Unpublished report, the Technological Institute, Northwestern Univ. (1958).
3. Krynine, D. P., "Some Theoretical Considerations on Landslides." ENR, 107:93 (1931).
4. Appleford, C. W., "Method of Handling the Problem of Pole Embedment." Civil Engineering, 5:311 (1935).
5. Williams, T. E. H., "Soil Failure During Overturning of Piles." Engineering, 173:134 (1952).
6. Minikin, R. R., "Winds, Waves, and Maritime Structures." Charles Griffin and Co., Ltd. (1950).
7. Krynine, D. P., "Soil Mechanics." McGraw-Hill (1947).
8. Stobie, J. C., "Pole Footings." Jour. of the Inst. of Engineers, Australia, 2:58 (1930).
9. Meyerhoff, G. G., "The Ultimate Bearing Capacity of Foundation," Geotechnique, 2:312 (1951).
10. Hansen, J. B., "The Ultimate Resistance of Rigid Piles Against Transversal Forces." Danish Geotechnical Inst., Bull. 12 (1961).
11. Mackenzie, T. R., "Strength of Deadman Anchors in Clay." M.S. thesis, Princeton Univ. (1955).

12. Vesic, A. B., "Beams on Elastic Subgrade and the Winkler's Hypothesis." Proc., 5th Internat. Conf. Soil Mech. and Found. Eng., 1:845 (1961).
13. Biot, A. M., "Bending of an Infinite Beam on an Elastic Foundation." Jour. of Applied Mech., 4:1, A1-A7 (1937).
14. Miche, R., "Investigations of Piles Subject to Horizontal Forces, Application to Quay Walls." Journal, School of Engineering, Giza, No. 4 (1930).
15. Titze, E., "Widerstand des Pfahles gegen wagrechte Krafte." Technical Hochschule, Wien(1932).
16. Palmer, L. A., and Thompson, J. B., "The Earth Pressure and Deflection Along the Embedded Length of Pile Subjected to Lateral Thrust." Proc., 2nd Internat. Conf. Soil Mech. and Found. Eng., 5:156 (1948).
17. Terzaghi, Karl, "Evaluation of Coefficients of Subgrade Reaction." Geotechnique, 5:297-326 (1955).
18. Anderson, W. C., "Foundations to Resist Tilting Moments Imposed on Upright Cantilevers Supporting Highway Signs." HRB Bull. 247, 1-3 (1960).
19. Davisson, M. T., and Gill, H. L., "Laterally Loaded Piles in a Layered Soil System." Submitted for publication, ASCE (1963).
20. Czerniak, E., "Resistance to Overturning of Single, Short Piles." ASCE Proc., Vol. 83, ST2 (March 1957).
21. Shilts, W. L., Graves, L. D., and Driscoll, G. G., "A Report of Field and Laboratory Tests on the Stability of Posts Against Lateral Loads." Proc., 2nd Internat. Conf. Soil Mech. and Found. Eng., 5:107(1948).
22. Davisson, M. T., "Behavior of Flexible Vertical Piles Subjected to Moment, Shear and Axial Load." Ph.D. thesis, Univ. of Illinois (1960).
23. Nakamura, M., "Uber Den Erdwidenstand Gegen Maste Unter Besonderer Berucksichtigung Der Zusammendruckbarkeit Des Bodens." Bauingenieur, 16:21/24, 269 (1935).
24. Matsuo, H., "Tests on the Lateral Resistance of Piles." Research Institute of Civil Engineering, Ministry of Home Affairs, Report No. 46; in Japanese (1939).
25. Grandholm, Hjalmar, "On the Elastic Stability of Piles Surrounded by a Supporting Medium." Ing. Vet. Akad, Hand. 89, Stockholm (1929).
26. Matlock, Hudson, and Reese, L. C., "Generalized Solutions for Laterally Loaded Piles." ASCE Trans., 127:Pt. I, 1220-1251 (1962).
27. Prakash, Shamsher, "A Review of the Behavior of Partially Embedded Poles Subjected to Lateral Loads." M.S. thesis, Univ. of Illinois (1961).
28. Carpentier, H., "Note sur le Calcul des Fondations des Pylones Supportant les Lignes de Transmission d'Energie." Revue Generale de L'Electricite, 14:13, 439 (1923).
29. Demogue, R., "Stabilite des Supports de Lignes Telephones." Annales des Postes Telegraphes et Telephones, 27:8, 706 (1938).
30. Seiler, J. F., "Effect of Depth of Embedment on Pole Stability." Wood Preserving News, 10:152 (1932).
31. Drucker, M. A., "Embedment of Poles, Sheeting and Anchor Piles." Civil Engineering, 4:622, Discussion, 5:311, 589 (1934).
32. Rowe, P. W., "The Single Pile Subject to Horizontal Force." Geotechnique, 6:70 (1956).
33. Green, G. E., "A Model Study of the Lateral Stability of a Single Pole." M.S. thesis, Northwestern Univ. (1961).
34. Kent, B. P., "A Pole Stability Theory Supported by Model Study." M. S. thesis, Univ. of Arizona (1961).
35. Schutz, G., "Neue Gesichtspunkte fur die Berechnung und Ausfuhrung von Mastfundamenten." Electrotechnische Zeite, 44:30, 708 (1923).
36. Baldini, F., "Note sur le Calcul des Fondations des Poteaux Metalliques Supportant des Lignes Electriques." Bulletin, Assoc. des Ingenieurs Electriciens, Series 7(2), 151 (1924).
37. Stotzer, O., "Berechnung von Mastfundamenten." Electrotechnische Zeite, 45:49, 1346 (1924).
38. Goodrich, C. M., "Concrete Foundations for Poles in Earth." Trans. Engineering Inst. of Canada, 36:64 (1927).

39. Wilcoxen, L. C., "Horizontal Forces Acting on a Pile." ENR, 107:978 (1931).
40. Jager, H., "Zur Erddruck-berechnung Stabformiger Maste." Zeitschrift des Osterr. Ingenieur-und Architekten-Vereines, 84:141 (1932).
41. Wolff, C. V., "Members Wholly or Partially Buried and Subjected to Lateral Force." Concrete and Construction Engineering, 28:632 (1933).
42. Raes, P. E., "Theory of Lateral Bearing of Piles." Proc. 1st Internat. Conf. Soil Mech. and Found. Eng., 1:166 (1936).
43. Griffith, J. R., "Construction Design Charts." Western Construction News, 14:10, 350 (1939).
44. Abbett, R. W., "Stability of Cantilever Poles in Sandy Soils." Civil Engineering, 11:301, Discussion, 11:434 (1941).
45. Minikin, R. R., "Design of Jetties." Dock and Harbour Authority, 23:124 (1943).
46. O'Neil, H. M., "Analogy of Horizontal Forces on Partially Buried Structures." ENR, 131:324 (1943).
47. Fordham, A. A., "The Lateral Pressure of Earth Against Footings Subjected to Overturning Moment." Structural Engineer, 22:7, 298 (1944).
48. Kohler, K., "Beitrag zur Berechnung von Einspannfundamenten fur Freileitungen." Assoc. Suisse des Electriciens Bulletin, 37:35, 729 (1946).
49. Pender, E. B., "Lateral Support Afforded to Piers Founded in Sand." Jour. Inst. of Engineers, Australia, 19:7, 151 (1947).
50. Gray, C. M., "Pole Foundations." Trans. Electric Supply Authority Engineers Assoc., New Zealand, 16:44 (1947).
51. Lummis, J., "Design Charts for Concrete Footings." Electric Light and Power, 27:8, 62 (1949).
52. Robbins, N. G., "Piers Supported by Passive Pressures." Civil Engineering, 27:276 (1957).
53. Nelidov, I. M., "Finding Depth of Footing for a Pole Subjected to Lateral Loads." Civil Engineering, 28:196, Discussion, 28:527, 767 (1958).
54. Sandeman, J. W., "Lateral Pile Tests." Van Nostrand Engineering Magazine, 23:493 (1880).
55. Winchester, L. S., "An Experimental Determination of the Strength of Full-Sized Telephone Poles." Electrical World, 57:667 (1911).
56. Stieves, W. M., "Concrete-Steel Fence Posts." Engineering Record, 69:7, 186 (1914).
57. Chardin, A., "Experiences sur la Stabilite des Massifs de Fondation des Pylones de Lignes Electriques." Revue Generale de L'Electricite, 17:17, 637 (1925).
58. Browne, W. H., Jr., and Fontaine, J., "Tests of North Carolina Poles for Electrical Distribution Lines." North Carolina State College of Agric. and Eng. Exp. Sta. Bull. 3 (1929).
59. Rifaat, J., "Die Spundwand als Erddruckproblem." A. G. Gebr, Leemann and Co., Zurich (1935).
60. Agatz, A., "Der Kampf des Ingenieurs Gegen Erde und Wasser im Grundbau." Julius Springer, Berlin (1936).
61. Osipovich, A. A., "230 K. V. Wood Pole Structures, Design and Tests." Electrical World, 123:84 (1945).
62. Anderson, W. C., "Pole Foundation to Resist Tilting Moments." Electric Light and Power, 26:10, 96 (1948).
63. Gruyter, J. De., and Van Schieveen, Ir. H. P., "Modelproeven met Fundaties voor Hoogspanning Masten." De Inginieur, 60:B61 (1948).
64. Loos, W., and Breth, H., "Modellversuche uber Biegebeanspruchung von Pfahlen und Spundwanden." Der Bauingenieur, 24:9, 264 (1949).
65. Wilkins, R. J., "The Bending of a Vertical Pile Under Lateral Forces." Civil Engineering (London), 46:355 (1951).
66. Marjerrison, M. N., "Stability of Poles Set in Pumice Soil." Electric Light and Power, 30:106 (1952).
67. Osterberg, J. O., "Discussion, Supplement to Symposium on Lateral Load Tests on Piles." ASTM Special Tech. Pub. No. 154, A (1954).
68. Caswell, R. W., and Andrews, F. E., "Foundation Stability of Wood Poles, H-frame Structures for Transmission Lines." AIEE Trans., 73:245 (1954).

69. Mors, H., "Mastumbruch-und Fundament-versuche Wendlingen." Stahlbau, 25:20 (1956).
70. Lazard, A., "Moment Limite de Renversement de Fondations Isolees." Proc. 4th Intern. Conf. Soil Mech. and Found. Eng., 1:349 (1957).
71. Steel, Myron, "Resistance of Poles Subject to Overturning Moments." B.S. thesis, Univ. of Utah (1937).
72. Walsenko, Alex, "Overturning Properties of Short Piles." M.S. thesis, Univ. of Utah (1958).
73. Behn, F. E., "Tests of Tilting Moment Resistance of Cylindrical Reinforced Concrete Foundations for Overhead Sign Supports." HRB Bull. 247, 14-33 (1960).
74. Christensen, N. H., "Model Tests with Transversally Loaded Rigid Piles in Sand." Danish Geotechnical Inst., Bull. 12, Copenhagen (1961).
75. Rowe, P. W., Discussion of "Evaluation of Coefficients of Subgrade Reaction" by Karl Terzaghi. Geotechnique, 6:94-98 (1956).
76. Peck, R. B., and Davisson, M. T., Discussion of "Design and Stability Considerations for Unique Pier" by James Michalos and D. P. Billington. ASCE Trans., 127: Pt. IV, 413-424 (1962).

Appendix

NOTATION

Note: The units are expressed in terms of force F and length L.

Symbol			Units
B	=	width of pole normal to the loading	L
c	=	cohesion	FL^{-2}
D	=	embedded length of pole	L
D_o	=	depth to point of rotation	L
D_1	=	depth of upper point relative maximum w	L
e	=	eccentricity of P from pole axis	L
E	=	Young's modulus for the pole	FL^{-2}
H	=	unsupported length of the pole	L
H_p	=	distance from ground surface to P	L
I	=	moment of inertia of pole cross-section	L^4
k	=	subgrade modulus	FL^{-2}
k_x	=	k as a function of depth	FL^{-2}
K	=	value of k at depth D	FL^{-2}
M_c	=	moment couple	FL
M_g	=	resultant moment at ground surface	FL
n	=	coefficient governing k_x	
n_h	=	constant of horizontal subgrade reaction, K/D for n = 1	FL^{-3}
N_c	=	bearing capacity factor for cohesion	
N_q	=	bearing capacity factor for overburden pressure	
P	=	vertical load	F
P_{cr}	=	critical vertical load	F
q'	=	vertical effective stress	FL^{-2}
Q	=	horizontal load on pole	F
Q_g	=	resultant horizontal load at ground surface	F
R	=	relative stiffness factor for n = 0, $\sqrt[4]{EI/K}$	L
T	=	relative stiffness factor for n = 1, $\sqrt[5]{EI/n_h}$	L
V	=	shear in the pole	F
V_D	=	shear in the pole at depth D	F
w	=	soil reaction	FL^{-1}
w_u	=	ultimate soil reaction	FL^{-1}
w_x	=	w as a function of depth	FL^{-1}

x	=	depth coordinate from ground surface	L
y	=	horizontal deflection of pole	L
y_g	=	y at ground surface	L
y_{gi}	=	y at ground surface due to θ_i	L
α	=	P/P_{cr}	
θ	=	pole rotation	
θ_i	=	initial pole rotation	
φ	=	angle of internal friction	

Lateral Stability of Rigid Poles Partially Embedded in Sand

ROBERT L. KONDNER, Associate Professor of Civil Engineering, The Technological Institute, Northwestern University, Evanston, Ill., and
JAMES A. CUNNINGHAM, Instructor of Civil Engineering, Tri-State College, Angola, Ind.

Functional relationships are developed for the load-deflection characteristics of a rigid, vertical pole, embedded in sand and subjected to a horizontal load applied above the ground line. The study is based on non-dimensional techniques and the physical variables included in the theoretical analysis are the ground-line deflection, depth of embedment, geometry of the pole cross-section, applied force, moment arm, time of loading and soil parameters. The soil parameters used include the density, angle of internal friction, flow characteristics, and relative density of the sand. Non-dimensional techniques in conjunction with small-scale model studies are used to determine the explicit form of the interrelationship among the above physical variables for a pole embedded in a very dense, uniform, fine dune sand of constant properties and subjected to an applied horizontal force. Hyperbolic prediction equations are given from which the load-deflection characteristics of a prototype pole might be estimated. The superposition of ground-line couple and ground-line thrust relationships to represent the more general case of a horizontal load applied above the ground line is investigated. The results of the present formulation are compared with both model and field studies previously reported by other investigators.

THE lateral stability of a pole embedded in soil has, to date, defied an altogether satisfactory analysis. In order to obtain a rigorous solution to the problem, the boundary forces or displacements must be known and a stress-strain-time relationship for the soil in question must be available. It is the assumptions that must be made in order to fulfill these two requirements that seriously reduce the reliability of analytical results.

This paper uses the techniques of dimensional analysis and small-scale model experiments to study the behavior of a rigid circular pole embedded in a dense, uniform, fine dune sand of constant properties and subjected to a lateral force applied above the ground surface. Kondner (1, 2, 3, 4, 5, 6, 7) has previously demonstrated the effectiveness of these methods in the field of soil mechanics. These methods allow the development of a prediction equation on a semi-empirical basis without requiring assumptions regarding boundary conditions or stress-strain laws for the soil.

A discussion of the literature on poles has been given by Kondner and Green (6).

The following factors are reported in this paper:

1. The applied moment-ground-line deflection relationship for a single circular pole embedded in sand.
2. The effect of pole diameter, depth of embedment and moment arm on the applied moment-ground-line deflection relationship.

Paper sponsored by Committee on Stress Distribution in Earth Masses.

3. Investigation of the applicability of the superposition of ground-line couple and ground-line thrust relationships to represent the general case of a horizontal load applied above the ground line.

4. Comparison of the results of model testing with known field test results.

The work of Kondner and Green (6) was the first study to the authors' knowledge employing dimensional analysis and small-scale model tests for the purpose of examining the stability of laterally loaded poles. Their investigation dealt with the general formulation of non-dimensional functional relationships for the lateral stability of rigid poles, development of experimental apparatus, and effects of horizontal ground-line thrusts.

Later work by Kondner, Krizek and Schimming (7) demonstrated the effects of applied couples.

The purpose of the present investigation is to formulate a moment-deflection relationship for the given soil-pole system when the pole is subjected to an applied lateral force at various distances above the ground surface. Preliminary considerations indicated that superposition of the ground-line thrust and ground-line couple cases was not equivalent to the general case. Thus, detailed considerations of superposition effects are investigated.

THEORETICAL ANALYSIS

Experiments are frequently conducted in which the independent physical quantities under consideration are varied, thus giving results that are seemingly different. Examination of the results in a non-dimensional form often leads to the realization that many of the tests were in actuality a duplication of effort. The method of dimensional analysis is one of the most effective ways of obtaining useful data with a minimum expenditure of experimental and computational effort. This method can be summarized as follows.

If there are m physical quantities containing n fundamental units, which can be related by an equation, then there are (m-n), and only (m-n), independent, non-dimensional parameters (called π terms) such that the π terms are arguments of some indeterminate, homogeneous function $\varkappa$.

$$\varkappa (\pi_1, \pi_2, \pi_3, \ldots, \pi_{m-n}) = 0 \tag{1}$$

In Eq. 1 and hereafter the symbol $\varkappa$ denotes "some function of," but not necessarily the same function for each equation. This notation is used to avoid the use of numerous subscripts and superscripts as a means of differentiating between the functional forms.

To apply this procedure properly, a wise choice of the physical quantities involved must be made. Omission of significant variables may lead to very simplified but erroneous results while the consideration of unimportant variables may greatly reduce the usefulness of the results and considerably increase the expended experimental effort.

The quantities under consideration in this investigation are given in Table 1. A force, length, and time system of fundamental units has been used.

Once these physical quantities are chosen, a methodical process is used to obtain the π terms contained in the functional formulation. The explicit form of the functional relationship must then be determined experimentally. Since there are 12 physical quantities and 3 fundamental units, there must be 9 independent, non-dimensional π terms. These π terms can be methodically obtained by choosing 3 physical quantities, which contain all 3 fundamental units and cannot be formed into a non-dimensional parameter by themselves, such as (M, t and L), and combining them with each of the remaining quantities one at a time. For example, combining them with γ gives

$$\pi = M^{\alpha} t^{\beta} L^{\rho} \gamma^{\lambda} = F^{\circ} L^{\circ} T^{\circ} \tag{2}$$

Substituting the fundamental units of each of the physical quantities involved in Eq. 2 gives

$$(FL)^{\alpha}\ (T)^{\beta}\ (L)^{\rho}\ (FL^{-3})^{\lambda} = F^{\circ}L^{\circ}T^{\circ} \tag{3}$$

Equating exponents of the fundamental units gives:

$$\alpha + \lambda = 0\ \beta = 0\ \alpha + \rho - 3\lambda = 0 \tag{4}$$

Solving Eq. 4 by letting $\alpha = 1$ gives

$$\alpha = 1\ \beta = 0\ \lambda = -1\ \rho = -4 \tag{5}$$

Therefore, the π term under consideration is

$$\pi = M/\gamma L^4 \tag{6}$$

By successive application of the above procedure, the remaining π terms may be obtained. The resulting π terms may be algebraically transformed to yield a new set of non-dimensional, independent π terms which have a more significant form with regard to the experimentation.

The following nine non-dimensional, independent π terms were used for this investigation:

$$\pi_1 = x/C\ \pi_2 = M/\gamma CL^3\ \pi_3 = C/L$$
$$\pi_4 = D/L\ \pi_5 = C^2/A\ \pi_6 = \phi$$
$$\pi_7 = \gamma tC/\eta\ \pi_8 = D_d\ \pi_9 = \theta \tag{7}$$

The π terms of Eq. 7 may be substituted into Eq. 1 to obtain the functional relationship:

$$x/C = \varkappa\ (M/\gamma CL^3,\ C/L,\ D/L,\ C^2/A,\ \phi,\ \gamma tC/\eta,\ D_d,\ \theta) \tag{8}$$

Physical significance can be attached to the π terms appearing in Eq. 8. The dependent variable x/C is a deflection ratio. Shape effects are given by the term C^2/A. The term D/L is a relative measure of moment arm to the embedment and may be thought of as an embedment ratio. A geometric factor C/L, called the slenderness ratio, pertains to the distribution of the cross-section area of the pole. The term $M/\gamma CL^3$ is the ratio of the applied moment to a soil strength parameter and is called the moment-strength ratio. Creep effects are included in the $\gamma tC/\eta$ term which is the ratio of the time of loading to a characteristic relaxation time of the soil. The significance of the angle of internal friction, rotation angle, and relative density of the sand are well known and they are by definition non-dimensional.

TABLE 1

PHYSICAL QUANTITIES CONSIDERED IN THE DIMENSIONAL ANALYSIS OF A RIGID POLE EMBEDDED IN SAND

Physical Quantity	Symbol	Fundamental Units
1. Deflection at ground line	x	L
2. Depth of embedment	L	L
3. Cross-sectional area of pole	A	L^2
4. Perimeter of pole	C	L
5. Moment at ground line	M	FL
6. Moment arm	D	L
7. Dry density of sand	γ	FL^{-3}
8. Angle of internal friction	φ	$F^{\circ}L^{\circ}T^{\circ}$
9. Viscosity of sand	η	$FL^{-2}T$
10. Time of loading	t	T
11. Relative density	D_d	$F^{\circ}L^{\circ}T^{\circ}$
12. Rotation of pole	θ	$F^{\circ}L^{\circ}T^{\circ}$

The form of the functional relation (Eq. 8) can be greatly simplified by restricting the scope of the study. If attention is confined to poles of circular cross-section, the shape factor C^2/A is a constant value equal to 4π, regardless of the diameter. Preliminary work by Kondner and Green (6) indicates that by proper choice of the loading rate the effect of the term $\gamma tC/\eta$ can be minimized and hence eliminated from Eq. 8. Further work by Kondner, Krizek and Schimming (7) indicates that the ratio C/L has only a small influence on the results when the moment strength ratio is of the form $M/\gamma CL^3$. This was verified in the present work. For the present study, the rotation θ is dependent and expressable in terms of the other geometric variables.

Because the soil studied was a particular sand, maintained at a constant dense state by a vibratory preparation process, the angle of internal friction and relative density were constant for the present study. Thus, the functional relation of Eq. 8 can be written as

$$x/C = \chi\,(M/\gamma CL^3,\ D/L) \tag{9}$$

subject to the restrictions placed on C^2/A, ϕ, D_d and loading rate.

EXPERIMENTAL PROCEDURE

Although the functional relationships for the general loading conditions of the rigid pole problem have been formulated for both cohesive and cohesionless soils (Kondner in an unpublished work in 1961), it was considered desirable for this initial phase of investigation to use sand rather than clay as the soil medium because sand properties are easier to control in the laboratory than those of clay and the time effects are generally considered to be less complex.

Sand

The particular sand used was a uniform, fine dune sand from Wolf Lake, Ind., provided by Raymond Concrete Pile Company, Chicago. The sand had a gradation curve as shown in Figure 1 and was air-dried in the laboratory to a moisture content of about $\frac{1}{4}$ percent. For a dense state (i.e., density = 108 pcf), this sand had an angle of friction ϕ of 37^0, as determined from a series of triaxial compression tests. Subsequent to the beginning of each test, the sand was vibrated to a constant density of 107 pcf. Thus, the relative density was very close to one.

Poles

The model poles consisted of various lengths of polished aluminum or steel tube, plugged at the lower end. The properties of these poles are given in Table 2.

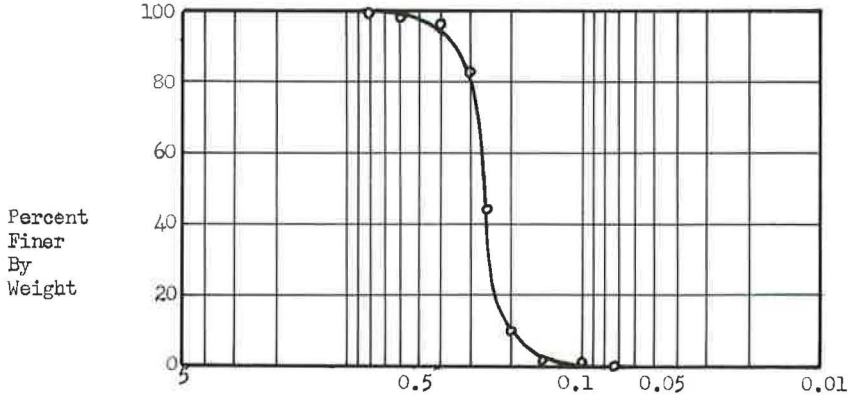

Figure 1. Sand gradation curve.

TABLE 2

PROPERTIES OF MODEL POLES

Pole	Material	Diameter (in.)	Area, A (sq in.)	Weight (g)	Perimeter, C (in.)
1	Aluminum	0.501	0.197	30	1.573
2	Aluminum	0.626	0.307	62	1.966
3	Steel	0.707	0.393	143	2.221
4	Steel	0.927	0.674	216	2.911
5	Steel	1.248	1.222	229	3.921
6	Steel	1.515	1.801	478	4.755

Apparatus

A schematic diagram of the apparatus used in the study is shown in Figure 2. A cut-down oil drum was welded to a table-type concrete vibrator and mounted on a sturdy timber base. In order to minimize extraneous vibrations during the test, the timber base was supported on rubber blocks. The tank contained 330 lb of dry sand and the volume was determined from a calibration curve previously obtained. The load was applied to the model pole by hanging weights on a cord attached to the pole and passing over a small pulley.

Techniques

To eliminate any source of error resulting from loads due to the internal spring forces of the indicator dials, these springs were removed and the gage arms were secured to the pole by elastic bands.

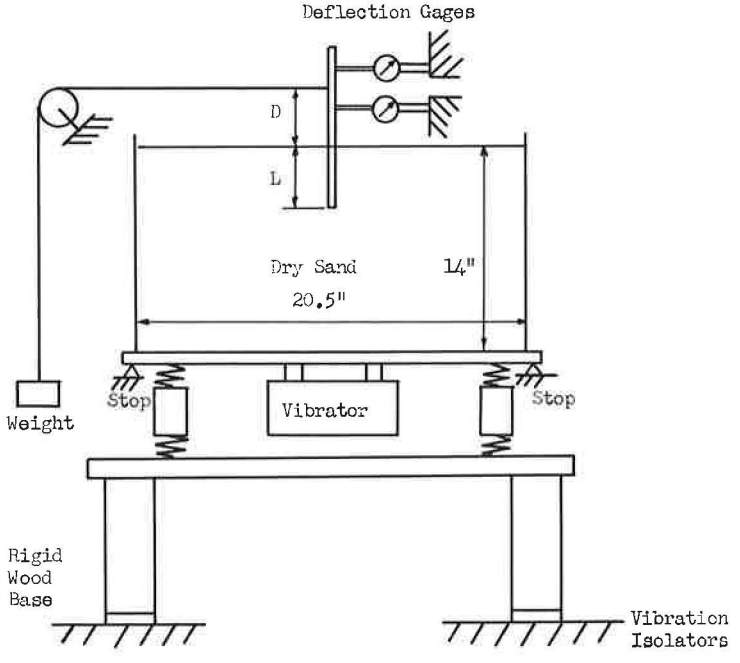

Figure 2. Experimental apparatus.

An investigation of the nature of the creep response indicated that after approximately two minutes the deflection continues at an extremely slow rate and ultimately tends toward a limiting value for a sufficiently large time. Therefore, it appears very reasonable to neglect the large-time portion of the deflection vs time curve and adopt a moment increment-time interval of two minutes. A similar conclusion was reached by Kondner and Green (6) in their analysis of the ground-line thrust problem.

EXPERIMENTAL RESULTS

The results analyzed were obtained from tests performed on model poles embedded in a dense sand and subjected to a lateral load at varying distances above the ground line. Loads were applied at a rate of 200 g per 2 min except for shallow embedments and large moment arms when the load increment was reduced to either 50 or 100 g.

As mentioned previously, Kondner, Krizek and Schimming (7) performed tests using an applied couple only and showed that the C/L ratio has little effect on results plotted in the form x/C vs $M/\gamma CL^3$. Consequently, tests were run keeping the D/L ratio at values of 0.2, 0.4, 0.6, 0.8, 1.0 and 1.2, while randomly changing pole size and hence C/L ratio. The schedule of tests (Table 3) gives the values of D and L for each pole in order to obtain some desired value of D/L and C/L. An intensive test program was carried out according to Table 3 and many tests were repeated to insure duplicability.

Results of the tests plotted in the form x/C vs $M/\gamma CL^3$ for each of the D/L ratios are shown in Figure 3. Inasmuch as no phenomenological pattern was noticeable as a result of using various poles and C/L ratios, each curve represents an average curve of a number of tests. An example of the type of scatter observed is shown in Figure 4 where the D/L ratio is 0.4. To obtain a unique relationship between $M/\gamma CL^3$, x/C, and D/L, a constant value of $\gamma tC/n$ would have been required for all tests. Theoretically, this could be done by varying the loading rate or loading increment for each test. But, such loading rates cannot yet be predicted in the field of soil mechanics. Thus, the scatter in Figure 4 probably includes some error due to time effects and C/L effects as well as experimental error.

The shape of the moment-strength ratio vs deflection ratio curves is definitely that of a non-linear material. These curves tend asymptotically to their respective upper limits as x/C becomes large.

If the data given by the average curves of Figure 3 are replotted in the form of the reciprocal of the secant modules, $x/C + M/\gamma CL^3 = x\gamma L^3/M$ vs x/C, the straight lines

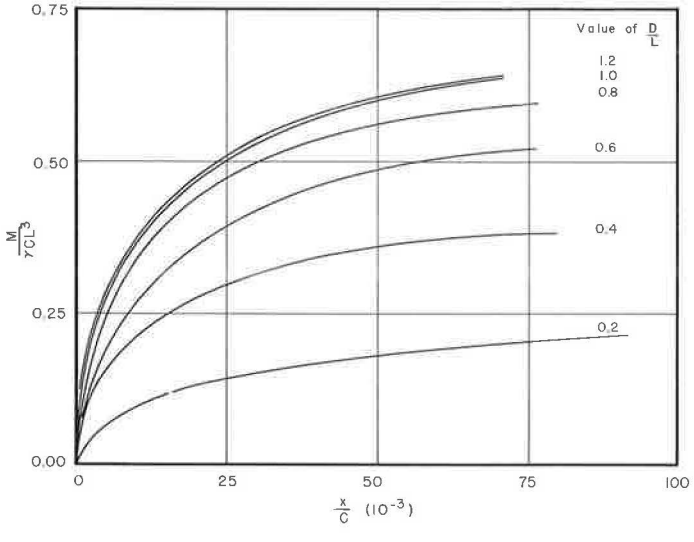

Figure 3. Non-dimensional plot of $M/\gamma CL^3$ vs x/C for various values of D/L.

in Figure 5 can be used to represent the responses. These lines show that the explicit form of the functional relation between $M/\gamma CL^3$ and x/C can be represented as a two-constant hyperbolic equation

$$x\gamma L^3/M = a + b(x/C) \tag{10}$$

or

$$\frac{M}{\gamma CL^3} = \frac{x/C}{a + b(x/C)} \tag{11}$$

where a and b are the intercept and the slope, respectively, of each of the straight lines and are, therefore, functions of D/L.

Physical significance can be attached to the constants a and b (Kondner 8, 9). Differentiating Eq. 11 with respect to the deflection parameter and evaluating the derivative for zero deflection gives

$$\left[\frac{d\,(M/\gamma CL^3)}{d\,(x/C)}\right]_{x/C=0} = \frac{1}{a} \tag{12}$$

Thus, the reciprocals of the intercepts of the straight lines in the transformed hyperbolic plots of Figure 5 represent the initial tangent modulus of the $M/\gamma CL^3$ vs x/C relation and are a function of D/L.

By taking the mathematical limit of the moment-strength ratio in Eq. 11 as the deflection parameter x/C becomes excessive, the ultimate value of the strength ratio becomes

$$\left(\frac{M}{\gamma CL^3}\right)_{ult} = \lim_{x/C \to \infty} \left(\frac{M}{\gamma CL^3}\right) = \frac{1}{b} \tag{13}$$

TABLE 3

TEST SCHEDULE

D/L	C/L				
	0.4	0.6	0.8	1.0	1.2
0.2	Pole 3 L = 5.55 D = 1.11	Pole 4 L = 4.85 D = 0.97	Pole 5 L = 4.90 D = 0.98	Pole 6 L = 4.76 D = 0.95	Pole 6 L = 3.96 D = 0.79
0.4	Pole 3 L = 5.55 D = 2.22	Pole 4 L = 4.85 D = 1.94	Pole 5 L = 4.90 D = 1.96	Pole 6 L = 4.76 D = 1.90	Pole 6 L = 3.96 D = 1.58
0.6	Pole 3 L = 5.55 D = 3.33	Pole 4 L = 4.85 D = 2.91	Pole 5 L = 4.90 D = 2.94	Pole 6 L = 4.76 D = 2.85	Pole 6 L = 3.96 D = 2.38
0.8	Pole 3 L = 5.55 D = 4.44	Pole 4 L = 4.85 D = 3.88	Pole 5 L = 4.90 D = 3.92	Pole 6 L = 4.76 D = 3.80	Pole 6 L = 3.96 D = 3.17
1.0	Pole 3 L = 5.55 D = 5.55	Pole 4 L = 4.85 D = 4.85	Pole 5 L = 4.90 D = 4.90	Pole 6 L = 4.76 D = 4.76	Pole 6 L = 3.96 D = 3.96
1.2	Pole 1 L = 7.27 D = 8.71	Pole 4 L = 4.85 D = 5.83	Pole 5 L = 4.90 D = 5.89	Pole 4 L = 2.91 D = 3.49	Pole 6 L = 3.96 D = 4.76

Note: All dimensions are inches.

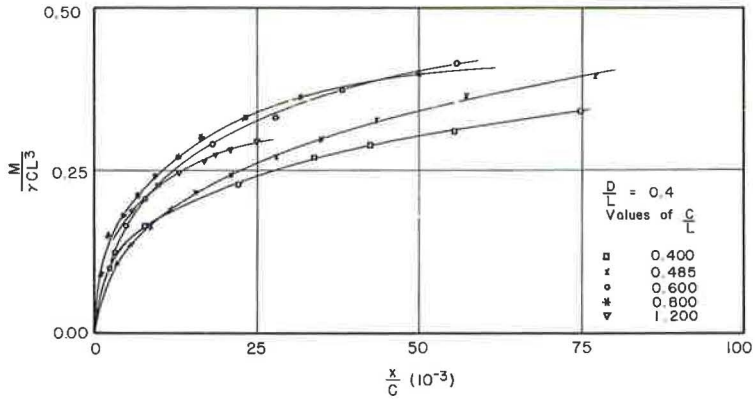

Figure 4. Non-dimensional plot of $M/\gamma CL^3$ vs x/C for various values of C/L : D/L = 0.4

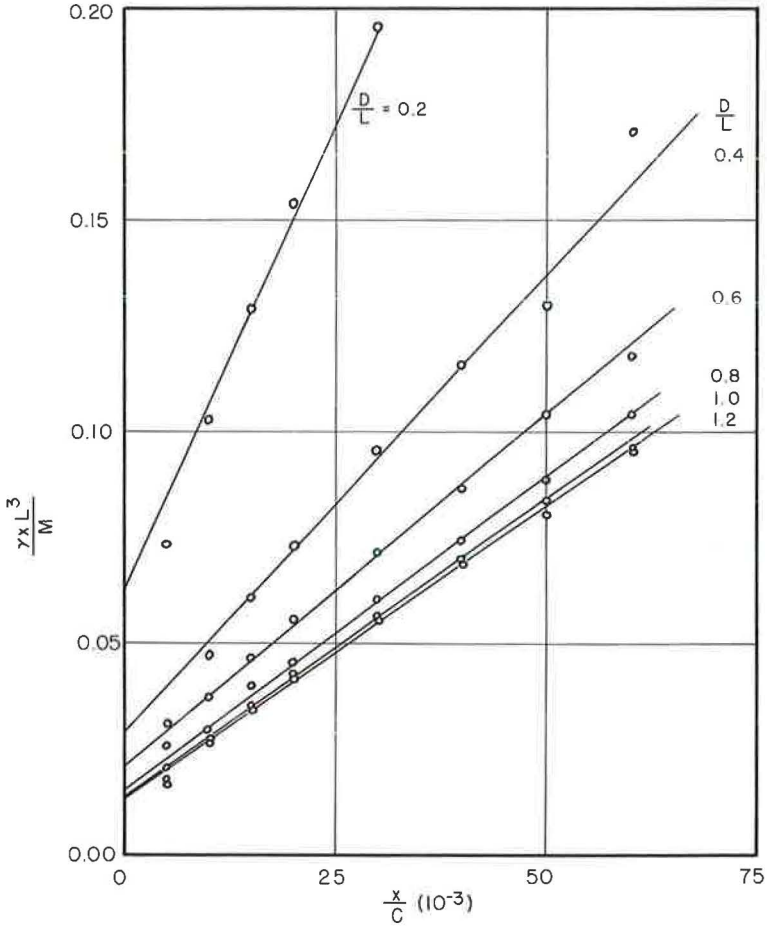

Figure 5. Transformed hyperbolic form of $M/\gamma CL^3$ vs x/C for various values of D/L.

Therefore, the inverse of the slopes of the straight lines in Figure 5 represent a measure of the ultimate value of the moment-strength ratio and are a function of D/L.

To determine the relation between D/L and the intercept a, D/L for each straight line is plotted against the parameter D/L + a (Fig. 6). The equation of the straight line is again of the two constant hyperbolic form and can be written as

$$a = \frac{1.022 \times 10^{-2}\ D/L}{D/L - 0.258} \qquad (14)$$

Likewise, the relation between D/L and the slope of each straight line b is

$$b = \frac{1.217\ D/L}{D/L - 0.150} \qquad (15)$$

as shown in Figure 7.

Substitution of Eqs. 14 and 15 in Eq. 11 gives

$$\frac{M}{\gamma CL^3} = \frac{x/C}{\left(\frac{1.022 \times 10^{-2}\ D/L}{D/L - 0.258} + \frac{1.217\ D/L}{D/L - 0.150}\right)\frac{x}{C}} \qquad (16)$$

The moment-strength parameter of Eq. 16 is a function of both the deflection parameter x/C and the moment arm parameter D/L.

Figure 8 compares the ultimate values of the moment-strength ratio given by Eq. 13 with the average measured values. The dashed line indicates a perfect correlation factor of one; the solid line gives the correlation factor of 0.904. Thus, the ultimate moment-strength ratio can be written in terms of a stability or failure number

$$\left(\frac{M}{\gamma CL^3}\right)_f = k\left(\frac{D/L - 0.150}{1.217\ D/L}\right) \qquad (17)$$

in which k is the correlation factor of Figure 8.

It must be emphasized that the relations given in Eqs. 14, 15, 16, and 17 are restricted to the range of values of D/L investigated; namely, $0.2 \leq D/L \leq 1.2$.

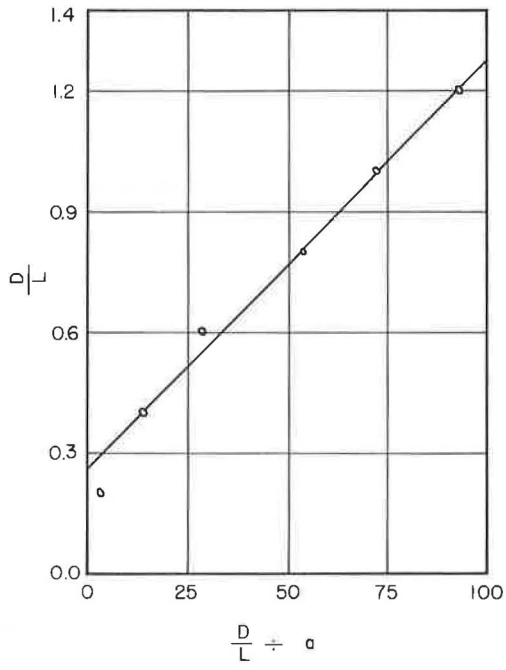

Figure 6. Transformed hyperbolic form of D/L vs hyperbolic intercept.

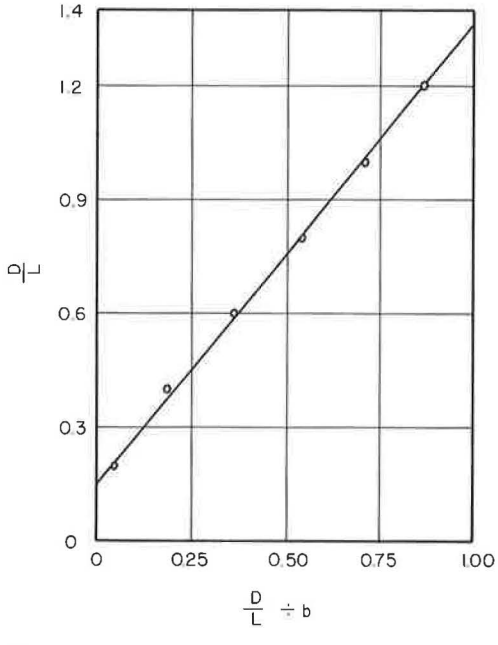

Figure 7. Transformed hyperbolic form of D/L vs hyperbolic slope.

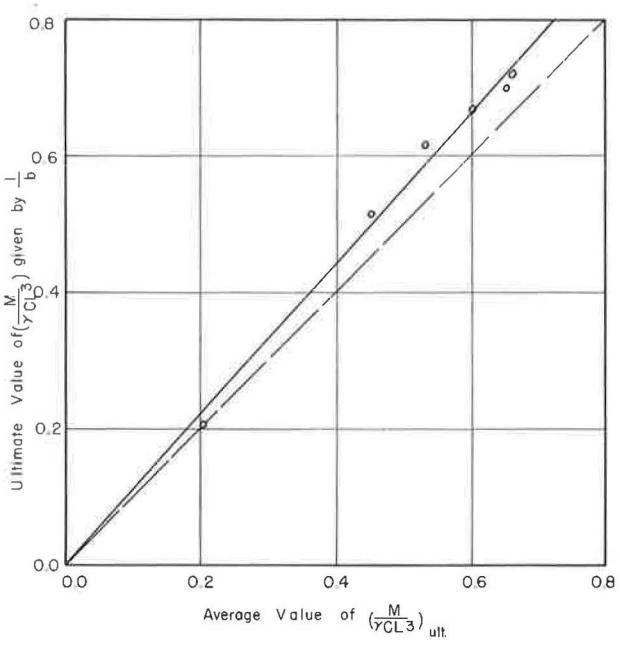

Figure 8. Correlation of $\left(\frac{M}{\gamma\ CL^3}\right)_{ult}$ given by 1/b vs average value of $\left(\frac{M}{\gamma\ CL^3}\right)_{ult}$.

SUPERPOSITION CONSIDERATIONS

Preliminary investigation showed that the response for the general case of a pole subjected to a horizontal load above the ground line could not be obtained by superimposing the two cases of a horizontal ground-line thrust (6) and the equivalent ground-line couple (7) although the loadings are statically equivalent. This illustrates the non-linearity of the pole problem in general and the stress-strain response of the soil in particular. Because of this non-linearity the tests presented herein represent a fairly general situation and not simply a combination of two special cases. Based on the present results, a more complete investigation of the applicability of superposition was performed.

The method used was to compare the deflection parameter x/C of the general case with the sum of the deflection parameters of the other two cases $[(x/C)_F + (x/C)_M]$ with given values of the moment-strength parameter $M/\gamma CL^3$ for each value of D/L. The thrust-strength parameter can be written as

$$F/\gamma CL^2 = M/\gamma CL^3 + D/L \tag{18}$$

Kondner and Green (6) showed that the relation between the thrust-strength parameter $F/\gamma CL^2$ and the deflection parameter x/C can be represented by

$$F/\gamma CL^2 = 0.72 \log_{10} (500\, x/C + 1) \tag{19}$$

or solving for x/C

$$x/C = \frac{\exp (3.21 F/\gamma CL^2) - 1}{5,000} \tag{20}$$

Kondner, Krizek and Schimming (7) showed that the relationship between the couple-strength parameter $\left(\frac{M}{\gamma CL^3}\right)_c$ and the deflection parameter x/C is of the form

$$\left(\frac{M}{\gamma CL^3}\right)_c = \frac{x/C}{0.0048 + 0.57\, x/C} \tag{21}$$

or solving for x/C

$$\frac{x}{C} = \frac{0.0048\left(\frac{M}{\gamma CL^3}\right)_c}{1 - 0.57\left(\frac{M}{\gamma CL^3}\right)_c} \tag{22}$$

The results obtained in the paper show that the relation between the moment-strength parameter $M/\gamma CL^3$) and the deflection parameter x/C is of the form

$$\frac{M}{\gamma CL^3} = \frac{x/C}{a + b\,x/C} \tag{23}$$

where a and b are functions of D/L as given in Eqs. 14 and 15.

Solving for x/C

$$\frac{x}{C} = \frac{a\left(\frac{M}{\gamma CL^3}\right)}{1 - \frac{bM}{\gamma CL^3}} \tag{24}$$

The results of solving each of Eqs. 20, 22 and 24 for given values of $M/\gamma CL^3$ and D/L are shown in Figure 9. For a given value of $M/\gamma CL^3$, the deflection parameter x/C is much greater for the general case (solid curve) than for the sum of the other two cases (dashed curve). This demonstrates the fact that the superposition principle cannot be applied and hence the limitations of linear theories. Such limitations are also generally contained in theoretical analyses using a soil modulus approach.

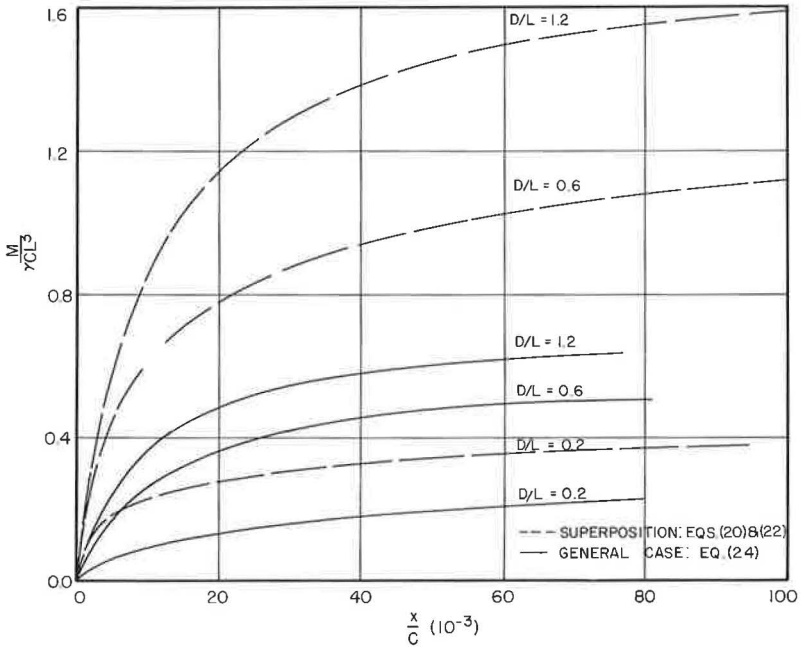

Figure 9. Non-dimensional plot of $M/\gamma CL^3$ vs x/C demonstrating superposition correlation.

CORRELATIONS WITH OTHER INVESTIGATIONS

A report of field and laboratory tests on the stability of posts subjected to lateral loads was reported by Shilts, Graves and Driscoll (10). Tests were performed on both full-scale posts and on large-scale model poles embedded in sand, similar to the testing done for the investigation presented herein. The data were presented in the form of a load-deflection curve for each test. Generalized conclusions were drawn concerning the effect of soil density, depth of embedment and shape of post. An equation was derived describing the relation between the movement of the post at ground level and an average soil pressure caused by a lateral load.

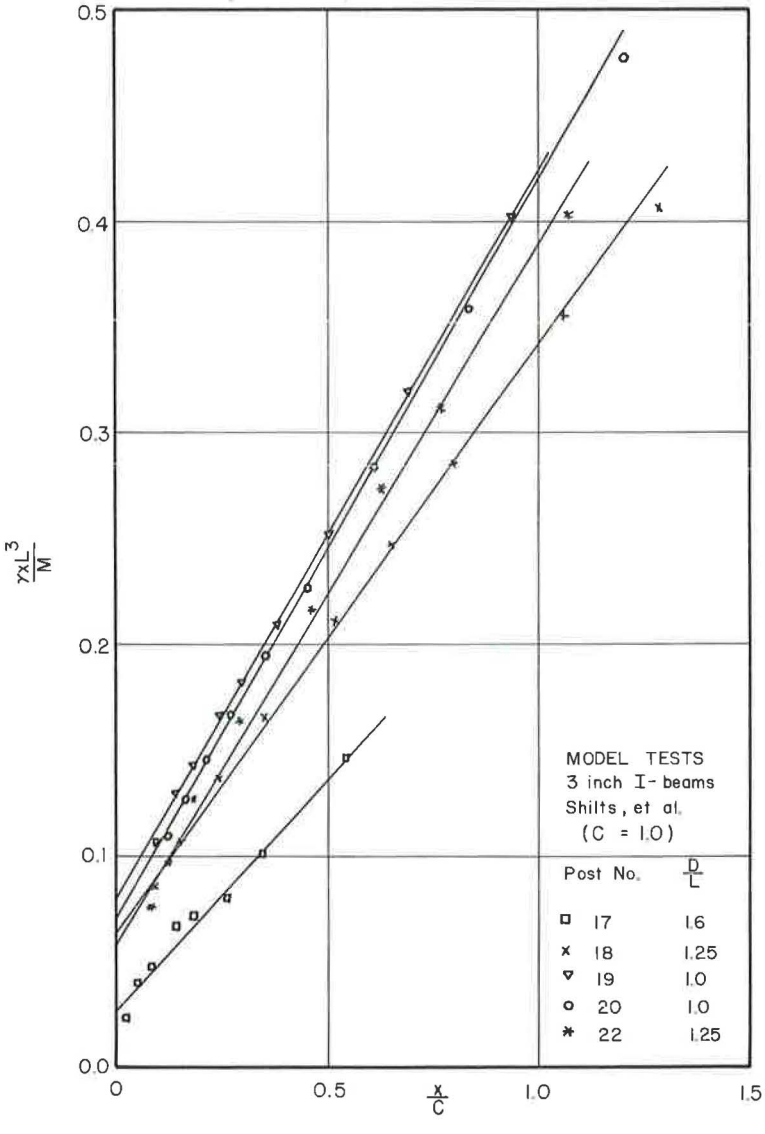

Figure 10. Transformed hyperbolic forms of $M/\gamma CL^3$ vs x/C for 3-in. I-beams at various values of D/L.

Model Tests

Figure 10 shows the same load-deflection data plotted in non-dimensional form using a normalized value of the circumference. All the data deal with model tests on 3-in. I-beams, so there is no shape effect present. The similarity in form between Figure 10 and Figure 5 is noticeable. In both cases, the slopes of the straight lines decrease as the D/L value increases; also, the intercept value decreases with increasing D/L values. A quantitative comparison is impossible because of the small number of tests performed and the question of what is a realistic value to use for the perimeter C of an I-beam.

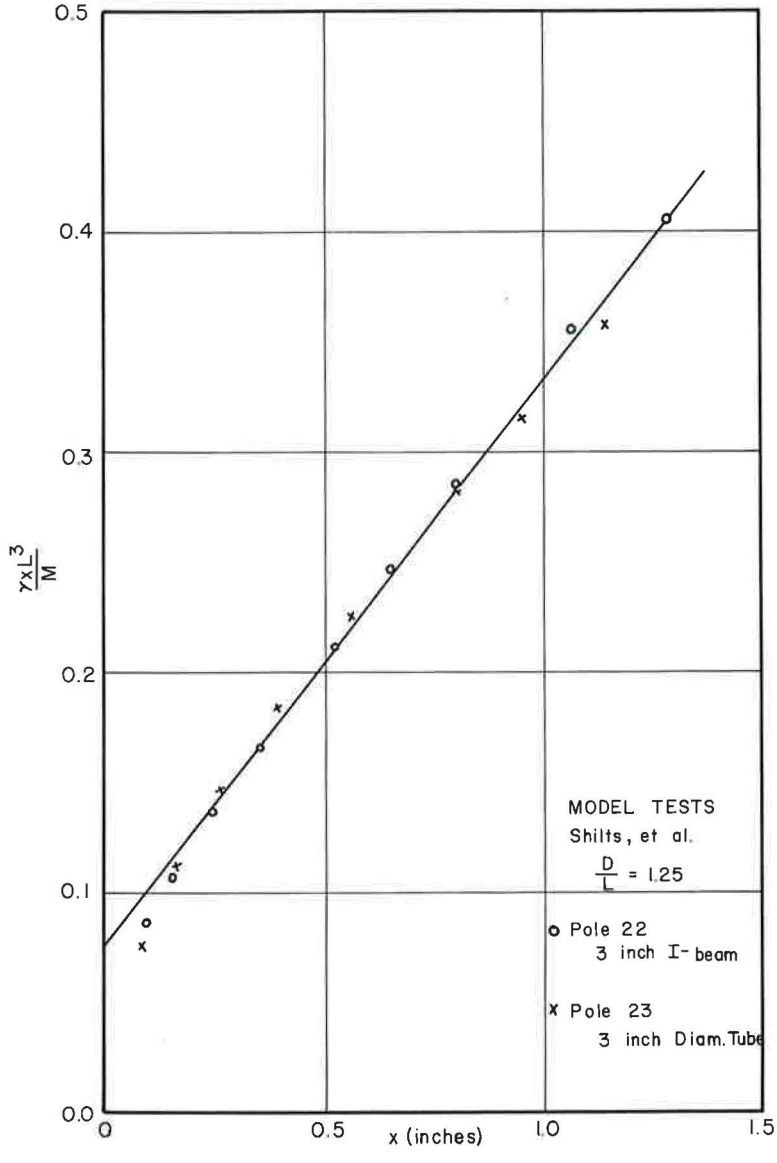

Figure 11. Transformed hyperbolic form of $M/\gamma CL^3$ vs x for two shapes at a constant value of D/L.

Figure 11 is a transformed hyperbolic plot for two tests performed on model poles with the same D/L ratio but different shapes. One is a circular pole with a 3-in. diameter and the other an I-beam with a 3-in. depth. They lie essentially along the same straight line. This seems to indicate that an I-beam has the same resistance as a circular pole with a diameter equal to the depth of the I-beam. If this is the case, a quantitative comparison can be made between the circular poles investigated in this paper and the I-beams tested by Shilts, Graves and Driscoll (10). Such a comparison is shown in Figure 12.

The data for the I-beam are plotted non-dimensionally using a value of C equal to that of a circular pole with a diameter equal to the depth of the I-beam. The data for the round pole are taken directly from Figure 5. Since the two plots are for the same value of D/L, one would expect them to coincide on a non-dimensional plot. Their failure to coincide could be due to a difference in relative density of the sand used for the two sets of tests. For the tests presented herein the density was controlled very carefully through the use of a vibrator.

The test pit and models used for the I-beam tests were larger and probably subject to less control, and hence resulted in a loose state. A comparison of the two curves of Figure 12 strengthens this conclusion. The slope of the straight line for the I-beam tests is greater and hence the ultimate value of the moment parameter, as given by the

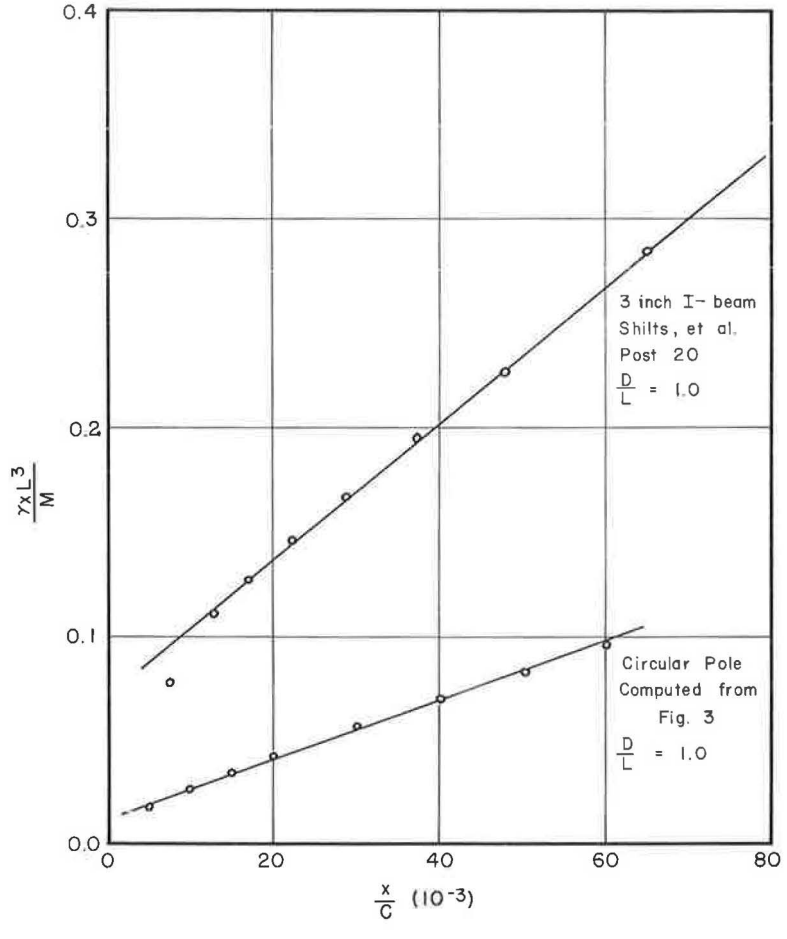

Figure 12. Transformed hyperbolic form of $M/\gamma CL^3$ vs x/C for a 3-in. I-beam and a 3-in. circular pole, D/L = 1.0.

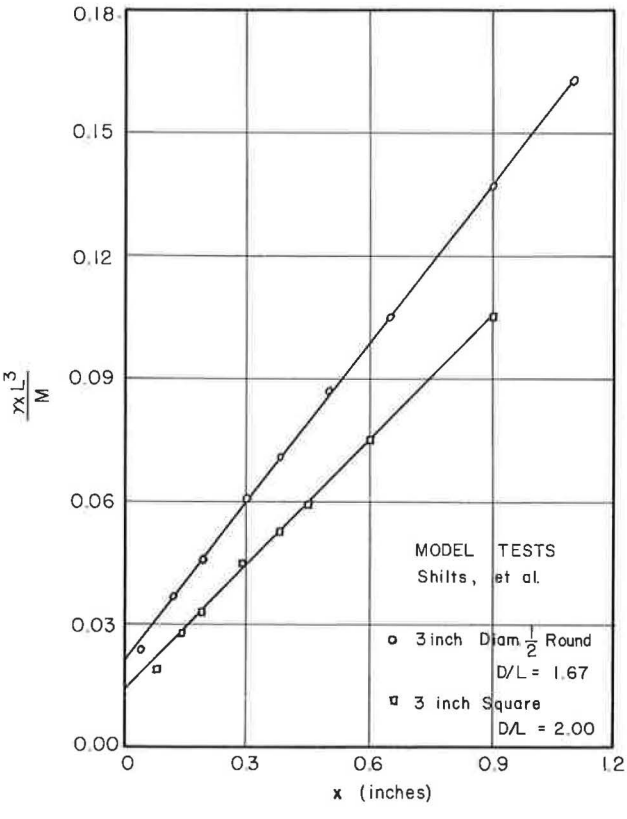

Figure 13. Transformed hyperbolic form of $M/\gamma CL^3$ vs x for two shapes at different values of D/L.

inverse of the slope, is less than that of the round pole tests. This would be expected if the sand were loose (lower relative density). In addition, the intercept value is higher for the I-beam tests which means the initial tangent modulus is lower for the plot of $M/\gamma CL^3$ vs x/C. This also would be expected if the sand were in a loose state. Thus, the failure of the two curves of Figure 12 to coincide can be attributed to either one or both of two causes: (a) the relative density of the sand varied in the two different experimental apparatus and/or (b) an I-beam is not equivalent to a circular pole with a diameter equal to the depth of the I-beam.

Shape effects have previously been mentioned several times. This study was confined to the testing of round poles. However, some results are given for other shapes by Shilts, Graves and Driscoll (10). They are given in non-dimensional form in Figure 13. Although not enough tests were performed to formulate a quantitative analysis, it is interesting that these plots also take the form of a two-constant hyperbola. This leads one to believe that further investigation on poles with various shapes will not lead to new relationships between load and deflection, but will only change the slope and intercept factors (a and b) by making them shape dependent.

Field Tests

The field test data on full-scale posts presented by Shilts, Graves and Driscoll (10) are shown plotted non-dimensionally in Figure 14. Posts 1, 5 and 6 were chosen because they were the only tests carried to a significantly large deflection. An average density of 109.5 pcf was used in the calculations. The abscissa, x, was not plotted non-dimensionally because of the question of the suitable choice of a value for the perimeter, C. The only effect due to the inclusion of the perimeter would be to change the abscissa scale; thus, the form of the plot would not be altered.

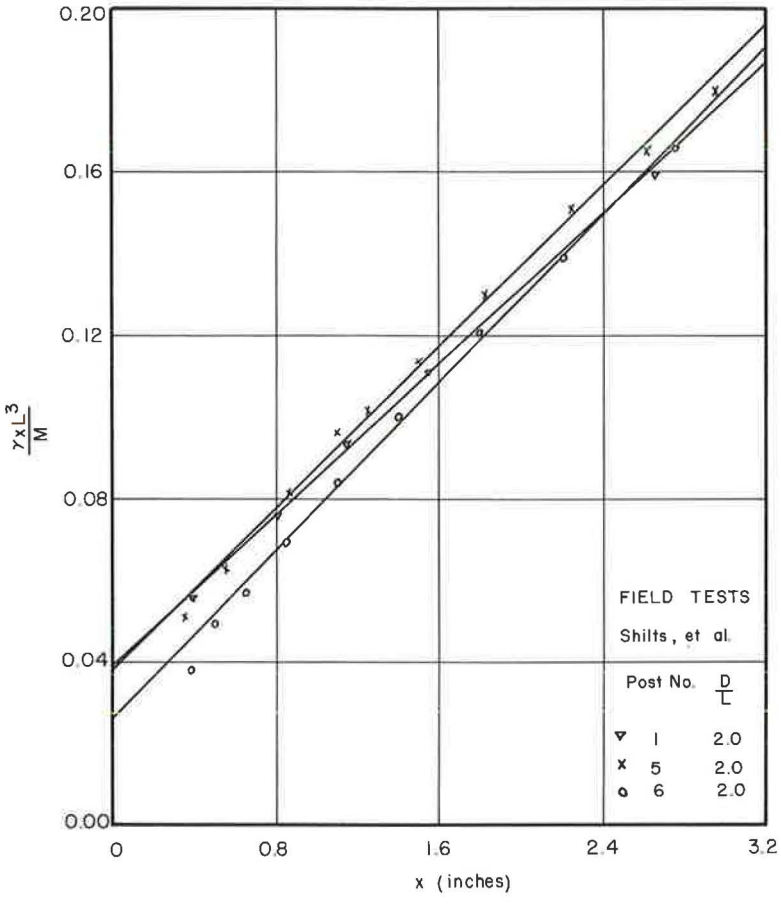

Figure 14. Transformed hyperbolic form of $M/\gamma CL^3$ vs x, field tests.

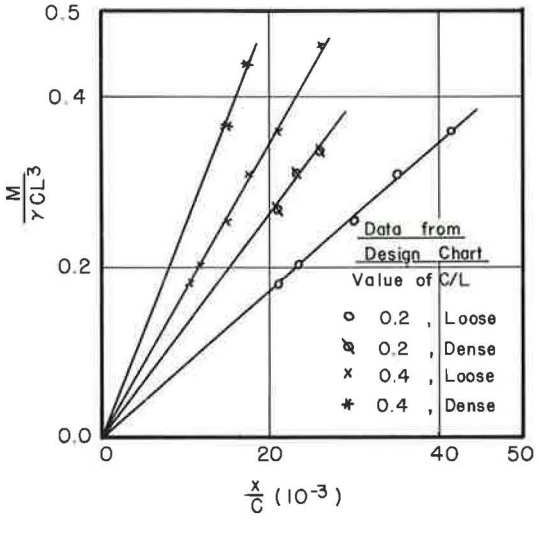

Figure 15. Non-dimensional plots of $M/\gamma CL^3$ vs x/C for various C/L values and density conditions.

It is not significant that the lines nearly coincide because if the abscissa were non-dimensionalized the curves would spread out inasmuch as post 1 is an Olmstead post, post 5 is a 7-in. steel I-beam with wings, and post 6 is an Olmstead post set in soil cement of 2-ft diameter.

The important aspect to note is that the form of the response is the same as that obtained for the model tests; namely, that of a two-constant hyperbolic representation.

Design Chart

A publication by the American Wood Preservers Institute (11) gives a design chart that is used by the Outdoor Advertising Association of America to obtain the required depth of embedment for posts subject to overturning loads. This chart was designed using information from Shilts, Graves and Driscoll (10). By knowing the load to be carried, the height of the load above the ground surface, the diameter of the pole to be used, and by estimating an allowable soil stress, an embedment depth can be found which will supposedly restrict the deflection at the ground-line surface to 0.5 in.

If a depth of embedment, height of load above ground surface, and allowable soil stress are first chosen and the chart then used to arrive at a load which can be carried for each diameter of pole, then the same non-dimensional parameters $M/\gamma CL^3$, x/C, D/L can be calculated.

For a constant value of D/L such a procedure will yield a horizontal line for each different depth of embedment on a plot of $M/\gamma CL^3$ vs x/C.

Replotting the same data as a function of the embedment parameter C/L will yield a group of straight lines (Fig. 15). Thus, the design chart has represented a non-linear response by a set of linear relations. The value of the moment-strength parameter (Fig. 15) varies only from 0.182 to 0.458. This same range of values for the moment parameter of Figure 3 at a large D/L value can be reasonably approximated by a straight line. However, the further this straight line is extended, the worse the approximation becomes. For example, if a small enough pole were chosen so that the value of x/C was very large, use of Figure 15 would predict a very large value of the $M/\gamma CL^3$ term. In fact, the ultimate value is infinite. This is unreasonable. The difficulty lies in the use of an arbitrary 0.5-in. ground-line deflection as the design criterion. This may be acceptable as a criterion for the movement of a building member, but as a stability criterion for a pole an arbitrary maximum deflection is not satisfactory. A large pole that has deflected ½ in. may be perfectly safe, whereas a small pole that has deflected the same amount may be near failure (Fig. 3). A satisfactory stability criterion might possibly be expressed as some ratio of deflection to pole size, such as x/C.

To demonstrate the important effect of relative density, Figure 15 shows two sets of curves for which nothing is changed except the relative density (allowable soil stress on the design chart). The curves for the high relative density are steeper than for the low case, showing that the high value will withstand more load for a given deflection.

Model pole tests in the form of $M/\gamma CL^3$ vs x/C, where each curve is a function of C/L have been reported (7). The curves were two-constant hyperbolas with a slope concave downward. Figure 16 plots the data from the design chart in this form. The curves are concave upward, indicating that a pole-sand system would act as a "hard" system with the moment increasing more rapidly than the deflection. Such a response is unrealistic. This does not mean that the design chart has no value, but it should be restricted to certain ranges of parameters and care should be exercised in its use.

Correlation of the design chart with the experimental results indicates that it would be highly desirable to conduct a carefully planned and controlled field study of full-scale pole systems utilizing the non-dimensional functional relationships presented. It is felt that if such a program is designed and conducted on the basis of non-dimensional techniques, there is a better chance of developing rational design criteria for the entire response range from initial loading through failure with a minimum of effort.

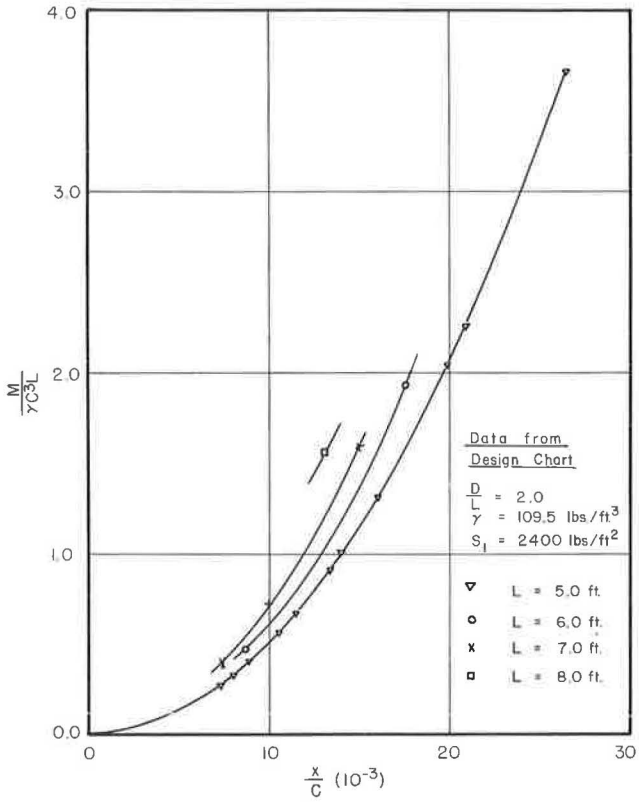

Figure 16. Non-dimensional plot of $M/_{\gamma}C^3L$ vs x/C for D/L = 2.0 and various values of L.

CONCLUSION

Quantitative results show that the superposition of ground-line couple and ground-line thrust relationships to represent the more general case of a horizontal load applied above the ground line is not valid.

ACKNOWLEDGMENTS

This research was conducted under support given by the National Science Foundation, research grant NSF-GP-359.

The authors also wish to express their appreciation to the various investigators whose previously published results have been utilized in this paper.

REFERENCES

1. Kondner, R. L., "A Non-Dimensional Approach to the Vibratory Cutting, Compaction and Penetration of Soils." Tech. Report No. 8, Dept. of Mechanics, Johns Hopkins Univ. (Aug. 1960).
2. Kondner, R. L., and Edwards, R. J., "The Static and Vibratory Cutting and Penetration of Soils." HRB Proc., 39:583-604 (1960).
3. Kondner, R. L., and Krizek, R. J., "A Non-Dimensional Approach to the Static and Vibratory Loading of Footings." HRB Bull. 277 37-60 (1960).
4. Kondner, R. L., "A Penetrometer Study of the 'In-Situ' Strength of Clays." Materials Research and Standards, ASTM, 2:3 (March 1962).
5. Kondner, R. L., "Friction Pile Groups in Cohesive Soils." Jour. of Soil Mech. and Found. Div., ASCE, 88:3, 117-149 (June 1962).

6. Kondner, R. L., and Green, G. E., "Lateral Stability of Rigid Poles Subjected to a Ground Line Thrust." HRB Bull. 342, 124-151 (1962).
7. Kondner, R. L., Krizek, R. J., and Schimming, B. B., "Lateral Stability of Rigid Poles Subjected to an Applied Couple." Tech. Report, Civil Eng. Dept., Northwestern Univ., p. 36 (1962).
8. Kondner, R. L., "Hyperbolic Stress-Strain Response: Cohesive Soils." Jour. of Soil Mech. and Found. Div., ASCE, 89:1, 115-143 (Feb. 1963).
9. Kondner, R. L., "Hyperbolic Stress-Strain Relation in Direct Shear." Tech. Report, Civil Eng. Dept. Northwestern Univ., p. 35 (1962).
10. Shilts, W. L., Graves, L. D., and Driscoll, G. G., "A Report of Field and Laboratory Tests on the Stability of Posts Against Lateral Loads." Second International Conf. of Soil Mech. and Found. Eng., Rotterdam (1948).
11. "How to Design Pole-Type Buildings." 3rd Ed., American Wood Preservers Institute (1962).
12. Bridgman, P. W., "Dimensional Analysis." New Haven (1931).

Vertical Stresses Under Certain Axisymmetrical Loadings

MILTON E. HARR and CHARLES W. LOVELL, JR.,
Associate Professors of Civil Engineering, Purdue University

This paper is concerned with the definition of vertical normal stresses in an isotropic, linearly elastic half-space loaded axisymmetrically by an element that is flexible and produces only normal loadings at the contact with its foundation. Following the presentation of a general formulation for any axisymmetrical loading function, integrations are performed for some specific loading functions. The variation of vertical normal stress with vertical and lateral position in the mass is graphically illustrated for a uniform loading and for a parabolic loading function. For a conical loading function, centerline vertical normal stresses only are computed.

Centerline stresses are compared for the three loading functions. In addition, stresses at various vertical and lateral positions are compared for the parabolic loading function and an approximation of it afforded by a series of disks. Practical use of the particular vertical stress solutions is suggested by example, including a preload embankment for a tank structure.

•STRESS conditions within a loaded earth mass are of interest to the potential solution of a variety of engineering problems. The magnitude and distribution of vertical normal pressures are required particularly in the determination of settlements.

In the stress analysis it is necessary to define: (a) the loaded area and the distribution of pressures over it; (b) the boundaries of the soil layer(s) loaded and the stress and/or displacement values at these boundaries; and (c) the relation between stress and strain in the loaded layer(s).

The equations and plots presented are for a set of assumptions that can be expressed both physically and theoretically (Fig. 1). A single homogeneous and semi-infinite layer (uniform half-space) has applied to its horizontal boundary a load distribution that is symmetrical about the vertical z axis. The loading element is a flexible one, and there is no friction between it and the loaded element ($\tau_{zx} = \tau_{zy} = 0$). The soil layer is both isotropic and linearly elastic. It is assumed that the strains are small and that the soil behaves as a continuum. Body forces are set equal to zero.

Within the restrictions of these assumptions, a general formulation for any axisymmetrical loading is developed. This is followed by integrations which produce particular solutions for certain specific loadings. Although much of the material presented here may be found in various forms in other references, it was felt that an orderly development of it, with certain original contributions, in a widely available engineering publication would be of considerable value. Practical applications of these particular solutions, both in direct and superposition of components form, are suggested.

FORMULATION OF GENERAL AXISYMMETRICAL LOADING

The formulation of the vertical normal stress (σ_z) at any point in an isotropic and linearly elastic half-space due to any flexible and frictionless axisymmetrical

Paper sponsored by Committee on Stress Distribution in Earth Masses.

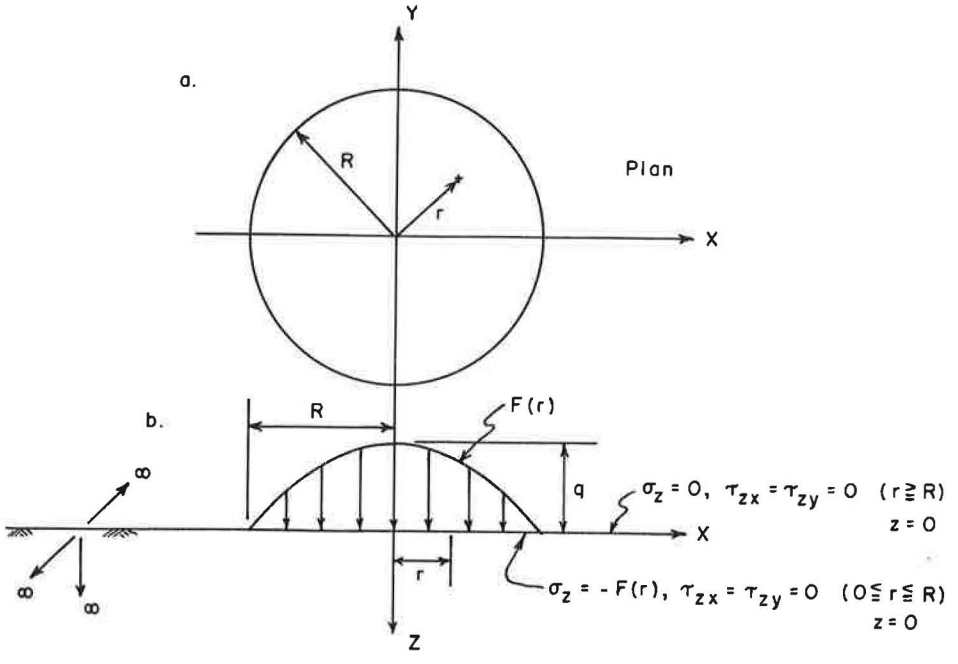

Figure 1. General axisymmetrical loading.

loading[1] (Fig. 1) can be stated as follows (1):

$$\sigma_z = \left[\frac{\partial \phi}{\sigma z} - z\frac{\partial^2 \phi}{\sigma z^2}\right] \tag{1}$$

in which

$\phi = \int_0^\infty D(\alpha)\, J_0(r\alpha) e^{-\alpha z}\, d\alpha$, $D(\alpha)$ = unknown coefficient to be determined from boundary conditions at $z = 0$ (plane of loading);

$J_0(r\alpha)$ = Bessel's function of the first kind of zero order; and

$r = \sqrt{x^2 + y^2}$

The axisymmetric loading function (interior to the circle of radius R) can be expressed as the Fourier-Bessel integral,

$$F(r) = \int_0^\infty \alpha J_0(r\alpha)\, D(\alpha)\, d\alpha \tag{2}$$

in which

$D(\alpha) = \int_0^\infty xF(x)\, J_0(\alpha x)\, dx$; and

$F(x)$ = the intensity of loading at $z = 0$.

[1] The generalized Boussinesq problem.

DISTRIBUTION OF VERTICAL STRESS UNDER UNIFORMLY LOADED CIRCULAR AREA

For this case F(x) = q = constant, and hence, from Eq. 2,

$$F(r) = Rq \int_0^\infty J_1(R\alpha)\, J_0(r\alpha)\, d\alpha \tag{3a}$$

At the loading surface (z = 0), and from Eq. 1,

$$(\sigma_z)_{z=0} = \left(\frac{\partial \phi}{\partial z}\right)_{z=0}$$

where, by substitution for ϕ,

$$(\sigma_z)_{z=0} = -\int_0^\infty \alpha D(\alpha)\, J_0(r\alpha)\, d\alpha \tag{3b}$$

On the loading surface, as

$$F(r) = -(\sigma_z)_{z=0}$$

from Eqs. 3a and 3b,

$$D(\alpha) = RqJ_1\frac{(R\alpha)}{\alpha}$$

Substituting $D(\alpha)$ in Eq. 1, the vertical normal stress at any radial distance r and any depth z is

$$\sigma_z = -Rq \int_0^\infty J_1(R\alpha)\, J_0(r\alpha)\, (1+z\alpha)e^{-z\alpha} d\alpha \tag{3c}$$

Performing the indicated integration in Eq. 3c, Egorov (1) obtained

$$\sigma_z = q\left\{A - \frac{m}{\pi\sqrt{m^2+(1+t)^2}}\left[\frac{m^2-1+t^2}{m^2+(1-t)^2}\,E(k) + \frac{1-t}{1+t} + \pi_0(k, n)\right]\right\} \tag{3d}$$

in which

$E(k)$, $\pi_0(k, n)$ = complete elliptic integrals of the second and third kind, respectively, of modulus k and parameter n (4);

$m = z/R$;

$t = r/R$;

$k^2 = \dfrac{4t}{m^2+(t+1)^2}$;

$n = -\dfrac{4t}{(t+1)^2}$; and

$$A = \begin{cases} 1, & r<R \\ \tfrac{1}{2}, & r=R \\ 0, & r>R \end{cases}$$

For the special case of vertical normal stress under the center of the uniformly loaded circular area (r = 0),

$$(\sigma_z)_{r=0} = q\left[1 - \frac{m^3}{\sqrt{(1+m^2)^3}}\right] = q\left\{1 - \frac{1}{\left[\left(\frac{R}{z}\right)^2+1\right]^{3/2}}\right\} \tag{3e}$$

Equation 3d is plotted as Figure 2.

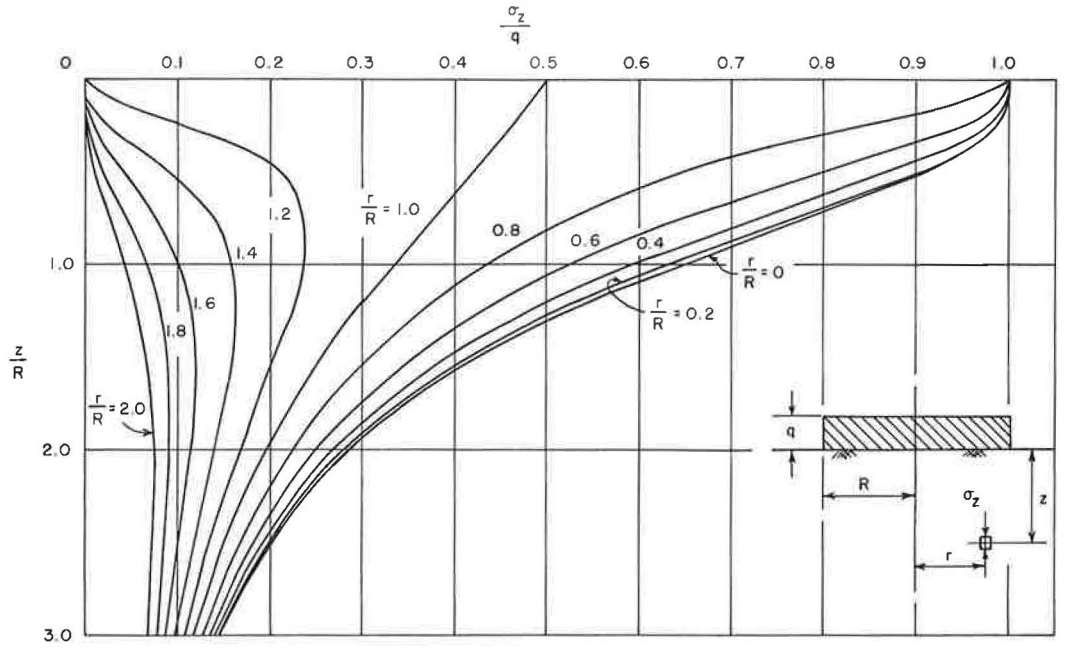

Figure 2. Uniform load (flexible and frictionless) over a circular area—after Egorov (1).

For examples of other approaches to this solution see Terzaghi (2) and Jurgenson (3). The presentation here follows more closely to that of Egorov (1).

DISTRIBUTION OF VERTICAL STRESS UNDER CIRCULAR AREA WITH PARABOLIC LOADING FUNCTION

The loading is a parabola of revolution, symmetrical about the z axis (Fig. 1b). For this case $F(x) = q\,(1 - x^2/R^2)$, hence from Eq. 2,

$$D(\alpha) = q\int_0^R J_0(\alpha x)\left[1 - \frac{x^2}{R^2}\right]x\,dx$$

Performing the indicated integration (cf. Eq. 9, p. 63, McLachlan, 5):

$$D(\alpha) = \frac{2q}{\alpha^2}\,J_2(\alpha R)$$

Substituting $D(\alpha)$ into the expression for ϕ (Eq. 1) and in turn substituting in Eq. 1, the vertical normal stress is

$$\sigma_z = -\,2q\int_0^\infty\left(\frac{1+\alpha z}{\alpha}\right)J_2(\alpha R)\,J_0(r\alpha)e^{-z\alpha}d\alpha \qquad (4a)$$

or

$$\frac{\sigma_z}{2q} = \int_0^\infty J_2(\alpha R)\,J_0(\alpha r)e^{-z\alpha}\,\frac{d\alpha}{\alpha} + z\int_0^\infty J_2(\alpha R)\,J_0(\alpha r)e^{-z\alpha}d\alpha$$

$$= I_1 + I_2 \qquad (4b)$$

The integrals I_1 and I_2 were obtained (cf. p. 399, Watson, 6) for values of $z > R$ as

$$I_1 = \frac{1}{8\left(1+\frac{z^2}{R^2}\right)} \sum_{m=0}^{\infty} (-1)^m \left[\frac{\frac{r^2}{R^2}}{4\left(1+\frac{z^2}{R^2}\right)}\right]^m \frac{(2m+1)!}{(m!)^2} \, {}_2F_1$$

$$m+1,\ \tfrac{3}{2}-m;\ 3;\ \frac{R^2}{R^2+z^2} \tag{4c}$$

$$I_2 = \frac{\frac{z}{R}}{8\left(1+\frac{z^2}{R^2}\right)^{3/2}} \sum_{m=0}^{\infty} (-1)^m \left[\frac{\frac{r^2}{R^2}}{4\left(1+\frac{z^2}{R^2}\right)}\right]^m \frac{(2m+1)!}{(m!)^2} \, {}_2F_1$$

$$m+\tfrac{3}{2},\ 1-m;\ 3;\ \frac{R^2}{R^2+z^2} \tag{4d}$$

where the hypergeometric function

$${}_2F_1(\alpha,\ B;\ \rho;\ z) = \frac{(\alpha)_n (B)_n z^n}{n!\,(\rho)_n}$$

and

$$(\alpha)_n = \alpha(\alpha+1)\,(\alpha+2)\ \ldots\ (\alpha+n-1)$$

It has been proved that I_1 and I_2 are absolutely convergent only in the case $|r| < z$.

The series in Eq. 4c and 4d were programmed and computed for a large range of values. A plot of the resulting stress distribution as a function of z/R is shown in Figure 3. The dashed curves are only approximate, as a consequence of the range of convergence of Eqs. 4c and 4d for large values of r/R.

When $r = R$ (beneath the perimeter of the loaded area), the integrals I_1 and I_2 simplify to (cf. p. 402, Watson, 6).

$$I_1 = \tfrac{1}{2}\left(\frac{R^2}{4z^2}\right) + \frac{R^2}{2z^2} \sum_{m=1}^{\infty} (-1)^m \left(\frac{R}{z}\right)^{2m} \frac{(m+1)\,(2m+1)^2}{[(m+2)!]^2} \tag{4e}$$

$$I_2 = \frac{R^2}{4z^2} + \frac{R^2}{4z^2} \sum_{m=1}^{\infty} (-1)^m \left(\frac{R}{z}\right)^{2m} \frac{1}{(m!)^2\,(m+2)^2} \tag{4f}$$

DISTRIBUTION OF VERTICAL STRESS UNDER CENTER OF CIRCULAR AREA WITH PARABOLIC LOADING FUNCTION

For this case, $r = 0$, hence $J_0(0) = 1$, and Eq. 4b reduces to

$$\left(\frac{\sigma_z}{2q}\right)_{r=0} = \int_0^{\infty} \frac{J_2(\alpha R)}{\alpha} e^{-\alpha z}\, d\alpha + z \int_0^{\infty} J_2(\alpha R) e^{-\alpha z}\, da \tag{5a}$$

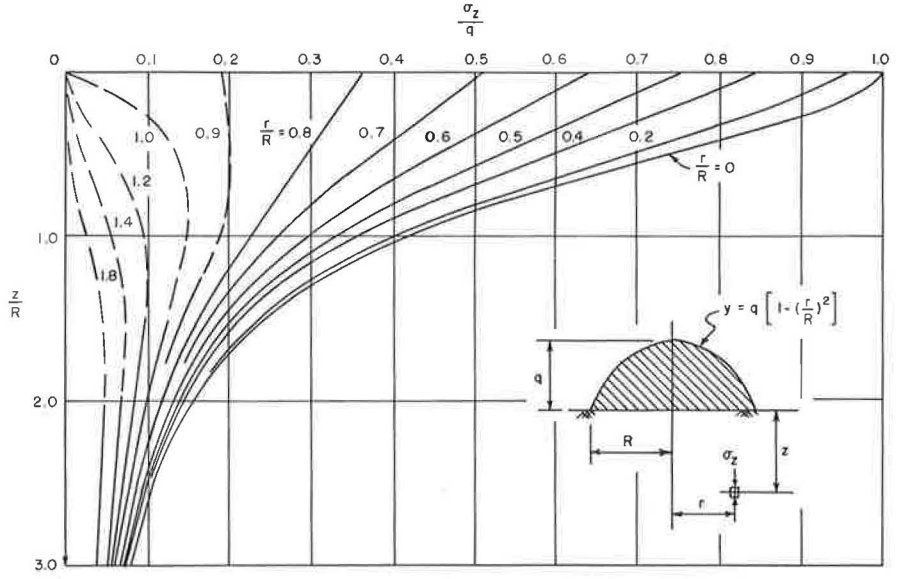

Figure 3. Parabolic load (frictionless and flexible) over a circular area (dashed portions are approximate).

Performing the indicated integration (cf. Eqs. 7 and 8, p. 386, Watson, 6),

$$\left(\frac{\sigma_z}{q_0}\right)_{r=0} = \left[\frac{1}{\frac{z}{R}+\sqrt{1+\left(\frac{z}{R}\right)^2}}\right]^2 \left[1 + \frac{2\left(\frac{z}{R}\right)}{\sqrt{1+\left(\frac{z}{R}\right)^2}}\right] \tag{5b}$$

DISTRIBUTION OF VERTICAL STRESSES UNDER CENTER OF CIRCULAR AREA WITH CONICAL LOADING FUNCTION

The solution for this case may be obtained in two steps. For simplicity, the loading function will be taken as shown in Figure 4a. The solution for this function may then be subtracted from that for a uniform loading (Eq. 3e) to obtain the desired solution for the conical loading (symmetric about the z axis).

Boussinesq (7) gave for the vertical normal stress under a point load Q at the surface of a lineally elastic and isotropic half space,

$$\sigma_z = \frac{3Qz^3}{2(r^2+z^2)^{5/2}}$$

in which r and z are the space coordinates of the point of vertical normal stress σ_z.

In Figure 4a, the differential load dQ is

$$dQ = \frac{\rho}{qR}\,\rho d\beta d\rho$$

and the vertical normal stress under the center is

$$(\sigma_z)_{r=0} = \int_0^{2\pi}\int_0^{R} \frac{\frac{3q}{R}z^3}{2\pi}\,\frac{\rho^2 d\rho d\beta}{(\rho^2+z^2)^{5/2}}$$

$$(\sigma_z)_{r=0} = \frac{3qz^3}{R} \int_0^R \frac{\rho^2 d\rho}{(\rho^2+z^2)^{5/2}}$$

Performing the indicated integration (cf. Eq. 205.05, Dwight, 8),

$$(\sigma_z)_{r=0} = q \left\{ \frac{\left(\frac{R}{r}\right)^2}{\left[\left(\frac{R}{z}\right)^2+1\right]^{3/2}} \right\} \tag{6}$$

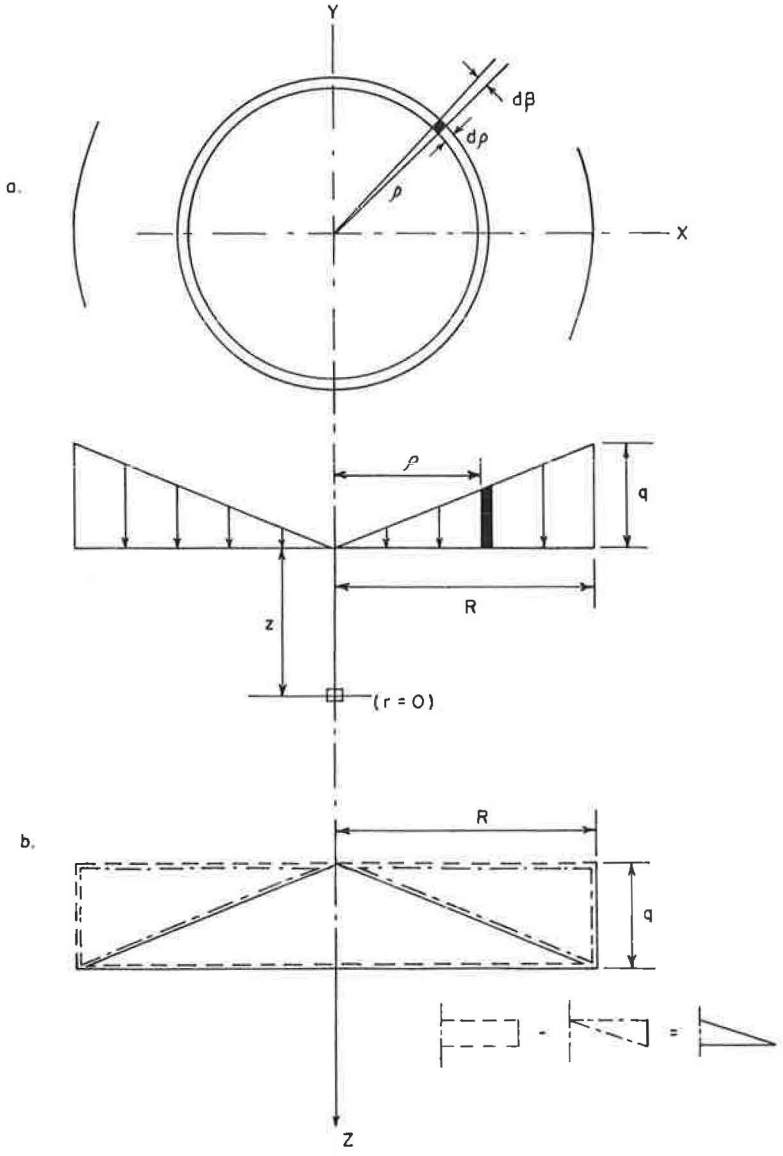

Figure 4. Center stress under conical loading, by parts (flexible and frictionless).

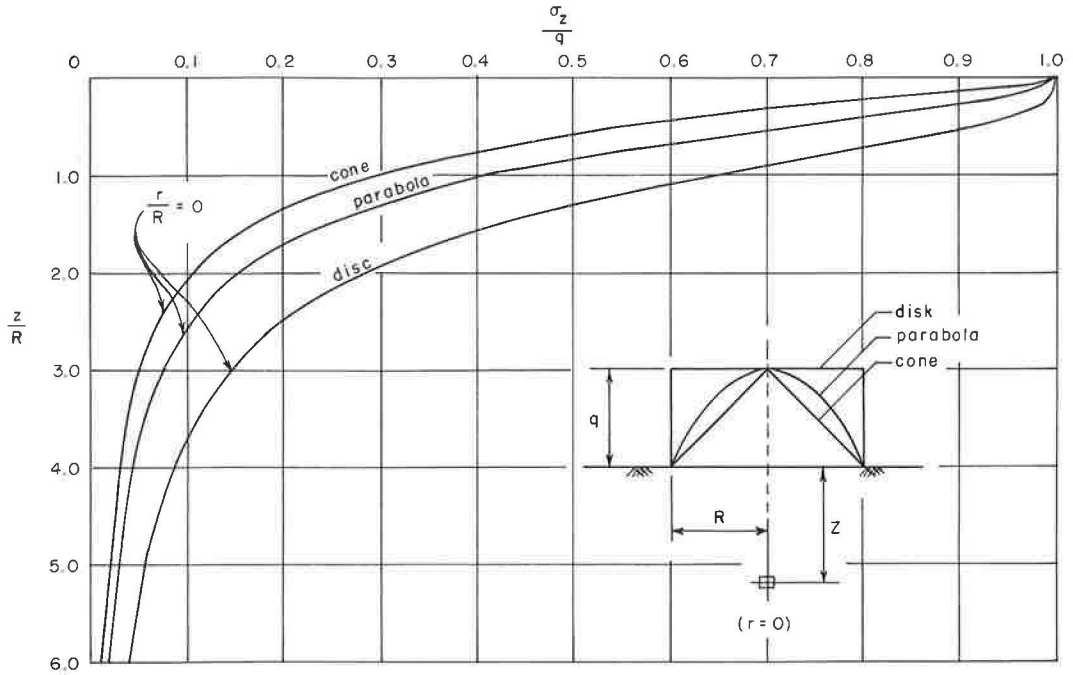

Figure 5. Three loading functions (flexible and frictionless) over a circular area.

As shown in Figure 4b, the desired stress along the z axis for the conical loading may be obtained by subtracting the stress produced by the loading function of Figure 4a from that produced by a uniform load. Or the vertical normal stress under the center of a conical load is the difference in values produced by Eqs. 3e and 6.

$$(\sigma_z)_{r=0} = q\left[\left\{1 - \frac{1}{\left[\left(\frac{R}{z}\right)^2+1\right]^{3/2}}\right\} - \left\{\frac{\left(\frac{R}{z}\right)^2}{\left[\left(\frac{R}{z}\right)^2+1\right]^{3/2}}\right\}\right]$$

$$(\sigma_z)_{r=0} = q\left\{1 - \frac{1}{\left[\left(\frac{R}{z}\right)^2+1\right]^{1/2}}\right\} \qquad (6a)$$

Equation 6 a is plotted in Figure 5. Integration for vertical normal stress under conical loading at values of 4/R other than r/R = 0 requires tedious numerical methods, and is not currently available. Therefore, it is pertinent to consider what approximations might be effected in the solution of practical problems involving conical loading functions and vertical stresses at r/R > 0.

APPROXIMATION OF DISTRIBUTION OF VERTICAL STRESSES UNDER CIRCULAR AREA WITH CONICAL LOADING FUNCTION—PRACTICAL PROBLEMS

The two obvious approaches to an approximation of the conical loading function are (a) replacement by a comparable continuous loading function, and (b) replacement by a stepped loading function. Figure 5 uses the former approach and compares the center stresses for a disk, parabola and cone of equal maximum load intensity q. These stresses are everywhere different, except at the surface, and have an order which

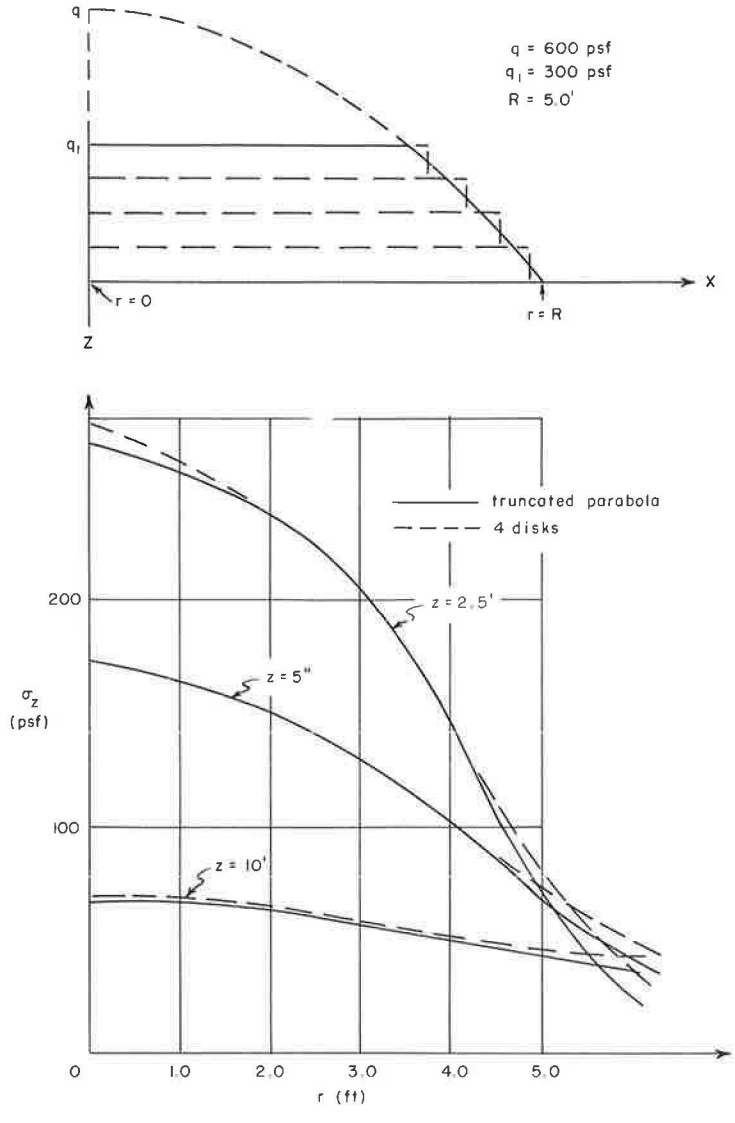

Figure 6. Approximation of parabolic loading function by series of disks.

would be predicted from the nature of the loading function. Along the centerline where vertical normal stresses are the largest, the parabola is seen to be a fair approximation of the cone.

A stepped loading function afforded by a series of thin disks built up in the z direction could presently be compared with the conical loading function only for the centerline stresses. Such an approximation is compared with the parabolic loading function in truncated form[2] at positions of $r \geq 0$ by the example of Figure 6. It is shown that the approximation can be quite good with a reasonable number of steps, particularly over those portions of the loaded soil which have large vertical normal stress. Logically, the conical loading function could also be satisfactorily approximated by a reasonable number of steps. On the basis of relationships shown and inferred, both the parabolic

[2]The truncation is accomplished by passing an XY plane through the figure generated by the loading function at any value $q_i < q$ (Fig. 3).

and the series of disks approximations are conservative (produce higher vertical normal stresses than the conical loadings).

Practicing engineers may be able to cite from their own experiences a number of practical loading situations which have in total or part the approximate shape of a truncated cone. One such example is the soil preload for a tank foundation described by Lambe (9). In this example, the soil preload was approximated by an "equivalent cylinder" or a stack of circular plates in the calculation of certain foundation stresses, including vertical ones. An additional alternative in the solution of vertical normal stresses for such a problem is afforded by a parabolic approximation (Fig. 3), handling the truncation by parts. The centerline stresses for a continuous conical loading function are available in Figure 5, again handling the truncation present in the practical problem by parts.

Another potentially pertinent field loading is the terminal portion of an embankment, such as occurs at a structural abutment. In simplified form, the loading could be envisioned as a halved truncated paraboloid, joined on its vertical face by a long strip of trapesoidal shape. Solution would be by parts.

SUMMARY

A general formulation for the vertical normal stresses produced in a lineally elastic homogeneous and isotropic mass of semi-infinite extent loaded symmetrically with respect to an axis normal to its horizontal surface was presented. The loading element was assumed to be flexible and without friction with respect to the foundation soil. Integrations were performed and data plotted which conveniently permit the determination of vertical normal stress at any point in the mass due to a circular area of uniform loading (Fig. 2), and with a parabolic loading function (Fig. 3). Centerline vertical normal stresses for a conical loading function were developed (Figs. 4 and 5), and the approximation of a conical loading function (either in whole, or truncated) by either a parabolic function or a stepped function of circular disks was discussed. It was suggested that the methods and data presented have practical applicability for foundation soil loadings such as preloads for tanks and "rounded" embankment terminals.

REFERENCES

1. Egorov, K. E., "Concerning the Question of Computing Stresses Under Foundations with Footings in the Shape of Rings." Mekanika Gruntov (Soil Mechanics), 34-57, Grosstroiizdat, Moscow (1958).
2. Terzaghi, Karl, "Theoretical Soil Mechanics." Wiley, New York, 376-382 (1943).
3. Jürgenson, Leo, "The Application of Theories of Elasticity to Foundation Problems." Contribution to Soil Mechanics, 1925-1940, 148-183, Boston Soc. of Civil Engineers (1940).
4. Harr, M. E., "Ground Water and Seepage." McGraw-Hill, 293-296 (1962).
5. McLachlin, N. W., "Bessel Functions for Engineers." 2nd Ed. Clarendon Press, Oxford, England (1955).
6. Watson, G. N., "A Treatise on the Theory of Bessel Functions." 2nd Ed., University Press, Cambridge, England (1952).
7. Boussinesq, J., "Application des Potentiels a l'Etude de l' Equilibre et du Mouvement des Solides Elastiques." Gauthier-Villars, Paris (1885).
8. Dwight, H. B., "Tables of Integrals (Revised Edition)." Macmillan (1947).
9. Lambe, T. W., "Pore Pressures in a Foundation Clay." ASCE. Proc. 88, No. SM2, pt. 1, 19-47 (April 1962).

Discussion

ROBERT L. SCHIFFMAN, Professor of Soil Mechanics, Rensselaer Polytechnic Institute, and Lecturer in Civil Engineering, M.I.T.—This paper presents some very useful and interesting new results in the evaluation of stress and displacement components in an elastic half-space subjected to normal surface tractions.

The general formulation of the axisymmetric problem, in terms of integrals with Bessel kernels goes back to Lamb (10). More recently Sneddon (11) has formalized integral transform techniques to this same end.

If the free surface of an elastic half-space were loaded axisymmetrically, by normal loads only, of distribution [-p(r)], the stress and displacement components at any point (r, z) within the half-space would be

$$u_r(r,z) = \frac{1+\nu}{E}\left[(1-2\nu)N_1^0(r,z) - zN_1^1(r,z)\right] \tag{7a}$$

$$u_z(r,z) = -\frac{1+\nu}{E}\left[(2-\nu)N_0^0(r,z) + zN_0^1(r,z)\right] \tag{7b}$$

$$\sigma_{rr}(r,z) = N_0^1(r,z) - zN_0^2(r,z) - \frac{1-2\nu}{r}N_1^0(r,z) + \frac{z}{r}N_1^1(r,z) \tag{7c}$$

$$\sigma_{\theta\theta}(r,z) = 2\nu N_0^1(r,z) + \frac{1-2\nu}{r}N_1^0(r,z) - \frac{z}{r}N_1^1(r,z) \tag{7d}$$

$$\sigma_{zz}(r,z) = N_0^1(r,z) + zN_0^2(r,z) \tag{7e}$$

$$\sigma_{rz}(r,z) = zN_1^2(r,z) \tag{7f}$$

in which

$$N_q^p(r,z) = \int_0^\infty m^p M(m)\, e^{-mz} J_q(mr)\, dm \tag{7g}$$

and

$$M(m) = -\int_0^a p(r) J_0(mr)\, dr \tag{7h}$$

The sign convention in the preceding formulation follows the theory of elasticity in which tension is positive, and compression is negative.

These formulations hold for all cases within the semi-infinite solid ($z>0$). If the loading function $p(r)$ is discontinuous, some problems arise in the calculation of the stress and displacement components at the discontinuity. This question has been discussed by Love (12).

The surface settlement w, follows from Eq. 7a:

$$w \equiv u_z(r,0) = -\frac{2(1-\nu^2)}{E}N_0^0(r,0) \tag{8a}$$

in which

$$N_0^0(r,0) = \int_0^\infty M(m) J_0(mr)\, dm \tag{8b}$$

Along the centroidal axis ($r = 0$), the component of shear stress σ_{rz} is zero, and the radial stress component σ_{rr} is equal to the tangential component of stress $\sigma_{\theta\theta}$.

$$\sigma_{rr}(0,z) = \sigma_{\theta\theta}(0,z) = \frac{1}{2}\left[(1+2\nu)N_0^1(0,z) - zN_0^2(0,z)\right] \tag{9a}$$

$$\sigma_{zz}(0,z) = N_0^1(0,z) + zN_0^2(0,z) \tag{9b}$$

in which

$$N_0{}^p(0,z) = \int_0^\infty m^p M(m) e^{-mz}\, dm \tag{9c}$$

If the loading function, p(r), is prescribed as a constant p_0, over a circular area of radius a, the formulation will reduce to the well-known Boussinesq relations (13).

The authors have analyzed the vertical stress components σ_{zz} due to a parabolic loading function of the form

$$p(r) = \frac{p_0}{a^2}(a^2 - r^2) \tag{10}$$

Substituting Eq. 10 in Eqs. 7g and 7h results in

$$M(m) = -\frac{2p_0}{m^2} J_2(ma) \tag{11a}$$

and

$$N_q{}^p(r,z) = -2p_0 \int_0^\infty m^{p-2} e^{-mz} J_2(ma) J_q(mr)\, dm \tag{11b}$$

The integral (Eq. 11b) can be evaluated in terms of an infinite series of hypergeometric functions as shown in this paper (6).

Substituting Eq. 11a into Eq. 8 results in a general expression for the surface settlement w.

$$w = \frac{4(1-\nu^2)p_0}{3E} {}_2F_1\left(\frac{1}{2}, -\frac{3}{2}; 1, \frac{r^2}{a^2}\right) \tag{12}$$

where $({}_2F_1)$ is the hypergeometric function, and is defined by the authors in its infinite series form. The surface settlement at the center (r = 0) of the loaded area w_0 is

$$w_0 = \frac{4(1-\nu^2)p_0 a}{3E} \tag{13}$$

The surface settlement at the edge (r = a) of the loaded area w_e is

$$w_e = \frac{16(1-\nu^2)p_0 a}{9\pi E} \tag{14}$$

In their paper, the authors analyze the development of vertical stress components. In settlement analysis, the principal stress components are often of major concern (9). In general, the calculation of the principal stress components requires a knowledge of the four independent components of stress (vertical, radial, shear, and tangential). Along the centroidal axis, however, the shear stress component is zero, and the radial and tangential components of stress are equal. Thus the vertical and radial stress components are the principal stress components.

The two integrals of interest in the computation of the radial stress component are (N_0^1) and (N_0^2). These integrals have the form,

$$N_0^1(0,z) = -2p_0 \int_0^\infty \frac{1}{m} e^{-mz} J_2(ma)\, dm \tag{15a}$$

and

$$N_0^2(0,z) = -2p_0 \int_0^\infty e^{-mz} J_2(ma)\,dm \tag{15b}$$

Evaluation of Eq. 15 and substitution in Eq. 9 results in expressions for both the radial and vertical stress components (6):

$$\sigma_{rr}(0,\zeta) = \sigma_{\theta\theta}(0,\zeta) = -p_0\left[\frac{1+2\nu}{2} I_1 - \zeta I_2\right] \tag{16a}$$

$$\sigma_{zz}(0,\zeta) = -p_0\left[I_1 + 2\zeta I_2\right] \tag{16b}$$

in which

$$I_1 = \left[(1+\zeta^2)^{1/2} - \zeta\right]^2 \tag{16c}$$

$$I_2 = \left[(1+\zeta^2)^{1/2} - \zeta\right]^2 (1+\zeta^2)^{-1/2} \tag{16d}$$

and

$$\zeta = z/a \tag{16e}$$

The numerical values for the radial and vertical stress components can be obtained from the same set of depth dependent formulas. The profile of the radial stress component along the centroidal axis is shown in Figure 7.

The conical loading can theoretically be treated in the manner just described. This method, however, will lead to certain computational difficulties. The integrals N_q^p cannot, in general, be evaluated in closed form. The function M(m) will be an infinite series of Bessel functions (6). Subsequently, the function N_q^p will be an infinite series of infinite integrals with the series summed over the order of the Bessel kernel.

In the special case, where the stress and displacement components are desired only along the centroidal axis (r = 0), a direct integration of the point load solution, as used by the authors is desirable (13). By this method the surface settlement w_0 at the center of a conical loading whose maximum load p_0 is at r = 0 is

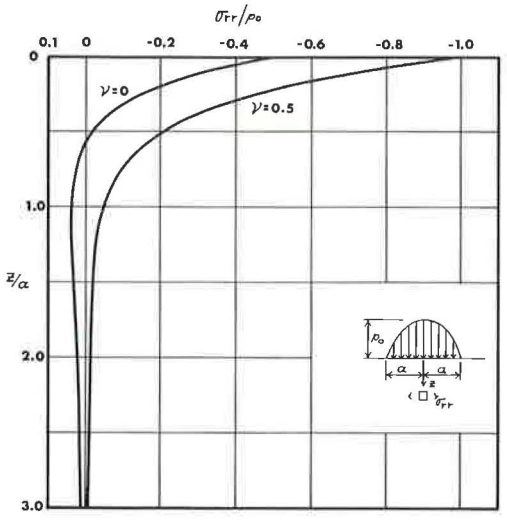

Figure 7. Radial stress component along centroidal axis (parabolic loading).

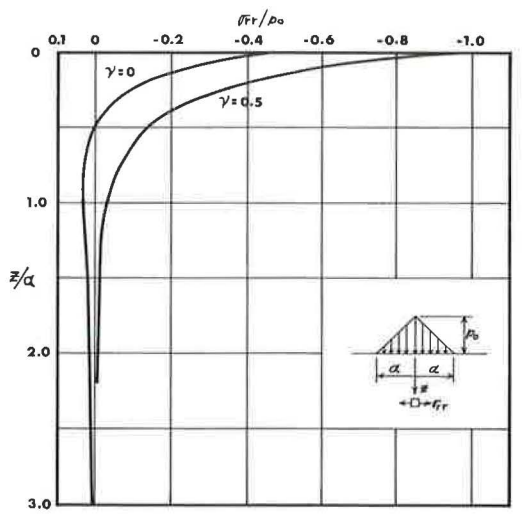

Figure 8. Radial stress component along centroidal axis (conical loading).

$$w_0 = \frac{(1-\nu^2)p_0 a}{E} \tag{17}$$

The radial stress component along the centroidal axis of the described conical loading has the expression

$$\sigma_{rr}(0,\zeta) = \sigma_{\theta\theta}(0,\zeta) = -\frac{p_0}{2}\left[(1+2\nu) + I_3 - 2(1+\nu)I_4\right] \tag{18a}$$

in which

$$I_3 = \zeta(1+\zeta^2)^{-1/2} \tag{18b}$$

$$I_4 = \zeta \log_e\left[\frac{1+(1+\zeta^2)^{1/2}}{\zeta}\right] \tag{18c}$$

Figure 8 shows the profile of the radial stress component beneath the center of the loaded area.

REFERENCES

10. Lamb, H., "On Boussinesq's Problem." Proc., London Math. Society, 34:276-284 (1902).
11. Sneddon, I. N., "Fourier Transforms." McGraw-Hill (1951).
12. Love, A. E. H., "The Stress Produced in a Semi-Infinite Solid by Pressure on Part of the Boundary." Phil. Trans., Roy. Soc., London, (A), 228, 377-420 (1929).
13. Timoshenko, S., and Goodier, J. N., "Theory of Elasticity." 2nd Ed., McGraw-Hill (1951).

Effects of Repeated Loading on Gravel and Crushed Stone Base Course Materials Used in the AASHO Road Test

JOHN H. HAYNES, Soils Engineer, Mason-Johnson and Associates, and
ELDON J. YODER, Professor of Highway Engineering, Purdue University

This paper presents the results of a laboratory investigation of the behavior of the AASHO Road Test gravel and crushed stone mixtures subjected to repeated loading. Cylindrical specimens were stressed triaxially to levels approximating those which would be found in the base course of a highway pavement. The repetitive loadings were applied with equipment developed in the laboratories of the School of Civil Engineering at Purdue University.

The materials used were obtained from the site of the AASHO Road Test. The gravel and crushed stone with grain size distribution equal to that used in the Road Test and compacted to the mean density levels found in the field were the subject of primary interest. Variation in percent fines and degree of saturation were considered to have a great effect on these basic gradations. Therefore, the percent passing the No. 200 mesh sieve was varied so that three mixtures of each material were obtained. These three mixtures were tested at three levels of saturation.

The effects of these variables on the deformation-rebound characteristics of the materials under repeated loads were studied. From these studies, the advantages and disadvantages of each material, concerning its value as a base course material, were found and are reported in detail. Also, a comparison between the laboratory and field performance of the two AASHO materials is presented.

•THE variable of base course type was included at several locations in the flexible test sections of the AASHO Road Test at Ottawa, Ill. These special test sections were in the form of wedges, 160 ft in length. Base thickness and type were the only variables in the various sections.

Materials used in the special base course studies included cement-treated gravel, bituminous-treated gravel, untreated crushed stone and untreated gravel. The test sections were divided into 40-ft subsections for purposes of analysis; performance was related to the mean thickness of base. A 3-in. surface was used in the special sections in which stone and gravel were compared. No subbase was used in Loop 3 whereas in Loops 4 and 5, 4 in. of subbase was included in the design. The typical section as outlined in the AASHO Road Test Report (5) included a shoulder of crushed stone materials.

During the winter of 1960, personnel from the Road Test contacted Purdue University to determine if tests could be performed to evaluate the special base course materials. It was hoped that a test would be devised wherein appropriate strength pa-

Paper sponsored by Committee on Stress Distribution in Earth Masses.

rameters could be assigned to the materials which in turn could be related to relative performance. It soon became apparent that it would be extremely difficult to devise a single test that would describe the properties of all of the materials since tensile strength was of importance when considering the bituminous-and cement-treated gravels, whereas the properties defining the gravel and crushed stone were associated with cohesion and angle of internal friction. As a result, it was decided to study in detail the gravel and crushed stone materials with the hope of determining why these materials behaved as they did under conditions of test traffic.

A series of repeated triaxial tests was performed on the crushed stone and gravel base course materials. Specimens were compacted to density and moisture levels compatible with those existing in the prototype pavement. This paper summarizes the data obtained and presents an analysis of the test data in light of relative performance in the road. Some inconsistencies were noted when considering the relative performance of these materials in the laboratory as opposed to the field. As a result, the analysis is, to some extent, qualitative in nature, but it is hoped that it will be of interest to the engineering profession and will assist engineers in formulating criteria for design.

GRAVEL AND CRUSHED STONE BASES AND THEIR FIELD PERFORMANCE

The crushed limestone used in the special test sections was the same type as that used in the factorial sections. It was a well-graded material having sharp angular grains, and the gravel base material was a well-graded uncrushed gravel. Average grain size distribution curves for each are shown in Figure 1. These grain size curves were obtained by averaging values determined from many tests made on samples taken from the road. The crushed stone base contained 11.5 percent passing a No. 200 mesh sieve; the gravel base contained 9.1 percent passing a No. 200 mesh sieve. The crushed stone was non-plastic and the gravel had a plasticity index of 3.5 percent.

The maximum dry densities, based on Standard AASHO compaction, were 139 and 140 pcf for the crushed stone and gravel, respectively. Field compaction was 101 percent for the crushed stone and 104 percent for the gravel. It should be remembered that these are average values and they must be treated as such.

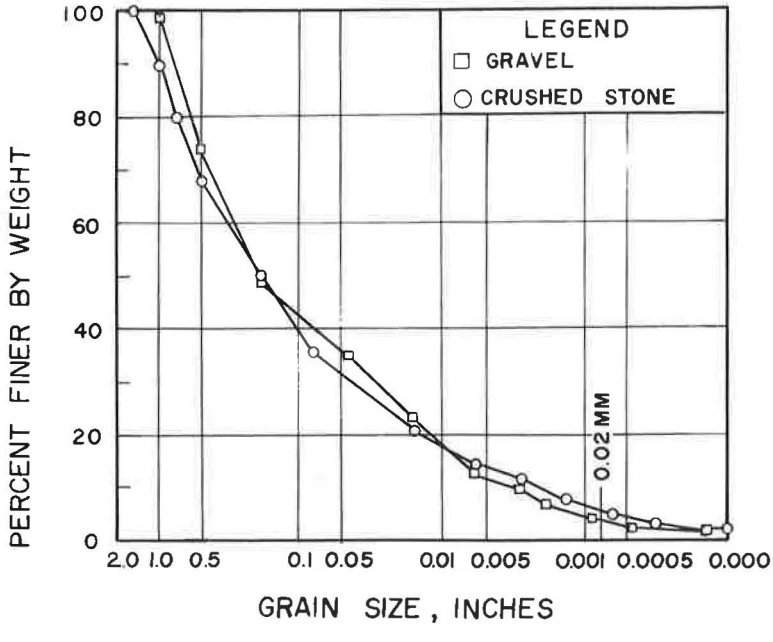

Figure 1. Grain size distribution curves.

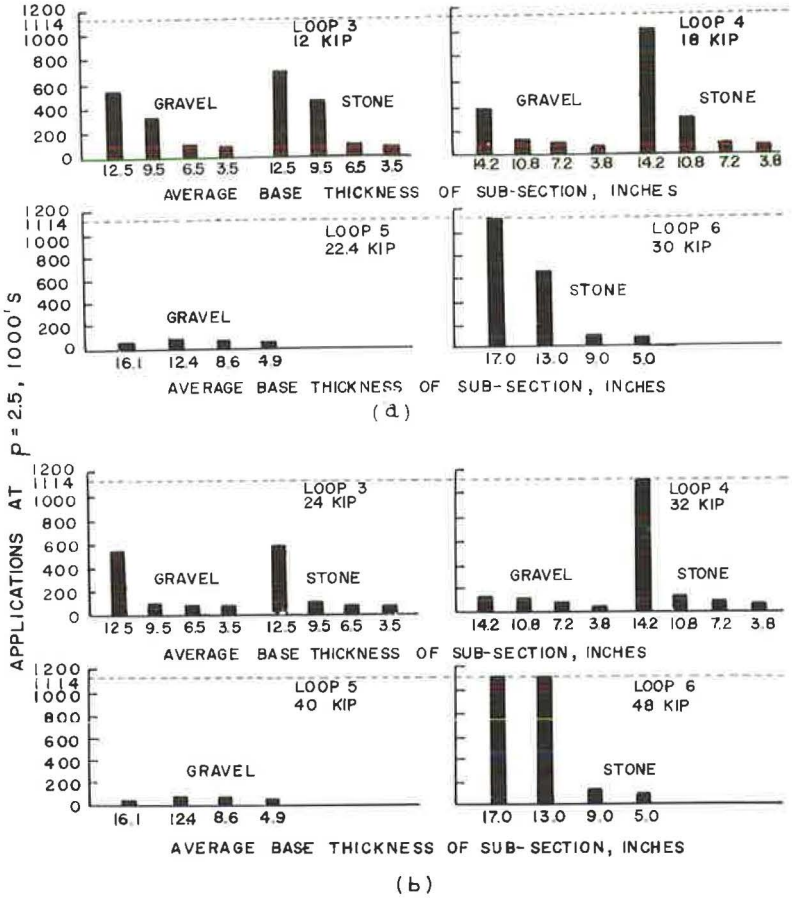

Figure 2. Performance data, special base type experiment: (a) single-axle loads, (b) tandem-axle loads (2).

The field performance of the gravel sections was inferior to that of the crushed stone. In fact, the relative performance of the gravel was such that it was not included in a major portion of the analysis presented in the AASHO Road Test Report. Benkelman, Kingham and Schmidt (2) state, "The gravel base sections failed early in the test and are omitted from the analysis of performance." ... "It appears that the gravel material possessed a level of internal stability that might be considered adequate for loads operating on Loop 3, nearly so for the loads on Loop 4 but definitely not for those on Loop 5."

Figures 2, 3 and 4 show field performance data for the gravel and crushed stone bases. The number of load applications at a serviceability index equal to 2.5 was invariably less for gravel sections than for the other base materials (Fig. 2). In the case of Loop 5 (22.4-kip load), there was no apparent orderly relationship between depth of gravel base course and load application at serviceability index 2.5. This suggests an inherent weakness in the gravel material itself.

Figure 3 shows pavement deflection as a function of base thickness at various seasons. The deflection values of the pavements built over the crushed stone bases were (with one exception) greater than the deflections of corresponding pavements containing the gravel base. Deflection of pavements over both base materials was higher in the spring than in the fall. Figure 4 shows seasonal deflections for the 9-in. base thickness. Here again, with one exception, the stone bases resulted in greater deflection than the gravel bases.

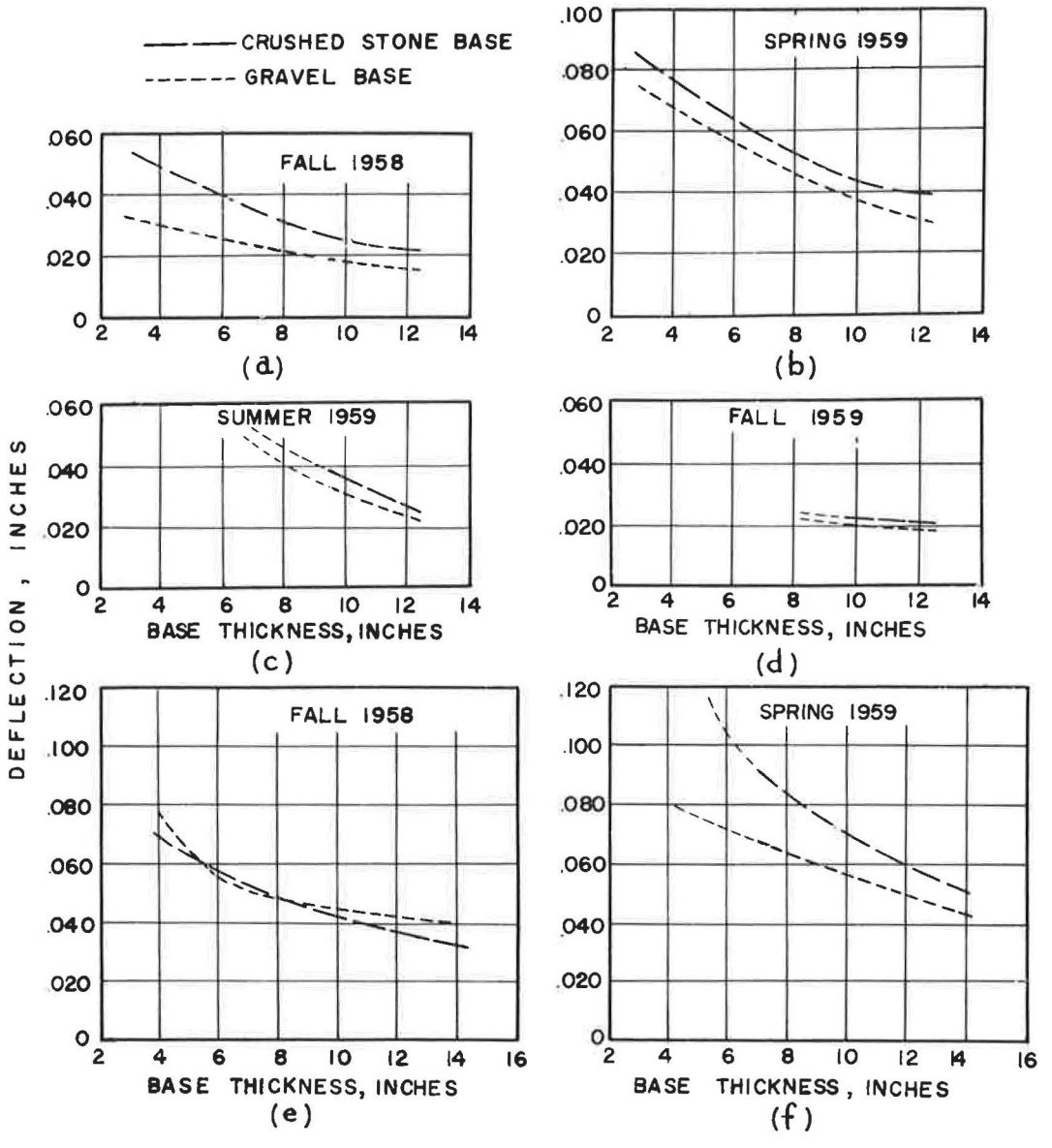

Figure 3. Special base type experiment, relationship between base thickness and deflection, a, b, c and d 12-kip single-axle load, Loop 3; e and f 18-kip single-axle load, Loop 4 (5).

The deflection data (Figs. 3 and 4) were obtained by use of the Benkelman beam. This test measures the pavement's surface deflection due to the application of a static load. The measured value includes the deflection of pavement surface, base, subbase and subgrade.

LABORATORY TESTING PROGRAM

The repeated loading device (Fig. 5) consists of a conventional triaxial cell with load supplied by means of compressed air. The device contains a pressure cylinder

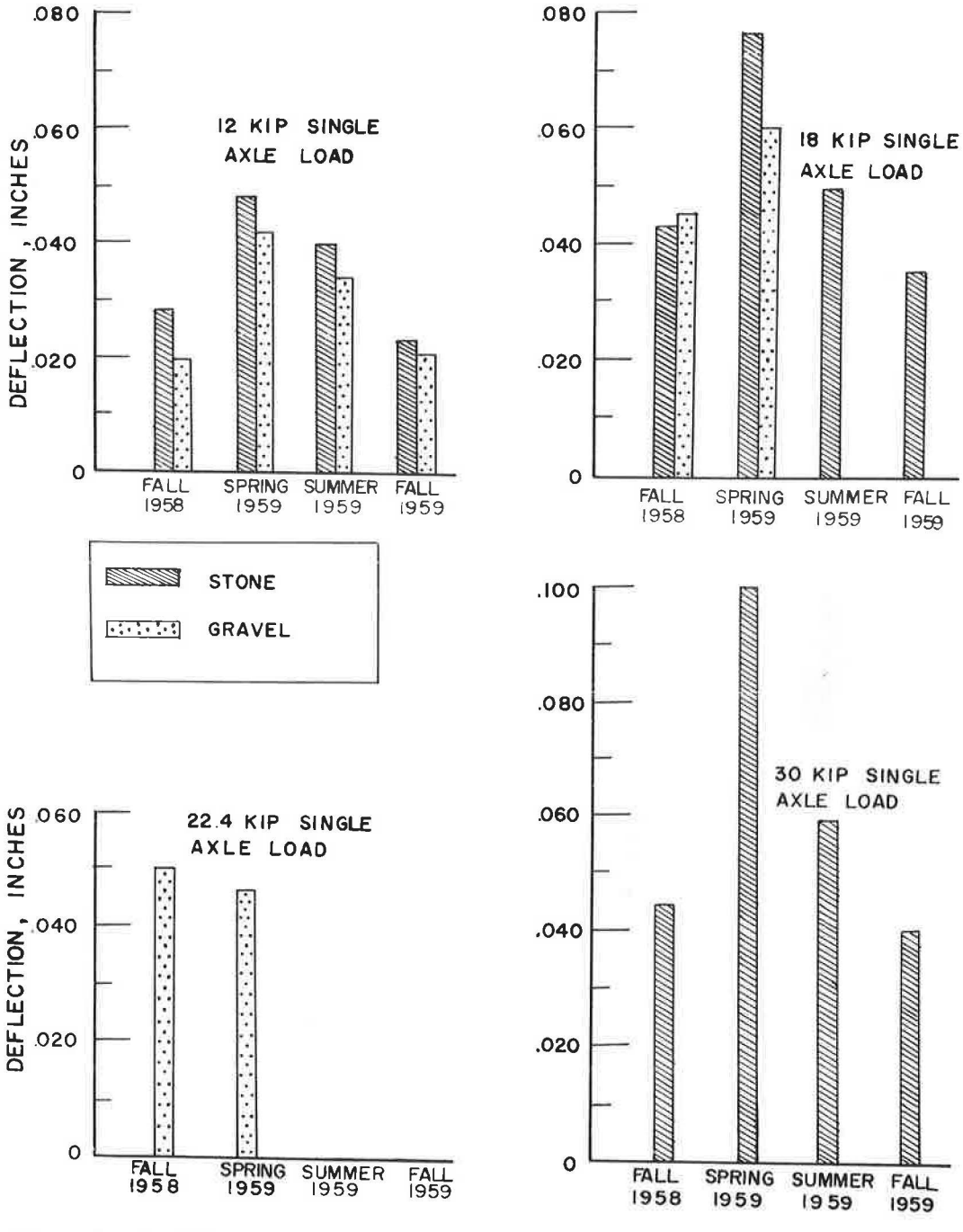

Figure 4. Special base experiment, seasonal deflection for 9-in. base thickness (5).

and solonoid valves that can be controlled electrically to apply repeated loads of varying magnitude, interval and duration. Records of total deformation, elastic rebound, and permanent deformation at various intervals throughout the test were obtained. A 15-psi confining pressure was used on the specimens throughout the testing program. A deviator stress of 70 psi was selected on the basis of approximate stresses that existed at the base course level in the Road Test pavement.

The materials from the Road Test were separated in the laboratory on various sieves. The aggregates were then recombined to yield a gradation corresponding to the average measured in the test pavements (Fig. 1). Three levels of amount of material passing a No. 200 sieve (6.2, 9.1, and 11.5 percent) were studied, resulting in the study of six gradations, three for the crushed stone and three for the gravel. As comparisons of laboratory and field performance were of interest, all samples were tested at field dry density levels, 141 pcf for the crushed stone and 145 pcf for the gravel.

Table 1 summarizes the density data obtained in the study. Loose density was obtained by pouring the material into a container of known volume and maximum density was obtained by controlled vibratory compaction. Relative densities corresponding to field conditions were 92 and 80 percent for the gravel and crushed stone, respectively.

Moisture content was also of interest in this study as it was postulated that degree of saturation would have great effect upon performance. An attempt was made to maintain three levels of degree of saturation, 70, 85 and 100 percent. However, due to slight variations in moisture content and dry unit weight, the resulting degrees of

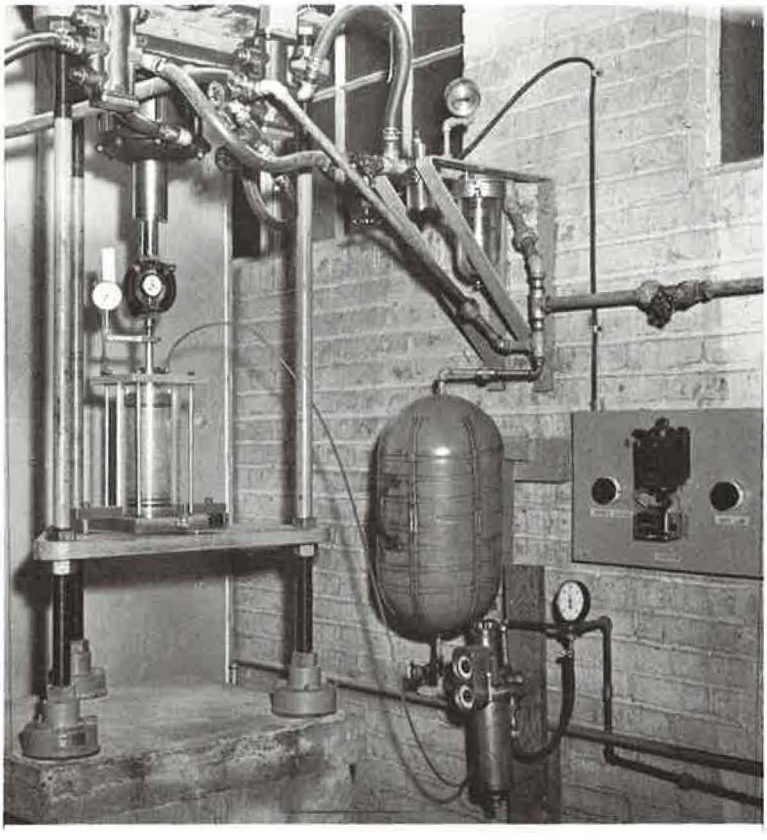

Figure 5. Equipment for repeated load tests.

TABLE 1

SUMMARY OF RELATIVE DENSITY DATA

Material	Gradation (% passing No. 200 sieve)	Loose Density (pcf)	Avg. Field Density[a] (pcf)	Max. Density (pcf)	Relative Field Density[b] (%)
Gravel	6.2	126.6	145.0	145.6	97
	9.1[c]	127.0	145.0	146.6	92[c]
	11.5	126.7	145.0	145.8	96
Crushed stone	6.2	113.3	141.0	141.6	98
	9.1	113.5	141.0	144.9	88
	11.5[c]	118.9	141.0	146.3	80[c]

[a] Also density used in laboratory tests.
[b] Difference between field and loose densities divided by difference between maximum and loose densities.
[c] Average values from road.

saturation varied from 63 to 98 percent. All samples were compacted at a moisture content corresponding to a degree of saturation of 70 percent. The test samples were compacted using impact procedures. A 5.5-lb hammer having a free fall of 12 in. was used. The compactive effort was varied for each gradation and a series of dry density points was obtained. These points, when plotted against a semilog scale of compactive effort, produced a straight-line relationship. All test samples were then compacted at the required compactive effort to produce the desired dry density.

The compacted test samples were then either tested at the 70 percent saturation level or, if higher saturation levels were desired, the moisture content was raised to the approximate degree of saturation desired. This was accomplished by means of the saturation mold shown in Figure 6. The moisture content in the samples was increased by applying a vacuum to the mold and allowing water to enter through perforations in the mold. By continually weighing the samples during the wetting process, it was possible to obtain approximate degrees of saturation selected for the test. The samples were then wrapped and stored in a controlled humidity room for an additional day so that moisture equilibrium could be achieved.

Originally, it was hoped to test both the gravel and crushed stone samples at a degree of saturation approaching 100 percent. However, the crushed stone materials were so pervious that the water invariably migrated toward the bottom of the sample with the result that, except for low degrees of saturation, moisture distribution was not uniform throughout the length of the sample. This was particularly true for those samples above about 80 percent saturation. This phenomenon, however, did not occur in the gravel specimens and it was possible to maintain a relatively uniform moisture gradient throughout these samples. As a result, tests reported in this paper for the crushed stone materials are for degrees of saturation up to 81 percent, whereas the degrees of saturation reported for the gravel are as high as 98 percent.

Figure 7 shows a typical load-time trace for two load cycles. Load was measured by means of a proving ring; load impulse was transmitted from strain gages mounted on the proving ring to an electronic pen recorder. A slight residual load was maintained on the sample between deviator load intervals.

Figures 8, 9, 10 and 11 show the deflection and rebound histories of the test samples. The values of deflection represent accumulative axial deflection from beginning of test. The values of rebound represent individual load cycle rebound. Each curve represents the average for two test samples. The results obtained from tests on the three gradations for both the crushed stone and gravel materials are shown. There is a general orderly relationship between degree of saturation and deflection at any given cycle.

Figure 6. Saturation mold and cell.

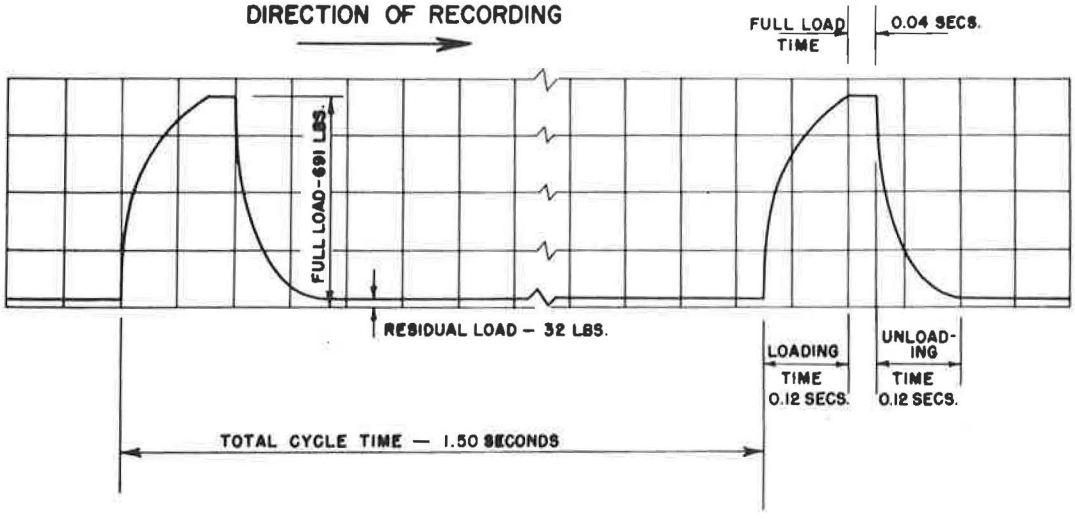

Figure 7. Typical load — time trace for 2 load cycles.

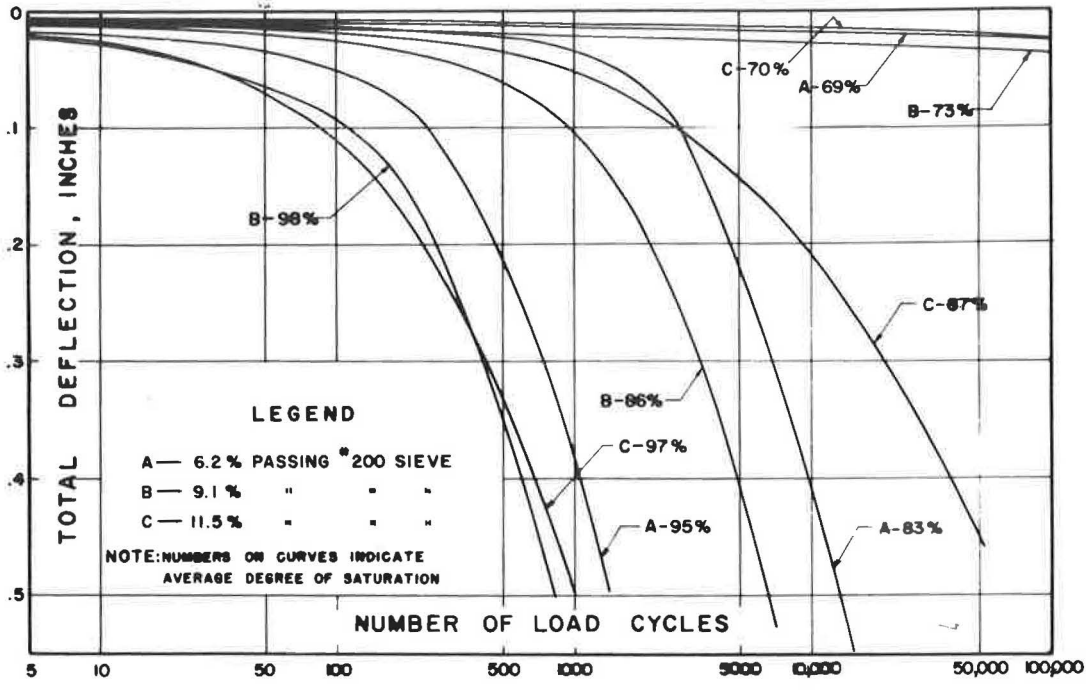

Figure 8. Deflection history of gravel specimens.

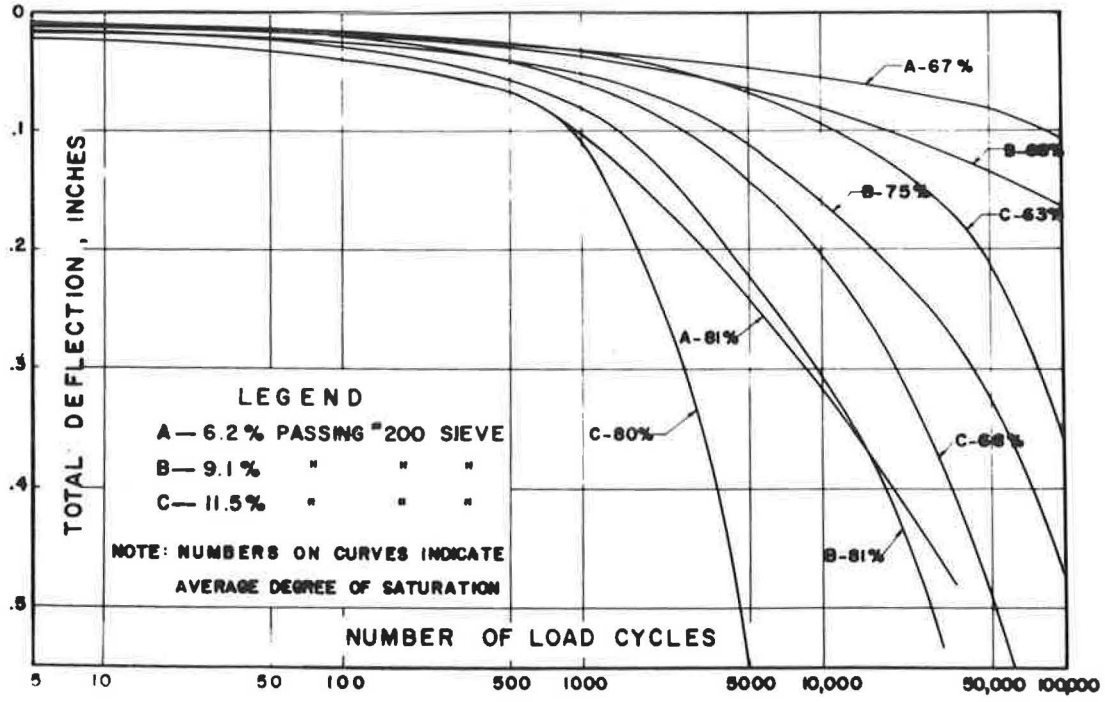

Figure 9. Deflection history of crushed stone specimens.

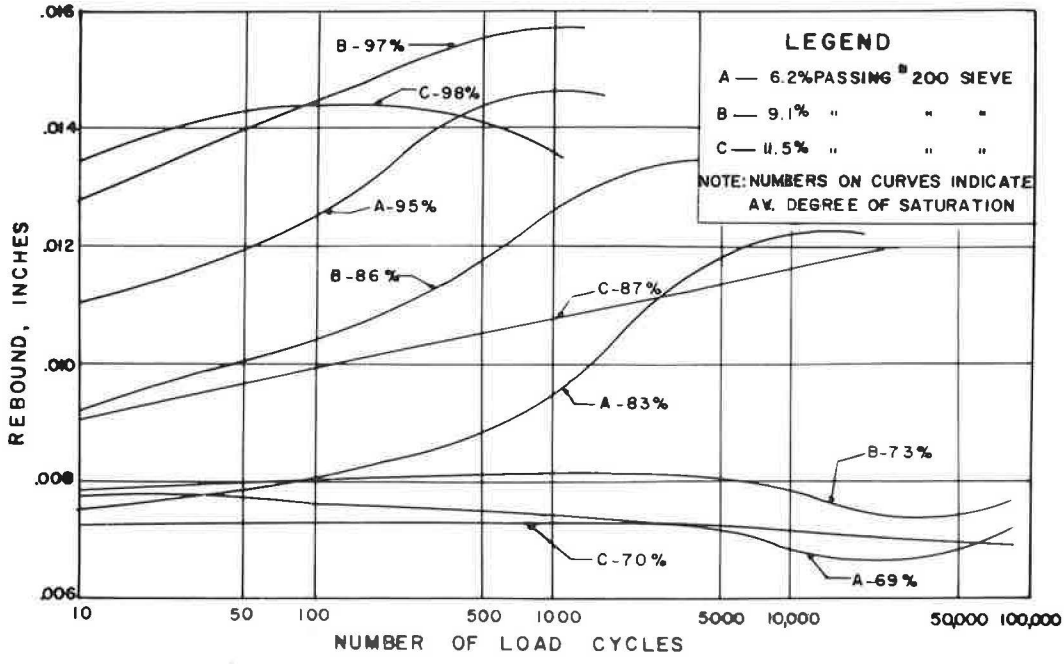

Figure 10. Rebound history of gravel specimens.

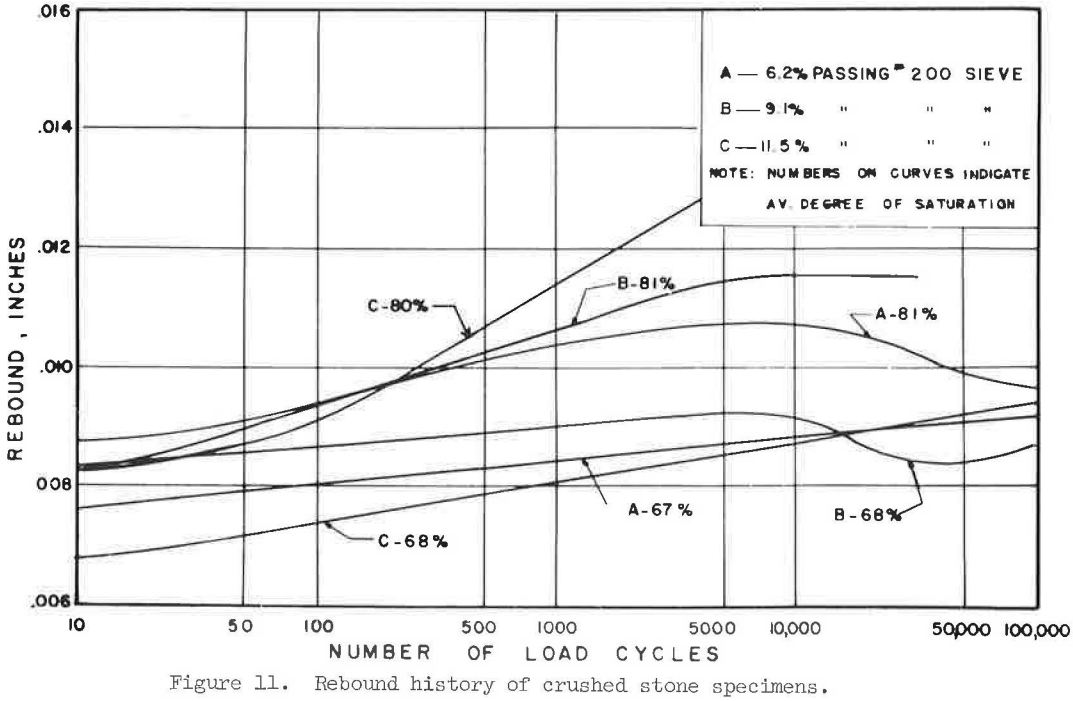

Figure 11. Rebound history of crushed stone specimens.

GENERAL CONCLUSIONS

It is an established principle of pavement design that it is necessary to consider the pavement structure as a whole. Every design engineer could list numerous factors that must be considered when designing a pavement. These might include soil type, type and volume of traffic, climatic conditions (precipitation and freezing temperatures), grade and alignment of the road bed, drainage characteristics of the materials in the pavements, strength properties of the components, and many others. An interaction exists among these factors. An illustration of this pertains to the selection of base course materials in the northern tier of states as contrasted to the types of base course materials used in the southern states. The adverse effects of frost action in the northern states in some cases override other design considerations making it necessary to construct base courses using non-frost susceptible materials. Other illustrations could be given which relate base course quality to internal drainage of the subgrade, rainfall belts, etc.

The primary purpose of the base co. se in flexible pavement is to provide shearing resistance and some stiffness to the pavement structure. Thus, it is apparent that permanent stability and relative thickness of the component layers of the pavement are of primary concern.

In connection with the performance of the gravel and crushed stone base courses used in the AASHO Road Test, consideration should be given to two factors that may be significant. First, the cross-section of the flexible pavement contained a granular shoulder (crushed stone) and the subbase was carried through the shoulder from ditch to ditch. Second, the road test experiment was conducted in an area where frost can be a problem, particularly from the standpoint of loss of pavement support during the frost-melt period. The area under consideration has a mean freezing index of about 500 degree-days and the mean maximum depth of frost penetration below the pavement surface (by measurement) was 40 in. in February 1959, 25 in. in March 1960, and 32 in. in February 1961.

It should be re-emphasized that from the standpoint of field performance, the crushed stone materials were superior to the gravel materials. This was true even though surface deflection under load was many times greater for the crushed stone bases than for the gravel bases.

Figure 12 shows variation of deflection and rebound with saturation level during repeated loading in the laboratory for the crushed stone and gravel samples. These deflection and rebound data were taken from Figures 8 through 11. The gravel samples were tested at degrees of saturation ranging from about 69 percent up to about 98 percent. The degree of saturation of the crushed stone samples, however, varied between 63 and 82 percent. The most striking feature of these test results is that, for a given degree of saturation, the crushed stone samples deflected and rebounded more than corresponding gravel samples.

Data in Table 1 show that the relative densities of the crushed stone samples, with one exception, were lower than for corresponding gravel samples. The average relative density values for field conditions were 92 percent for the gravel bases and 80 percent for the crushed stone bases. Differences in relative densities no doubt explain in part why the gravel deflected less than the stone in the laboratory at corresponding degrees of saturation.

Information was obtained from Road Test personnel regarding in-place moisture contents of the base materials at various times of the year. Degree of saturation in each case was computed from field moisture content data, average density data and specific gravity values furnished by Road Test personnel. Table 2 summarizes these data.

The degree of saturation of the crushed stone at time of placement in the summer of 1958 was 68 percent. By the spring of 1959, the value had decreased to 56 percent, and the following spring, its value was 55 percent. Tests made in the summer of 1960 indicated a degree of saturation of 44 percent. Corresponding to these values, the gravel material was placed at a degree of saturation of 94 percent and when tested in the spring of 1959, the gravel was found to be 86 percent saturated.

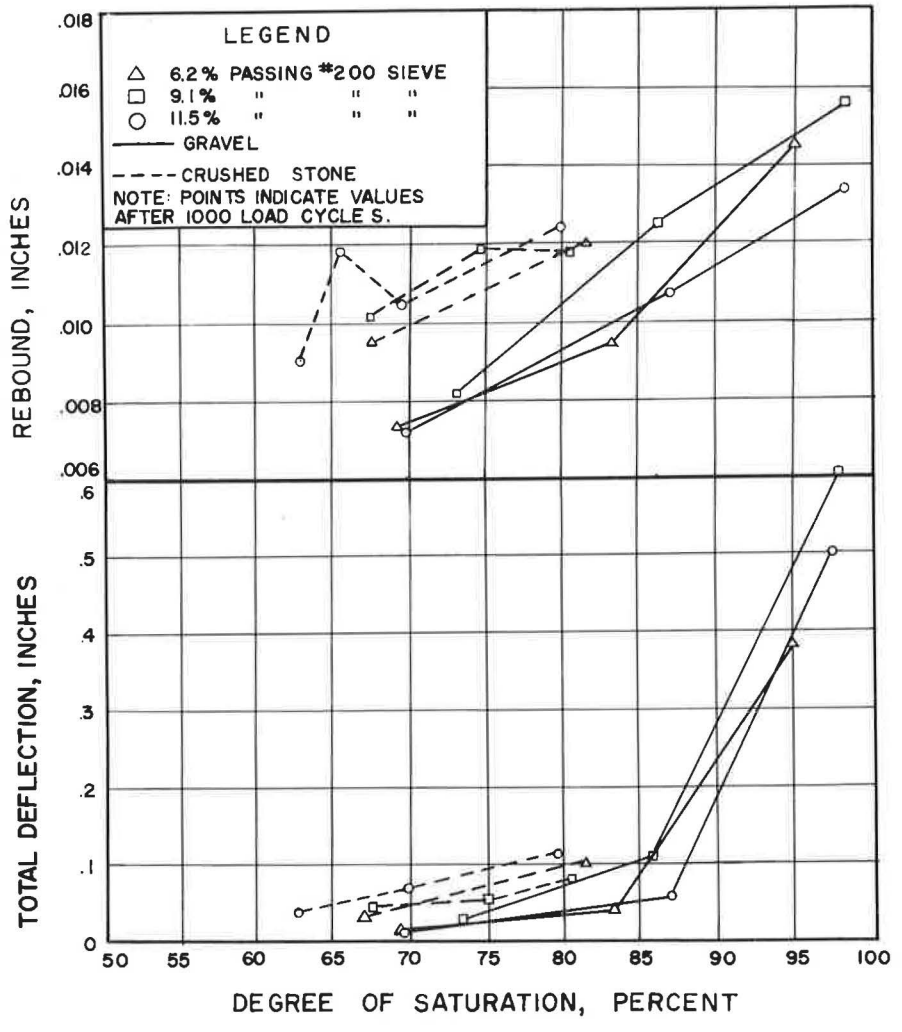

Figure 12. Deflection and rebound after 1,000 load cycles.

TABLE 2

ACCUMULATIVE DEFLECTION AND SINGLE-CYCLE REBOUND OF TRIAXIAL SPECIMENS[a]

Date	Degree Saturation %		Lab. Accumulative Deflection (in.)		Lab. Single-Cycle Rebound (in.)	
	Gravel	Stone	Gravel[b]	Stone[c]	Gravel[b]	Stone[c]
Fall 1958	94	68	0.45	0.06	0.0145	0.011
Spring 1959	86	56	0.11	< 0.04	0.0125	< 0.009
Spring 1960	—	55	—	—	—	—
Summer 1960	—	44	—	—	—	—

[a] After 1,000 load applications and at moisture conditions corresponding to various dates during the road test.
[b] 9.1 percent fines.
[c] 11.5 percent fines.

Table 2 lists accumulative sample deflection from beginning of test and single-cycle rebound values of the laboratory specimens at degrees of saturation equal to those indicated by field tests. These deflection and rebound data were taken from Figure 12. Using field degree of saturation as a basis of comparison, the gravel specimens had larger total deflection and single cycle rebound values than the crushed stone specimens.

Comparisons of laboratory values of accumulative sample deflection (accumulated axial deflection of the test sample from beginning of test) at 1,000 load cycles provide a method of evaluation of the stability of the test specimens in the laboratory. A comparison of the stability of the two materials in the field is provided by reference to the performance data shown in Figure 2. Using the values of total deflection given in Table 2 as qualitative performance values and by a comparison of these values with the charts of field performance given in Figure 2, it can be seen that good correlation of field and laboratory data was achieved.

It is understood that failure of the gravel base courses nearly always took place during the spring of the year. The period of time which elapsed between spring breakup and the date the moisture content determinations were made are not known. Therefore, it is impossible to estimate the exact moisture level at the critical time of frost melt. However, for purposes of comparison, a conservative estimate of the degree of saturation at the end of the spring thaw must be the computed value of 86 percent for the gravel base. In all probability the value was higher sometime during the spring thaw. Tests made in Indiana (6) indicate the degree of saturation of this type of material often approaches 100 percent during the critical spring-melt period. This period, incidentally is short lived and, in many cases, only lasts from several days to several weeks depending on the amount of precipitation which occurs during the frost melt. The degree of saturation of 86 percent for the gravel is in contrast to 56 percent for the crushed stone.

Figure 13 shows variation of coefficient of permeability with density for these two materials. For the density levels at which the materials were placed in the field, the coefficient of permeability of the gravel was about 0.01 ft per day as compared to about 7.5 ft per day for the crushed stone material.

On the basis of their grain size distribution (Fig. 1), both of these materials are potentially frost susceptible. However, as indicated by the high permeability of the crushed stone, the voids of the crushed stone mixture were no doubt too large to promote capillary rise. Furthermore, as indicated by the field degrees of saturation, free water was quickly dissipated at the shoulder base contact.

Inasmuch as the gravel gradation falls into the frost-susceptible class and its coefficient of permeability is practically nil, active frost action would be expected. Further, as this base is difficult to drain, free water resulting from surface infiltration would remain in the base for a longer period of time. Pore pressures associated with the high degree of saturation of the gravel materials probably affected performance to a high degree. Barber (1) has shown that pore pressures in base courses can result in greatly reduced bearing capacity, which alone could probably account for the difference in performance of the two materials.

The laboratory test data suggest that performance of the materials in the field was closely associated with the design of the pavement section coupled with the drainage characteristics of the gravel and crushed stone. Thus, it becomes unimportant that one material was a gravel and the other a crushed stone, but it is significant that the stone was free drainage, whereas the gravel was not. Angularity of grains per se no doubt had an effect on the strength of the materials but in addition (for constant gradation) crushed materials nearly always have higher permeability than predominately rounded materials.

The laboratory data indicate that the crushed stone used in the special test sections (for a given degree of saturation and at field density) was more resilient than the gravel. This observation is suggested when considering the rebound values obtained during the repeated triaxial tests.

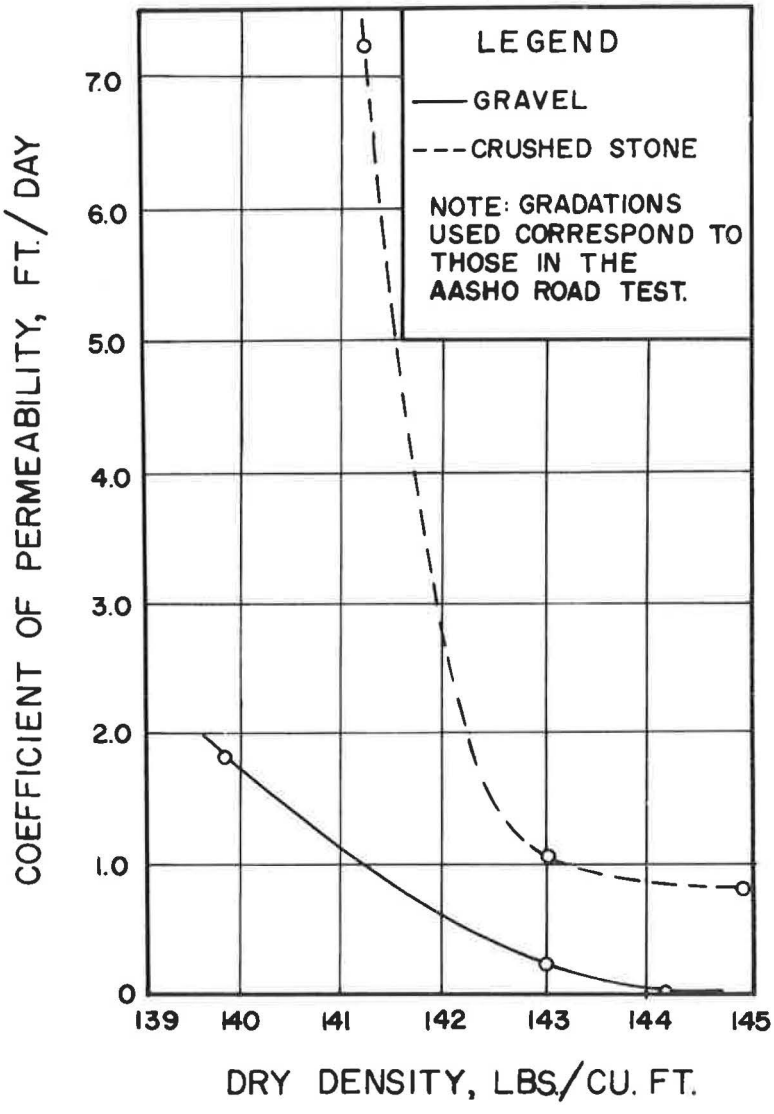

Figure 13. Variation of coefficient of permeability with dry density.

SUMMARY

Data presented herein have not explained fully the reason for difference in performance of the gravel and crushed stone materials. There is an apparent anomaly, using measured deflection of the test pavement under load and rebound values found in the laboratory, when comparing these values at the degree of saturation of the materials found in the road. Further research should be conducted to clarify this point. There is, however, good correlation, using field moisture levels as a comparison, between field and laboratory stability of the two materials.

Data presented have illustrated some of the factors which affected stability of the gravel and crushed stone materials used in the Road Test. The authors believe it is significant that the coefficient of permeability of the crushed stone was appreciably higher than that of the gravel. It is also significant that the gravel's field degree of

saturation was appreciably greater than the stone's and in the laboratory, at these moisture levels, the gravel specimens deflected more and showed greater rebound than the stone. This suggests that climatic factors, geometric section, and permeability had significant effect on the performance of the two materials.

REFERENCES

1. Barber, E. S., and Steffens, G. T., "Pore Pressures in Base Courses." HRB Proc., 37:468-492 (1958).
2. Benkelman, A. C., Kingham, R. Ian, and Schmitt, H. M., "Performance of Treated and Untreated Aggregate Bases." Pre-print volume supplement, International Conf. on Struct. Design of Asphalt Pavements (August 1962).
3. U. S. Army, Corps of Engineers, "Engineering and Design, Pavement Design for Frost Conditions" E. M.-1110-345-306.
4. Havers, J. A., and Yoder, E. J., "A Study of Interactions of Selected Combinations of Subgrade and Base Course Subjected to Repeated Loading." HRB Proc., 36:443-478 (1957).
5. "The AASHO Road Test: 2 — Materials and Construction"; "Report 5 — Pavement Research." HRB Special Reports 61B and 61E (1962).
6. Shelburne, T. E., and Woods, K. B., "1943 Survey of Secondary Roads (Spring Break Up)." Report to the Advisory Board of the Joint Highway Research Project, Purdue University (1943). (Unpublished.)
7. Yoder, E. J., and Woods, K. B., "Compaction and Strength Characteristics of Soil Aggregate Mixtures." HRB Proc., 26:511-520 (1946).

Effect of Structure on Resilient Rebound Characteristic of Soils in The Piedmont Province of Virginia

BOYCE D. TATE, Major and Assistant Professor, Virginia Military Institute, Lexington; and
H. G. LAREW, Associate Professor of Civil Engineering, University of Virginia, Charlottesville

This paper reports the results of laboratory studies conducted to determine which of the Piedmont soils were more resilient and the cause of this resilience. This property has, in the past, led to the wasting of much of this material in highway construction work and has often caused fatigue type failures on pavements under which it has been placed.

Repeated-load triaxial tests on laboratory compacted sample were employed to determine the amount of elastic or resilient rebound for each soil. In general it was found that as the percent of the mineral mica increased the resilient rebound increased, but as the plasticity index of the soil increased the resiliency decreased. Soils from the C-horizon were more resilient than those from the B-horizon. For soils from the C-horizon the resiliency increased with increasing grain size.

Stereo-optical microscope studies of samples before and after repeated triaxial tests showed that soil structure played a major role in causing the resiliency in these soils. It was conclusively shown that soils with a disperse-like structure were much more resilient than those with a flocculant-like structure. Both soil structure and resiliency were influenced greatly by molding moisture content and method of compaction.

•FOR some time it has been known that certain fine-grained soils were more elastic than others and with the advent of repeated-load testing of soils, this has become even more apparent to those who have studied the effects of repeated loads on soils.

When a soil possessing elastic or resilient properties is used in such a manner that a load is first placed upon it and then removed, such as is the case of a soil beneath a highway pavement or airport runway, the resulting elastic or resilient effect can be quite detrimental to the pavements.

The soils in the Piedmont Province of Virginia are generally fine-grained, residual materials which often exhibit elastic properties. They have been formed from a complex system of underlying igneous and metamorphic rocks and are often quite deep, exceeding 100 ft in certain areas. Quite often these soils contain an appreciable percentage of mica flakes.

Recent laboratory studies (1, 2) conducted to determine the effect of repeated axial loading on the strength and deformation characteristics of fine-grained soils revealed the marked elastic qualities of the Piedmont soils. As a result of these studies it was

Paper sponsored by Committee on Stress Distribution in Earth Masses.

believed that soil structure (i.e., the arrangement of soil particles and the electrical forces acting between adjacent particles which influence this arrangement) was primarily responsible for this elastic quality.

The arrangement of fine-grained soil particles generally falls into two main categories, flocculated and dispersed—called cardhouse and oriented by some investigators (3). In the flocculated arrangement, the particles tend to bond themselves in an edge-to-surface type of orientation. This is generally thought to be caused by the electrical charges on the surfaces and edges of each particle. In the dispersed arrangement, Lambe (4) notes that the particles lay more generally parallel, with very little surface-to-edge bond.

Figure 1 is the result of a rather extensive investigation by Lambe (5)into the structure of compacted clay.

At point A the presence of a small amount of water results in a high concentration of electrolyte which prevents the diffuse double layer of ions surrounding each particle from developing fully. The double layer depression leads to low interparticle repulsion, resulting in a tendency towards flocculation of the colloids and a consequent low degree of clay particle orientation in the compacted soil. This type of structure is a flocculated arrangement of soil particles. If the water content is increased to point B, the electrolyte concentration is reduced, resulting in an expansion of the double layer, increased repulsion between particles and a low degree of flocculation, that is, an increased degree of particle orientation. Further increase in water content at point C increases this effect and results in a still greater particle orientation.

A system of parallel particles, which is approached at point C, represents the dispersed type of particle arrangement. Thus, in general, it may be stated that compaction of a clay soil "dry of optimum" tends to produce a flocculated arrangement of particles, while compaction of the same soil "wet of optimum" tends to produce a dispersed structure.

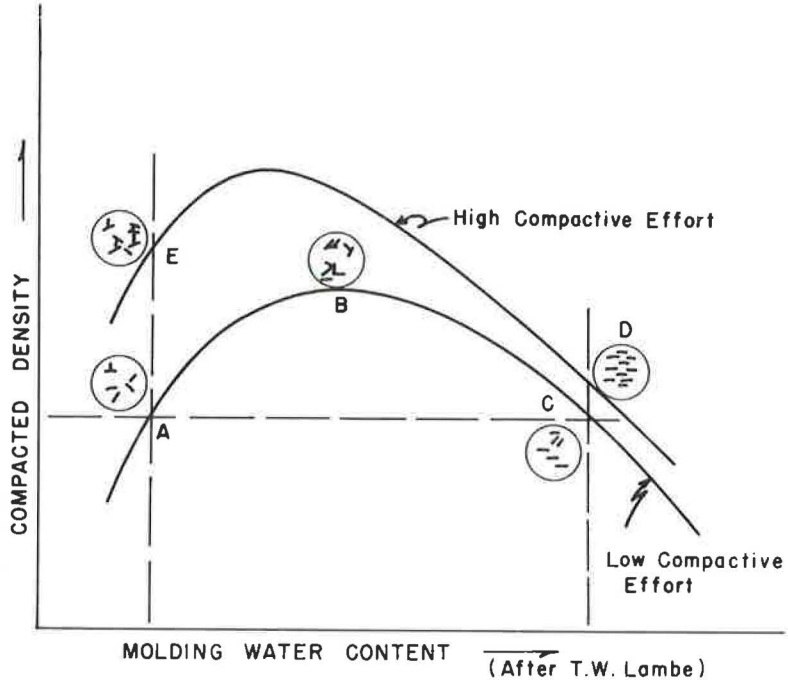

Figure 1. Effect of compactive effort, density, and molding water content on the structure of compacted clays as found by Lambe (4).

Soil Studied

Culpeper — Obtained from Rte.250 by-pass at Charlottesville.

Glenelg — Obtained from Rte.606 near Herndon, 0.6 miles toward Rte.7 from junction of Rte.602.

Madison — Obtained from Rte.58, approximately 8 miles west of Danville.

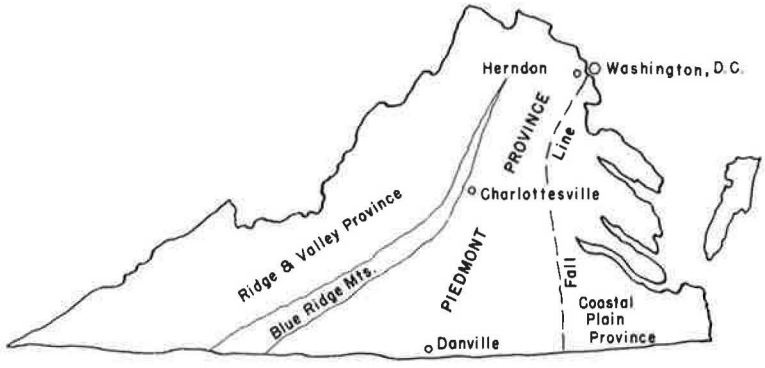

Figure 2. Sites where soil samples were taken.

TABLE 1

INDEX PROPERTIES AND MINERALOGICAL DATA

Characteristic	Culpeper B-Horizon	Culpeper C-Horizon	Glenelg C-Horizon	Glenelg B-Horizon	Madison B-Horizon	Madison C-Horizon
Specific gravity	2.78	2.74	2.76	2.74	2.77	2.86
Atterberg limits:						
Liquid limit	47.0	32.0	47.0	35.4	63.7	42.5
Plastic limit	39.0	31.5	33.0	27.0	42.4	37.0
Plasticity index	8.0	0.5	14.0	8.4	21.3	5.5
Shrinkage limit	34.0	28.5	30.7	24.5	39.0	48.0
Standard AASHO compaction:						
Optimum moisture content, %	26.5	18.5	22.0	21.2	28.5	18.0
Max. dry unit weight, pcf	93.0	99.4	101.6	98.5	94.0	106.3
Mineralogical composition[a]:						
Kaolinite	33	15	25	25	50	30
Quartz	33	42	45	45	15	10
Mica	33	42	30	30	25	60
Goethite	minor	minor	minor	minor	minor	minor
Hematite	minor	minor	minor	minor	minor	minor
Gibbsite	minor	—	—	—	10	minor
Illite-vermiculite	minor	minor	minor	minor	minor	minor
Order of relative elasticity	(1.40) 5	(7.20) 2	(3.80) 4	(6.40) 3	(1.00) 6	(9.20) 1
Unified classification	ML	ML	ML	ML	MH	ML
AASHO classification	A-2-7	A-2-4	A-4	A-4	A-1-b	A-1-b

[a]Approximate percent of total soil.

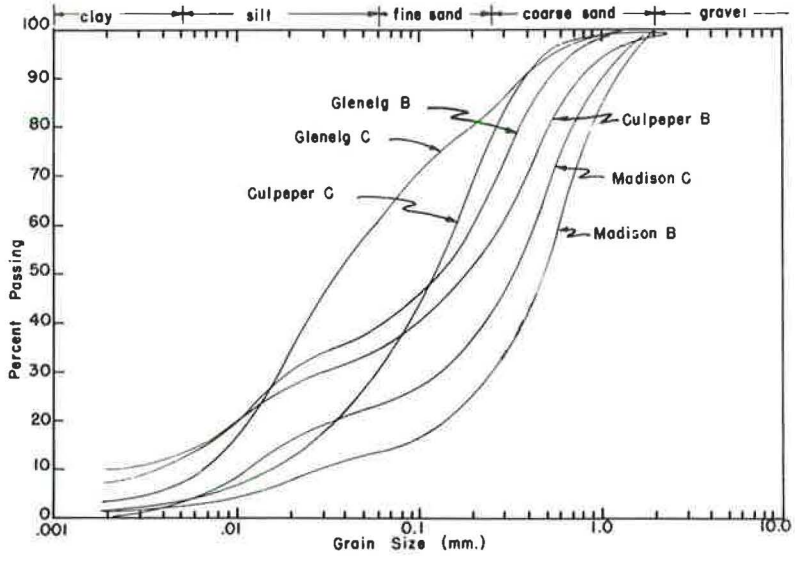

Figure 3. Gradation curves.

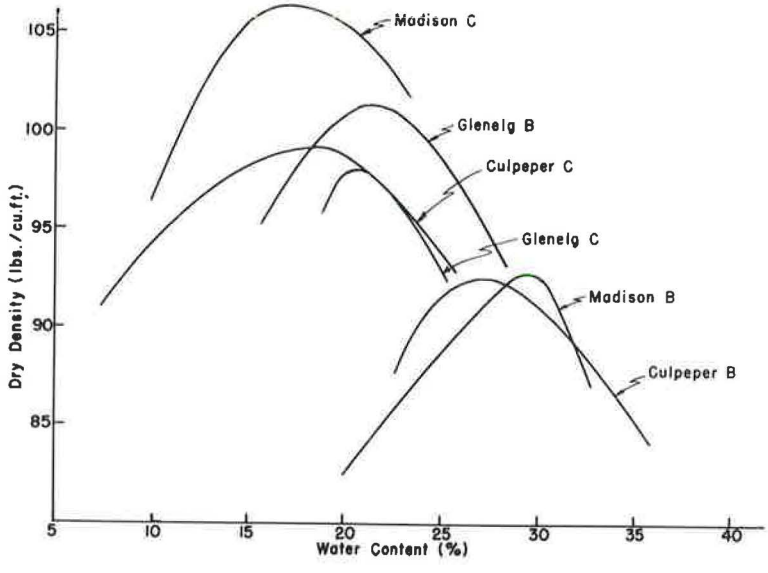

Figure 4. Standard compaction curves.

More recent studies by Pacey (6), using optical techniques developed by Mitchell (7), and studies by Seed and Chan (8) tend to support Lambe's concept of structure of compacted clay.

The purpose of the study described in this paper was to determine which of the Piedmont soils was more elastic and why it was more elastic. Since soil structure was believed to be an important contributing factor, this aspect was given special attention.

SOIL STUDIED

To locate the most elastic soils in the Piedmont Province of Virginia, three sites were chosen with the aid and advice of materials engineers of the Virginia Department of Highways. Both disturbed and undisturbed samples were obtained from the B- and C-horizons at each site. In each case, the soil was known to be highly elastic and to have given trouble on highway construction projects. Figure 2 shows the locations from which the soils were obtained. Characterization tests and mineralogical studies were conducted and the results are given in Table 1.

The soil obtained from near Herndon was a Glenelg (pedological classification) soil which consisted largely of mica, quartz and kaolinite. The soil taken from the Charlottesville site was a Culpeper soil and its mineralogical content was quite similar to the Glenelg soil. The soil secured from near Danville was a Madison soil. Its mineralogical content was nearly the same as the other two, except that a larger quantity of mica was present in the C-horizon.

Table 1 also gives the relative elastic rebound classification of each soil as obtained from repeated load tests upon compacted samples.

Grain size distribution curves and comparative standard compaction curves are plotted for each soil (Figs. 3 and 4).

APPARATUS AND PROCEDURE

Tests were first performed on compacted samples from both the B- and C-horizons of the three soils to determine the relative order of elasticity of each. A statically compacted cake of each of the six soils was prepared at or near the optimum moisture content and maximum dry density. Each cake was cut into four samples and one sample from each cake was tested to failure under the action of a gradually applied, axial load in a triaxial device. Stress-strain curves for the six soils resulting from these conventional triaxial tests showed that their ultimate strengths were quite similar at their respective optimum moisture contents and dry densities. Because this was true, a level of repeated deviator stress $\Delta\sigma_r$ to the deviator stress causing failure on the conventional triaxial test $\Delta\sigma_s$ was approximately equal for each of the soils. A ratio of $\Delta\sigma_r/\Delta_s$ was chosen and loads producing this ratio were applied to samples of the statically compacted soil in a repeated-load triaxial device, described elsewhere by Larew and Leonards (1). The confining pressure employed in all cases was 10 psi.

Under the levels of repeated deviator stress employed, the resilient rebound of each sample reached a constant or equilibrium value after not more than a few thousand load applications. This value of equilibrium elastic rebound was recorded for each soil, and the soil with the least resilient rebound was found to be the Madison soil from the B-horizon. Using the equilibrium elastic rebound of this soil as a standard of reference (unity as given in parentheses in Table 1), each soil's relative resiliency was calculated (also given in parentheses in Table 1). Each soil was then given a rating from 1 to 6 with the Madison C-horizon soil, which was the most resilient, receiving the number 1 rating. This soil was chosen for the more extensive program of studies.

A series of soil cakes 4.0 in. in diameter and 4.6 in. high was prepared from the Madison C soil on the dry side, near and on the wet side of optimum moisture content by both static and dynamic methods. The dynamically compacted samples were prepared in a Proctor compaction mold by Proctor compaction procedures. Soil cakes were compacted statically in the same manner as reported by Larew and Leonards (1), except that a standard Proctor mold, with aluminum plugs to fit into the ends, was used. The cakes were compacted at approximately the same moisture contents as those compacted dynamically.

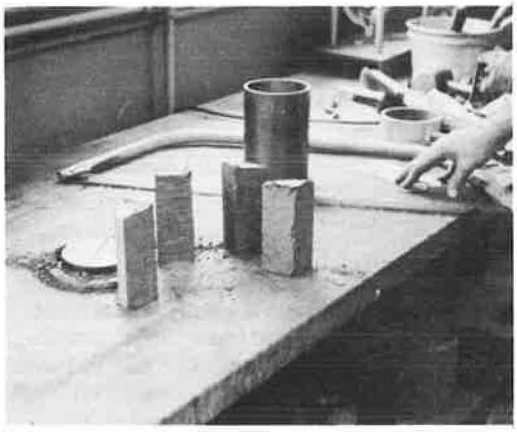

Figure 5. Four vertically cut samples from a compacted soil cake.

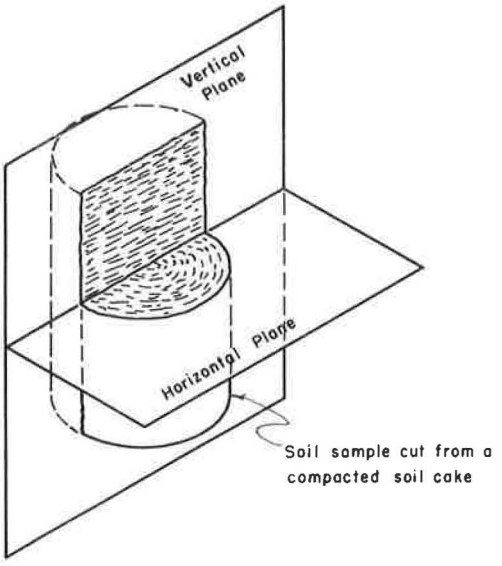

Figure 6. Soil sample cut by horizontal and vertical planes, indicating cross-sections studied under stereomicroscope.

Cakes prepared at these three moisture content levels were extruded from the mold, cut into four samples each, waxed and stored for later testing. Figure 5 shows four samples which were cut from the 4.0-in. diameter mold prior to waxing. These samples were later trimmed to specimens which were 2.8 in. high and 1.4 in. in diameter and then subjected to both static and repeated-load triaxial tests.

The static triaxial compression tests were performed on one sample from each soil cake. The sample was enclosed in a thin, rubber membrane and no confining pressure was used during the tests. The results were used to obtain the compressive strength of a sample from each cake.

Each repeated-load triaxial sample was enclosed in 2 thin rubber membranes. The chamber around the sample was filled approximately one-half full of water to prevent the sample from drying during the test. Except for the very small amount of hydrostatic pressure developed by the water in the chamber, no confining pressure was applied to the sample. Sample drainage was prevented in both static and repeated load tests.

In each case the load applied by the repeated load device was 0.9 of the axial load causing failure in a static test on an identical sample, i.e., $\Delta\sigma_r/\Delta\sigma_s = 0.9$. The rate of loading was essentially constant at 20 cpm. The elastic rebound was observed for approximately 100,000 load applications and the equilibrium elastic rebound reached during each test was recorded. None of the samples failed during the 100,000 load applications.

The structure on both horizontal and vertical surfaces through the samples were studied under the stereomicroscope and photographed before and after testing. The direction of these surfaces in a sample is sketched in Figure 6. Pairs of stereophotographs were taken through the lens of the stereomicroscope with a Polaroid Land camera. Careful observations and notes were kept concerning observed particle orientation and structural features for each sample as it was being studied under the microscope. These recorded observations and the stereophotographs formed the basis for conclusions concerning the effects of soil structure.

Inasmuch as the original tests were performed on vertically cut samples from a compacted cake (Fig. 7), it was decided that similar tests should be performed on samples with identical water content and compacted density, but cut horizontally from a compacted cake (Fig. 8). These tests were performed on those soils and for those moisture contents, densities and methods of compaction that produced both the greatest and least amount of elastic rebound in the earlier tests on vertically cut samples. The

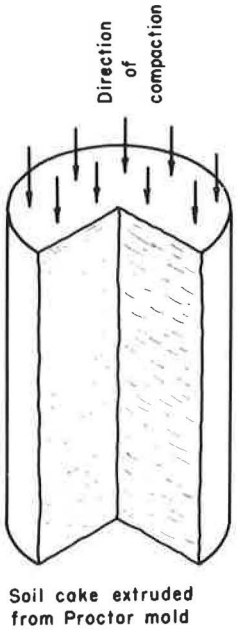

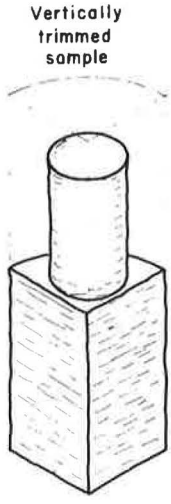

Figure 7. Orientation of sample to be tested vertically.

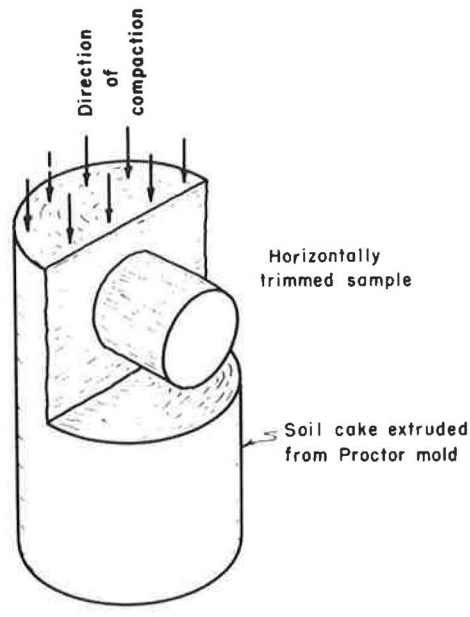

Figure 8. Orientation of sample to be tested horizontally.

procedures for repeated-load triaxial testing and observations were identical to those followed for the vertically cut samples.

RESULTS

Table 1 and Figures 3 and 4 show the index properties, mineralogical data, grain-size distribution curves and compaction curves for each of the six soils studied in the preliminary investigation. The order of their relative elasticity is given in Table 1. The Madison C soil exhibited the greatest amount of elastic rebound in the preliminary tests and was chosen for the later and more extensive studies.

Tables 2, 3, 4 and 5 and Figures 9 and 10 show the results of the repeated load tests performed in the study of this soil. Figure 10 shows that for vertically cut samples, a rather decided difference in the elastic rebound was obtained between the two methods of compaction employed. The statically compacted samples were the more elastic; the dynamically compacted samples were the least elastic. Moreover, the elastic rebound was, for both methods of compaction, quite sensitive to moisture content of the compacted samples, being maximum in both cases at or near optimum moisture content. From the test data and the microscopic study and observations, it was rather obvious that the orientation of the mica flakes in the compacted cakes was responsible for this difference in elastic rebound. Figures 11 and 12 are sketches of the postulated and observed particle arrangements in both statically and dynamically compacted samples. Figures 13, 14, 15 and 16 are stereophotographs that show the presence or absence of particle orientation in a few selected but typical samples.

The Madison C soil with the largest percentage of mica exhibited the greatest rebound. Tests on vertically and horizontally cut samples showed that this occurred when the particle arrangement was primarily normal to the direction of loading and least when the arrangement of particles was parallel to the direction of loading. It was rather obvious that a beam or plate-like deformation of particles was causing the elastic rebound. One can observe this action with the stereomicroscope by loading and unloading pure dry mica which has been placed in a glass container. When a load

TABLE 2

VERTICALLY CUT SAMPLES OF MADISON C SOIL COMPACTED ON DRY SIDE OF OPTIMUM[a]

Sample	Initial Water Content (%)	Compacted Dry Density (pcf)	Dry Density During Test (pcf)	Loss in Density (pcf)	Equilibrium Rebound (in. × 10^{-3})	Equilibrium Rebound (% of init. height)
(a) Dynamic or Impact Compaction						
1	13.93	102.69	95.53	7.16	20.0	0.75
1	15.69	101.13	95.55	5.58	21.5	0.76
3	15.39	101.40	95.84	5.56	22.5	0.80
Avg.	15.00	101.74	95.64	6.10	21.3	0.77
(b) Static Compaction						
1	14.77	107.38	91.87	15.51	28.2	1.00
2	14.99	107.17	92.56	14.61	26.0	0.92
3	15.04	110.18	99.25	10.93	22.0	0.78
4	15.18	110.05	100.00	10.05	22.5	0.80
Avg.[b]	15.00	108.59	95.65	12.94	24.5	0.87

[a]Subjected to 100,000 repeated load applications.
[b]Average interpolated from varying density.

TABLE 3

VERTICALLY CUT SAMPLES OF MADISON C SOIL COMPACTED NEAR OPTIMUM[a]

Sample	Initial Water Content (%)	Compacted Dry Density (pcf)	Dry Density During Test (pcf)	Loss in Density (pcf)	Equilibrium Rebound (in. × 10^{-3})	Equilibrium Rebound (% of init. height)
(a) Dynamic or Impact Compaction						
1	18.55	105.53	98.73	6.80	23.0	0.80
2	18.34	105.71	99.60	6.11	25.0	0.88
3	18.35	105.70	99.34	6.36	21.3	0.75
4	17.21	106.73	99.98	6.75	21.0	0.74
Avg.	18.11	105.92	99.41	6.51	22.6	0.79
(b) Static Compaction						
1	18.20	111.48	99.09	12.39	30.5	1.08
2	18.48	111.21	97.58	13.63	28.5	1.01
3	17.70	111.95	99.18	12.77	27.0	0.96
4	17.85	111.81	99.11	12.70	28.4	1.01
Avg.	18.06	111.61	98.74	12.87	28.6	1.02

[a]Subjected to 100,000 repeated load applications.

TABLE 4

VERTICALLY CUT SAMPLES OF MADISON C SOIL COMPACTED ON THE WET SIDE OF OPTIMUM[a]

Sample	Initial Water Content (%)	Compacted Dry Density (pcf)	Dry Density During Test (pcf)	Loss in Density (pcf)	Equilibrium Rebound (in. × 10^{-3})	Equilibrium Rebound (% of init. height)
(a) Dynamic or Impact Compaction						
1	20.40	104.90	100.30	4.60	23.0	0.82
2	20.67	104.67	99.63	5.04	18.5	0.66
3	20.92	104.45	100.41	4.04	18.0	0.64
4	21.24	104.17	100.08	4.09	22.6	0.80
Avg.	20.81	104.55	100.11	4.44	20.5	0.73
(b) Static Compaction						
1	19.76	111.35	100.85	10.50	23.0	0.81
2	20.33	110.82	99.39	11.43	26.0	0.93
3	20.46	110.70	99.10	11.60	27.0	0.96
Avg.	20.18	110.96	99.78	11.18	25.3	0.90

[a]Subjected to 100,000 repeated load applications.

TABLE 5

HORIZONTALLY CUT SAMPLES OF MADISON C SOIL[a]

Sample	Initial Water Content (%)	Dry Density During Test (pcf)	Equilibrium Rebound (in. × 10^{-3})	Equilibrium Rebound (% of init. height)
(a) Dynamic or Impact Compaction (Wet of Optimum)				
1	21.0	100.9	9.5	0.34
2	21.1	100.2	11.0	0.39
3	21.7	100.9	10.0	0.36
Avg.	21.3	100.7	10.2	0.36
(b) Static Compaction (Near Optimum)				
1	18.1	99.7	9.0	0.32
2	18.2	101.8	6.0	0.21
3	18.6	99.7	7.7	0.27
4	18.1	101.2	7.0	0.25
Avg.	18.5	100.6	7.4	0.26

[a]Subjected to 100,000 repeated load applications.

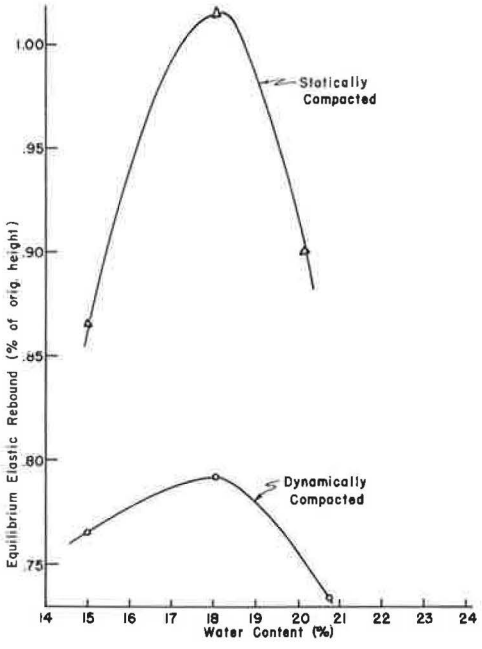

Figure 9. Equilibrium elastic rebound vs water content for all Madison C soil samples tested vertically.

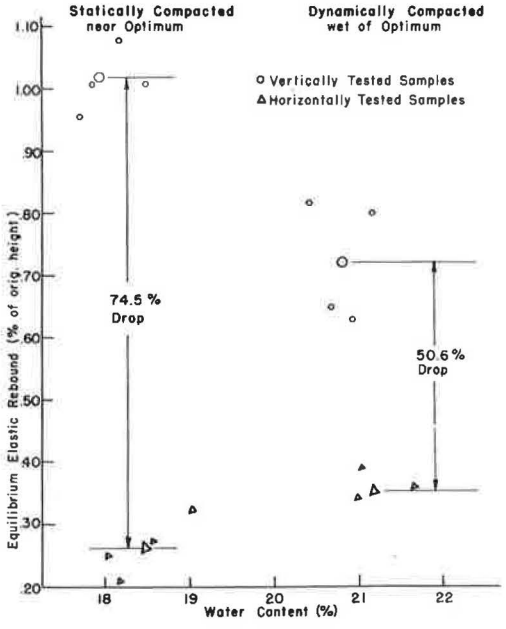

Figure 10. Comparison of elastic rebound for Madison C soil when subjected to repeated loading in vertically and horizontally cut samples.

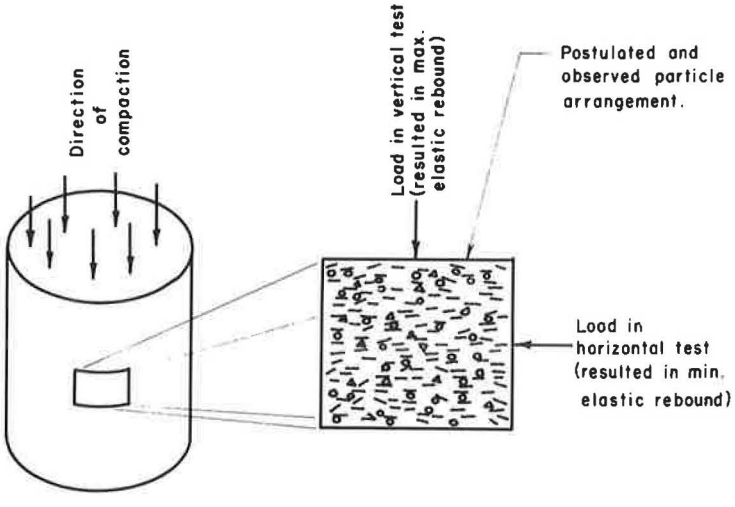

Figure 11. Samples of Madison C soil compacted statically, near optimum—postulated and observed particle arrangement.

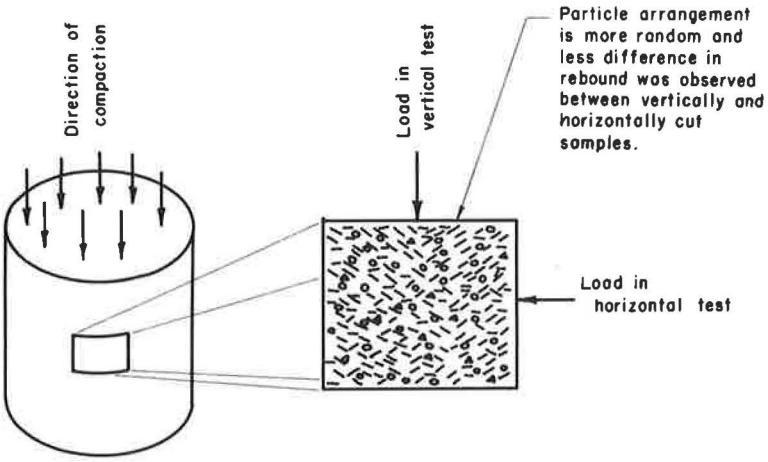

Figure 12. Samples of Madison C soil compacted dynamically, wet of optimum—postulated and observed particle arrangement.

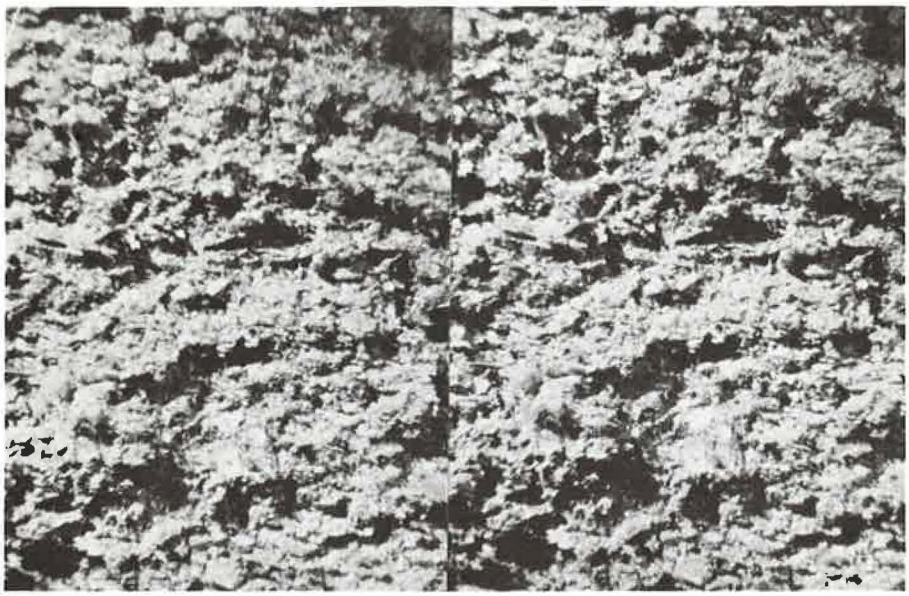

Figure 13. Stereophotograph of vertical section of Madison C soil compacted statically near optimum. Magnification is x 10. Structure is quite stratified and orientation of mica flakes is generally horizontal.

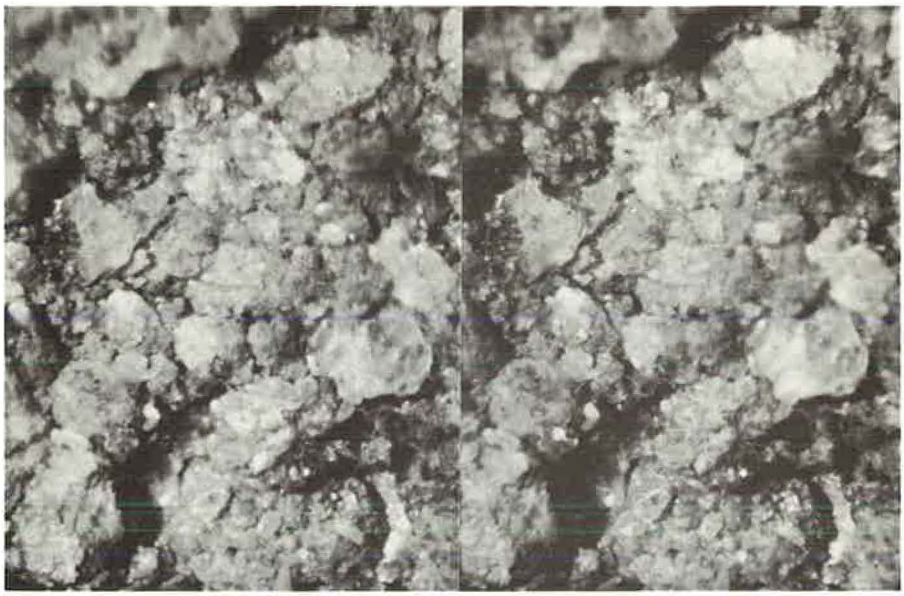

Figure 14. Stereophotograph of a horizontal section through the same sample as in Fig. 13. Magnification is x 40. The flat surfaces that are so prevalent are the mica flakes which are oriented generally horizontal.

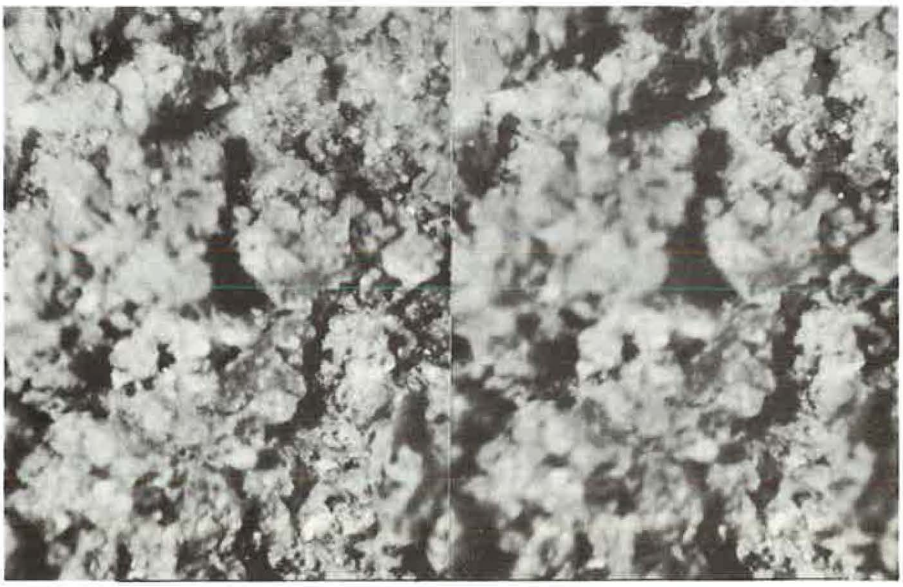

Figure 15. Stereophotograph of vertical section of Madison C soil compacted dynamically, wet of optimum. Magnification is x 40. Structure is much less stratified than in previous sample. Though some of the mica flakes are oriented horizontally, they are generally in a more random position.

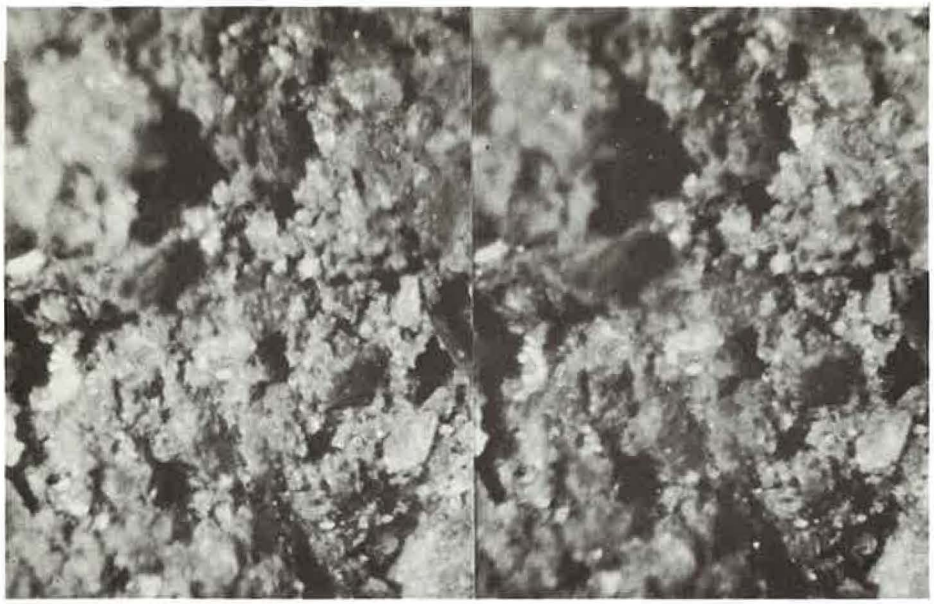

Figure 16. Stereophotograph of horizontal section through the same sample as in Fig. 15. Magnification is x 40. When compared with Fig. 15, it is difficult to distinguish the two, yet they are views of different cross-sections. Particle orientation is generally random in both sections.

is applied the mica flakes deflect just as a beam or plate does. As the load is released, the mica flakes return to their original position, primarily due to the resilience of the mica. The presence of water, other minerals, and some clay-like material in all of the soils studied, reduced, but did not eliminate this resilience. The granular particles of the other minerals tended to act as simple supports for the mica flakes while the clay-like material formed a matrix around the larger particles and acted as a cushion for the deflecting mica flakes.

As mentioned previously, the method of compaction affected the amount of elastic rebound. Moreover, the microscopic studies revealed a decided difference in particle orientation in the samples compacted by different methods. This difference can be observed in stereophotographs (Figs. 14, 15 and 16) and can be explained as follows:

As the soil was compacted statically, the entire surface area of the soil in the mold was loaded uniformly and compressed. The mica flakes tended to orient themselves in the most stable position or horizontally (Fig. 11).

When the soil was compacted with the drop hammer (dynamically), the end area of the drop hammer was considerably smaller than the inside area of the mold and tended to knead or displace the particles into a more random position (Fig. 12) with each blow of the hammer.

Tables 2, 3 and 4 indicate that the dry density of the samples as compacted was different from the dry density at the time of the tests. This change (a decrease) in density was caused by the elastic expansion of the compacted cakes immediately after removal from the compaction mold. This was a property of this material that could not be eliminated and led to considerable difficulty when attempting to control densities.

During the course of this investigation, an attempt was made to compact cakes with a kneading compacter. However, it was not possible to compact a soil cake that had a uniform density throughout with the kneading compacting machine that was available. The density would vary as much as 4 pcf between the top and the bottom of the cake.

The lack of control of the pressure applied by the compacting foot was primarily responsible for this difficulty. Further attempts to employ this method of compaction were abandoned.

CONLUSIONS

This study has established that elastic rebound in the soils studied is dependent upon the amount of mica present in the soil and the orientation of the mica flakes. Because of the highly resilient quality of the mica flakes, the orientation of the flakes in the compacted soil greatly affects the elastic rebound. Particle orientation, in turn, is affected by the method of compaction. The greatest elastic rebound developed when the particle orientation was essentially perpendicular to the direction of the applied load and was least when the particles were arranged more nearly parallel to the direction of the applied load. Seed, Chan and Lee (9) have found this same relationship true for compacted clays.

Indications are, however, that the structure of a micaceous silt of the type studied does not necessarily follow the concept of compacted clay structure as proposed by Lambe (5) and others. Where Lambe's theory normally indicates an increasingly dispersed structure as the moisture content increases, the micaceous silt exhibited a more dispersed structure at or near optimum moisture content and a more flocculated or random structure on the dry and wet sides of optimum. It should be emphasized that a considerable difference in particle size existed between the colloidal clay-like particles in Lambe's studies and the very much larger mineral particles of the micaceous silt. This study in no way invalidates Lambe's hypothesis concerning compacted clay structure, but it does indicate that it is not applicable in the case of these micaceous silts.

Studies are currently under way in the Soil Mechanics Laboratory at the University of Virginia to find practical ways of reducing the amount of elastic rebound of these micaceous silts so that they may be employed in a wider scale in highway construction work.

ACKNOWLEDGMENTS

Appreciation is expressed to C. E. Echols, H. L. Kinnier and R. E. L. Gildea of the University of Virginia, and to the Virginia Department of Highways, Virginia Research Council and the Bureau of Public Roads for the assistance they gave.

Funds were provided by the National Science Foundation through the Research Laboratories for Engineering Sciences at the University of Virginia. Funds for the preparation of this paper were provided by the University Civil Engineering Department, C. N. Gaylord, Chairman, and the Faculty Committee on Fellowships and Grants of the Virginia Military Institute.

REFERENCES

1. Larew, H. G., and Leonards, G. A., "A Strength Criterion for Repeated Loads." HRB Proc., 41:529-556 (1962).
2. Ahmed, S. B., and Larew, H. G., "A Study of the Repeated Load Strength Moduli of Soils." Proc. International Conf. on Struct. Design of Asphalt Pavements, Univ. of Michigan (August 1962).
3. Trollope, D. H., and Chan, C. K., "Soil Structure and Step-Strain Phenomenon." Jour. of Soil Mech. and Found. Div., ASCE Proc., Paper 2431, Vol. 86, No. SM2 (April 1960).
4. Lambe, T. W., "Structure of Inorganic Clay." ASCE Proc., Vol. 79, Separate No. 315 (Oct. 1953).
5. Lambe, T. W., "Structure of Compacted Clay." Jour. of Soil Mech. and Found. Div., ASCE Proc., Paper 1654, Vol. 84, No. SM2 (May 1958).
6. Pacey, J. G., Jr., "The Structure of Compacted Soils." Soil mechanics thesis, MIT (1956).

7. Mitchell, J. K., "The Fabric of Natural Clays and Its Relation to Engineering Properties." HRB Proc., 35:693-713 (1956).
8. Seed, H. B., and Chan, C. K., "Structure and Strength Characteristics of Compacted Clays." Jour. of Soil Mech. and Found. Div., ASCE Proc., Paper 2216, Vol. 85, No. SM5 (Oct. 1959).
9. Seed, H. B., Chan, C. K., and Lee, C. E., "Resilience Characteristics of Subgrade Soils and Their Relation to Fatigue Failures in Asphalt Pavements." International Conf. on Struct. Design of Asphalt Pavements, Univ. of Michigan (1962).

Bearing Capacity of Deep Foundations in Sand

ALEKSANDAR B. VESIĆ, Associate Professor of Civil Engineering, Georgia Institute of Technology Soil Mechanics Laboratory

Large-scale model experiments have been made to provide information on factors which influence bearing capacity of deep foundations in sand. Cylindrical and prismatical foundations of various sizes resting at different depths in homogeneous sand masses of different relative densities were loaded statically to failure. Special loading cells permitted separate registration of point and skin loads throughout the tests. Additional tests with models of sand colored in layers were made to study the mechanism of shear failure in the soil mass. The model experiments were accompanied by standard laboratory tests for determination of physical characteristics of the soils used.

An analysis of shear patterns observed indicates that, depending on relative density of sand, all three types of failure previously described in the literature may occur at shallow depths: general shear failure, local shear failure and punching shear failure. However, at greater depths only punching shear failure occurs, irrespective of the relative density of sand.

The unit point and skin resistances of the foundation increase linearly with depth only at shallow depths. At greater depths, both resistances show a hyperbolic increase and reach asymptotically constant final values. These final values are independent of overburden pressure and appear to be functions of relative density of sand only. This is explained by the "arching" of sand above the foundation base.

Analyses of observed ultimate loads indicate that a fair estimate of bearing capacity can be made by assuming failure surfaces in accordance with observed shear patterns.

•FROM the point of view of soil mechanics, there are two general types of deep foundations. The first type may be represented by a foundation installed by some process of excavation or drilling which does not induce significant changes in density or structure of the bearing soil. Practically all piers and caissons and some piles belong to this type. The other type may be represented by a deep foundation forced into the ground by driving or a similar operation, that induces significant changes in adjacent soil. Most piles belong to this second type.

SCOPE

The present paper is an investigation of ultimate bearing capacity of deep foundations in homogeneous masses of sand. This problem is considered to be fundamental. Only after a thorough understanding of principles of behavior of deep foundations in homogeneous masses of soil will it be possible properly to see and treat the problems of different types of deep foundations encountered in engineering practice.

Paper sponsored by Committee on Stress Distribution in Earth Masses.

Theoretical Considerations

The basic problem of bearing capacity of deep foundations in sand can be formulated as follows: A rigid foundation of known shape and dimensions is placed at a depth D in a homogeneous mass of sand of defined physical properties (Fig. 1). A static, vertical, central load is applied on the top. What is the ultimate load Q that this foundation can support?

The load is generally transmitted partially along the foundation shaft or skin, partially at the foundation base or point. The two bearing components of the load, the skin load Q_s and the base or point load Q_p are usually considered separately. The total ultimate load is then expressed as the sum of these two components:

$$Q = Q_p + Q_s = p_o A_p + s_o A_s \qquad (1)$$

Here p_o represents the unit base resistance and s_o unit skin resistance of the foundation (psi or kg/cm^2). A_p and A_s are, respectively, bearing areas of the base and the skin.

The solution of the problem of bearing capacity of the base has been sought in the past primarily by an approach base on the classical work by Prandtl (1, 2), and Reissner (3). They presented a solution of the problem of penetration of a rigid stamp into an incompressible (rigid-plastic) solid (Fig. 2). That solution, first applied to the problem of bearing capacity of soils by Caquot (4) and Buisman (5) is usually written in the following general form (6):

$$p_o = c\, N_c\, \zeta_c + q\, N_q\, \zeta_q + \tfrac{1}{2}\, \gamma\, B\, N_\gamma\, \zeta_\gamma \qquad (2)$$

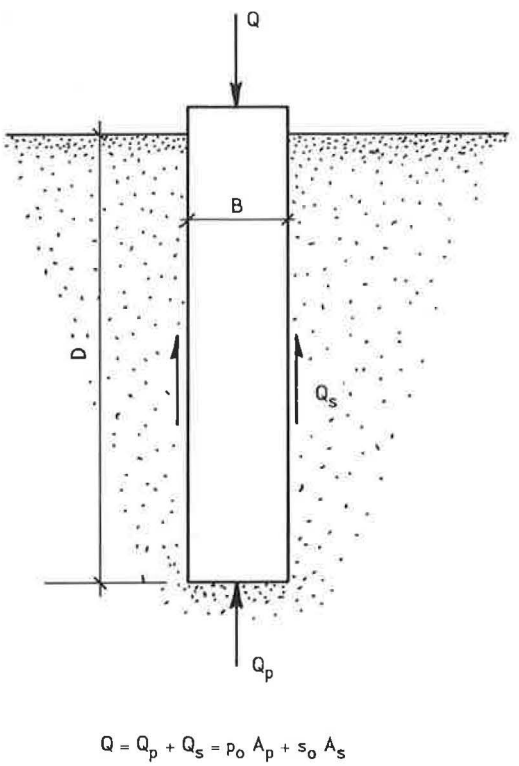

Figure 1. Basic problem of bearing capacity of a deep foundation.

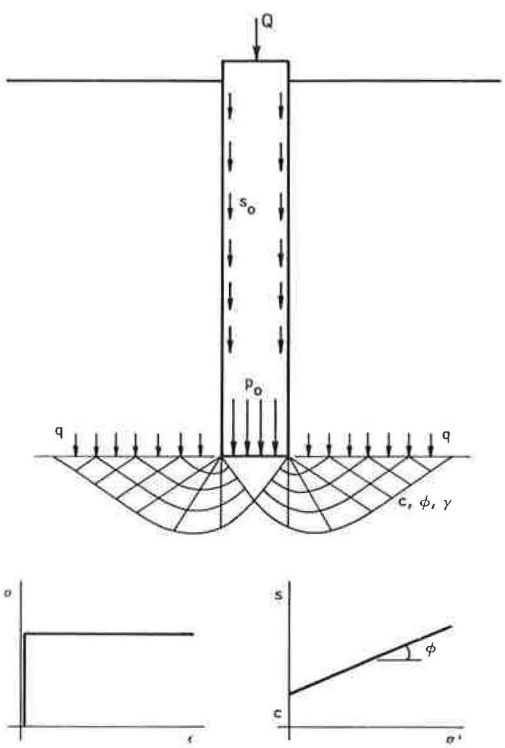

Figure 2. Prandtl-Reissner solution as applied by Caquot and Buisman.

In Eq. 2, c represents the shear strength intercept (cohesion) of the soil, q the overburden pressure, γ the unit weight of the soil involved in shear and B the foundation width. N_c, N_q, N_γ are bearing capacity factors for a strip foundation and ζ_c, ζ_q, ζ_γ are shape factors. Both N and ζ factors are, generally, dimensionless functions of the angle of shearing resistance ϕ.

In the case of foundations in sand c = 0 and

$$p_o = q\, N_q\, \zeta_q + \tfrac{1}{2}\, \gamma\, B\, N_\gamma\, \zeta_\gamma \qquad (3)$$

Using the same general approach but different shear patterns with rupture lines reverting to the shaft (Fig. 3) De Beer (7, 8) and Jaky (9) have obtained another solution of the same problem with considerably higher bearing capacity factors. Their work has been further extended by Meyerhof (10, 11), and others.

All of the previously mentioned solutions were obtained by considering a plane problem (long rectangular foundation). Some work in developing solutions for an axially symmetrical problem (circular foundation) has also been done, primarily in the USSR (12). However, there is still a general tendency to determine the shape factors empirically.

Another possible approach to the problem of base bearing capacity originated in the work by Bishop, Hill and Mott (13), and Skempton, Yassin and Gibson (14), who have considered the problem of expansion of a spherical or cylindrical cavity inside an infinite mass of an ideal solid. In such a case there exists around the cavity a highly stressed zone where the material, by assumption, behaves as a rigid-plastic solid. Outside that zone it behaves as an ideal elastic (or linearly deformable) solid.

The solutions of this kind have been applied to the problem of bearing capacity of deep foundations by Gibson (15), Skempton, Yassin and Gibson (14) and Ladanyi (16). According to these solutions the bearing capacity p_o can be computed by an expression analogous to Eq. 2 without the third term, however. In conditions of infinite mass or of very great depth this third term becomes negligible compared with other two terms. Consequently, both theoretical approaches indicate that at greater depths the bearing capacity of the base should be practically independent of its size and proportional to the overburden pressure q. Based on this conclusion and some limited experimental evidence, it has been generally admitted that the point bearing capacity of pile foundations in sand should be equal to the point resistance of a deep cone penetrometer.

Values of bearing capacity factors N_q found by different theoretical solutions mentioned are shown in Figure 4 left. The diagram on the right shows the corresponding factors $\zeta_q N_q = N_q'$ for circular foundations, as proposed by different investigators. This diagram contains also the empirical curves for N_q recommended by Brinch Hansen (17, 19) and Caquot and Kerisel (18). There is an appreciable difference in proposed numerical values.

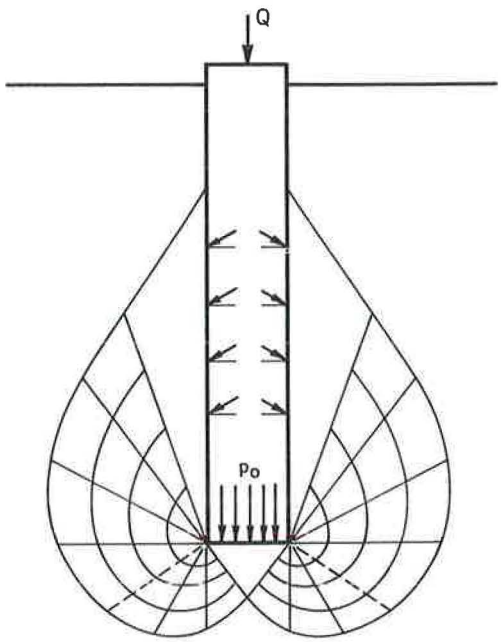

$$p_o = c\, N_c\, \zeta_c + q\, N_q\, \zeta_q + 1/2\, \gamma\, B N_\gamma \zeta_\gamma$$

$$s_o = c_a + K_s \tan \delta\, q_s$$

Figure 3. Shear pattern with rupture lines reverting to the shaft.

The unit skin resistance s_o consists of two terms: one representing adhesion c_a; the other, friction along the skin:

$$s_o = c_a + p_s \tan \delta \tag{4}$$

The term δ denotes the angle of skin friction and p_s average normal pressure on the skin. This pressure is generally assumed to be proportional to the corresponding average overburden pressure along the skin q_s. In sand $c_a = 0$ and

$$p_s = K_s \, q_s \tag{5}$$

K_s is a dimensionless number, which can be called coefficient of skin pressure. With this, the following expression for skin resistance in sand is obtained:

$$s_o = K_s \tan \delta \, q_s \tag{6}$$

Eq. 6 suggests that, in homogeneous soil conditions, unit skin resistance s_o should be proportional to the average overburden pressure q_s.

Previous Experiments

Among numerous experimental studies related to the problem, comparatively few have been of sufficiently general nature to permit drawing definite conclusions concerning the influence of the different parameters involved.

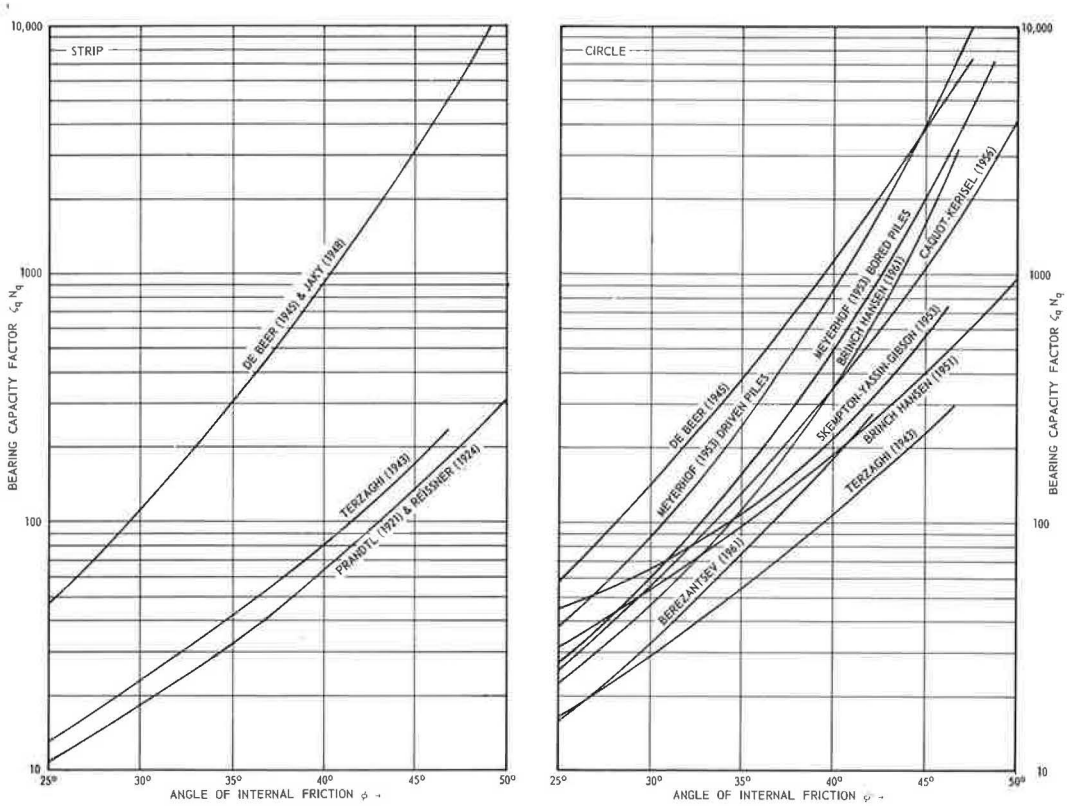

Figure 4. Theoretical bearing capacity factors.

Successful field experiences with predetermination of ultimate bearing capacity of piles by means of deep cone penetration tests (5, 7, 20, 21, 22, 23, 24, 25) have built a certain confidence in the general validity of the theoretical approaches described. It has been found in very many instances that the point bearing capacity of driven piles was indeed comparable to that of a deep cone penetrometer. One of the solutions proposed was being used with apparent success for evaluation of shear strength of sand in situ (8). Also, small-scale model tests (10, 15) as well as several well-documented full-scale tests on piles and piers (32) indicated N_q values in the wide general range predicted by the theories.

Some experiences, however, were not that encouraging. For instance, scale effects of a nature opposite to those predicted by the theories have been reported (26, 27). Observations of shear patterns in sand around deep foundations (28, 29, 30, 31) showed failure surfaces to be localized to the immediate vicinity of the foundation base. To the author's knowledge, not a single test ever indicated failure surfaces reverting to the shaft. The latest large-scale experiments, undertaken by the Institut de Recherches Appliquees du Beton Arme (IRABA) near Paris, led Kerisel (32) to conclude, without a rational explanation, that both foundation depth and size significantly influence the bearing capacity factor N_q. He suggested that N_q was not a unique function of φ but a complex function of φ, D/B and B. This conclusion will be discussed subsequently.

Investigations of the problem were undertaken several years ago with the general aim to contribute, if possible, to the understanding of phenomena occurring beneath and around deep foundations in sand. Both laboratory and field studies were envisaged in different phases of work. As a pilot study, it was proposed to perform large-scale model tests with foundations buried and driven to various depths in uniform masses of sand of different densities. This paper reports on the first phase of the work: tests with buried foundations.

TEST APPARATUS AND MATERIALS

A pile testing facility was constructed adjacent to the Soil Mechanics Laboratory. Figure 5 shows characteristic sections of this facility in different phases of operation. Figure 6 shows a general view.

Test Pit and Loading Equipment

The main feature is a large cylindrical test pit 8 ft 4 in. in diameter and 22 ft deep (Fig. 5), in which models of deep foundations can be placed in any kind of soil under controlled conditions. The pit is connected to a 12-in. sump that allows regulation and control of water level in the models. A 200-ton capacity reaction frame permits vertical or horizontal loading of models by means of corresponding hydraulic jacks. An adjustable A-frame at the upper level serves as support for pile-driving equipment as well as for miscellaneous equipment used in placing and excavating sand for models. This frame permits driving of piles vertically or at any batter up to 3:1 by means of a drop-hammer sliding along the leads. The entire facility is served by a 1.5-ton service crane.

For small-scale tests a steel box 50 by 50 in. square 70 in. deep with a 5-ton loading frame was constructed.

Loading of models was performed generally by means of hydraulic jacks of appropriate capacity (up to 200 tons). The load measurements were made by a corresponding set of proving rings and electronic load cells with a precision of less than 1 percent. Displacement measurements were made by ordinary micrometer dial gages (0.0001-in. precision).

Model Foundations

Two types of foundations were generally built: cylindrical, with circular bases 2.13-, 4- and 6.75-in. diameter, and prismatical, with 2.44- by 12.44-in. rectangular bases. The lengths varied according to the foundation depths (Table 1) between 10 and 113 in.

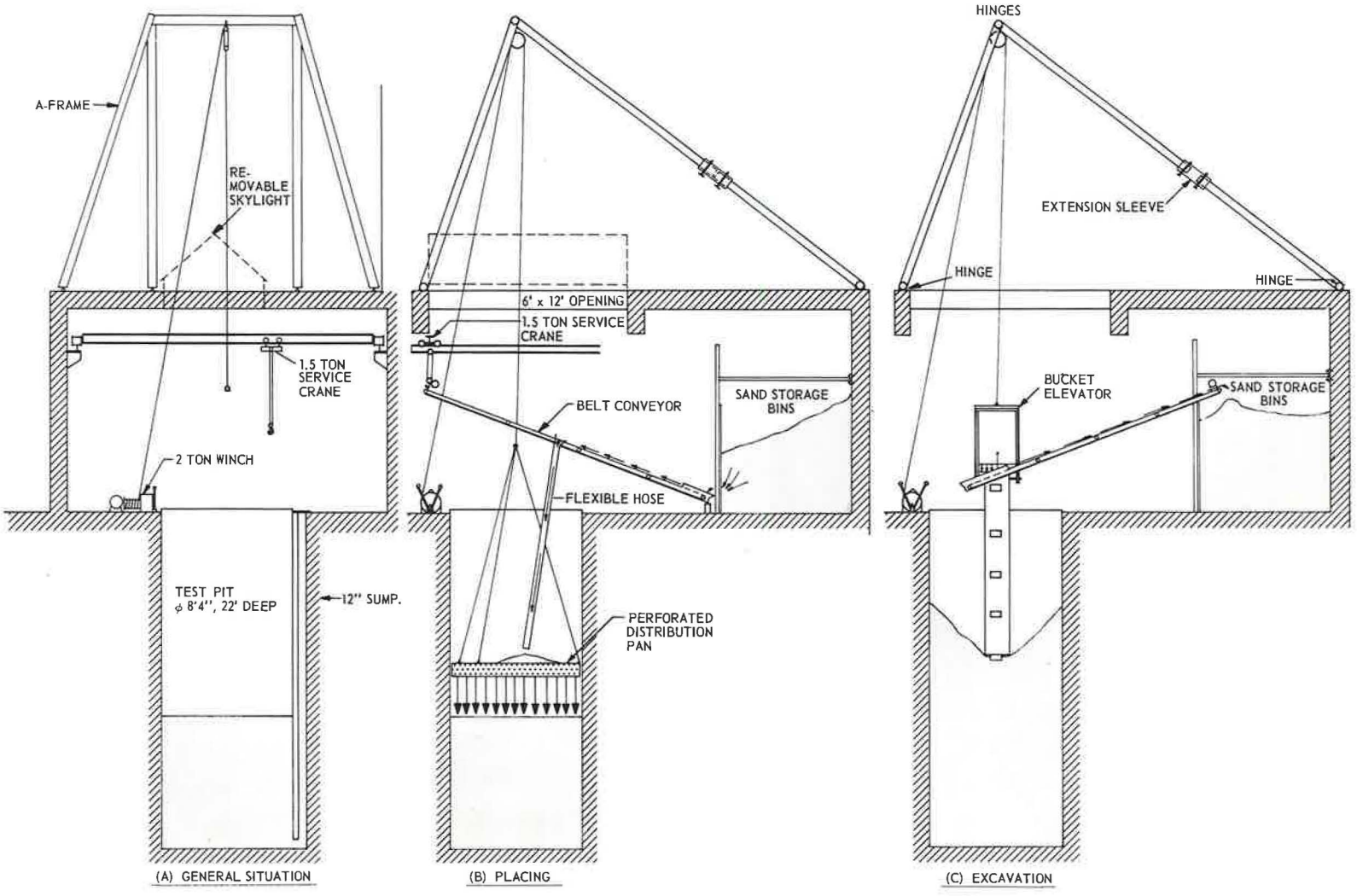

Figure 5. Testing area in different phases of operation.

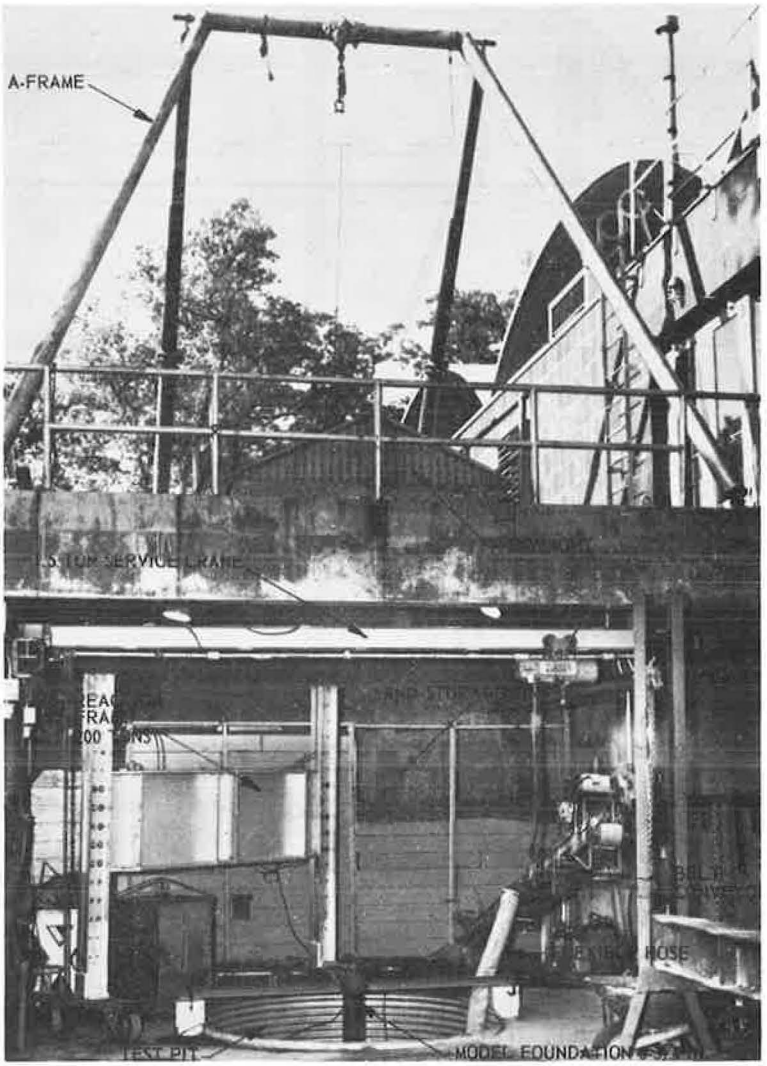

Figure 6. Testing area.

TABLE 1

SUMMARY OF LOADING TESTS

Series	Test Numbers	Foundation			Different Sand Densities	Container Size (in.)
		Shape	Size (in.)	Depth (in.)		
A[a]	21 - 40	Circular	2.13	0, 10, 20 30, 40	4	50 × 50 × 70
B[b]	1 - 20	Rectangular	2 × 12 2.44 × 12.44	0 10, 20 30, 40	4	50 × 50 × 70
C	41 - 52	Circular	3.94 4	0 40 80	4 3	50 × 50 × 70 100ϕ, 264
D	61 - 70	Circular	6 6.75	0 60, 100	4 3	100ϕ, 264
E	81 - 84	Circular	8	0	4	100ϕ, 264

[a] Skin diameter, 2 in.
[b] Skin dimensions, 2.25 × 12.25 in.

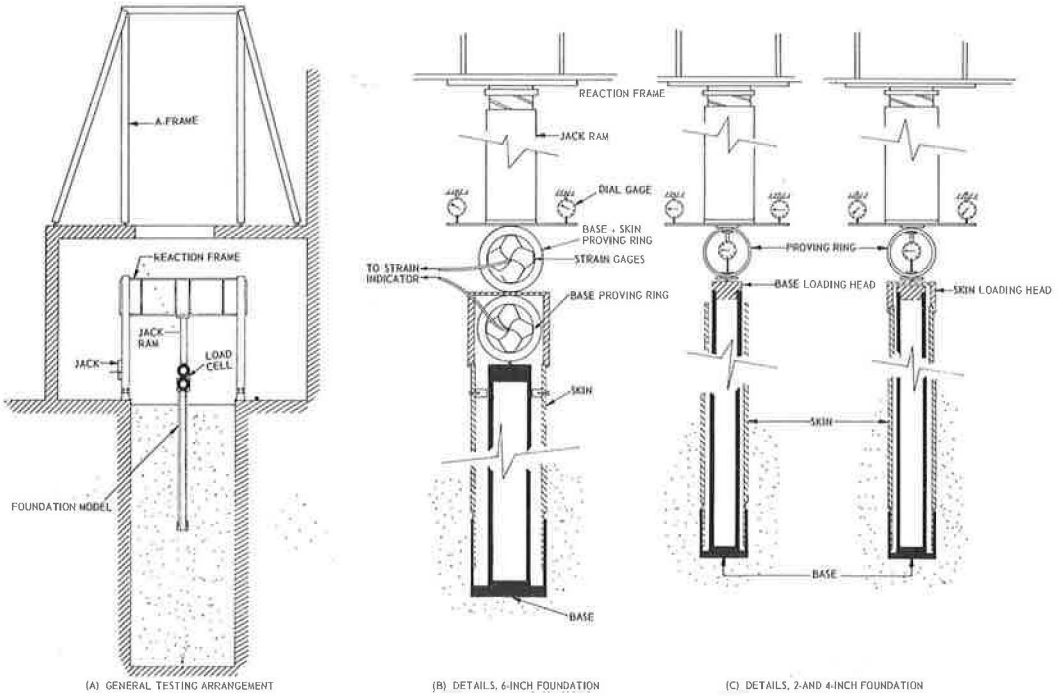

Figure 7. Model foundations.

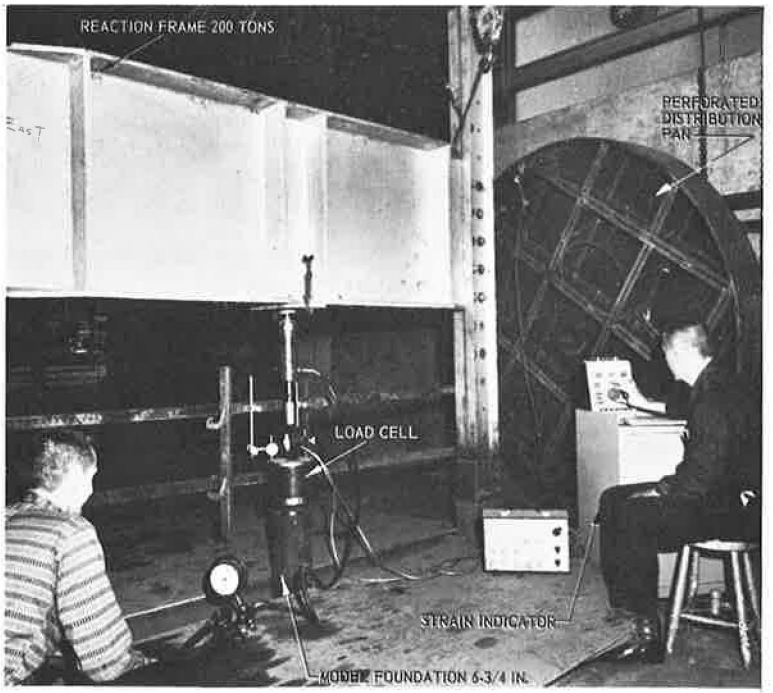

Figure 8. Test in progress.

The foundations were constructed on a principle similar to that of a deep cone penetrometer. They consist of a steel casing inside which a steel shaft independently connects the loading head with the base. In the case of 2- and 4-in. diameter foundations (Fig. 7) separate loading of base and skin of the foundation is possible through exchange of the loading head. In the case of 6-in. diameter foundations (Fig. 7b) the loading head is constructed so as to allow separate registration on the strain-indicator of base and total (base + skin) load. Figure 8 shows an outside view of this special head.

The flat bearing surfaces of the bases are covered by sandpaper to assure perfect roughness. To prevent caving-in of sand while the base only is pushed, the latter is protected by a cap tightly fitted with the bottom of the casing. To minimize friction between the cap and casing, the contact surface is kept clean and perfectly lubricated.

Properties of Sand

All the tests in this investigation were performed with a medium sand originating from the Chattahoochee River, near Atlanta. The sand was sieved through a window screen (equivalent to 1.44-mm sieve opening). The grain size distribution curve (Fig. 9) and microscopic examinations indicate a medium, uniform sand composed mostly of subangular quartz particles, but rich in mica. The material has been air-dried prior to use in tests. The water content, controlled throughout the investigation, varied between 0.2 and 0.3 percent.

Maximum and minimum densities of this sand, as determined by standard procedures are given in Table 2, which also contains corresponding minimum and maximum porosities n and void ratios e.

Shear strength characteristics of the sand were determined by standard triaxial tests (constant cell pressure and positive deviator stress). A total of 54 air-dry samples 2.8 in. in diameter and approximately 6 in. high were prepared at four different densities, and tested using cell pressures varying from 5 to 80 psi. A strain-controlled loading machine was used for all the tests with the axial strain rate 0.02 in. per min (Table 3).

Assuming the Coulomb-Mohr criterion of failure to be valid, an ordinary plot of these results in τ vs σ or $\sigma_1 - \sigma_3$ vs $\sigma_1 + \sigma_3$ presentation can be made. Such a plot indicated that the strength envelopes of the sand in question are slightly curved. For better insight into the nature of this curvature the results are also plotted as $\sigma_1 - \sigma_3$ vs $1/\sigma_3$, a plot proposed by Hansen and Odgaard (33). In such a presentation a straight-line strength envelope appears as a straight line having the equation

$$\frac{\sigma_1 - \sigma_3}{\sigma_3} = \frac{2 \sin \varphi}{1 - \sin \varphi} + \frac{2 \cos \varphi}{1 - \sin \varphi} \frac{c}{\sigma_3} \qquad (7)$$

Figure 10 shows that a reasonably good straight-line approximation of the actually curved envelopes can be obtained by separately considering tow ranges of confining pressures σ_3, namely, $\sigma_3 < 10$ psi and $\sigma_3 > 10$ psi.

For $\sigma_3 < 10$ psi ($1/\sigma_3 > 0.10$ psi) the $\sigma_1 - \sigma_3/\sigma_3$ values are practically independent of $1/\sigma_3$, which means that the shear strength intercept c_0 is zero. The angles of internal friction φ_0 corresponding to observed shear strengths are given in Table 2 (Col. 9) and plotted in Figure 11, which shows that φ_0 can be expressed as a function of e approximately by

$$\tan \varphi_0 = \frac{0.68}{e} \qquad (8)$$

For 80 psi $> \sigma_3 >$ 10 psi the $\sigma_1 - \sigma_3/\sigma_3$ values can be approximated by linear functions of $1/\sigma_3$; which indicates that the shear strength intercept c_1 is different from zero. Table 2 (Cols. 10 and 11) gives values in-

TABLE 2

MINIMUM AND MAXIMUM DENSITIES OF CHATTAHOOCHEE RIVER SAND

Density	Dry Unit Weight (pcf)	Void Ratio, e	Porosity n (%)
Minimum	79.0	1.10	52.4
Maximum	102.5	0.615	38.1

TABLE 3

TRIAXIAL TEST RESULTS

Test No.	γ_d (pcf)	Void Ratio, e	Mean Void Ratio	Cell Pressure, σ_3 (psi)	Stress Difference at Failure, $\sigma_1 - \sigma_3$ (psi)	Axial Strain at Failure (%)	$\frac{\sigma_1 - \sigma_3}{\sigma_3}$	Angle of Internal Friction, φ_0	Strength Intercept, c_0 (psi)	Angle of Internal Friction, φ_0	Strength Intercept, c_1 (psi)
(1)	(2)	(3)	(4)	(5)	(6)	(7)	(8)	(9)	(10)	(11)	(12)
1	84.6	0.957		5	13.3	2.7	2.65				
2	84.6	0.952		10	27.4	7.6	2.74				
3	84.6	0.957		10	31.0	4.6	4.10				
4	84.4	0.961		20	49.1	6.6	2.46				
6	84.0	0.970	0.957	40	90.4	11.9	2.26	35° 20'	0	32°	1.08
8	84.6	0.957		80	182.0	8.1	2.28				
34	85.1	0.945		10	24.5	13.2	2.45				
40	84.6	0.957		40	96.0	7.4	2.40				
46	84.4	0.96		7	18.3	3.8	2.62				
47	84.6	0.956		7	20.6	2.8	2.94				
48	84.7	0.955		5	14.5	2.4	2.90				
5	90.5	0.830		20	62.2	4.6	3.11				
7	90.1	0.838		40	117.3	9.3	2.93				
11	89.6	0.847		5	16.9	2.9	3.39				
12	90.1	0.838		10	32.6	4.5	3.26				
13	90.1	0.838	0.836	20	62.4	8.2	3.12	38° 40'	0	35° 10'	1.55
14	90.1	0.838		40	108.6	10.7	2.72				
15	90.5	0.830		10	40.5	4.4	4.05				
31	91.3	0.813		20	60.1	6.4	3.00				
32	90.3	0.833		40	118.3	9.6	2.96				
33	90.5	0.830		55	156.2	9.4	2.84				
35	90.7	0.827		10	34.0	7.0	3.40				
38	89.0	0.859		40	115.7	6.4	2.89				
49	90.1	0.838		7	22.8	4.0	3.26				
50	90.2	0.836		7	25.0	3.4	3.57				
51	90.1	0.838		5	15.9	3.0	3.18				
16	94.8	0.747		5	22.5	3.0	4.51				
17	94.5	0.751		10	43.1	4.5	4.31				
18	95.0	0.742		20	78.3	6.7	3.92				
19	95.4	0.737		40	142.0	7.1	3.55				
20	95.4	0.737	0.745	75	247.9	9.2	3.30	42° 50'	0	38° 20'	2.42
39	94.3	0.755		35	125.7	4.6	3.60				
52	94.8	0.747		7	28.3	3.8	4.04				
53	94.9	0.745		7	31.0	3.0	4.44				
54	95.0	0.742		5	20.5	3.1	4.10				
21	97.9	0.691		5	24.3	5.0	4.87				
22	98.8	0.676		10	48.2	4.3	4.82				
23	98.7	0.678		20	79.4	5.4	3.97				
24	98.5	0.681		35	140.9	7.9	4.02				
25	98.7	0.678	0.681	70	250.7	9.8	3.58	45°	0	40°	2.85
26	98.6	0.680		40	146.1	8.9	3.65				
36	98.2	0.685		10	48.7	4.8	4.87				
41	98.5	0.681		5	23.5	3.0	4.87				
42	98.7	0.678		10	47.0	3.2	4.70				
43	98.5	0.681		20	83.2	6.7	4.16				
44	98.6	0.680		7	32.6	3.6	4.66				
45	98.4	0.682		7	34.1	3.9	4.87				

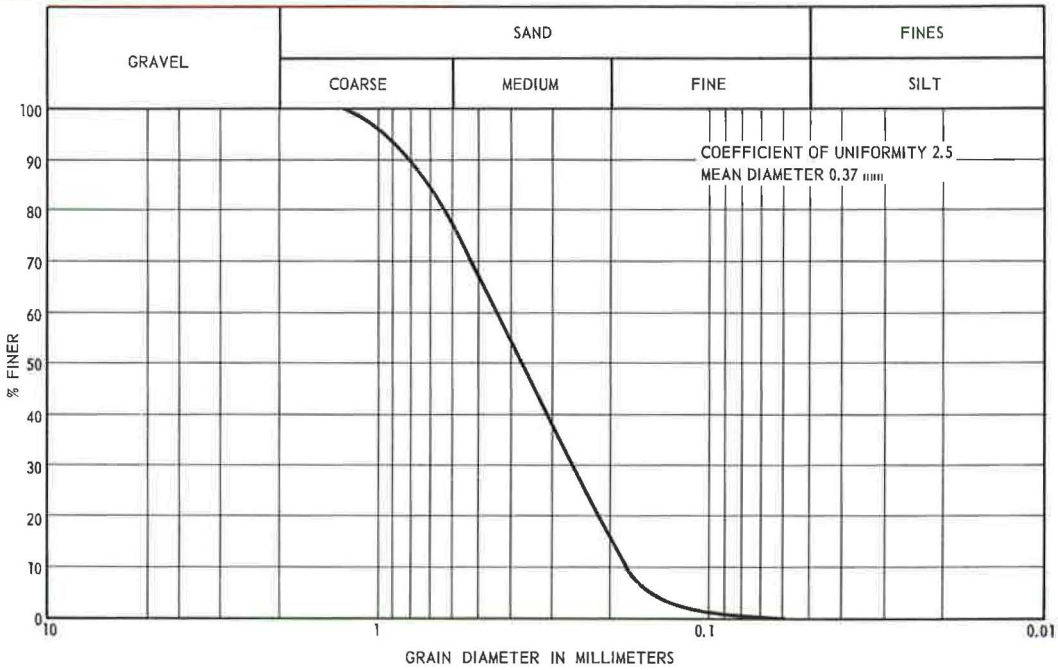

Figure 9. Grain-size distribution curve.

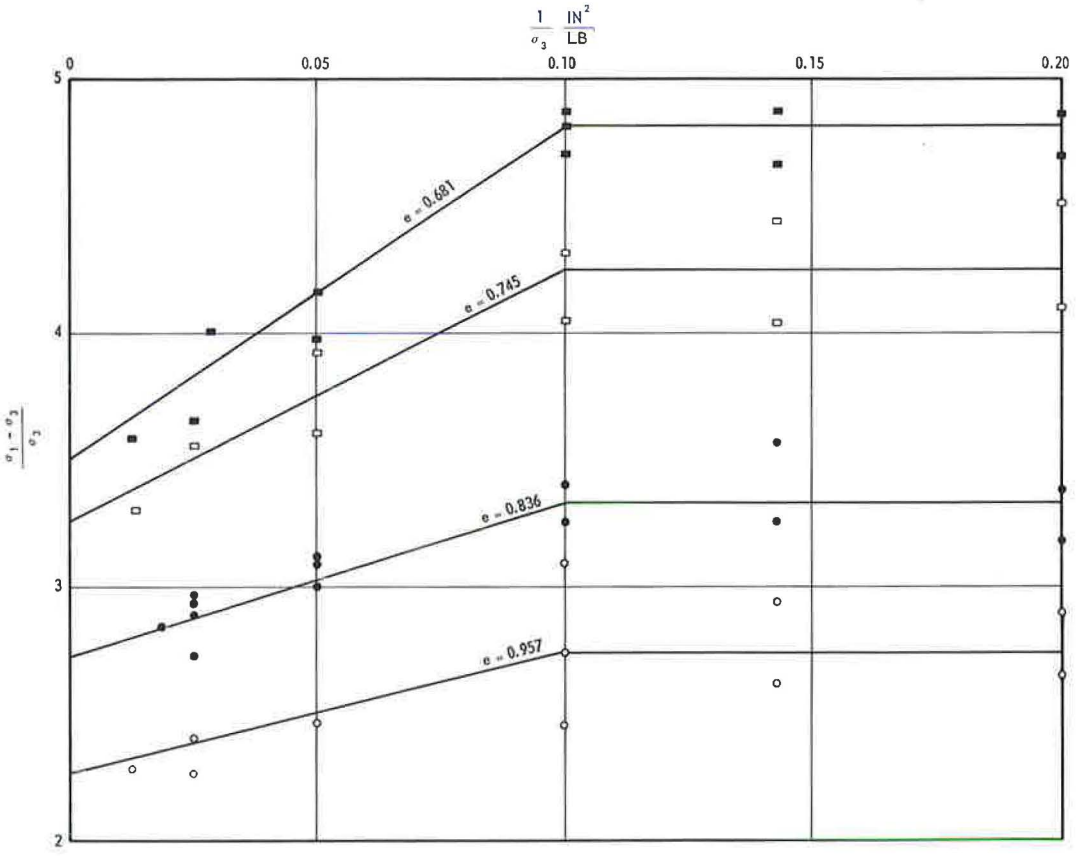

Figure 10. Triaxial test results.

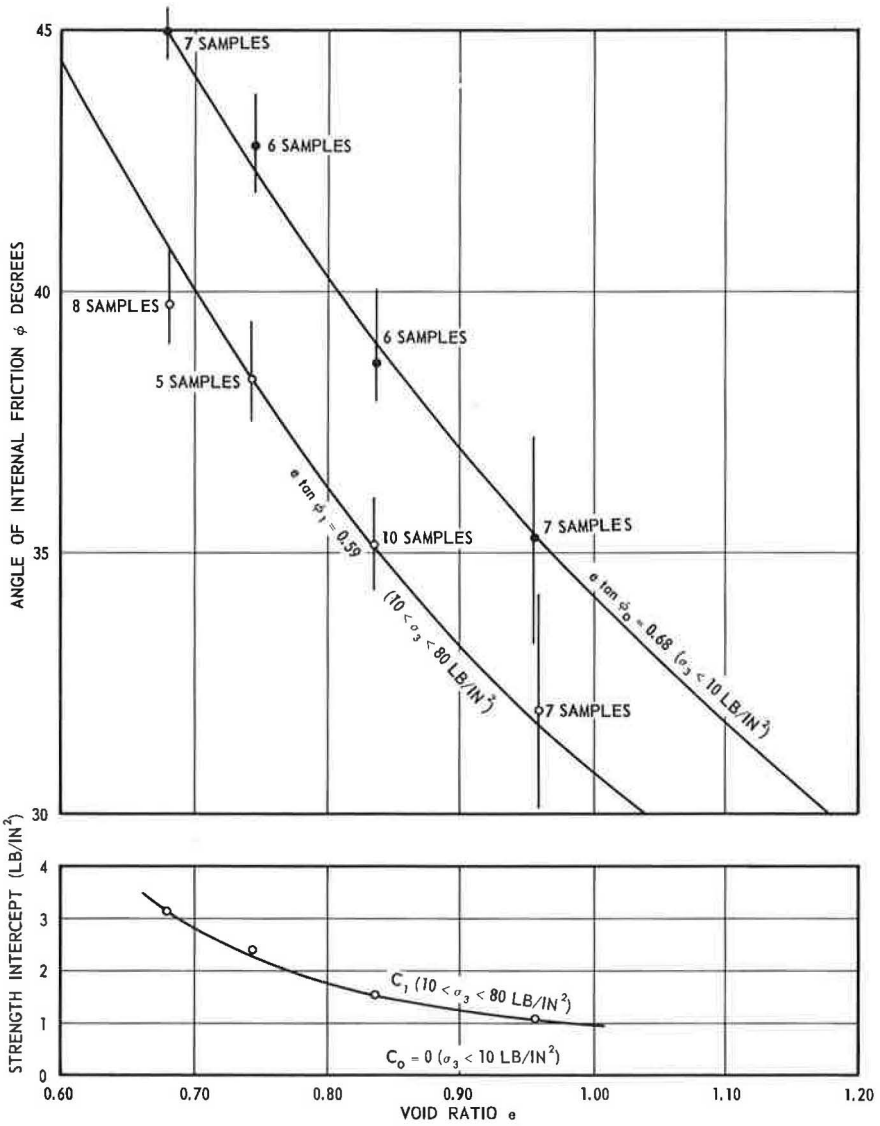

Figure 11. Shear strength parameters as a function of initial void ratio.

dicated by Figure 10 (left). The same c_1 and φ_1 values as functions of initial void ratio e are shown in Figure 11. The following analytical expression gives a good approximation of φ_1 as a function of e:

$$\tan \varphi_1 = \frac{0.59}{e} \tag{9}$$

DESCRIPTION OF TESTS

Placing of Sand and Control of Density

All the models for this investigation have been constructed in the following way. First, sand of desired uniform density was placed up to the planned elevation of the foundation base. The model foundation was then brought to full contact with the care-

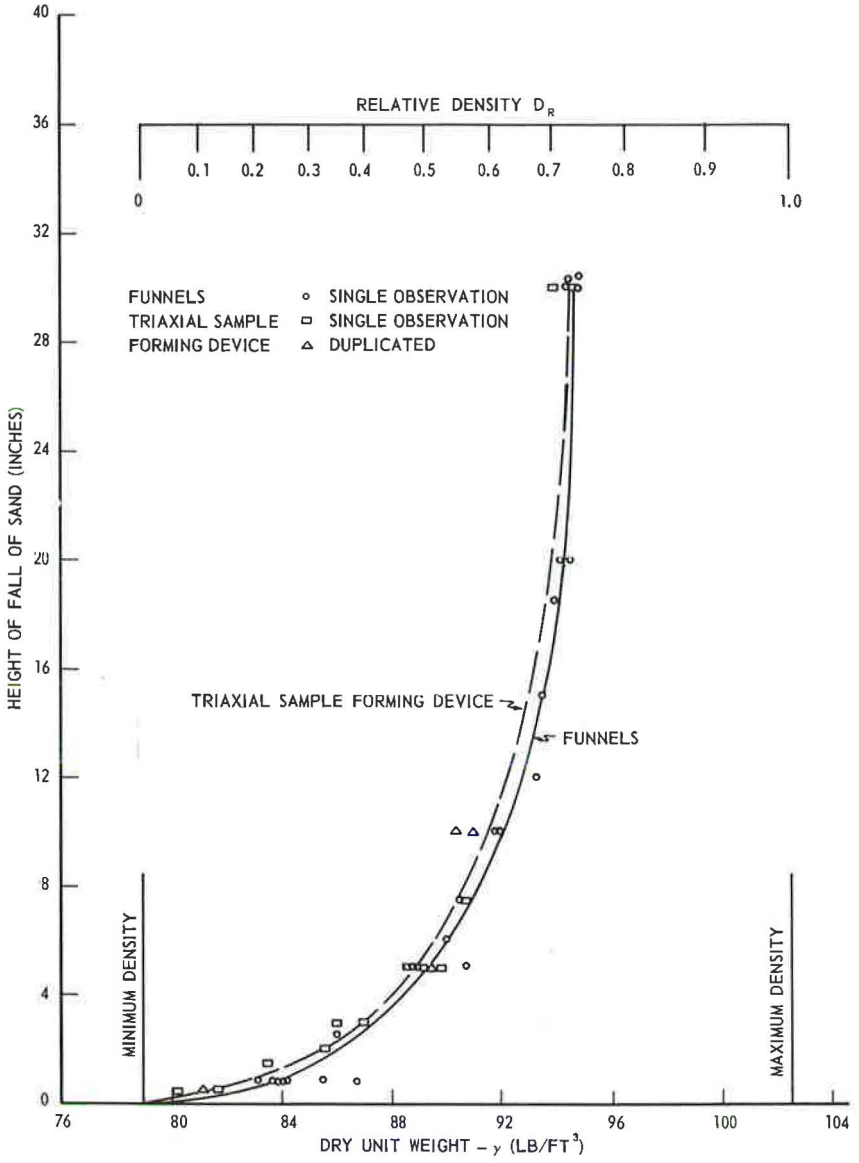

Figure 12. Relative density of sand as function of height of fall.

fully prepared horizontal sand surface and fixed in place so that it could not move during the subsequent operation of filling the sand above the base of the footing. Following former experience (34), exceptionally uniform loose- and medium-dense sand models (D_R < 0.70) were built by pouring sand from containers with perforated bottoms (Fig. 5b). It was confirmed again that the density of sand models so built is a unique function of the height of free fall of sand as long as other variables (rate of flow) remain the same (Fig. 12).

Denser sand models (D_R > 0.70) were built by surface vibration of 4-in. thick sand layers obtained by pouring sand 30 in. from the perforated container. Electric vibrators with a frequency of 3,600 cpm, attached to steel plates of appropriate shape, were used for surface vibration. Lead surcharge was added as necessary to achieve maxi-

mum compaction. All possible care was exercised to obtain uniform density throughout a model.

The homogeneity of sand in models was checked by penetrometer soundings. A simple static-cone micropenetrometer was constructed. This device has a $\frac{1}{2}$-in. point diameter and a $\frac{3}{8}$-in. shaft diameter of the casing. The assembly can be pushed into the sand by means of a screw jack at about 4 in. per min. Total resistance (point + skin) was recorded in several positions across the model and plotted against depth for each test. To convert the measurements of this kind into density, an empirical relationship was established between total resistance reduced to unit area of the point end dry unit weight of the material (Fig. 13). This was achieved by sounding sand models in a 24- by 16- by 60-in. box placed on a scale and filled by the same methods as used for building larger models.

Review of Tests Performed

Following the previously outlined program, six series of tests were performed. The main characteristics of five series of regular loading tests are given in Table 1.

The sixth series of tests, Series M, numbered 101 to 105, was devoted to the study of failure phenomena under foundations. Models of soil were built of distinct layers of sand to which cements of two different colors were added (10% by weight). After performing the loading test in the usual way, water was added to the models to cause setting of the layered mass. A few days later, the hardened block was cut through characteristic sections where shear patterns at failure were visible for observation and analysis.

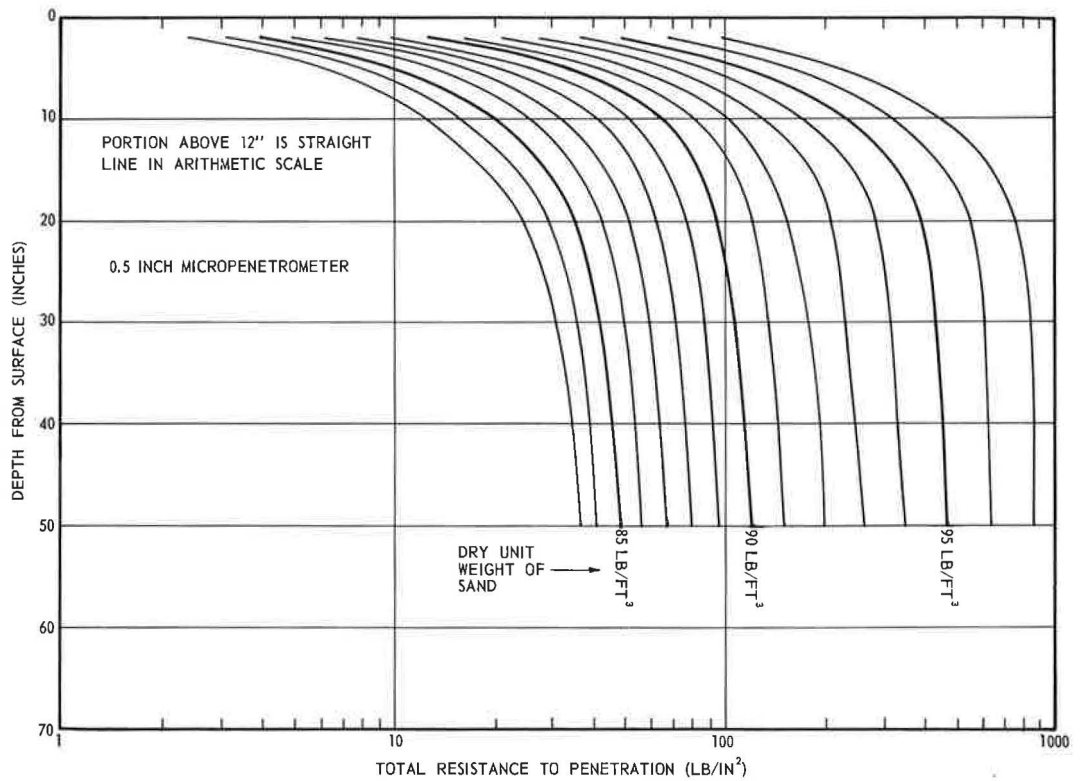

Figure 13. Relationship between depth and total penetration resistance for different sand densities.

Loading Procedure

The loading procedure for tests at the surface was similar to that followed in ordinary plate load tests. The load was applied in increments of about $1/20$ of the estimated failure load at 1-min intervals.

The loading procedure for tests beneath the surface was, in principle, the same. However, three separate loading stages existed in each test of series A, B and C. First, the foundation base was pushed until failure was reached; second, the same procedure was repeated with the foundation shaft; and third, after the shaft reached the base, both were pushed together and the total resistance was recorded.

Inasmuch as the loading head of the 6.75-in. foundations was of different construction (Fig. 7), the loading stages in D-tests differed somewhat from those just described. By pushing the foundation base to failure, the loading head was brought to contact with the skin and the entire foundation was forced into the soil. Special proving rings (Fig. 7) registered base and skin loads separately during this second stage.

Displacements of foundation base and skin were recorded at 1-min intervals by two micrometer dial gages placed near the loading head (Fig. 7). Also, in tests of series D, displacements of the sand surface were measured at different locations around the foundation.

TEST RESULTS

Significant results of the loading tests performed are given in Tables 4 through 9. Characteristic load-settlement diagrams of surface tests are shown in Figures 14 through 16. The black points indicate ultimate and first failure loads. The criterion by which these loads were established will be discussed subsequently.

Characteristic load-settlement diagrams of base and skin loading tests at greater depth are shown in Figures 17 through 19 and 20 through 22. Black points indicate ultimate loads.

Characteristic failure patterns at greater depth obtained in tests with colored sand are shown in Figures 23 through 25. Figure 23 shows what happens when a circular shaft penetrates through dense sand ($D_R \sim 0.9$) from a relative depth of $D/B = 10$ to a relative depth of $D/B = 19$. Figure 24 shows the analogous phenomenon for a rectangular foundation penetrating from $D/B = 10$ to $D/B = 11$, and Figure 25 for a rectangular foundation penetrating from $D/B = 5$ to $D/B = 6$.

Types of Failure

Three characteristic types of failure were observed in surface tests. Foundations on relatively dense sand ($D_R > 0.70$) fail suddenly with very pronounced peaks of base resistance (Fig. 26a) when the settlement reaches about 7 percent of the foundation width. The failure is accompanied by the appearance of failure surfaces at the sand surface and by considerable bulging of sheared mass of sand. The phenomenon corresponds exactly to that described earlier by Terzaghi (6) as "general shear failure."

Foundations on sand of medium density ($0.35 < D_R < 0.70$) do not show a sudden failure. As the settlements exceed about 8 percent of the foundation width small sudden shears within the sand mass are apparent from observations of load and settlement gages. Simultaneously, bulging of the sand surface starts. At settlements of about 15 percent of foundation width, a visible boundary of sheared zone at the sand surface appears. However, the peak of base resistance may never be reached.

The phenomenon is of the same nature as that described by Terzaghi (6) and by De Beer and Vesić (34) as "local shear failure" (rupture par refoulement incomplet). In the latter investigation, however, the tests were stress-controlled, so that the beginning of large shears in the soil mass was much more pronounced and was always recorded as the first failure of the foundation.

Finally, foundations on relatively loose sand ($D_R < 0.35$) penetrate into the soil without any bulging of the sand surface (Fig. 26c). The base resistance steadily increases as the settlement progresses. The rate of settlement, however, increases and reaches a maximum at a settlement of about 15 to 20 percent of foundation width.

TABLE 4

SIGNIFICANT RESULTS OF LOADING TESTS WITH CIRCULAR PLATES AT THE SURFACE

Test No.	Plate Diameter, B (in.)	Dry Unit Weight of Sand, γ_d (pcf)	Ultimate Pressure, p_o (psi)	$\frac{p_o}{\frac{1}{2}\gamma B}$	Ultimate Settlement, w (psi)	$\frac{w}{B}$ (%)	Type of Failure[a]
(1)	(2)	(3)	(4)	(5)	(6)	(7)	(8)
34	2.13	96.0	33.8	572	0.126	5.9	G
21	2.13	93.0	10.2 (7.6)[b]	173 (129)	0.272	12.8	L
22	2.13	89.8	7.4 (3.9)	134 (70.6)	0.414	19.5	L
23	2.13	82.6	2.4 (0.8)	48.2 (15.0)	0.463	21.8	P
44	3.94	96.7	53.8	432	0.227	5.8	G
41	3.94	93.8	19.8 (13.4)	186 (126)	0.446	11.3	L
42	3.94	91.0	13.0 (6.7)	126 (64.7)	0.621	19.2	L
43	3.94	83.3	3.1 (1.6)	32.5 (16.3)	0.582	14.8	P
61	6.00	96.2	73.4	432	0.425	7.1	G
62	6.00	93.0	31.0 (23.0)	193 (143)	0.869	14.5	L
63	6.00	91.7	19.3 (13.6)	121 (85.5)	0.875	14.6	L
64	6.00	95.0	5.3 (3.3)	35.9 (22.1)	0.852	14.2	P
84	8.00	96.2	79.2	432	0.667	8.3	G
81	8.00	95.2	55.9	262	0.737	9.2	G
82	8.00	95.2	42.1	193	0.695	8.7	G
83	8.00	88.0	9.0 (7.0)	44.2 (34.4)	1.08	13.5	L

TABLE 5

SIGNIFICANT RESULTS OF LOADING TESTS WITH RECTANGULAR PLATES AT THE SURFACE

Test No.	Plate Size (in.)	Dry Unit Weight of Sand, γ_d (pcf)	Ultimate Pressure, p_o (psi)	$\frac{p_o}{\frac{1}{2}\gamma B}$	Ultimate Settlement, w (in.)	$\frac{w}{B}$	Type of Failure[a]
(1)	(2)	(3)	(4)	(5)	(6)	(7)	(8)
16	2 × 12	96.4	47.0	842	0.212	10.6	G
1	2 × 12	93.6	22.1 (14.8)[b]	268	0.397	19.9	L
2	2 × 12	91.9	11.6 (8.3)	147	0.403	20.1	L
3	2 × 12	84.0	2.1 (1.4)	28.8	0.429	21.4	P

[a] G = general shear; L = local shear; P = punching shear.
[b] Numbers in parentheses refer to first failure.

TABLE 6

SIGNIFICANT TEST RESULTS – CIRCULAR DEEP FOUNDATIONS[a]

Test No.	Depth, D (in.)	Dry Unit Weight of Sand, γ_d (pcf)	Ultimate Base Resistance, p_o (psi)	Ultimate Settlement, w (in.)	$\frac{w}{B}$ (%)	Ultimate Skin Resistance, s_o (psi)	Ultimate Skin Displacement (in.)	Total Ult. Load (lb)	Ult. Displacement for Total Load (in.)
(1)	(2)	(3)	(4)	(5)	(6)	(7)	(8)	(9)	(10)
37	10	96.5	238.0	0.315	14.8	0.582	0.352	850	0.22
24		92.0	62.5	0.560	26.3	—	—	—	—
25		90.0	41.1	0.574	27.0	0.332	0.115	173	0.13
26		83.5	14.1	0.434	20.4	0.267	0.249	57	0.06
38	20	96.4	298.0	0.447	21.0	1.020	0.420	1,340	0.39
27		93.8	99.2	0.633	29.8	0.342	0.352	477	0.18
28		91.5	54.1	0.625	29.4	0.341	0.385	290	0.28
29		82.8	14.3	0.425	20.0	0.314	0.344	93	0.10
39	30	96.2	329.0	0.429	20.2	1.618	0.704	1,730	0.28
30		94.0	112.5	0.703	33.1	0.412	0.330	540	0.20
31		91.3	61.6	0.616	29.0	0.350	0.294	287	0.17
32		84.2	20.2	0.483	22.7	0.264	0.270	126	0.07
40	40	95.9	302.0	0.459	21.6	1.653	0.757	1,670	0.18
33		93.3	113.8	0.623	29.3	0.366	0.362	572	0.22
34		90.9	73.1	0.561	26.4	0.331	0.335	323	0.21
35		82.4	17.4	0.474	22.3	0.238	0.315	144	0.10

[a]Base diameter, 2.13 in.; skin diameter, 2.00 in.

TABLE 7

SIGNIFICANT TEST RESULTS – CIRCULAR DEEP FOUNDATIONS[a]

Test No.	D (in.)	γ_d (pcf)	p_o (psi)	w (in.)	$\frac{w}{B}$ (%)	Ult. Skin Resistance, s_o (psi)	Ult. Skin Displacement (in.)	Total Ult. Load (lb)	Ult. Displacement for Total Load (in.)
(1)	(2)	(3)	(4)	(5)	(6)	(7)	(8)	(9)	(10)
48	40	95.8	202.0	0.933	23.3	1.002	0.251	3,370	0.30
45		94.6	114.9	0.971	24.3	0.484	0.348	1,990	0.30
46		91.1	62.0	1.126	28.2	0.465	0.362	1,010	0.23
47		83.8	26.3	1.174	29.4	0.400	0.462	515	0.22
51	80	94.8	184.0	0.941	23.5	2.260	0.267	4,260	0.30
49		93.8	130.8	1.417	35.4	0.793	0.300	2,340	0.19
50		82.3	27.8	1.073	26.8	0.454	0.376	800	0.39

[a]Base and skin diameter, 4.00 in.

TABLE 8

SIGNIFICANT TEST RESULTS – CIRCULAR DEEP FOUNDATION[a]

Test No.	D (in.)	γ_d (pcf)	p_o (psi)	w (in.)	w/B (%)	Ult. Skin Resistance, s_o (psi)	Ult. Skin Displacement (in.)	Total Ult. Load (lb)
(1)	(2)	(3)	(4)	(5)	(6)	(7)	(8)	(9)
68	60	96.5	341.6	2.17	32.2	1.700	0.350	14,000
69		94.0	98.8	1.88	27.8	0.491	0.330	3,950
70		84.1	30.6	1.26	18.7	0.430	0.380	1,570
67	110	95.6	271.0	2.20	32.6	1.750	0.421	12,800
65	113	91.8	96.4	2.90	43.0	0.683	0.350	4,700
66	110	85.8	55.8	1.81	26.8	—	—	2,830

[a]Base and skin diameter, 6.75 in.

TABLE 9

SIGNIFICANT TEST RESULTS – RECTANGULAR DEEP FOUNDATIONS[a]

Test No.	Depth, D (in.)	Dry Unit Weight of Sand, γ_d (pcf)	Ult. Pressure, p_o (psi)	Ult. Displacement, w (in.)	$\frac{w}{B}$ (%)	Ult. Skin Resistance, s_o (psi)	Ult. Skin Displacement (in.)	Total Ult. Load (lb)	Ult. Displacement for Total Load (in.)
(1)	(2)	(3)	(4)	(5)	(6)	(7)	(8)	(9)	(10)
17	10	95.0	126.0	0.605	24.4			3,140	0.23
4		94.0	52.8	0.600	24.6			1,550	0.18
5		91.1	32.4	0.712	29.2			1,050	0.10
6		83.8	8.8	0.594	24.3			420	0.10
18	20	95.1	159.8	0.626	25.7	0.299	0.222	4,810	0.41
7		93.8	79.5	0.766	31.4	0.168	0.268	2,610	0.25
8		90.9	39.4	0.689	28.2	0.174	0.165	1,570	0.18
9		82.0	11.1	0.657	26.9	0.124	0.124	560	0.18
19	30	96.4	181.5	0.715	29.3	0.484	0.235	6,190	0.40
10		94.2	84.2	0.740	30.3	0.282	0.197	3,000	0.27
11		91.8	48.4	0.759	31.1	0.208	0.185	2,000	0.29
12		82.0	11.9	0.566	22.8	0.153	0.170	705	0.22
20	40	96.5	188.6	0.600	24.6	0.673	0.152	6,500	0.40
13		94.1	85.2	0.700	28.7	0.270	0.118	3,320	0.40
14		90.7	45.0	0.700	28.7	0.210	0.125	1,980	0.22
15		82.0	11.5	0.373	15.3	0.188	0.162	735	0.08

[a]Base width, 2.44 in.; base length, 12.44 in.; skin width, 2.25 in.; skin length, 12.25 in.

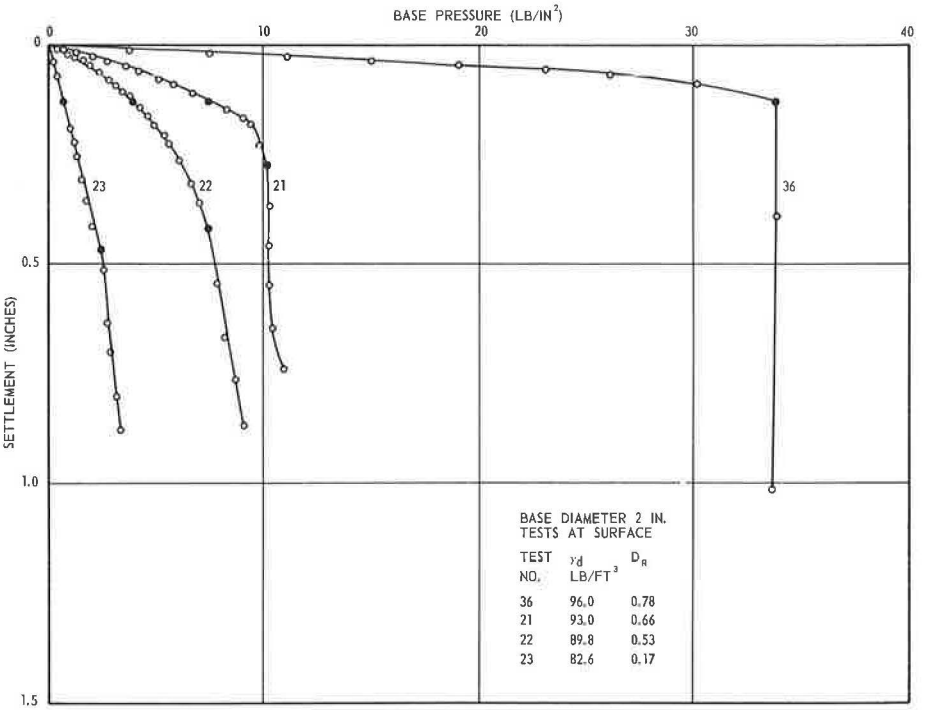

Figure 14. Typical results of surface tests.

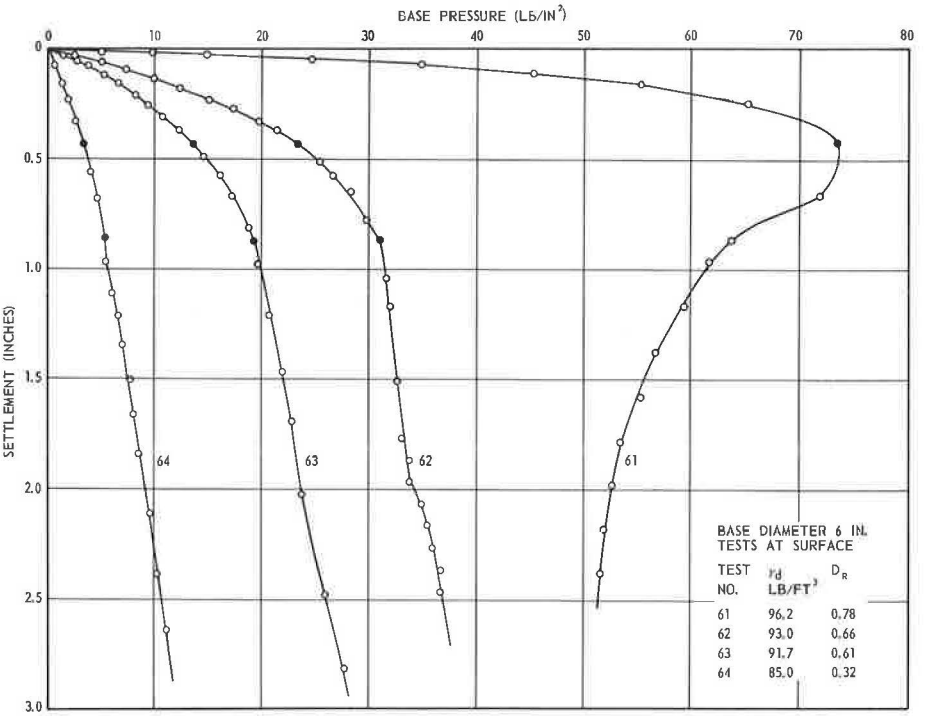

Figure 15. Typical results of surface tests.

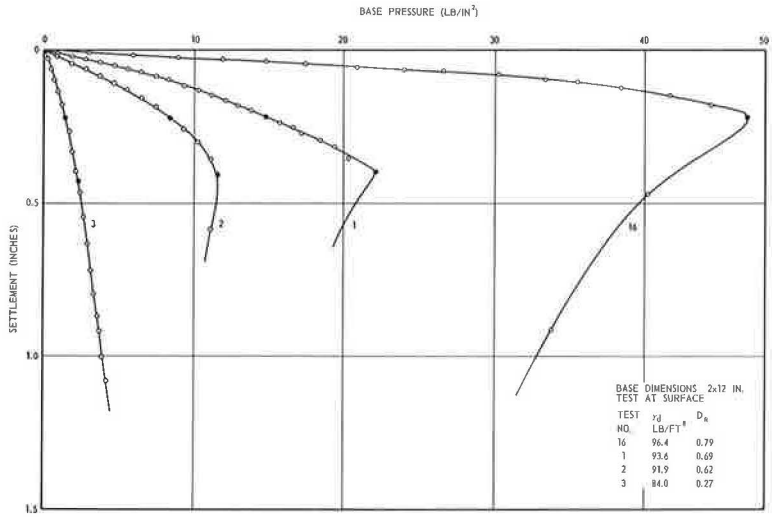

Figure 16. Typical results of surface tests.

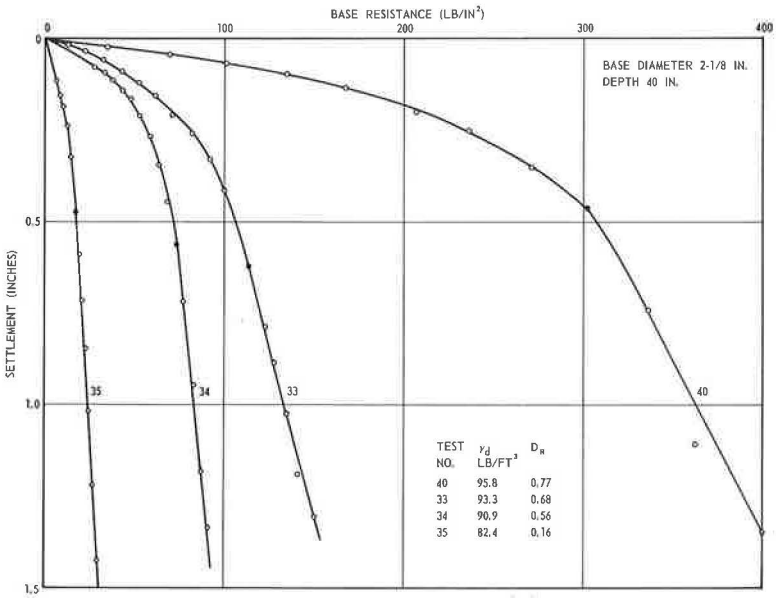

Figure 17. Typical results of base loading tests at greater depth.

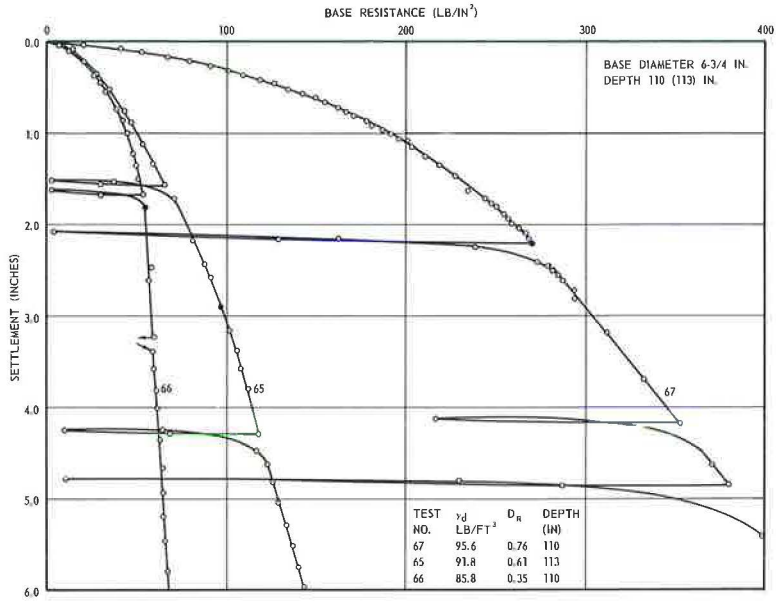

Figure 18. Typical results of base loading tests at greater depth.

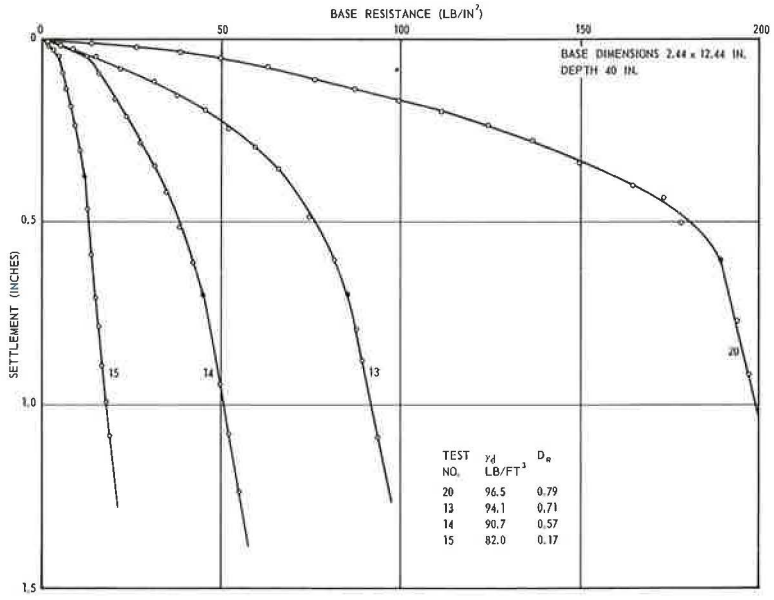

Figure 19. Typical results of base loading tests at greater depth.

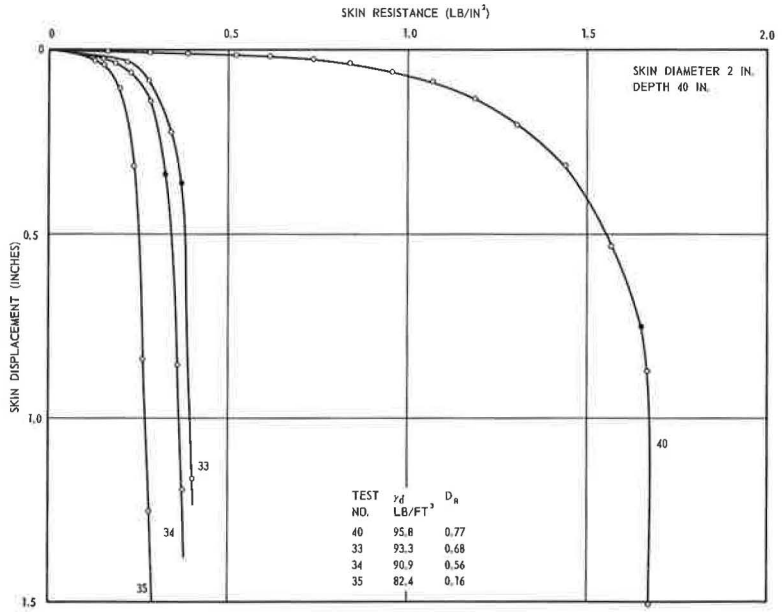

Figure 20. Typical results of skin loading tests.

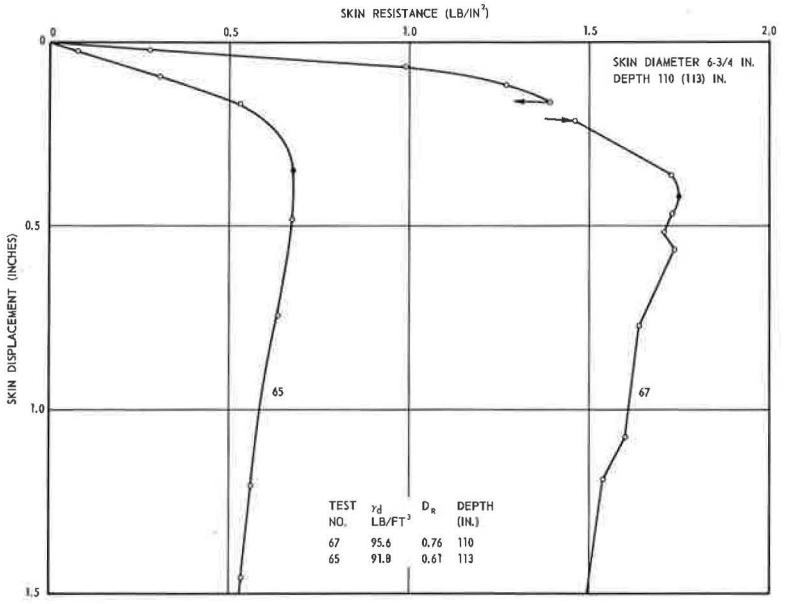

Figure 21. Typical results of skin loading tests.

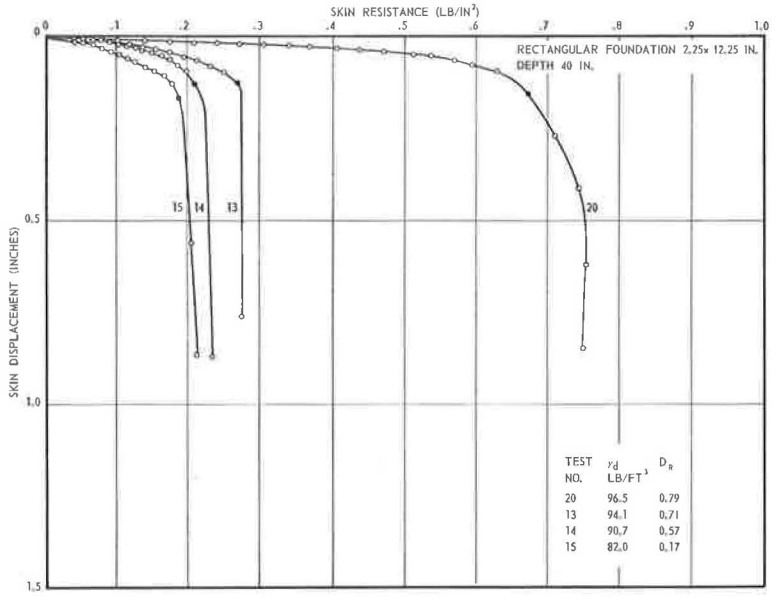

Figure 22. Typical results of skin loading tests.

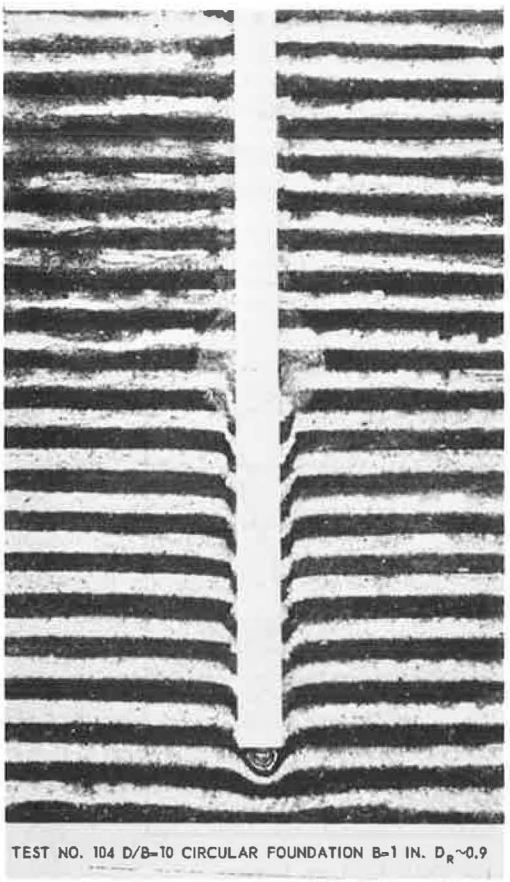

Figure 23. Shear pattern under a circular foundation placed at greater depth in very dense sand.

Figure 24. Shear pattern under a rectangular foundation placed at greater depth in very dense sand.

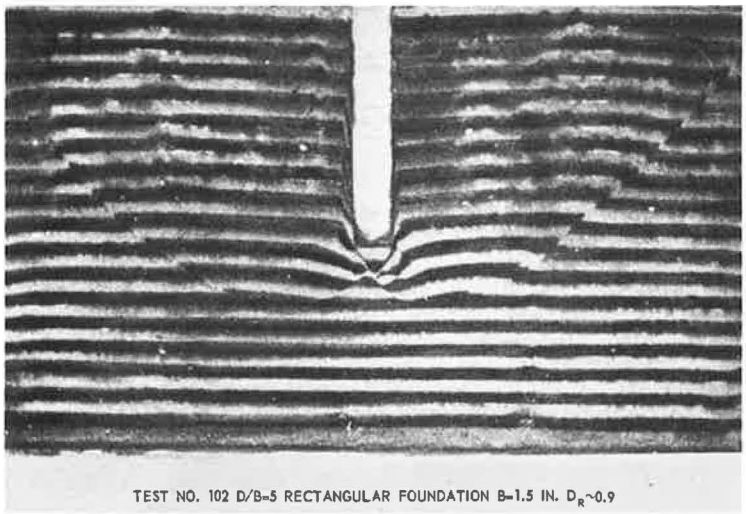

Figure 25. Shear pattern under a rectangular foundation placed at shallow depth in very dense sand.

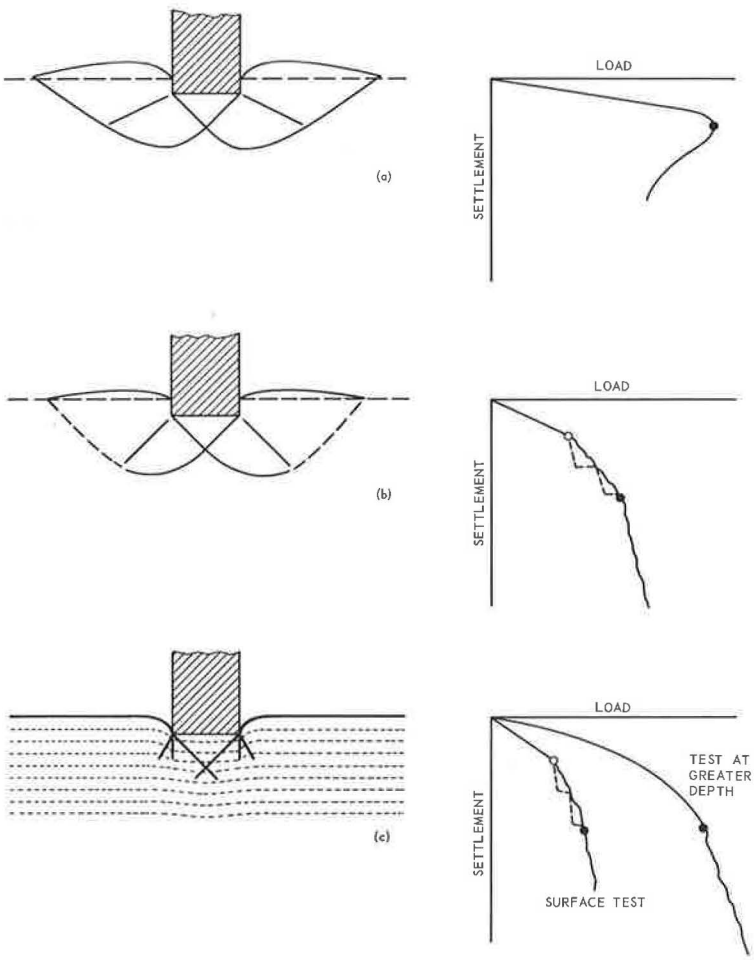

Figure 26. Types of failure.

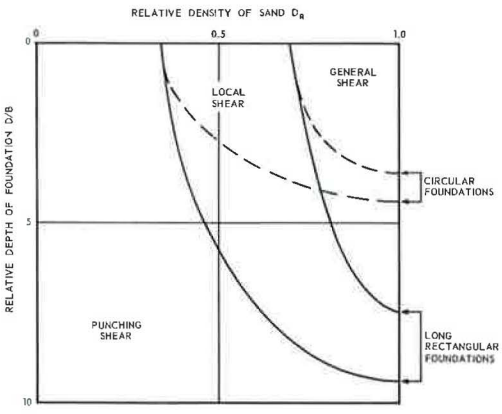

Figure 27. Types of failure at different relative depth D/B of foundations in sand.

Sudden shears can be observed in sequence as soon as the settlement reaches about 6 to 8 percent of foundation width. The failure surface, which is vertical or slightly inclined and follows the perimeter of the base, never reaches the sand surface. The phenomenon is essentially "punching shear failure," as described by De Beer and Vesić (34).

The same three characteristic types of failure are observed at shallow depths. However, as the relative depth D/B increases, the limiting relative densities at which failure types change increase. The approximate limits of types of failure to be expected as relative depth D/B and relative density of sand D_R vary are shown in Figure 27. There is a critical relative depth below which only punching shear failure occurs. For circular foundations this critical relative depth seems to be around D/B = 4, and for long rectangular foundations around D/B = 8.

It is important to note that the limits of types of failure depend on the compressibility of the material. More compressible materials will generally have lower critical relative depths. Following this trend, it is not difficult to explain why some materials may exhibit punching shear failure only.

Criterion of Failure or Ultimate Load

In accordance with observations just described the following criteria of failure or ultimate load were established:

1. In the case of general shear failure, the criterion is very clear: a peak of base resistance is always reached, corresponding to the appearance of failure surfaces at the sand surface, and to an abrupt change of rate of settlement from positive to negative.
2. In the case of local shear failure, there is not always a peak of base resistance, however, the rate of settlement reaches a maximum at the same load at which failure becomes visible at the surface. This load is considered as ultimate. In addition, first failure, clearly distinguishable only in stress-controlled tests, can be noted when settlements reach magnitudes at which the general shear failure occurs in dense sand (34).
3. In the case of punching shear failure, there is no peak of base resistance nor any appearance of failure surfaces. However, a peak of settlement rate can be noted. The corresponding load is considered as ultimate load.

Analogous criteria are adopted for skin loading tests.

DISCUSSION OF TEST RESULTS

Foundations at Surface

Figure 28 compares observed bearing capacities in surface tests with corresponding theoretical values. Measured values of $p/\frac{1}{2}\gamma B$ (col. 5, Tables 4 and 5) are shown as a function of dry unit weight of sand γ_d or relative density D_R. To have a better basis for comparison, the ultimate pressures of rectangular foundation have been multiplied by a shape factor 0.60 (a value recently confirmed by very extensive experiments, 35). Both first and ultimate failure pressures are shown for medium and loose sands. Figure 28 also shows theoretical bearing capacity factor N_γ after Caquot and Kerisel (36)

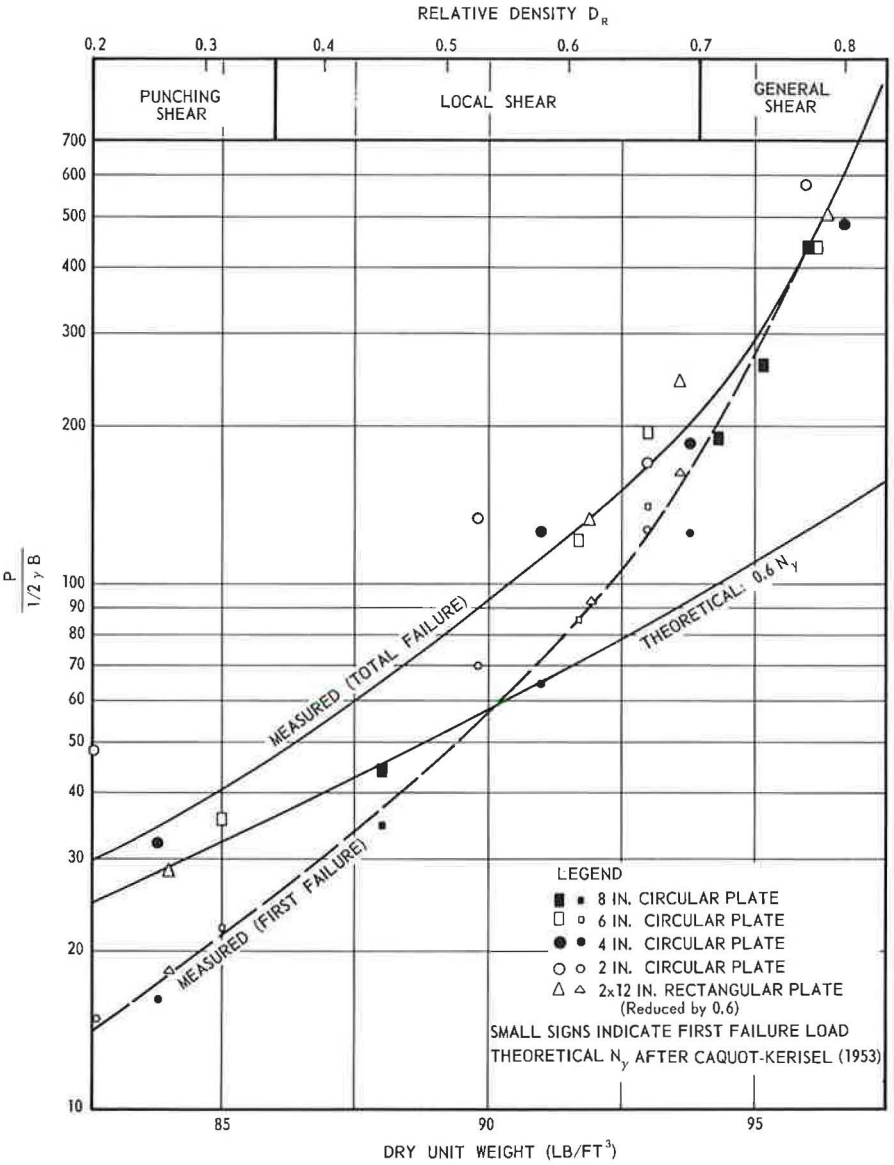

Figure 28. Observed bearing capacities of foundations at surface.

multiplied by shape factor 0.60. To present the factor N_γ as a function of dry unit weight or void ratio, the experimentally established relationship (Eq. 8) between the angle of internal friction ω and void ratio e is used.

Figure 28 shows that the observed ultimate bearing capacities are generally 1.2 to 4 times higher than corresponding theoretical values. This is in general agreement with findings of earlier experiments of similar nature (34, 33). A fully satisfactory explanation of this phenomenon has not yet been found.

The ranges of relative densities in which different types of failure occur (Fig. 28, top) also agree well with those found in an earlier investigation (34). It seems that the conventional classification of sands by relative density into loose ($D_R < 0.33$), medium ($0.33 < D_R < 0.67$) and dense ($D_R > 0.67$) has a certain meaning concerning the type of failure of shallow foundations on such materials.

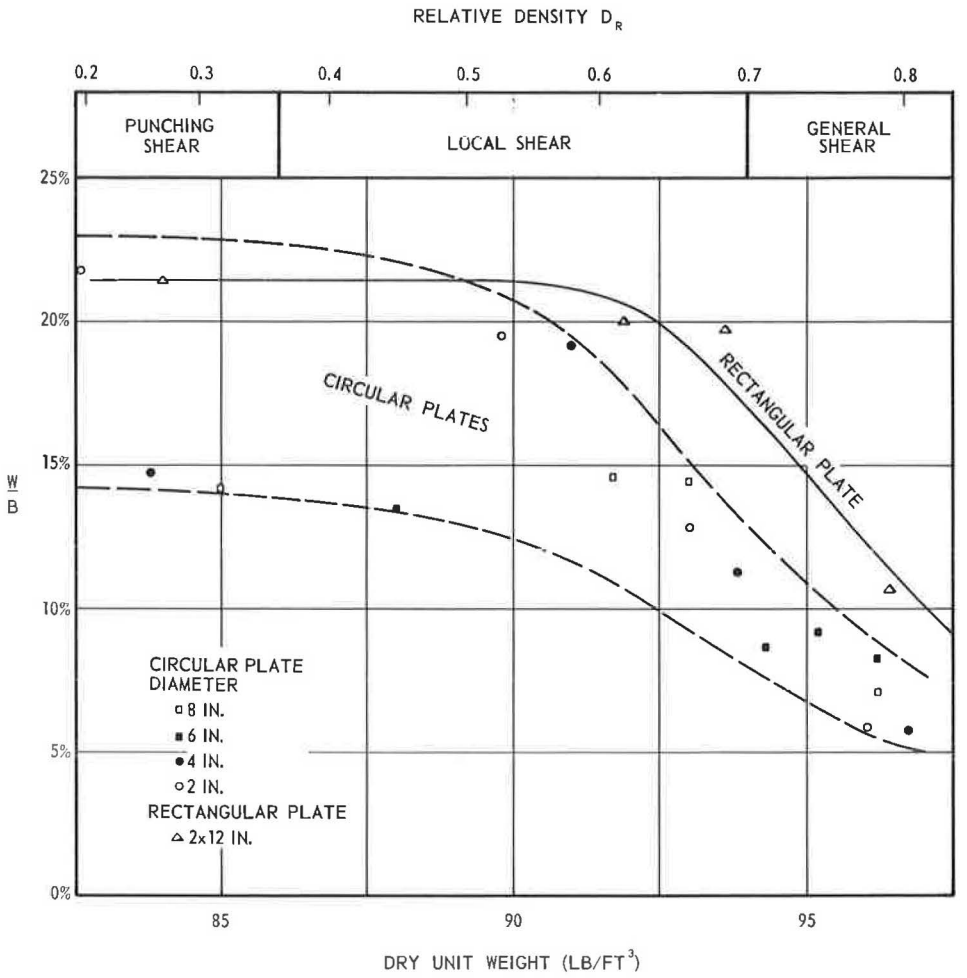

Figure 29. Settlement at failure for surface foundations.

Figure 29 shows the settlements at which ultimate loads were recorded, expressed as percentage of the foundation width. General shear failure usually occurs at settlements not exceeding 10 percent of foundation width; the other failure types take place at settlements of about 15 to 20 percent of the foundation width. This is in general agreement with former observations. However, slightly higher relative settlements at failure of rectangular foundations do not conform with some earlier findings (35). A similar trend was observed in tests with deep foundations (Fig. 32).

Base Resistance of Deep Foundations

Figures 30 and 31 show the general trend of increase in bearing capacity of the base with increase of foundation depth. Figure 30 shows the ultimate base resistance of 2.13-in. circular foundations as a function of foundation depth D. Figure 31 is an analogous plot for 2.44- by 12.44-in. rectangular foundations. A practically linear increase of bearing capacity with depth can be observed only at shallow depths, not exceeding approximately D/B = 4 for circular and D/B = 6 for rectangular foundations. As the foundation depth increases further, the rate of increase of bearing capacity with depth decreases. At a relative depth of approximately D/B = 15 the bearing capacity reaches asymptotically final values which appear to be functions of sand density only.

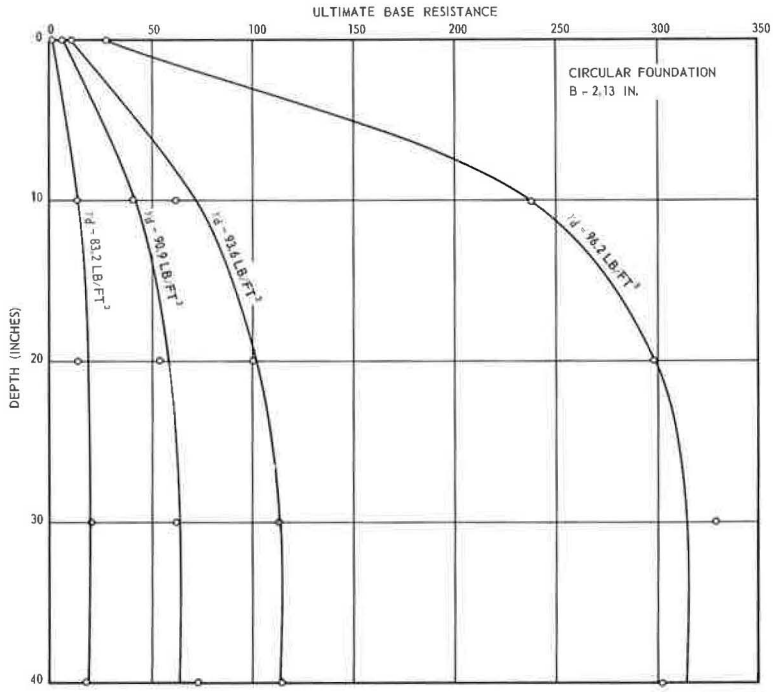

Figure 30. Measured bearing capacities of base—circular foundation, B = 2.13 in.

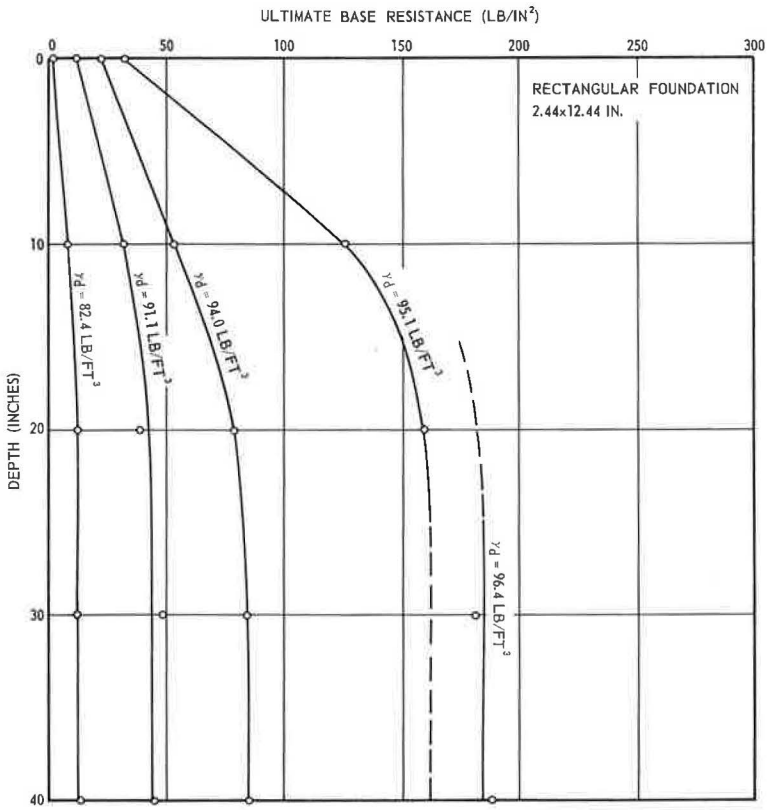

Figure 31. Measured bearing capacities of base—rectangular foundation, 2.44 x 12.44 in.

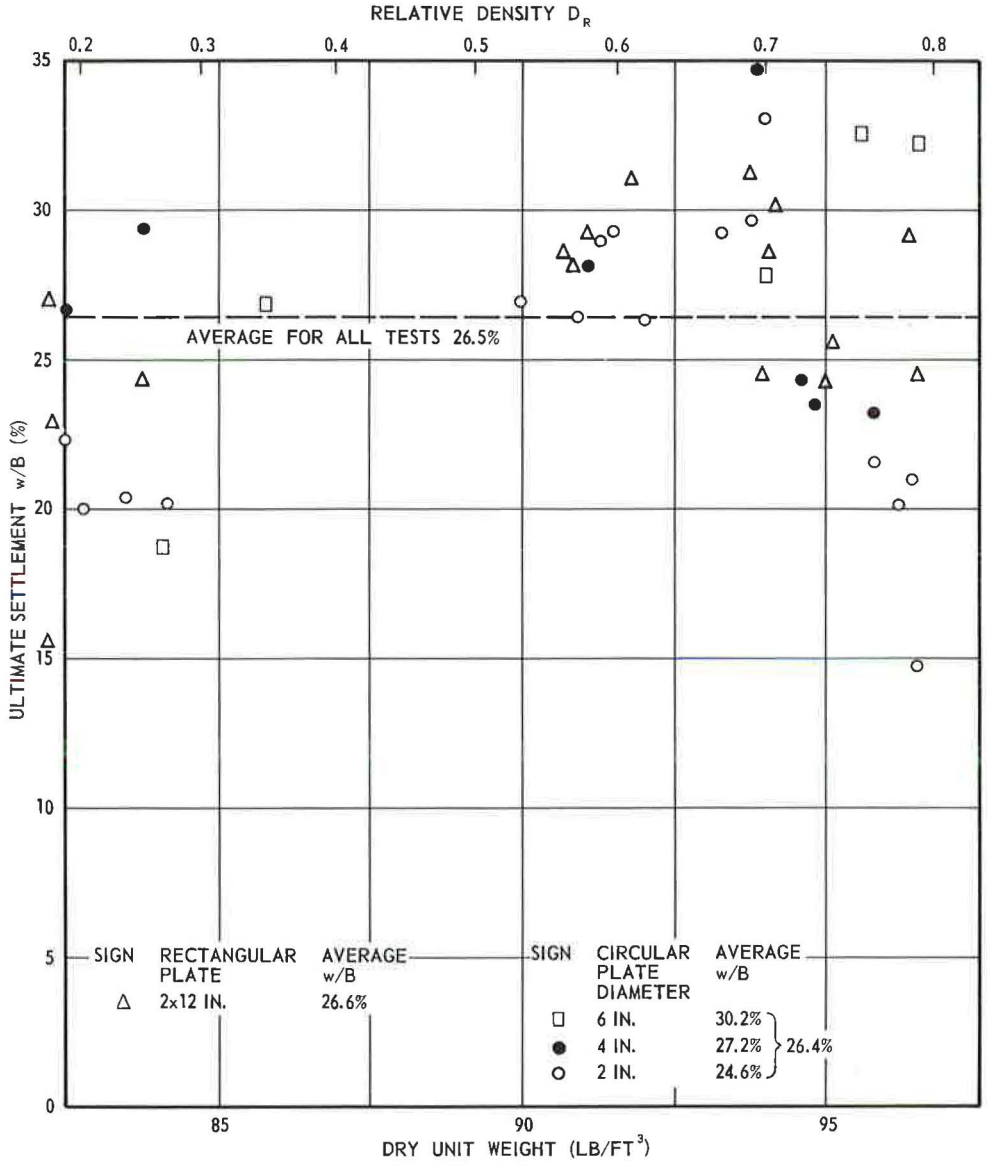

Figure 32. Ultimate settlement of deep foundations.

Base displacements or settlements needed to reach the ultimate loads are shown in Figure 32. Apparently, there is a tendency of ultimate settlements to increase with both foundation size and depth; however, this tendency is not pronounced. It may be stated that, in the range of foundations sizes and depth used in this investigation, ultimate loads are reached at settlements of about 20 to 30 percent of foundation depth. Figure 32 is in general agreement with isolated former observations.

A comparison of final bearing capacities of circular and long rectangular foundations indicates that the former are approximately 1.50 times higher. Figure 33 shows the average final bearing capacity of the base as a function of dry unit weight of sand, with bearing capacities of rectangular foundations multiplied by a shape factor of 1.50. Final bearing capacities observed in tests with 4- and 6.75-in. circular foundations are

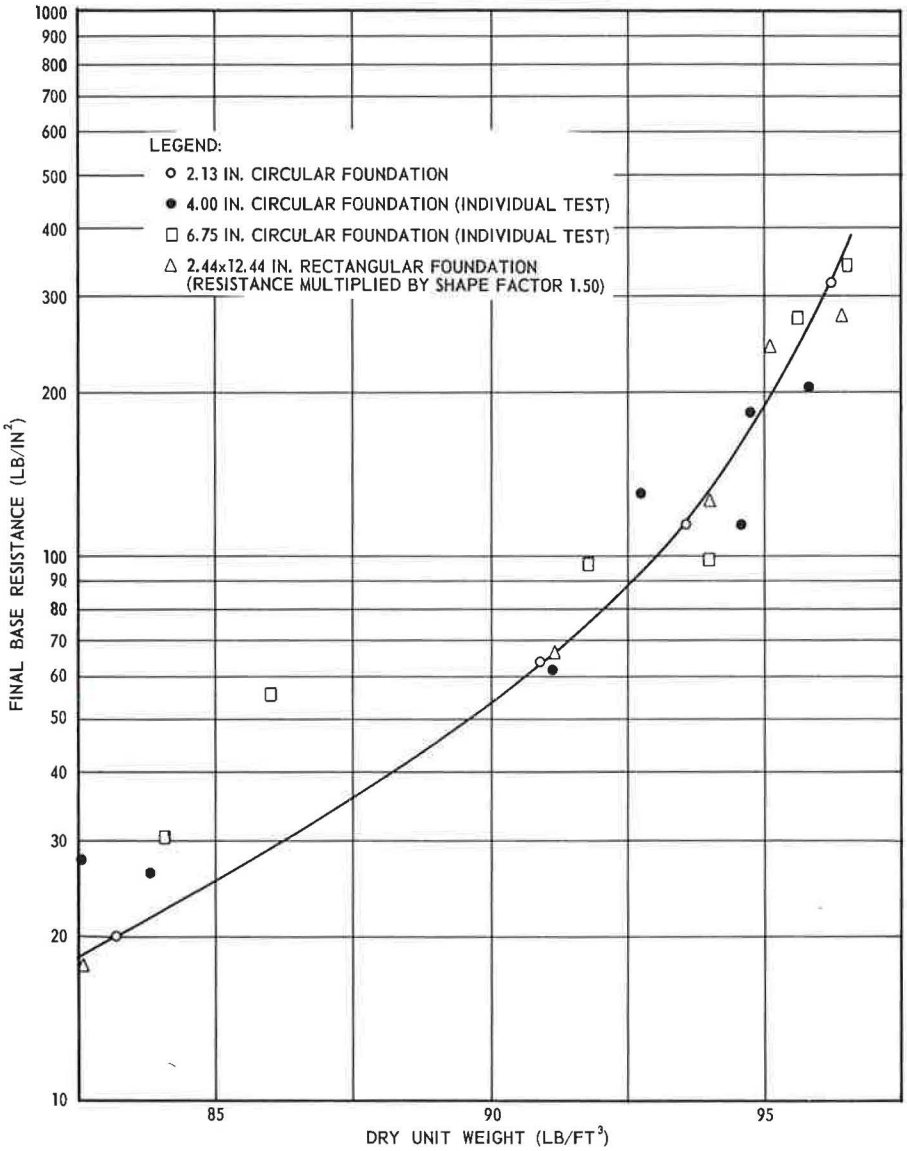

Figure 33. Ultimate base resistance at greater depth.

also plotted. The final bearing capacities are apparently independent of foundation size, at least for dense and medium dense sands.

A similar conclusion can be reached by studying Figure 6 of Kerisel's paper (32), although the numerical values obtained by the two investigations are not directly comparable due to differences in experimental approach and sand properties.

Skin Resistance of Deep Foundations

The variation of ultimate skin resistance s_0 with depth for 2-in. circular foundations is shown in Figure 34. For models in dense, vibrated sand, a long initial linear increase of s_0 with depth (up to D/B = 15) is followed by a sharp turn into a final skin resistance which remains constant as the depth increases further. For models in loose and medium-dense sand the shape of the initial part of the s_0 curve is not quite clear.

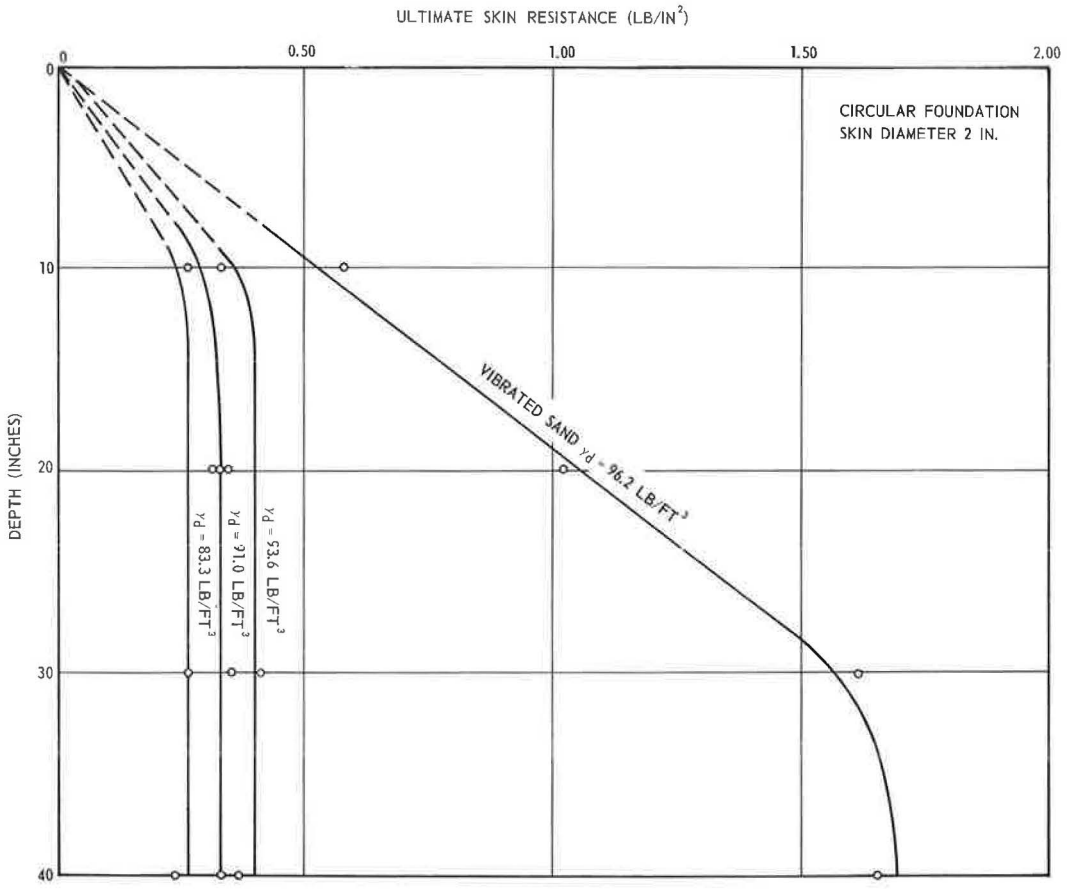

Figure 34. Ultimate skin resistance—circular foundation, 2 in.

It appears that there is also an initial linear increase limited to a depth of about four diameters. Beyond this depth the skin resistance turns sharply into a practically constant final value, varying with sand density only.

Figure 35 shows analogous diagrams for 2.25- by 12.25-in. rectangular foundations. The trend is similar, however, the initial part along which s_0 increases linearly with depth seems to be longer. The slope of the initial linear part is approximately three to four times less than the corresponding slope in the case of circular foundations. The final skin resistance, however, appears to be approximately 1.5 times lower for the rectangular shape.

Figure 36 shows the final average skin resistance as a function of dry unit weight of sand. Skin resistances of rectangular foundations multiplied by a shape factor of 1.5 are also plotted. The curve takes into account the fact that, due to method of placing of medium-dense sand, the density in the immediate vicinity of the skin was lower than the average density of the entire model, particularly in the case of 2-in. foundations.

The general shape of the s_0 curves found in the present investigation differs from that found in IRABA tests (32). However, it agrees well with numerous former observations on full-scale piers and caissons, which usually show a linear increase of s_0 at shallow depths, but a practically constant s_0 at greater depths.

Figure 37 shows skin displacements needed to reach ultimate skin resistance. It appears that these displacements are not dependent on foundation width and depth nor on sand density. For circular foundations they vary in the range of 0.30 to 0.40 in.; for rectangular foundations they are about one-half that magnitude. This finding con-

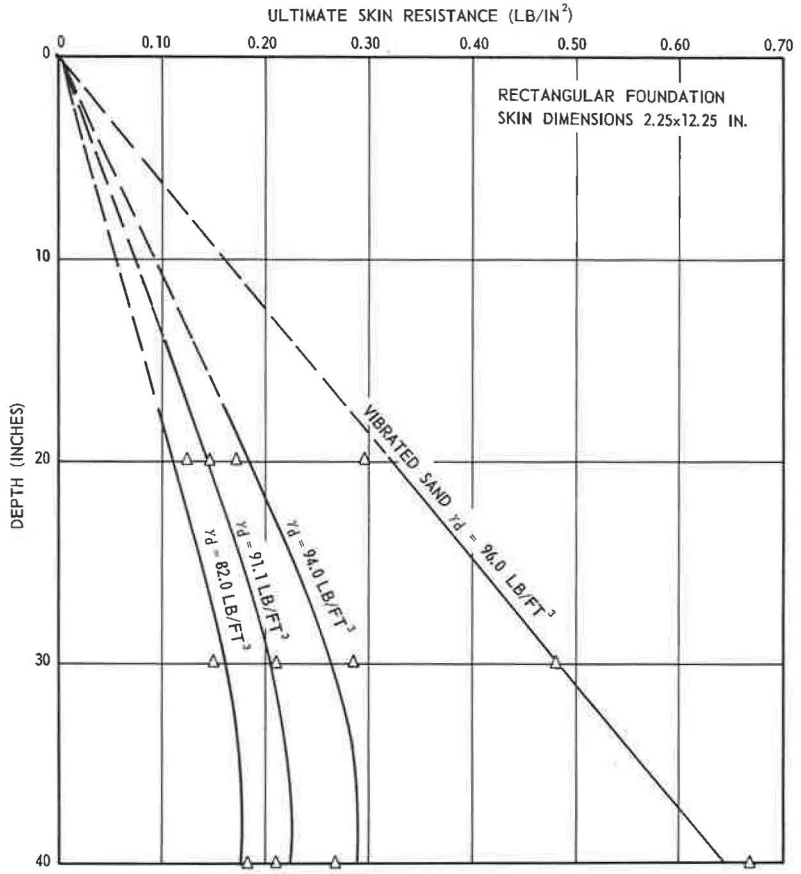

Figure 35. Ultimate skin resistance—rectangular foundation, 2.25 x 12.25 in.

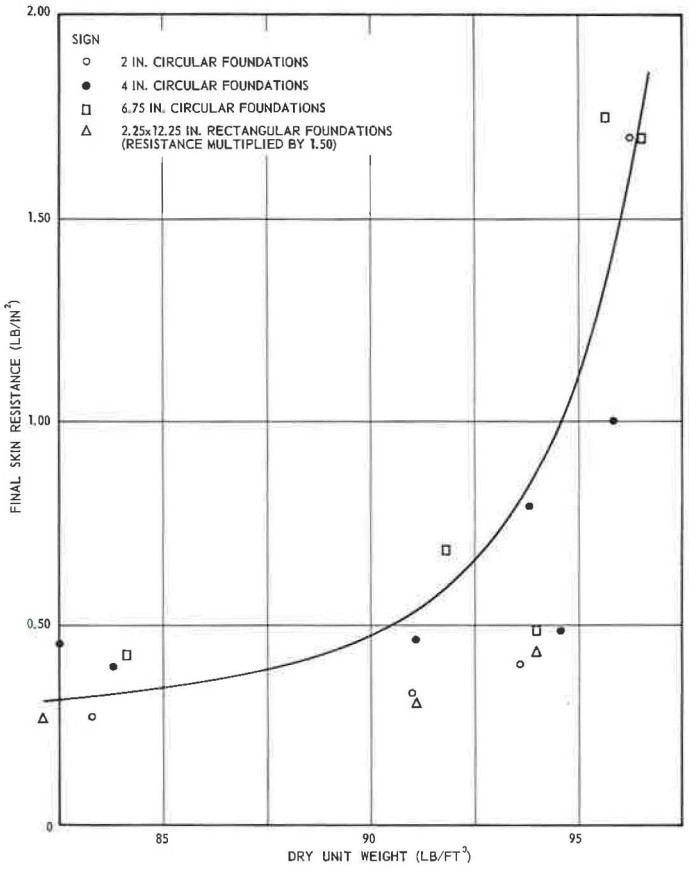

Figure 36. Final skin resistance at greater depth.

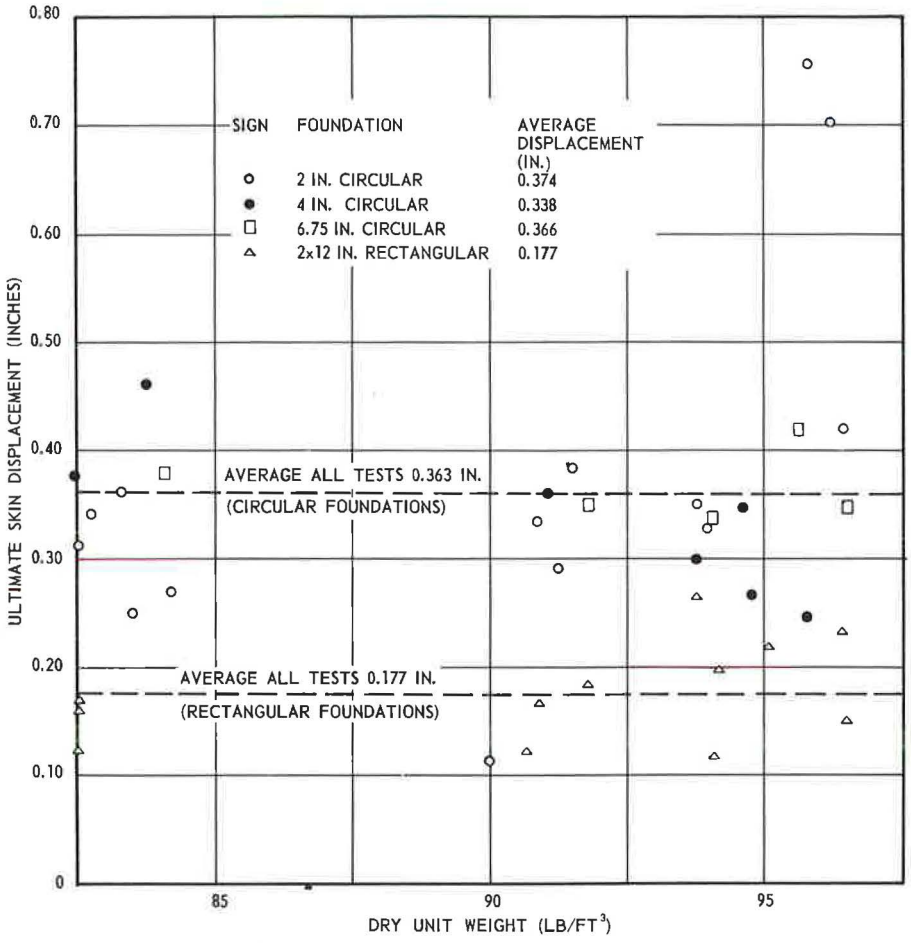

Figure 37. Ultimate skin displacement of deep foundations.

firms previously expressed beliefs that the mobilization of shear strength along a fixed rupture surface is governed by absolute displacement along that surface.

Bearing Capacity and Shape Factors at Shallow Depth

As previously mentioned, at shallow depths not exceeding D/B = 4 the increase of bearing capacity with depth appears to be linear as proposed by Eq. 3. Therefore the initial slopes of curves in Figures 30 and 31 indicate the experimental values of bearing capacity factor N_q at shallow depths. The N_q factors evaluated from these slopes are shown in Figure 38. To take into account the effect of shape, the depth term of circular foundations was reduced by an assumed shape factor of $\xi_q = 2.00$. Good agreement resulting from such an assumption indicates that shape factor ξ_q for a circular foundation in sand cannot differ greatly from 2. Terzaghi (6) proposed for that factor a value of 1.30 and Brinch Hansen (19), values increasing with φ from about 1.30 for $\varphi = 35°$ to 2.20 for $\varphi = 45°$.

As a basis for comparison, a curve of theoretical N_q values after Prandtl-Reissner is also shown (Fig. 38). To trace this curve the relationship (Eq. 8) between φ and e was assumed valid. This is justified by the probability that the average normal stress along a rupture surface under foundations does not exceed 10 percent of the foundation pressure.

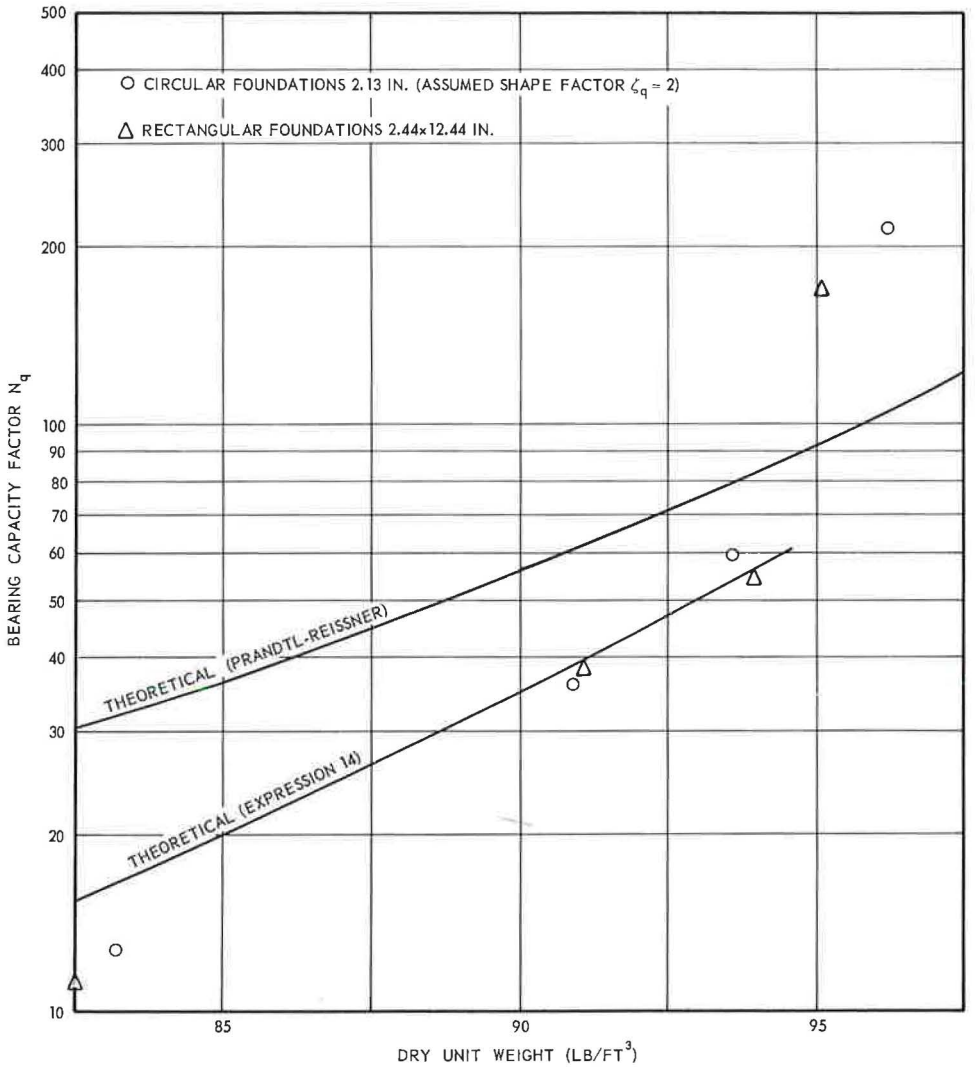

Figure 38. Measured bearing capacity factors N_q at shallow depth.

Higher N_q values for two very dense models can easily be explained. At high relative densities general shear failure still occurs at shallow depths (Figs. 25 and 27). As failure surfaces extend above foundation level, bearing capacity must be higher than indicated by Prandtl-Reissner theory which neglects shear resistance of the overburden (Fig. 2). If this resistance is taken into account a depth factor of approximately 2 should be introduced for D/B = 4 and $\varphi = 42°$ (10, 19). Therefore, excellent agreement of existing theory and experiments can be stated if the sand is dense. However, lower N_q values observed for medium and loose sand models cannot be explained by the existing theories, which consider general shear failure only.

Bearing Capacity in Local Shear Failure

To evaluate the bearing capacity factor N_q in the case of local or punching shear failure of a long rectangular foundation, a shear pattern based on observations on colored sand models will be considered (Fig. 39). It consists of an elastic zone ABC with two adjoining plastic zones BCD. The extent of development of these zones is determined by the angle θ at the apex.

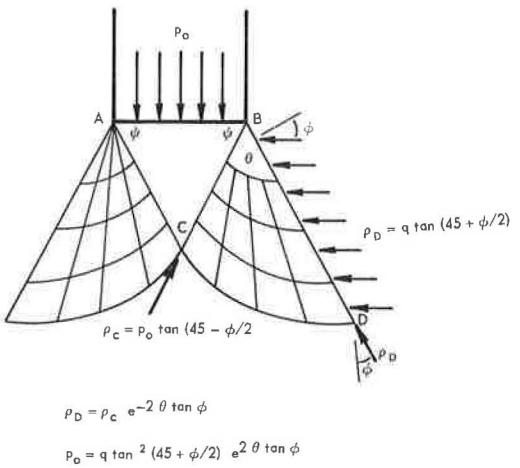

Figure 39. Analysis of punching or local shear failure.

It will be assumed that the overburden pressure q is great enough to allow neglecting the soil's own weight γ. Under such circumstances, solutions for weightless soil (3) can be applied to analyze stress conditions along CD. It is easy to show that the stress ρ_D acting on rupture line at D and the analogous stress ρ_C at C are connected by

$$\rho_D = \rho_C \, e^{-2\theta \tan \varphi} \qquad (10)$$

However,

$$\rho_C = \rho_A = p_o \tan (45 - \varphi/2) \qquad (11)$$

Also, assuming that the minor principal stress along BD is equal to overburden pressure q,

$$\rho_D = q \tan (45 + \varphi/2) \qquad (12)$$

Eliminating ρ_C and ρ_D from Eqs. 10, 11, and 12,

$$p_o = q \tan^2 (45 + \varphi/2) \, e^{2\theta \tan \varphi} \qquad (13)$$

By introducing $\theta = 1.9\,\varphi$, on the basis of observations, the following expression for N_q is obtained:

$$N_q = e^{3.8\,\varphi \tan \varphi} \tan^2 (45 + \varphi/2) \qquad (14)$$

Numerical values for different angles φ are given in Table 10. They are lower than classical Prandtl-Reissner values. Reasonable agreement between N_q values computed by Eq. 14 and observed experimentally are shown in Figure 38.

Bearing Capacity at Greater Depth

Earlier discussion of base and skin resistances p_o and s_o has shown (Figs. 30 through 36) that, beyond some limiting relative depth D/B, the increase of p_o and s_o with depth is not linear. As D/B increases over 15, p_o and s_o do not increase any more. Final values of p_o and s_o appear to be functions of density of sand only (Figs. 33 and 36).

These observations seem to contradict the fundamental structure of bearing capacity Eq. 3 and 6 derived by using theories of plastic or elastic-plastic equilibrium. As previously mentioned, similar observations made recently by Kerisel (32) have led him to conclude that the bearing capacity factor N_q is a complex func-

TABLE 10

BEARING CAPACITY FACTOR N_q IN THE CASE OF LOCAL OR PUNCHING SHEAR FAILURE

Angle of Internal Friction, φ (deg)	Bearing Capacity Factor, N_q
0	1.0
5	1.2
10	1.6
15	2.2
20	3.3
25	5.3
30	9.5
35	18.7
40	42.5
45	115
50	422

tion of φ D/B and B. As long as no explanation of these findings is offered this appears to be the only possible conclusion.

However, attempts to explain the obtained results by an appropriate rational analysis leave serious doubts as to the correctness of the conclusion. No matter how limited an extent of plastic zone adjacent to the foundation base is assumed, there still must be a certain increase of p_o as overburden pressure increases. Therefore, N_q cannot be zero for any increment of loading as long as the same material is dealt with. When loosening of sand structure or significant crushing of sand grains occurs, there is still a lower limit of angle of internal friction of the newly formed material. Consequently, sooner or later, there must be an increase of p_o if overburden pressure continues to increase.

On the basis of these and other considerations, the conclusion was reached that constant values of p_o at greater depth do not result from decrease in N_q alone as suggested.

The explanation of the phenomena observed must, therefore, be sought through the assumption that q is not proportional to initial overburden pressure, as conventionally assumed. In connection with this, the true meaning of q in different theories should be remembered. In Prandtl-Reissner theory q is defined as normal stress at failure on horizontal plane of the foundation base (Fig. 2). In De Beer-Jaky-Meyerhof theories it is defined as normal stress at failure on the lower portion of the foundation shaft (Fig. 3). There is no good reason to take these stresses a priori equal or proportional to the initial overburden pressure, if foundation is deeply embedded in sand.

To demonstrate the meaning of the results, it is assumed that both p_o and s_o increase linearly with q as indicated by Eq. 3 and 6, but that q is strictly q_f or effective normal stress at failure acting on an elemental horizontal plane next to the foundation (Fig. 40). In a plane problem, or a rectangular foundation placed at greater depth, Eq. 3 can be rewritten in the following form:

$$p_o = q_f N_q \tag{15}$$

$$s_o = q_f K_s \tan \delta \tag{16}$$

Eliminating q_f

$$N_q = \frac{p_o}{s_o} K_s \tan \delta \tag{17}$$

In analogous way the following expressions can be written for a circular foundation:

$$p_o = q_f N_q \zeta_q \tag{18}$$

$$s_o = q_f K_s \tan \delta \zeta_s \tag{19}$$

$$N_q = \frac{p_o}{s_o} K_s \tan \delta \frac{\zeta_s}{\zeta_q} \tag{20}$$

Thus, it is possible to evaluate N_q from results of tests at greater depth under mentioned assumptions without really knowing q_f. $K_s \tan \delta$ or $K_s \tan \delta \zeta_s$ can be evaluated from the initial straight-line part of the s_o line.

The results of such an evaluation are shown in Figure 41, where individual results from tests at greater depth with 2- 4- and 6.75-in. circular foundations as well as with 2- by 12-in. rectangular foundations are plotted. To plot comparable magnitudes, both shape factors ζ_s and ζ_q for circular foundations were taken equal to 3 although ζ_s appeared to slightly higher. Figure 41 also shows, for comparison, bearing capacity factor N_q after Prandtl-Reissner and after Eq. 14. It is evident that experimental values obtained by using Eqs. 17 and 20 are primarily functions of sand density and that they are independent of absolute magnitude of q_f. Their numerical values in dense sand are reasonably well estimated by using the Prandtl-Reissner classical expression for N_q with a shape factor of approximately 3 for circular foundations. In medium and loose sands experimental values are lower, and comparable to those estimated by Eq. 14.

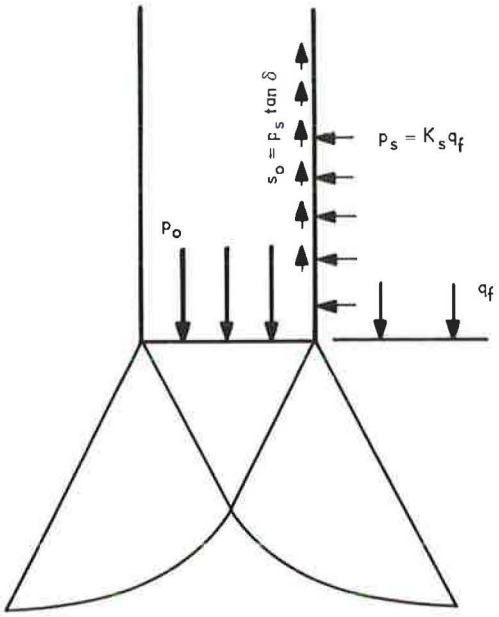

$$\frac{p_o}{q_f} = N_q = \frac{p_o}{s_o} K_s \tan \delta$$

Figure 40. Stress conditions in vicinity of base of deep foundation.

Some details of the analysis presented undoubtedly need further clarification, particularly the choice of shape factors which, due to limited number of tests performed, could not have been determined very accurately. It appears certain, however, that both base resistance p_o and skin resistance s_o are linear functions of vertical stress at failure, q_f. This stress is not necessarily equal nor proportional to the overburden pressure q. The nonlinear increase of base or skin resistance with depth can be explained by a similar increase of q_f with depth. If the base and skin resistance reach constant values at greater depth, it is because q_f also becomes constant at greater depth.

Analysis of Vertical Stress Around the Foundation

According to the preceding discussion, curves in Figures 30 and 31 indicate the nature of variation with depth of vertical stress at the base level, q_f. At shallow depths (D/B < 4), q_f is equal to the overburden stress q; at greater depths (D/B > 15), q_f reaches a constant value independent of overburden stress.

In a similar way, curves in Figures 34 and 35 indicate the variation of average vertical stress along foundation shaft q_s with foundation depth. From the shape of these curves it may be concluded that the distribution of vertical stresses q_z at any point z along the shaft must follow a curve similar to that in Figure 42c; namely, there should be a linear increase of q_z along a certain depth z_o, followed by a peak and gradual decrease to the final magnitude q_f. It is to be understood, however, that the foundation depth, sand density and some other factors may have influence on the shape of curves in question. Therefore, the peak mentioned may be more or less pronounced, or even nonexisting, leading to q_z curves of shapes between those in Figures 42c and 42b.

Looking for an explanation of this general trend of variation of q_z with depth, it was concluded that the nonlinear increase of bearing capacity with depth could be attributed to "arching" in sand above the foundation base. There exists, indeed, a striking similarity between curves in Figure 42 and curves of vertical pressure in a mass of sand above a yielding horizontal support (6, Fig. 18d).

On the basis of all the observations made, the following explanation of stress conditions around a deep foundation is suggested: When the foundation is loaded (Fig. 42a) the mass of sand beneath is compressed downward. At the same time sand around the foundation tends to follow the general downward movement of the mass. As a consequence of this, the originally horizontal stresses on a vertical plane n-n at a certain distance from the foundation become inclined. The inclination of these stresses is a function of the amount of displacement w of the foundation and of the distance z′ from the base level. If the foundation depth D is great enough, and if the base displacement w remains limited, there may be a distance z_o' beyond which the effect of downward movement is not felt any more. Above that distance stresses on vertical planes may remain horizontal, and the vertical stress q_z may be equal to overburden stress q.

The following arguments can be added in support of the explanation:

1. Measurements of displacements of sand surface during loading tests on foundations placed at greater depth (D/B > 8) showed downward movement of soil adjacent to the foundation.

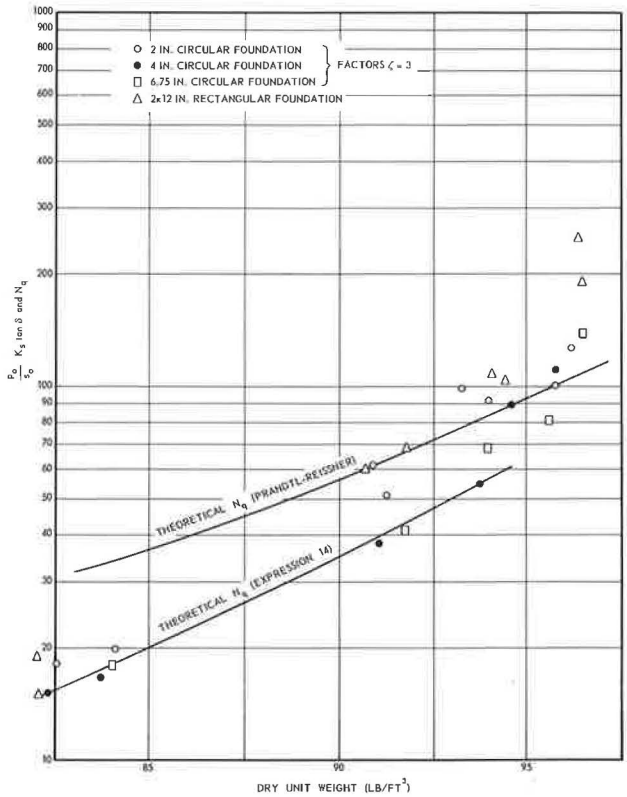

Figure 41. Bearing capacity factors at greater depth.

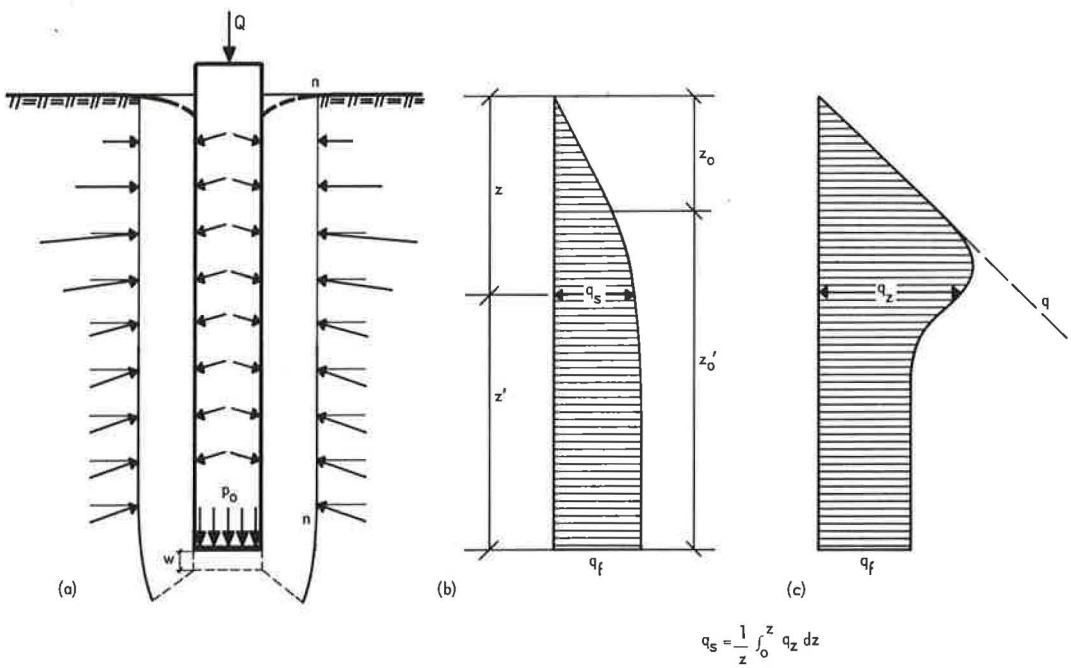

$$q_s = \frac{1}{z}\int_0^z q_z\,dz$$

Figure 42. Stress distribution around a deep foundation in sand.

2. Measurements of sand density around the foundation after load testing to failure indicated, in the case of models made of dense sand, considerable loosening in a zone immediately above base level, but a slight densification below that level.

3. Final resistances of the base and skin of rectangular foundations are found to be 1.50 times lower than corresponding resistances of circular foundations of the same diameter. However, measurements of real shape factor for base and skin resistances at greater depth indicate values of approximately 3. This leads to the conclusion that the final vertical stresses q_f around rectangular foundations are two times higher than corresponding stresses around circular foundations. The same ratio of final vertical stresses is found in the case of rectangular versus circular bins of the same diameter, where a similar phenomenon of arching occurs.

4. Under similar conditions there is less arching under smaller foundations, resulting in higher bearing capacity for the same relative depth D/B, because base displacements at failure increase proportionally to the foundation width. Displacement of a larger foundation will mobilize friction along relatively longer distance z_o.

5. Measurements of skin resistance along model foundations in sand have indicated distributions similar to curves in Figure 42 (38, 39).

Numerous other observations on actual deep foundations as well as on models can be cited in favor of the explanation offered. However, it should be realized that the problem in question is very complex, and that variables such as roughness of foundation skin or method of construction may also be of significant influence.

A special study of this problem, including the development of a method for rational analysis of stresses around deep foundations in a homogeneous sand stratum is in progress.

CONCLUSIONS

1. Shear patterns observed underneath buried model foundations in sand indicate that, depending on relative density of sand, all three types of failure previously described in the literature may occur at shallow depth: general shear failure, local shear failure and punching shear failure. However, at greater depths only punching shear failure occurs, irrespective of relative density of sand. Limits of types of failure to be expected vary with relative density or compressibility as well as with relative depth D/B of the foundation (Fig. 27).

2. At shallow depths, not exceeding four foundation widths ($D/B < 4$) the increase of point bearing capacity with depth is linear. In dense sand ($D_R > 0.70$) the bearing capacity factor N_q can be estimated with sufficient accuracy using an analysis based on conventional theory of general shear failure in a rigid-plastic solid. In loose or medium-dense sand, failure surfaces being localized, better agreement with test results may be stated if an expression for N_q derived under the assumption of local or punching shear failure is used.

3. At greater depths, generally exceeding 15 foundation widths, both base resistance p_o and skin resistance s_o reach constant final values. These values are independent of overburden pressure q and appear to be functions of relative density of sand only. This is explained by the arching of sand above the foundation base. It is demonstrated that both p_o and s_o are proportional to the effective vertical stress at failure, q_f at the level of foundation base.

4. The bearing capacity factory N_q at greater depth, defined as the ratio of base resistance p_o to vertical stress q_f, is practically independent of foundation size and is a function of relative density or angle of internal friction of sand. Observed bearing capacity factors N_q for long rectangular foundations at greater depth do not differ from those at shallow depth. However, the shape factor for circular foundations appears to be somewhat higher at greater depths.

5. Skin resistance along the foundation shaft is not necessarily increasing linearly with depth. Instead, it is proportional to the vertical stress q_z at the corresponding elevation. Vertical stress increases linearly only at shallow depths. If the foundation is deeply embedded in sand, the distribution of vertical stress, as well as of skin resistance, is likely to be similar to that in Figure 42.

6. The fundamental fallacy of conventional analyses of bearing capacity of deep foundations in sand consists in the assumption that q is always equal to the initial overburden stress at the level of foundation base. This may be correct if a deep foundation penetrates only slightly into a sand stratum overlain by compressible soil. However, it may be entirely wrong if a deep foundation is completely embedded in sand.

ACKNOWLEDGMENTS

The tests described in this paper have been performed in the Soil Mechanics Laboratory of Georgia Institute of Technology, Atlanta, Georgia. The investigation is being sponsored by the State Highway Department of Georgia and the U. S. Bureau of Public Roads. Thanks are due to officials of these institutions for their interest and support. The pile testing area has been constructed and equipped using funds allocated by the Engineering Experiment Station, Georgia Institute of Technology. The contributions of McKinney Drilling Company and Armco Drainage & Metal Products, Inc., are gratefully acknowledged.

The author is indebted to James M. Duncan, Don C. Banks, and Ray L. Holmes, Graduate Research Assistants, who assisted in construction of equipment and performed the loading tests. Special credit is due to Guillermo Restrepo, Graduate Student, for preparation and testing of two models with colored sand. Graduate Research Assistants, O. S. Lord, R. C. Williams, and W. L. Boyd, as well as Student Assistants, T. W. Russell, D. E. Hodges, and Houshang Rahimzadeh, also gave much valuable help in different phases of the project.

Finally, the author wishes to express his thanks to Robert E. Stiemke, Director of the Engineering Experiment Station, for his help and encouragement in the early stages of the project. He is also grateful to Mrs. Milena A. Sedmak Vesić for her interest and assistance in preparation of diagrams.

REFERENCES

1. Prandtl, L., "Uber die Harte plastisher Korper." Nachrichten Kon. Gesell. der Wissenschaffen, Math. Phys. Klasse, 74-85, Gottingen (1920).
2. Prandtl, L., "Uber die Eindringungsfestigkeit plastisher Baustoffe und die Festigkeit von Schneiden." Zeitschrift fur Angewandte Mathematik und Mechanik, 1: 1, 15-20 (1921).
3. Reissner, H., "Zum Erddruckproblem." Proc. First Intern. Conf. Applied Mech., 295-311, Delft (1924).
4. Caquot, A., "Equilibre des massifs a frottement interne." Gauthier-Villars, Paris (1934).
5. Buisman, A. S. K., "De weerstand van paalpunten in zand." De Ingenieur, 50: 25-28, 31-35 (1935).
6. Terzaghi, K., "Theoretical Soil Mechanics." Wiley (1943).
7. De Beer, E. E., "Donnees concernant la resistance au cisaillement deduites des essais de penetration en profondeur." Geotechnique, 1: 22-40 (1948).
8. De Beer, E. E., " Etude des fondations sur pilotis et des fondations directes." Annales des Travaux Publics de Belgique, 46: 1-78 (1945).
9. Jaky, J., "On the Bearing Capacity of Piles." Proc., Sec. Intern. Conf. Soil Mech. and Found. Engg., 1: 100-103, Rotterdam (1948).
10. Meyerhof, G. G., "The Ultimate Bearing Capacity of Foundations." Geotechnique, 2: 301-332 (1951).
11. Meyerhof, G. G., "Recherches sur la force portante des pieux." Annales de l' Institut Technique du Batiment et des Travaux Publics, 6: 63-64, 371-374 (1953).
12. Berezantsev, V. G., "Osesimetrichnaia zadacha teorii predel 'nogo ravnovesia sypuchei sredy." Gostechizdat, Moscow (1952).
13. Bishop, R. F., Hill, R., and Mott, N. F., "The Theory of Indentation and Hardness Test." Proc. of the Physical Soc., 57: 147-159 (1945).
14. Gibson, R. E., Discussion. Jour. Instit. of Civil Engineers, 34: 382 (1950).

15. Skempton, A. W., Yassin, A. A., and Gibson, R. E., "Theorie de la force portante des pieux." Annales de l'Institut Rechnique du Batiment et des Travaux Publics, 6: 63-64, 285-290 (1953).
16. Ladanyi, B., "Etude theorique et experimentale de l'expansion dans un sol pulverulent d'une cavite presentant une symetrie spherique ou cylindrique." Annales des Travaux Publics de Belgique, 62: 105-148, 365-406 (1961).
17. Brinch Hansen, J., "Simple Statical Computation of Permissible Pile Loads." Christiani and Nielsen Post, 14-17 (1951).
18. Caquot, A., and Kerisel, J., "Traite de Mecanique des Sols." 3rd edit. Gauthier-Villars, Paris (1956).
19. Brinch Hansen, J., "A General Formula for Bearing Capacity." Danish Technical Institute, Bull. 11, Copenhagen (1961).
20. Delft Soil Mechanics Laboratory, "The Predetermination of the Required Length and the Prediction of the Toe Resistance of Piles." Proc. Intern. Conf. on Soil Mech. and Found. Engg., I: 181-184, Cambridge, Mass. (1936).
21. Plantema, G., "Results of a Special Loading Test on a Reinforced Concrete Pile." Proc. Sec. Intern. Conf. Soil Mech. Found. Engg., IV: 112-118, Rotterdam (1948).
22. Huizinga, T. K., "Application of Results of Deep Penetration Tests to Foundation Piles." Building Research Congress, 173-179, London (1951).
23. Van der Veen, C., "The Bearing Capacity of a Pile." Proc. Third Int. Conf. Soil Mech. Found. Engg., II: 84-90, Zurich (1953).
24. Van der Veen, C., and Boersma, L., "The Bearing Capacity of a Pile Predetermined by a Cone Penetration Test." Proc. Fourth Intern. Confer. on Soil Mech. and Found. Engg., II: 76-78, London (1957).
25. Bogdanovic, Lj., "The Use of Penetration Tests for Determining the Bearing Capacity of Piles." Proc. Fifth Intern. Confer. Soil Mech. Found. Engg., II: 17-22, Paris (1961).
26. Geuze, E. C. W. A., "Resultats d'essais de penetration en profondeur et de mise en charge de pieux." Annales de l'Institut Technique du Batiment et des Travaux Publics 6: 63-64, 313-319 (1953).
27. De Beer, E. E., "Les essais de penetration en profondeur." Unpublished lecture, Yugoslavia (1955).
28. Kahl, H. and Muhs, H., "Uber die Untersuchung des Baugrundes mit einer Spitzendrucksonde." Die Bautechnik, 29: 81-88 (1952).
29. Kerisel, J., "Deformations et contraintes au voisinage des pieux." Bull. 10, A. B. E. M., Brussels (1953).
30. L'Herminier, R., "Remarques sur le poinconnement continu des sables et graviers." Annales de l'Institut Technique du Batiment et des Travaux Publics, 6: 63-64, 371-374 (1953).
31. Berezantsev, V. G., "Raschet prochnosti osnovania sooruzhenii." Gosstroiizdat, Ch. III, Moscow (1960).
32. Kerisel, J., "Foundations profondes en milieu sableux." Proc., Fifth Intern. Confer. Soil Mech. Found. Engg., II: 73-83, Paris (1961).
33. Hansen, Bent, and Odgaard, D., "Bearing Capacity Tests on Circular Plates on Sand." Danish Technical Institute, Bull. 8, 19 pp., Copenhagen (1960).
34. De Beer, E. E., and Vesić, A. B., "Etude experimentale de la capacite portante du sable sous des foundations directes etablies en surface." Annales des Travaux Publics de Belgique, 59: 3, 5-58 (1958).
35. De Beer, E. E., and Ladanyi, B., "Etude Experimentale de la capacite portante du sable sous des fondations circulaires etablies en surface." Proc. Fifth Intern. Confer. Soil Mech. Found. Engg., I: 577-585, Paris (1961).
36. Caquot, A., and Kerisel, J., "Sur le terme de surface dans le calcul des fondations en milieu pulverulent." Proc. Third Intern. Confer. Soil Mech. Found. Engg., I: 336-337, Zurich (1953).
37. L'Herminier, R., Habib, P., Tcheng, Y., and Bernede, J., "Fondations superficielles." Proc. Fifth Intern. Confer. Soil Mech. Found. Engg., I: 713-717, Paris (1961).

38. Zweck, H., "Mesures sur modeles reduits du frottement lateral et de la resistance de pointe des pieux." Annales de l'Institut Technique du Batiment et des Travaux Publics, 6: 63-64, 367-370 (1953).
39. Habib, P., "Essais de charge portante de pieux en modele reduit." Annales de l'Institut Technique du Batiment et des Travaux Publics, 6: 63-64, 361-366 (1953).

Dynamic Phenomena in Layered Structures

A. AVRAMESCO, Central Bridge and Highway Laboratory, French Ministry of Public Works, Paris, France

Much experimental and theoretical work is being done in France related to the application of vibration techniques to road structures. This paper is concerned with the approach through the theory of elasticity. An analysis is offered of some special cases of dynamic phenomena in layered systems, so as to bring forth some simple and general rules, and allow a rough interpretation of the experimental results. Among these phenomena are (a) in a semi-infinite medium, the dynamic effects due to a transient vehicle (role of the Rayleigh wave), (b) free waves in layered systems (namely, one layer on subgrade) when the Lamć's parameters of the two materials are in some characteristical ratios (Rayleigh waves), and (c) one or two layers on subgrade (some remarks on Love waves). The results thus obtained can be explained by the reflection and refraction theory of elastic waves allowing generalization to any member of layers. The paper also discusses some ideas on the relative importance of static and specifically dynamic effects depending on the distance of the source of disturbance.

•THE PROBLEM that arises in the rational design of road structures consists, under given conditions of traffic, subgrade, economics, etc., is the choice of the most suitable among the available materials, and the evaluation of the layer thicknesses. To solve this problem, it is necessary:

1. To know which stresses take place in a theoretically given structure. Since the work of Jeuffroy and Bachelez (1) different methods (2, 3) have been used in France, that of Lattes et al., (4) being more adapted to the unavoidable numerical computations.
2. Conversely, to carry out tests on existing roads so as to find out which values of elastic parameters can be associated with each material used. The testing implies knowledge of some general rules relating the response of a road to the applied load.

The present paper deals with both these points, using the theory of free waves in layered structures to show how they permit specific description of dynamic effects, and then describing some of their general features.

SEMI-INFINITE ELASTIC MEDIUM

Transient Load—Theoretical Approach

The study of a load traveling at uniform speed was undertaken at first with the idea of quantitatively comparing the resulting displacements and those of Boussinesq's solution in the corresponding static problem. Because it has been possible to give a completely explicit solution, and to find a material suitable for the experiment, this special case is dwelt on, although it is not characteristic of layered structures.

Paper sponsored by Committee on Stress Distribution in Earth Masses.

The method used to give the theoretical result is the well-known "superposition of solutions." Only the principal features of the analysis are indicated here, inasmuch as further details are given elsewhere (5, 6).

The problem is governed by the following equations:

$$(\lambda + \mu)\ \text{grad div}\ \vec{D} + \mu\, \Delta \vec{D} = d\, \frac{\partial^2 \vec{D}}{\partial t^2} \tag{1}$$

(equation of elasticity) in which λ and μ are Lamé's parameters, d is the density of the medium, $\vec{D}$ is the displacement vector, and t is time.

$$\sigma_{3j} = \lambda\ \text{div}\ \vec{D}\, \delta_{3j} + \mu \left(\frac{\partial u_3}{\partial x_j} + \frac{\partial u_j}{\partial x_3} \right) \tag{2a}$$

$$= -X_j\, \delta\,(x_1 - Vt,\ x_2) \quad \text{if } x_3 = 0 \tag{2b}$$

where Eq. 2a is the elastic relationship between stress and strain and Eq. 2b represents the boundary conditions, with x_1, x_2, x_3 being space coordinates (with origin 0 on the horizontal boundary plane, $0x_3$ vertical pointing downwards, $0x_1$ in the direction of the speed $\vec{V}$), u_1, u_2, u_3 the displacement components, X_1, X_2, X_3 the components of the assumed concentrated applied force, $\delta\,(x_1 - Vt,\ x_2)$ is Dirac's distribution, and δ_{3j} is Kronecker's delta.

In the following analysis x'_1 represents $x_1 - Vt$.

Note that

$$\delta\,(x'_1,\ x_2) = \frac{1}{4\pi^2} \lim_{L \to \infty} \iint_{V(L)} e^m\, da_1\, da_2$$

in which $V(L) = a_1^2 + a_2^2 < L^2$

and $\qquad M = i\,(a_1 x_1^1 + a_2 x_2)$

so that, if the displacements corresponding to

$$\sigma_{3j}^{(e)} = -\frac{x_j}{4\pi^2}\, e^m \quad \text{for } x_3 = 0 \tag{3}$$

are known, the solution of the problem is obtained by the superposition

$$\lim_{L \to \infty} \frac{1}{4\pi^2} \iint_{a_1^2 + a_2^2 < L^2} - - - \, da_1\, da_2$$

inasmuch as all the equations of the problem are linear.

If the elementary displacement is written in the form

$$\vec{D}^{(e)} = \overrightarrow{D_g} + \overrightarrow{D_r} \qquad \text{with} \begin{cases} D_g = \text{grad } g \\ D_r = \text{rot}^* \vec{R} \end{cases}$$

it is possible to choose:

$$g = -i\,C\,e^{i(a_1 x'_1 + a_2 x_2 + i\,c_g\,x_3)}$$

which gives $\overrightarrow{D_g}$, with

$$c_g = \left(a_1^2 + a_2^2 - d\,\frac{a_1\,V^2}{\lambda + 2\mu}\right)^{1/2} > 0$$

assuming $V^2 < \dfrac{\lambda + 2\mu}{d}$.

Also,

$$\overrightarrow{D_r} = \begin{cases} c_r\,A_1\,e^{i(a_1 x'_1 + a_2 x_2 + i c_r x_3)} \\ c_r\,A_2\,e^{i(a_1 x'_1 + a_2 x_2 + i c_r x_3)} \\ i\,(a_1 A_1 + a_2 A_2)\,e^{i(a_1 x'_1 + a_2 x_2 + i c_r x_3)} \end{cases}$$

with

$$c_r = \left(a_1^2 + a_2^2 - d\,\frac{a_1^2\,V^2}{\mu}\right)^{1/2} > 0$$

assuming $V^2 < \dfrac{\mu}{d}$. It should be noted that $\text{div } \overrightarrow{D_r} = 0$, which gives the term $+ i\,(a_1 A_1 + a_2 A_2)$.

In calculating the corresponding elementary stresses $\sigma_{3j}^{(e)}$ by Eq. 2a, and comparing the results with Eq. 3 for $x_3 = 0$, a linear system appears which determines C, A_1, A_2 (note that the use of c_g and c_r allows the elimination of the explicit use of λ, although this coefficient still plays a part through c_g).

This system is

$$2\,c_g\,a_1\,C + (a_1^2 + a_2^2)\,A_1 + a_1 a_2 A_2 = \frac{x_1}{4\pi^2\mu} \tag{4a}$$

$$2\,c_g\,a_2\,C + a_1 a_2 A_1 + (a_2^2 + c_r^2)\,A_2 = \frac{x_2}{4\pi^2\mu} \tag{4b}$$

---

*Curl.

$$(a_1^2 + a_2^2 + c_2^2)\, C + 2 c_r\, (a_1 A_1 + a_2 A_2) = - \frac{i x_3}{4 \pi^2 \mu} \qquad (4c)$$

The determinant of this system, to within a positive factor, is

$$f(\zeta^2) = 4 \left(1 - \frac{\zeta^2}{\Omega_g^2}\right)^{1/2} \left(1 - \frac{\zeta^2}{\Omega_r^2}\right)^{1/2} - \left(2 - \frac{\zeta^2}{\Omega_r^2}\right)^2 ,$$

$$\begin{cases} \zeta^2 = \dfrac{a_1^2 V^2}{a_1^2 + a_2^2} \\ \Omega_g^2 = \dfrac{\lambda + 2\mu}{d} \\ \Omega_r^2 = \dfrac{\mu}{d} \end{cases}$$

with $f(V_R^2) = 0$, V_R being the velocity of the Rayleigh wave,

Because $f(\zeta^2)$ is a factor in the denominator of C, A_1, A_2, and of the integrand in

$$\vec{D} = \lim_{L \to \infty} \iint_{a_1^2 + a_2^2 < L^2} D^{(e)}\, da_1\, da_2$$

$$\vec{D} \longrightarrow \infty \text{ if } V \longrightarrow V_R .$$

However, $\vec{D}$ can be calculated further, if $V < V_R$ (which is realized in all practical cases), by using the following change of variables:

$$x_1 = r \cos \alpha \qquad a_1 = \rho \cos \theta$$

$$x_2 = r \sin \alpha \qquad a_2 = \rho \sin \theta$$

The result, u_3, corresponding to a normal load (i.e., $X_1 = X_2 = 0$) (see Mandel and Avramesco (6) for generalization to u_1, u_2; X_1, $X_2 \neq 0$; non-concentrated load) is

$$u_3 = \frac{X_3}{2 \pi \mu r} \frac{\xi^2}{\Omega_r^2} \frac{\left(1 - \dfrac{\xi^2}{\Omega_g^2}\right)^{1/2}}{f(\xi^2)} \quad \text{with } \xi = V \sin \alpha$$

of which an approximate value, when $\xi / \Omega_r \ll 1$, may be obtained from

$$u_3 = \frac{x_3}{4 \pi \mu r} \frac{\lambda + 2\mu}{\lambda + \mu} \left[1 + \frac{\xi^2}{4 \Omega_r^2} \left(1 - 3x + \frac{2}{1x}\right) + \ldots\right]$$

These results are discussed under "Dynamic Effects" and compared with those of the experiment described in the following.

Transient Load—Experiment

Realization of an experiment giving evidence of the interference of Rayleigh's wave velocity faces two main difficulties: (a) On ordinary materials, the speeds that are to be reached are much too great; and (b) It is necessary to follow the phenomenon under a moving load.

Materials on which V_R is very low are found easily enough: they are rubbers and gelatines. Rubbers are discarded as really viscoelastic or nonhomogeneous.

An ordinary gelatine can be chosen, however, that is simple to prepare and for which different Young's moduli can be obtained by adding more or less water to a kind of glue.

The second difficulty is solved by the use of a special type of container (Fig. 1) which rotates while a ball attached to the end of a fixed rod runs on the surface of the gelatine. The gelatine is some 15 cm thick, which is sufficient to considering the mass as "infinitely deep." A small electric motor drives the container at the various desired speeds.

This experiment, as well as that described under "Free Waves," was suggested by Mr. Habib, Associate Director, Solid Mechanics Laboratory, Ecole Polytechnique, Paris.

As the speed of rotation increases, the part of the surface deformed under the ball becomes more and more important, although rather slowly, spreading especially in the direction perpendicular to $\vec{V}$. When the speed V_R is reached a shock wave appears, slightly distorted because the speed is not the same at the different distances from the center of rotation. If V is further increased, the well-known aspect of Mach's angle appears (Fig. 2), with

$$\varphi = \arcsin \frac{V_R}{V}$$

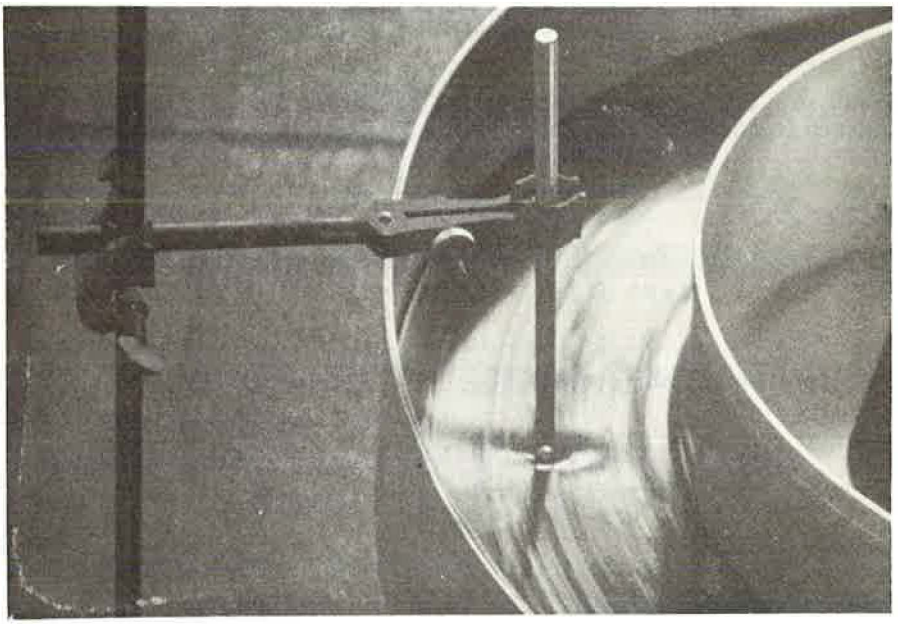

Figure 1.

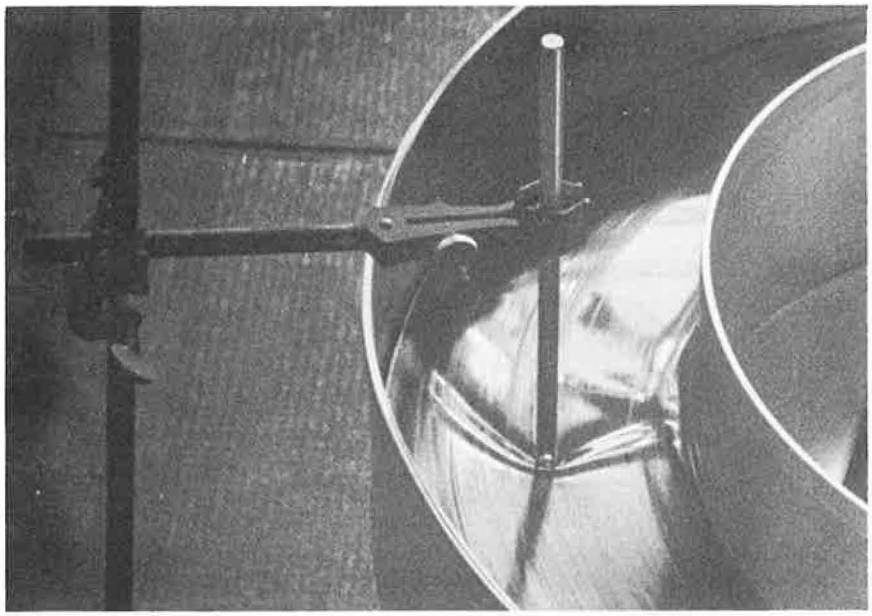

Figure 2.

The velocity, V_R, is of the order of 1.5 m/sec in the gelatine used. The measures of its Young's modulus by static methods give fairly good corresponding values to the V_R observed.

Dynamic Effects

First, the agreement between theory and experiment, except for the a priori evident interference of viscosity, should be noted. That is, if $V \longrightarrow V_R$, $\vec{D}$ is greatly increased, but does not become infinite. The experiment also shows that the important variations of $\vec{D}$ take place when V is not much less than V_R.

Figure 3 gives the theoretical results concerning u_3 for the Poisson's ratio $\nu = \frac{1}{4}$. For instance, an increment of some 7 percent of the static displacement is found for $V = 0.75\ \Omega_r$ (V_R is of the order of $0.9\ \Omega_r$). The approximate value given at the end of the section on "Transient Load—Theoretical Approach," which is fairly accurate in practical analysis, shows the small influence of the Poisson's ratio: the factor of $\xi^2 / 4\Omega_r^2$ is 3 for $\nu = \frac{1}{2}$ ($x = 0$) and $\nu = \frac{1}{4}$ ($x = \frac{1}{3}$), and varies little for $\nu \in [0, \frac{1}{2}]$.

It must be remembered that on ordinary subgrades the Rayleigh wave velocity is very seldom less than 100 m/sec (360 km/hr).

It is then possible to consider either that (a) no effect due to such a movement of a load will appear, and that this is some evidence that specifically dynamic effects may not be important in stress distributions, or that (b) this is evidence of the role of free waves, producing important deformations far from the source of disturbance.

It is certainly of mainly academic in-

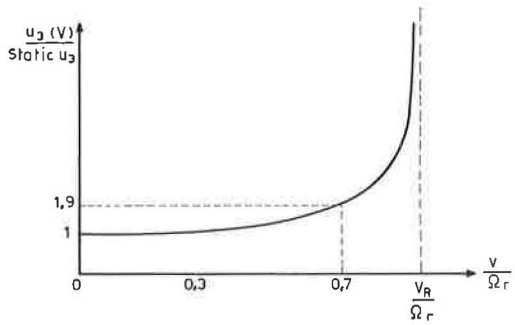

Figure 3.

terest by now to analyze this generation of a Rayleigh shock wave. But in layered systems, Rayleigh wave velocities are not always so large, and it is important to observe how, in this case, dynamic effects are closely connected to the existence of free waves.

The problem of the transient load on a semi-infinite homogeneous elastic medium has been solved. As for the vibrating load, different attempts have been made (2, 7, 8) that are not satisfactory, at least because they imply difficult computations or an implicit form of the results. However, many experiments have been carried out. They use two different kinds of apparatus—light or heavy—permitting one or several results (velocity, strains). These experiments are the same for a semi-infinite medium and for several layers, and the apparatus and methods are described in under the heading "Attempts at Generalization."

A complete program of experiments is being carried out with a light vibrator at the Polygone d'Essais du Laboratoire des Ponts-et-Chaussees in Rouen. The purpose of the first tests has been to determine some fundamental characteristics of the "subgrade"; that is, if it can be considered to be (a) homogeneous in both the horizontal and vertical directions, and (b) "semi-infinite" (i.e., if important disturbances are created by the underlying natural soil or by the cement blocks of the pit banks). These tests are important because they give evidence as to whether or not the theory of the Rayleigh wave can be applied.

A silty clay 1.5 m deep gives results as near to the theoretical result (V_R = constant for the different frequencies) as can be wished, for a chosen point at the surface. The horizontal homogeneity also can be considered as very good. No disturbances are created by the pit banks, inasmuch as the results are identical along all the axes of measurements (Fig. 4). The points at which the phase is the same as, or the opposite of, a certain reference, give the sequence of half wavelengths.

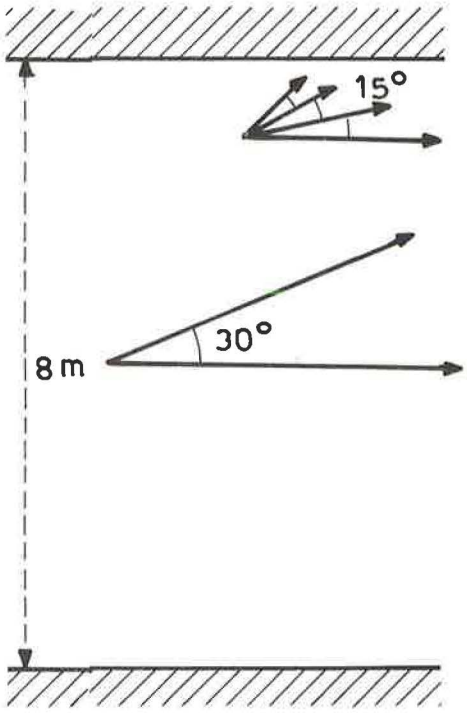

Figure 4.

FREE WAVES

One Layer on Subgrade--Rayleigh Waves

Many theoretical analyses and experimental computations have been carried out on the subject of free elastic waves in layered systems (9, 10). For the special case of one layer on a semi-infinite homogeneous subgrade, the author previously has provided an analysis (11). Some results of this last work are first reviewed, then are somewhat generalized in a following section.

The symbols of the previous section are still used, with λ and μ being Lamé's parameters, d the density of the medium, and

$$\Omega_g = \left(\frac{\lambda + 2\mu}{d}\right)^{1/2} \qquad \Omega_r = \left(\frac{\mu}{d}\right)^{1/2}$$

In the following the prime ($'$) refers to the subgrade. The equation of elasticity (Eq. 1) still holds in the different media and there is "perfect friction" on the horizontal plane between the surface, L, and the subgrade, L$'$; that is,

$$\left.\begin{aligned} \sigma_{3j}(L) &= \sigma_{3j}(L') \\ \mu_i(L) &= \mu_i(L') \end{aligned}\right\} \text{ on this plane} \quad (i, j = 1,2,3) \tag{6}$$

V is now the velocity of a free wave, measured at the free surface S of L, and N and l are the associated frequency and wavelength, respectively. It must be borne in mind that a free wave is (a) from the mathematical point of view, a solution of the equations of elasticity (Eq. 1) and continuity (Eq. 6) corresponding to $\sigma_{3j} = 0$ on S, and (b) from the physical point of view, a wave transmitted by the media in such a way that there is no downward-running energy. It also must be remembered that in layered media the wavelength of a free wave depends on its velocity—the frequency being then given by $N = V/l$—which is not true for a semi-infinite homogeneous medium (see "Semi-Infinite Elastic Medium,") in which V = constant $= V_R$ for any l.

If the reduced shear moduli are the same for L and L′ (that is, $\mu/d = \mu'/d'$) it is possible to show that $V \in [V_R, V'_R]$, in which V_R and V'_R are, respectively, the Rayleigh wave velocity in a semi-infinite homogeneous medium on its own with the same parameters as L and L′. Furthermore,

$$f(V_R^2) = 0 \qquad f'(V'^2_R) = 0$$

(see II. A for definition of f).

b) - as a priori evident

$$l \longrightarrow 0 \Longrightarrow V \longrightarrow V_R$$

$$l \longrightarrow \infty \Longrightarrow V \longrightarrow V'_R$$

which simply means that if the wavelength is very small (resp. great), it appears as if L (resp. L′) interfered alone and were semi-infinite.

It is remarkable that in this special case V lies between the two ordinary Rayleigh wave velocities, a simple result which unfortunately does not hold in general, as shown in the following.

If it is assumed that $\lambda' = \mu' = 0$, Lamb's solution is obtained (12) with, again,

$$l \longrightarrow 0 \Longrightarrow V \longrightarrow V_R$$

But there is at least one free wave for any V, one if $V^2 < \mu/d$, an infinity if $V^2 > \mu/d$.

When V and l tend to infinity the asymptotic frequencies are

$$N_g = k\,\frac{\Omega_g}{2p}$$

$$N_r = k\,\frac{\Omega_r}{2p}$$

in which k is any positive integer and p is the thickness of L.

The interpretation of this last result is simple: if V is the measured velocity of a free wave, there is between the ray perpendicular to the corresponding S = wave (resp. P = wave) transmitted in the medium, and S an angle

$$\varphi = \arccos \frac{\Omega_r}{V}$$

$$\left(\text{resp.} \quad \alpha = \arccos \frac{\Omega_g}{V}\right)$$

$$V \longrightarrow \infty \Longrightarrow \varphi \longrightarrow \frac{\pi}{2} \left(\text{resp. } \alpha \longrightarrow \frac{\pi}{2}\right)$$

and the analysis is then that of a stationary shear wave (resp. P-wave) perpendicular to the limiting free planes:

$$k \frac{l}{2} = p \quad \text{and since} \quad l = \frac{\Omega_R}{N_R} \left(\text{resp. } \frac{\Omega_g}{N_g}\right)$$

$$N_r = k \frac{\Omega_r}{2p} \left(\text{resp. } k \frac{\Omega_g}{2p}\right)$$

If λ' and $\mu' \longrightarrow \infty$,

$$l \longrightarrow 0 \Longrightarrow V \longrightarrow V_R$$

but here

$$V \geq V_R$$

with one solution l if $V^2 < \mu/d$, and an infinity if $V^2 > \mu/d$.

When V and $l \longrightarrow \infty$, the asymptotic frequencies are

$$N_g = (2k + 1) \frac{\Omega_g}{4p}$$

$$N_r = (2k + 1) \frac{\Omega_r}{4p}$$

which stand between those of the case examined in the previous section, as is evident because the lower limiting plane is now fixed.

The experiments of the transient load have been carried out for this case under conditions similar to those described under "Transient Load—Experiment." Some important points are as follows:

1. The theoretical approach is analogus to the method discussed in an earlier section, but it only leads to integrals, representing the displacements, which it so far has not been possible to calculate more explicitly.
2. A first experiment in which the thickness of gelatine varies under the running ball allows comparison of the corresponding phenomena and shows that several attenuated waves appear behind the first shock wave when $V \gg V_R$ and when the thickness is small enough.
3. The second experiment, with a small thickness of gelatine, shows that these typical attenuated waves are reflections of the initial one on the rigid surface of the "subgrade" (the container), under the gelatine.

Attempts at a Generalization

The interpretation of these rather different results is given by applying the general theory of reflection and refraction of elastic waves, the elements of which have been set forth by Sommerfeld (13) and with more or less further details elsewhere (9, 10, 11). This theory allows a generalization to more complex problems.

The results are given below without proofs, although these are sometimes quite simple:

1. Let J be the incident wave on a plane S; P a reflected P-wave, P′ a refracted P-wave; S a reflected S-wave, S′ a refracted S-wave; Ω_g, and Ω_r the P- and S-wave velocities in L (resp. Ω'_g and Ω'_r) in which propagate J, P, and S (resp. P′ and S′). The angles perpendicular to S and perpendicular to the wave surface) are, respectively, α, α', φ, φ' for P, P′, S, S′.

2. If V is the velocity of a wave, measured on S,

$$\frac{\sin\alpha}{\Omega_g} = \frac{\sin\alpha'}{\Omega'_g} = \frac{\sin\varphi}{\Omega_r} = \frac{\sin\varphi'}{\Omega'_r} = \frac{1}{V}$$

3. To J, either P- or S-wave, there are four corresponding waves P, P′, S, S′.

4. If, for instance, $\Omega_g < \Omega'_r$, to a penetrating P-wave in L there may correspond in L′ either a penetrating S-wave if $\sin\alpha < \Omega_g/\Omega'_r$ (α being the angle of incidence) or an attenuating S-wave if $\sin\alpha > \Omega_g/\Omega'_r$.

5. When to a penetrating incident wave in L there are corresponding attenuating waves in L′, no energy is transmitted from L to L′.

6. Both fixed or a free surface are perfectly reflecting.

It is now possible to explain why in two previous sections free waves are found for any $V > \Omega_r$: in such cases no energy is transmitted from L to L′. On the contrary, another section shows that to any V there can be a corresponding penetrating S′, which implies loss of energy from L, and is therefore contradictory with the definition of a free wave.

This result can be generalized as follows:

If Ω'_r is the velocity of S-waves in the lower medium of an elastic stratified structure, Σ, no free waves can exist but those for which $V < \Omega'_r$.

A first corollary is that if Ω'_r is the lowest S-wave velocity of Σ all free waves are attenuating ones.

A second corollary is that, since Love waves are penetrating in at least one of the layers, no Love waves can exist if Ω'_r is the lowest S-wave velocity of Σ.

The range of velocities where the free waves of a road structure will be encountered, can therefore be restricted and an attempt could be made to develop it further—for instance, in order to explain why it is $[V_R, V'_R]$ only, when the reduced shear moduli are the same for L and L′, etc.

In fact, the usefulness of such a limitation is not evident, for even the basic theorem is not practically true; the experiments show, on the contrary, that velocities $V \gg \Omega'_r$ can be observed. Whether these correspond to free waves or not is discussed in the following.

Experiments on vibration techniques applied to testing of road structures have been carried out in two distinct ways:

1. The method worked out by the Shell Laboratory of Amsterdam (14) uses large loads (a few tons) and low frequencies (up to some 50 hertz). The results of the different measurements made in an experiment have not really been given a clear and general interpretation prior to this. The opinion of the author, who followed the results obtained with the Shell machine hired by the French Laboratoire Central des Ponts-et-Chaussees, is that the created waves are a rather complex interference of free and forced

waves; the problem of the vibrating load has not yet been solved even for a semi-infinite homogeneous medium, much less for a stratified structure. It is not to be expected, therefore, that experiments should receive a simple interpretation, and a better knowledge of the theoretical phenomena would make possible much more use of them.

2. The light apparatus used by the British Road Research Laboratory (15) naturally involves some difficulties. For instance, it is considered by Jones (15) that when the lower medium, L', has a low Young's modulus and a Poisson's ratio near 0.5, an equation giving correct results may be obtained by replacing L' by a liquid in the theoretical structure, without it being denied that this meets no clear justification. However, the information thus obtained (a) is in more than qualitative agreement with other measures and predictions; (b) has proved itself of great value as a testing method on road structures; and (c) is to the knowledge of the author the only one displaying such good qualities for dynamic testing and experiments on roads.

CONCLUDING REMARKS

Other Experiments

Free waves provide the best methods for understanding the general outline of dynamic behavior in road structures, as has been emphasized throughout this paper. In fact, other experiments using free waves can be imagined and have been tried in France. The loadings are in the form of impacts, produced for instance by means of a heavy load falling on a kind of stiff spring. It is difficult to foretell the value of these experiments, as they have no connection whatsoever with the ordinary knowledge of layered structures, and so call for an entirely new and distinct interpretation.

Other Problems

In the case of Lamb's solution (12) the free wave velocity can be very low; in reality λ' and μ' are never null; but, if the lower medium is "soft enough" (low Young's modulus and Poisson's ratio really different from 0.5), the vehicle speed V_S may be great enough to bring about very important dynamic effects. This is especially true if one certain frequency is associated to V_S (ordinary loads being in fact both transient and vibrating). It may be that such an occurrence only seldom arises; however, a road does not fail only by ordinary light traffic, but also by such dangerous (and, if the road is well built, rare) interactions.

It must also be borne in mind that:

1. Free waves extend the field of interaction of the load; they can exist, by definition, anywhere under a free surface.
2. They certainly exist alone at the free surface far enough from the load, inasmuch as the remainder of the dynamic energy must have disappeared in the subgrade.
3. They correspond to the "resonances" of finite media.

These are some reasons why dynamic phenomena and free waves are so closely connected: because free waves, as easily propagating, are both the most dangerous and the most easily observed. Exactly what part they play in the real stresses and failures of roads cannot yet be described quantitatively.

REFERENCES

1. Jeuffroy, G., and Bachelez, J., "Essai d'explication methodique des experiences du WASHO." R.G.R. 308 (Sept. 1957).
2. Davin, M., "Etudes sur le comportement dynamique des sols stratifies." Mai-Juin 1958 des Ann. des Ponts-et Chaussees (Paris) (Mar.-Apr. and May-June 1958).
3. Bastiani, A., "The Explicit Solution of the Equations of the Elastic Deformations for a Stratified Road Under Given Load in the Dynamic Case." Internat. Conf. on Struct. Design of Asphalt Pavements, Univ. of Michigan, Ann Arbor, Mich.

4. Lattes, R., Lions, J.L., and Bonitzer, J., "Use of Galerkin's Method for the Study of Static and Dynamic Behavior of Road Structures." Internat. Conf. on Struct. Design of Asphalt Pavements, Univ. of Michigan, Ann Arbor, Mich.
5. Mandel, J., and Avramesco, A., "Deplacements produits par une charge mobile a la surface d'un semi-espace elastique." Compt.-rend. de l'Acad. Sc. 252: 3730-3732 (Paris).
6. Mandel, J., and Avramesco, A., "Deplacements produits sur un semi-espace elastique par une charge en mouvement rectiligne uniforme." To be published in Ann. des Ponts-et-Chaussees (Paris).
7. Byatt, W.J., and de Vault, G.P., "Mathematical Problems in Seismology." SC 4542 - TID 4500, Sandia Corp., Albuquerque, N.Mex., (1961).
8. de Hoop, T., Communication au Colloque international sur la propagation des ebranlements dans les milieux heterogenes (Marseille, Sept. 1961); colloques internationaux du C.N.R.S., 111, Paris (1961).
9. Ewing, W.M., Jardetzky, W.S., and Press, F., "Elastic Waves in Layered Media." McGraw-Hill, N.Y. (1957).
10. Brekhovskikh, L.M., "Waves in Layered Media." (Translated from Russian) Academic Press, N.Y. (1960).
11. Avramesco, A., "Etude de certaines ondes elastiques dans les milieux stratifies." To be published in Ann. des Ponts-et-Chaussees (Paris).
12. Lamb, H., Proc., Royal Soc. of London, A 93: 116 (1916).
13. Sommerfeld, A., "Mechanics of Deformable Bodies." Academic Press, N.Y. (1950).
14. Heukelom, W., Communication au Colloque international sur la propagation des ebranlements dans les milieux heterogenes (Marseille, Sept. 1961); colloques internationaux du C.N.R.S., 111, Paris (1961).
15. Jones, R., "Measurement and Interpretation of Surface Vibrations on Soil and Roads." HRB Bull. 277, pp. 8-29 (1960).

Bearing Capacity of Flexible Pavements Subject to Frost Action

BENGT B. BROMS, Associate Professor of Civil Engineering, Cornell University

The bearing capacity of flexible pavements is reduced considerably during the spring break-up period partly by reduction in relative density of the subgrade material as a result of frost action, partly by the saturation of the soil caused by thawing and partly by excess pore pressure resulting from the incomplete reconsolidation of the subgrade.

A method has been developed by which the ultimate bearing capacity of flexible pavements can be evaluated. This method is based on the assumption that the subgrade soils are fully saturated and that the wheel loads causing failure are applied so rapidly that no change in water content takes place during loading.

The calculated ultimate bearing capacity has been compared to that determined by a method proposed by Linell. Good agreement was found between the two methods.

•THE BEARING CAPACITY of flexible highway or airfield pavements is reduced considerably during the spring break-up period. Consequently it is often necessary to reduce drastically the allowable wheel or axle loads during this period in order to protect these pavements from damage. These restrictions on highway traffic often cause considerable economic hardship to the users. The present methods (1, 2) of estimating the maximum wheel or axle loads that can safely be allowed on pavements are based mainly on experience gained from observations of the behavior of similar pavements constructed on similar types of soils and subjected to similar loading conditions. The collection of field data and their interpretation are extremely tedious and difficult, but necessary.

Furthermore, the empirical methods presently available can only be used for conditions similar to those from which the methods were derived. It is difficult to calculate accurately the bearing capacity of new types of pavements constructed outside the area where these empirical methods were developed or supported by soils with unusual characteristics and subjected to unusual types of loading. When the empirical must be extended, if the actual bearing capacity is grossly overestimated, then the allowable wheel or axle loads could cause extensive damage to the pavements. On the other hand, if the actual bearing capacity is grossly underestimated, then the corresponding restrictions could be unduly severe.

ASSUMPTIONS

The hypothesis presented in this paper, which predicts the bearing capacity of flexible pavements during the spring break-up period, is based on the assumptions that failure of the pavement is caused by the failure of subgrade, that the subgrade is saturated, and that the load causing failure is applied so rapidly that no changes in water content of the soil take place during the load application. The proposed analysis is therefore not

applicable to the case when failure takes place within the base or within the wearing courses.

During the spring break-up period, the ground-water table is often located close to the ground surface and it is believed that the condition of complete saturation is, as a rule, fulfilled. If, however, the subgrade is only partially saturated, the proposed analysis underestimates the actual bearing capacity of the soils and yields conservative results.

The water content of most soils does not change appreciably if the load causing failure is applied rapidly. The loading rate necessary to prevent changes in water content depends on the permeability and compressibility of the soil, viscosity of the pore water, and the boundary conditions. The permeability of the soil is the most important of these factors. If the subgrade consists of clean sand the permeability of the soil is, in general, so high that large changes in water content of the soil can take place even if the load is applied very rapidly. In this case, the proposed analysis underestimates the actual bearing capacity of the soil and the actual bearing capacity could be several times the calculated one.

Subgrades composed of clean sand are not, as a rule, subjected to frost action and no reduction in bearing capacity from this course generally takes place during the spring break-up period. The normal increases in the elevation of the ground-water table during the spring would, however, affect the bearing capacity as it affects the effective pressures in the subgrade.

The permeability of most subgrade soils is low; a small percentage of silt or clay size particles reduces their permeability greatly. Under these conditions even a load applied relatively slowly will only cause small changes of the water content of the soil. Thus it is believed that the rate of loading as caused by heavy vehicles moving at about 30 mph does not cause appreciable changes in the water content of the soil. If, however, these changes are large, the proposed analysis underestimates the bearing capacity of the subgrade and yields conservative results.

In general, the assumptions have been chosen to give a lower limit of the bearing capacity of pavements.

DISTRIBUTION OF PORE AND EFFECTIVE PRESSURES BELOW PAVEMENTS

The total pressure within a mass of soil is in general divided into effective pressure and pore pressure. The effective pressure is transmitted through the solid phase, whereas the pore pressure is transmitted through the liquid phase of the soil.

Figure 1 shows a cross-section through a road with a total thickness of wearing and base course equal to a. At a depth of $h_1 + h_2$ below the surface of the road the total vertical pressure, the sum of the effective pressure and the pore pressure, is equal to p_1. The total vertical pressure at any depth is equal to the weight of the overlying material, then

$$p_1 = h_1 \gamma_{wet} + h_2 \gamma_{sat} \tag{1}$$

in which γ_{wet} and γ_{sat} are the average wet and saturated unit weights of the base and the subgrade material, respectively. The wet unit weight is equal to the unit weight of the partially saturated material. The lateral total pressure p_2 is in general smaller than the corresponding vertical total pressure p_1 (3, 4, 5). Its value depends on the properties of the soil, method of compaction, and the subsequent stress-history of the soil. Relatively little is known of the effects of the lateral pressures on the pore pressures caused by sudden application of load (6).

The initial pore pressure u_0 is governed by the location of the ground-water table as shown in Figure 1. The ground-water table is assumed to be located within the base course at a depth h_1 below the ground surface. The pore pressure u_0 can be computed as

$$u_0 = h_2 \gamma_w \tag{2}$$

The vertical effective pressure $\bar{p}_1$ is equal to the difference between the total pressure

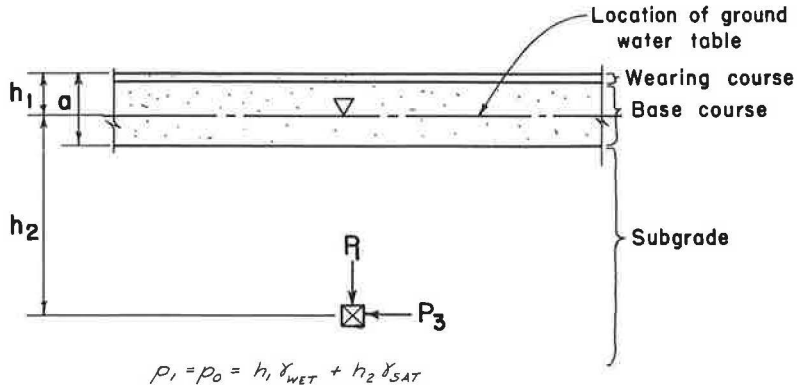

$p_1 = p_o = h_1 \gamma_{WET} + h_2 \gamma_{SAT}$

$p_3 \cong p_o = h_1 \gamma_{WET} + h_2 \gamma_{SAT}$

$u = h_2 \gamma_w$

$\bar{p}_1 = \bar{p}_o = h_1 \gamma_{WET} + h_2 \gamma_{SUB}$

$\bar{p}_3 \cong \bar{p}_o = h_1 \gamma_{WET} + h_2 \gamma_{SUB}$

γ_{WET} = Unit weight of the partially saturated pavement material.

γ_{SAT} = Saturated unit weight of base course or subgrade material.

γ_w = Unit weight of water

Figure 1. Stress distribution below flexible pavements.

and the pore pressure, then

$$\bar{p}_1 = h_1 \gamma_{wet} + h_2 \gamma_{sub} \quad (3)$$

where γ_{sub} is the submerged unit weight of the base and the subbase material. The lateral effective pressure equal to $K_o \bar{p}_1$ depends on the coefficient of lateral earth pressure at rest K_o. The value of K_o depends on the strength properties of the soil and on its stress history (7). (It is assumed in the following analysis that $K_o = 1.0$ in.)

The distribution of the initial total and effective stresses in any plane can be illustrated by means of Mohr's stress circles (Fig. 2). As it is assumed that the total and effective stresses are constant in all directions, the corresponding Mohr's stress circles for total effective stresses are points located at a distance p_o and $\bar{p}_o$ from the origin on the normal stress axis.

BEHAVIOR OF SOIL UNDER MOVING LOADS

Large excess pore pressures develop within the subgrade due to the application of moving load and the low permeability of the subgrade material. The pore pressures can be estimated by means of the pore pressure coefficients A and B if the loads are applied so rapidly that no change in water content takes place during the load application (7, 8, 9).

The wheel load causes an increase of the total all-around ambient pressure by dp_3 (Fig. 3). The portion of this pressure increase carried by pore pressure du_b is equal to the pore pressure coefficient B as expressed by

$$du_b = B dp_3 \quad (4)$$

The pore pressure coefficient B is equal to 1.0 for saturated soils (7, 10, 11). The total increase in ambient pressure is carried by an equal increase in pore pressure.

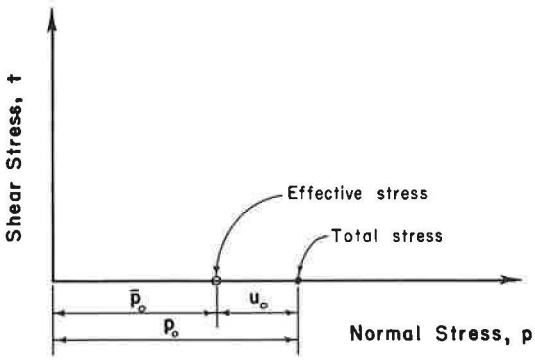

Figure 2. Mohr's stress circles for total and effective stresses.

The effective pressures in the soil are not, therefore, affected by a change of the total ambient pressures within a soil if the water content of the soil remains unchanged while the load increase is applied to the soil.

The applied load also causes an increase of the total deviator stress by $(dp_1 - dp_3)$. This deviator stress causes an increase of the pore pressure by du_a. The share carried by an increase in pore pressure for a saturated soil is equal to the pore pressure coefficient A, as expressed by

$$du_a = A\,(dp_1 - dp_3) \qquad (5)$$

Experiments have indicated that the pore pressure coefficient A at failure for a sandy or silty soil is mainly a function of the relative density of the soil. At failure, the coefficient A_f could be as low as -0.32 for a dense sand and as high as 0.08 for a loose sand (7, 11).

The total increase in pore pressure caused by a sudden increase in ambient and deviator pressure is $du_a + du_b$ (Fig. 3).

The distribution of total and effective stresses in any plane can be expressed at failure by means of Mohr's stress circles (Fig. 4). Failure of the soil takes place when the shear stress developed within a body of soil exceeds its shearing strength.

The shearing strength of a soil is governed by

$$s = c_s + \bar{p}_f \tan \phi_s \qquad (6)$$

in which c_s and ϕ_s are the apparent cohesion and apparent angle of internal friction of the soils as measured by the drained direct shear or triaxial test and $\bar{p}_f$ the effective normal pressure on the failure plane (13). The apparent cohesive strength c_s is equal to zero for sands, most silts, and normally consolidated clays (7). The apparent cohesive strength is larger than zero for compacted and for overconsolidated clays.

Failure of the soil takes place when the effective Mohr's stress circle is tangent to the envelop curve with a slope equal to ϕ_s. At the point of tangency the shear stress developed within the soil is equal to the shearing strength of the soil. The difference between the maximum and minimum principal stresses $(p_1 - p_3)_f$ at failure can be expressed in terms of the initial effective pressure p_o, the apparent angle of internal friction ϕ_s and the coefficient of lateral earth pressure at rest k_o, and the pore pressure coefficient A_f (7, 14) as follows:

$$(p_1 - p_3)_f = \frac{2p_o \sin \phi_3\,[K_o + A_f\,(1-K_o)]}{1 + (2A_f - 1)\sin \phi_s} \qquad (7)$$

This equation is derived on the assumption that c_s is equal to zero. The principal stress difference $(p_1 - p_3)_f$ depends only on the initial stress conditions ($\bar{p}_o$, k_o) and on properties of the soil (ϕ_s, A_f).

A saturated soil with low permeability and subjected to high rates of loading behaves as a frictionless material (7) with an undrained cohesive strength equal to the radius of the Mohr's stress circle as expressed by

$$c_u = \tfrac{1}{2}\,(p_1 - p_3)_f \qquad (8)$$

A loose saturated sand or silt with an angle of internal friction ϕ_s equal to 30° and a value of the pore pressure coefficient A_f and of the coefficient of lateral earth pressure at rest K_o of 0.08 and 0.5, respectively, has an apparent cohesive strength of $0.47\,\bar{p}_o$. The effective initial vertical pressure depends on the depth below the ground surface, the unit weight of the base course and the subbase material, and on the location of the ground-water table. For example, the apparent undrained cohesive strength C_u of loose saturated sand or silt is 88 psf at a depth of 2.0 ft below the ground surface if

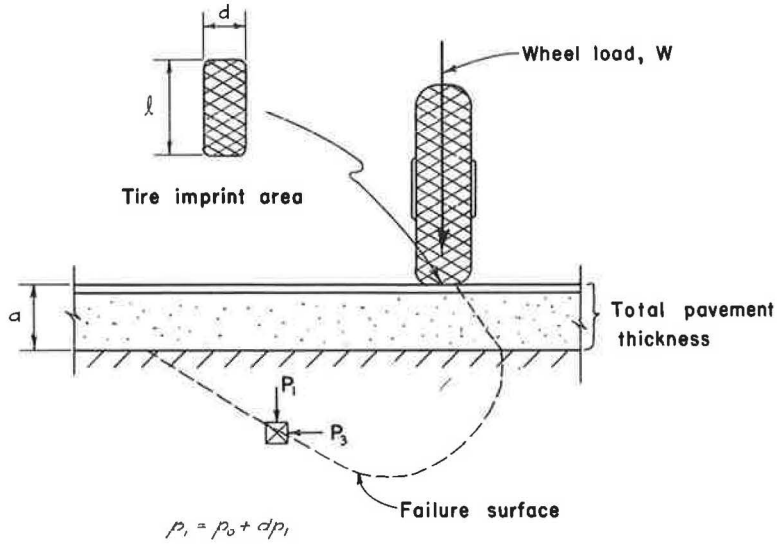

$$p_1 = p_o + dp_1$$

$$p_3 = p_o + dp_3$$

$$u = u_o + du_b + du_a$$

$$\bar{p}_1 = \bar{p}_o + dp_1 - du_b - du_a$$

$$\bar{p}_3 = \bar{p}_o + dp_3 - du_b - du_a$$

Where $du_b = B\,dp_3$

$$du_a = A(dp_1 - dp_3) = A(p_1 - p_3)_f$$

Figure 3. Stress increase caused by wheel loads.

the wet and saturated unit weight of the base course and subbase material are 120 and 130 psf, respectively, if the ground-water level is located at a depth of 1.0 ft below the ground surface, and if the thickness of the base course is also 1.0 ft.

The corresponding apparent cohesive strength of a dense sand or silt is 1,280 psf at the same depth with an angle of internal friction of 34^0 and a value of A_f and K_o equal to - 0.32 and 1.0, respectively.

The apparent cohesive strength of a soil in its dense state is therefore approximately fifteen times the undrained apparent cohesive strength of the same soil in its loose state. It can be seen that the pore pressure coefficient A_f has a large influence on the apparent cohesive strength of a soil.

EFFECTS OF FROST ACTION

It has been observed that soils containing even a small amount of fine-grained material are subjected to frost action. Horizontal bands or lenses of pure ice with variable thickness (15, 16) are formed within the frost-susceptible material and cause a volume expansion of the soil. These ice bands have a tendency to push apart the individual soil particle. When these ice lenses melt during the spring break-up period, the soil reconsolidates under the weight of the base and the wearing course. Static compression, however, is not very effective in compacting coarse-grained soils and the density of the reconsolidated material will be low. It is believed that frost action changes the relative density of the subgrade material from dense to loose, with a corresponding change of the apparent angle of internal friction and of the pore pressure coefficient A_f. The apparent cohesive strength of the subgrade is reduced to a fraction of its initial value during the spring break-up period with a corresponding reduction of its bearing capacity.

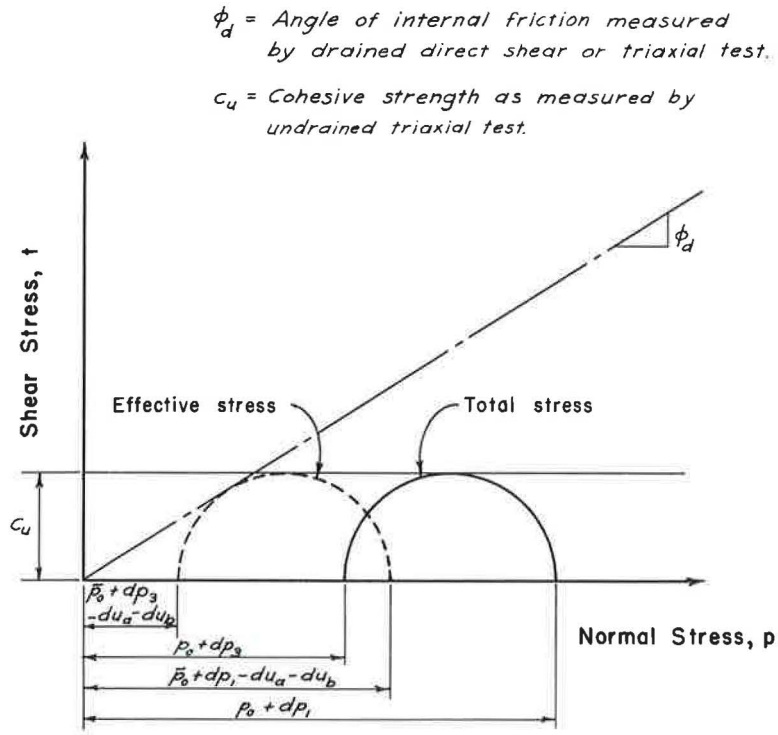

Figure 4. Mohr's stress circles at failure of the subgrade material.

Vibrations due to the moving traffic probably recompact the material in the subbase very effectively and after a few days of heavy traffic the initial density of the soil is restored.

The author has not found any information concerning the effects of frost action on the relative density and on the deformation characteristics of a soil. Further research is needed within this area before the behavior of soil under high rates of loading can be predicted accurately.

DISTRIBUTION OF STRESSES BELOW PAVEMENTS

The distribution of stresses within a mass of soil is in general calculated by means of the theory of elasticity. However, the intensity of the applied loads is so high at failure that the soil does not even approximately behave like an ideal elastic material, and elastic methods are not applicable. The distribution of load has, therefore, in this analysis been calculated by means of the 2:1 method (17, 18). This method assumes that the applied load at any depth is distributed over an area that increases in proportion to the depth below the point of loading, as shown in Figure 5.

It is assumed that at the depth a the total vertical pressure increase dp caused by the moving load W is equal to

$$dp = \frac{W}{(d + a)(\ell + a)} \tag{9}$$

It is assumed that this pressure increase is uniformly distributed over the area $(d + a)(\ell + a)$. The pressure increase dp is approximately equal to the increase calculated by means of theory of elasticity below the center of the loaded area. The actual distribution of pressure is bell-shaped and the intensity of the load at the edge of the loaded area is smaller than the calculated value. Thus the actual bearing capacity of the soil

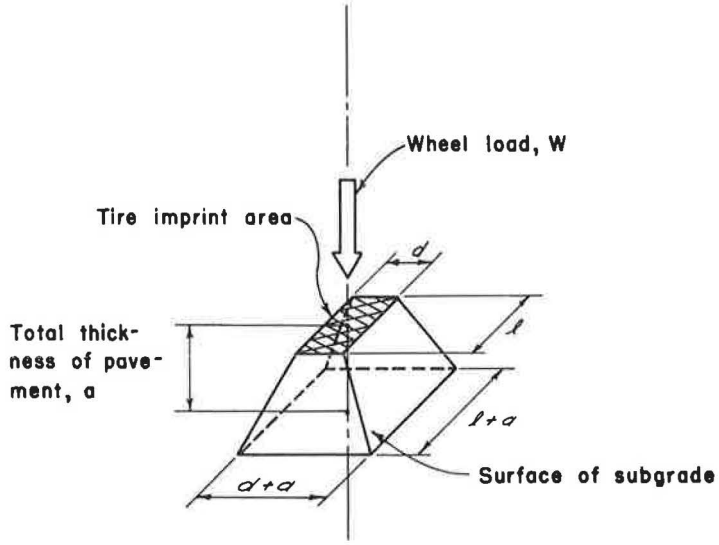

Figure 5. Assumed distribution of load at failure.

might be larger than computed, due to the approximations involved in the 2:1 method. The distribution of stresses within layered systems is not very well understood, particularly when the soil is close to failure.

ULTIMATE BEARING CAPACITY

The net ultimate bearing capacity q_{ult} of soil that acts as if it has an angle of internal friction of 0^0 can be calculated from

$$q_{ult} = c_u N_c \tag{10}$$

in which c_u is the undrained apparent cohesive strength of the subgrade material and N_c a bearing capacity factor, which depends on shape and size of the loaded area as well as the depth below the ground surface (19, 20, 21, 22). The net ultimate bearing capacity is equal to the ultimate capacity of the soil less the overburden pressure. The bearing capacity factor N_c is approximately equal to 7.5 for a circular or square shape of the loaded area, assuming that the thickness of the base course is approximately twice the size of the loaded area.

Failure of the soil takes place along a cylindrical failure surface extending to a depth of approximately 1.5 times the width of the loaded area. As the width of the loaded area at the depth a is equal to (a + d), the failure surface extends approximately to a depth of [a + 1.5 (a + d)] below the ground surface. The ultimate bearing capacity depends on the average shearing strength of the soil within this zone. The shearing strength of the soil is proportional to the initial effective pressure. Because the failure zone extends between the depth a to [a + 1.5 (a + d)], then the average shearing strength corresponds to the shearing strength at a depth of [a + 0.75 (a + d)] below the ground surface. The total bearing capacity of the pavement can then be evaluated by substituting Eqs. 7 and 8 into Eq. 10.

The ultimate capacity of flexible pavements subjected to frost action has been computed and shown in Figures 6 through 9. Calculations have been made for five different soils. The properties of the five soils are given in Table 1.

Soil 1 corresponds to a silt with a percentage of fines in excess of 15 percent. This material would probably be classified as type F4 material according to the Army Uniform Classification System (2) or as a ML or a MH material according to the Unified Soil Classification System (23). Soil 2 corresponds approximately to a silty sand with a content of fines in excess of 15 percent, Soil 3 to a silty gravel with a content of fines

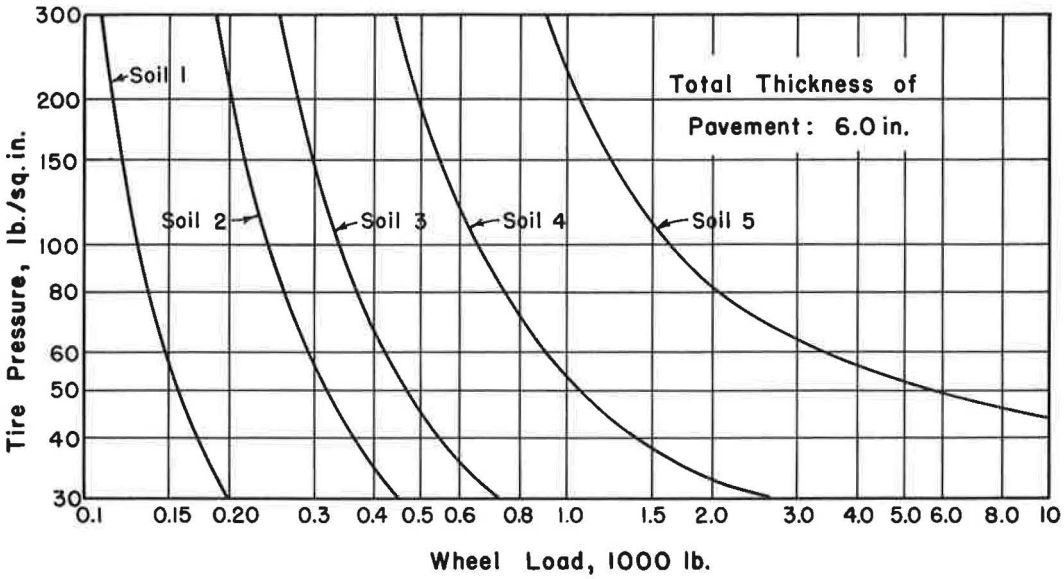

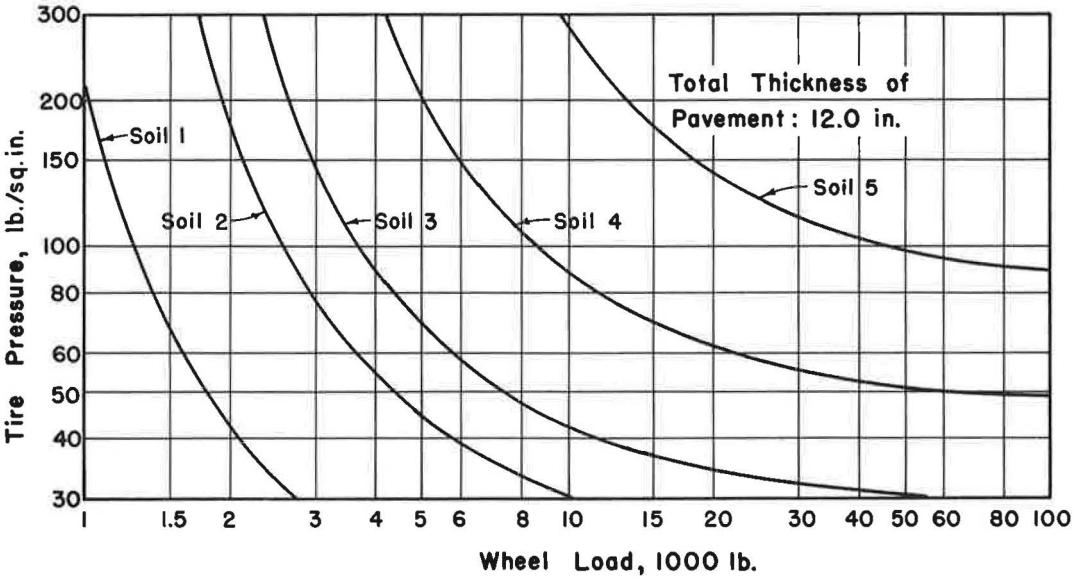

Figure 6. Ultimate bearing capacity of flexible pavements.

in excess of 15 percent. Soil 4 and Soil 5 correspond to a sand and a gravelly sand, respectively, with a percentage of fines less than 15 percent. In all calculations it has been assumed that the value of the coefficient of lateral earth pressure at rest is equal to 1.0.

The ultimate bearing capacity has been calculated under the assumption that the ground-water table is located at the surface of the subsoil at a depth a below the pavement surface. It has been assumed, furthermore, that the unit weights of the soil in the base course and the subbase are equal to 135 pcf and 125 pcf, respectively. The

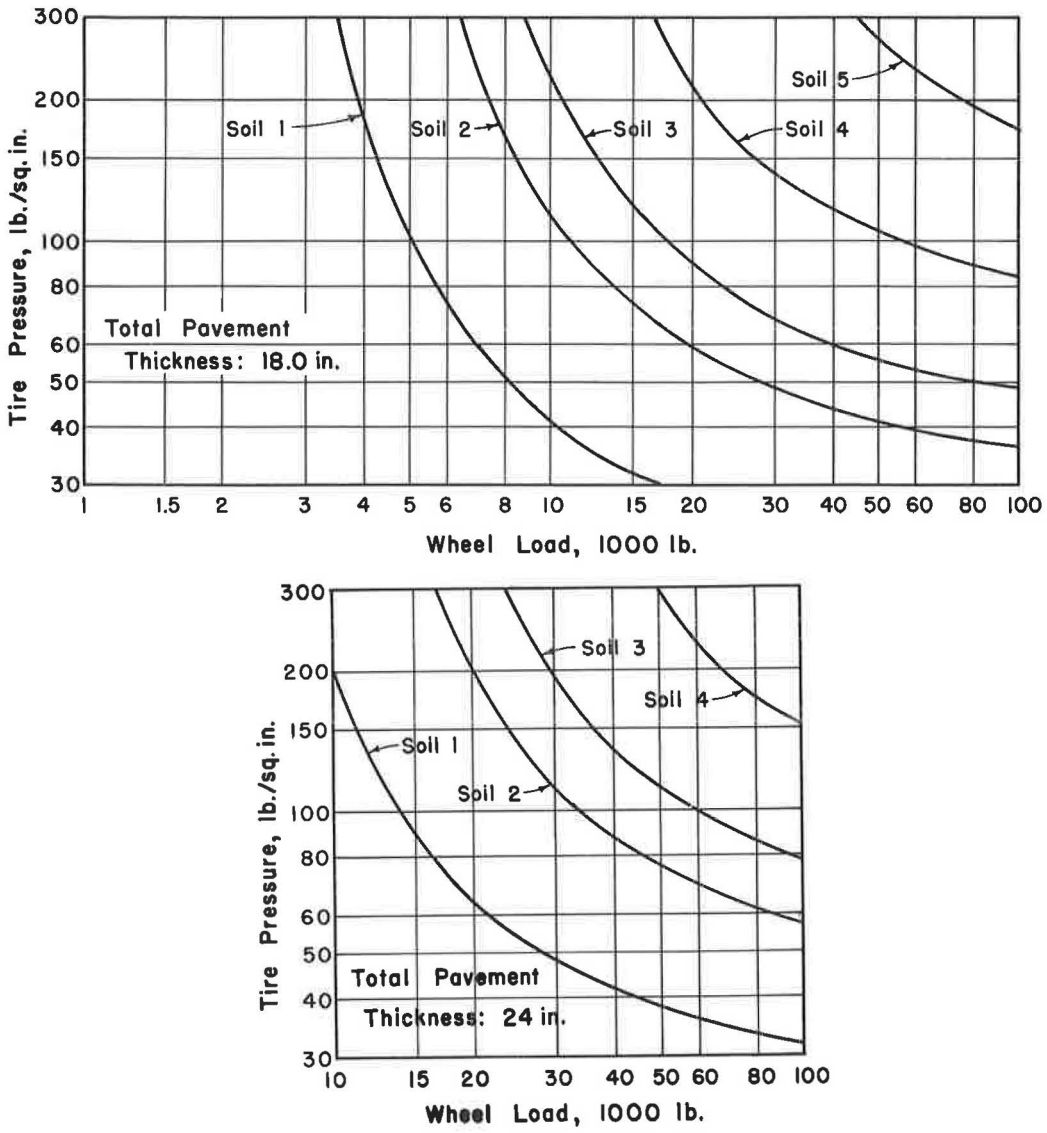

Figure 7. Ultimate bearing capacity of flexible pavements.

unit weight of water has been taken as 62.5 pcf. If the ground-water table is located within the base course, the bearing capacity is less than shown in Figures 6 through 9. It has been assumed further that the imprint area is either circular or square.

Figures 6 and 7 show the ultimate bearing capacity as a function of the contact pressure between the moving load and the pavement. The ultimate bearing capacity has been calculated for a total pavement thickness of 6, 12, 18, and 24 in. It can be seen that the total bearing capacity increases rapidly with decreasing contact pressures. This effect is especially pronounced for Soils 4 and 5.

Figures 8 and 9 show the ultimate load as a function of the thickness of the pavements calculated for the contact pressures of 100 and 300 psi, respectively. The ultimate capacity has been calculated for a total pavement thickness of 9 to 30 in.

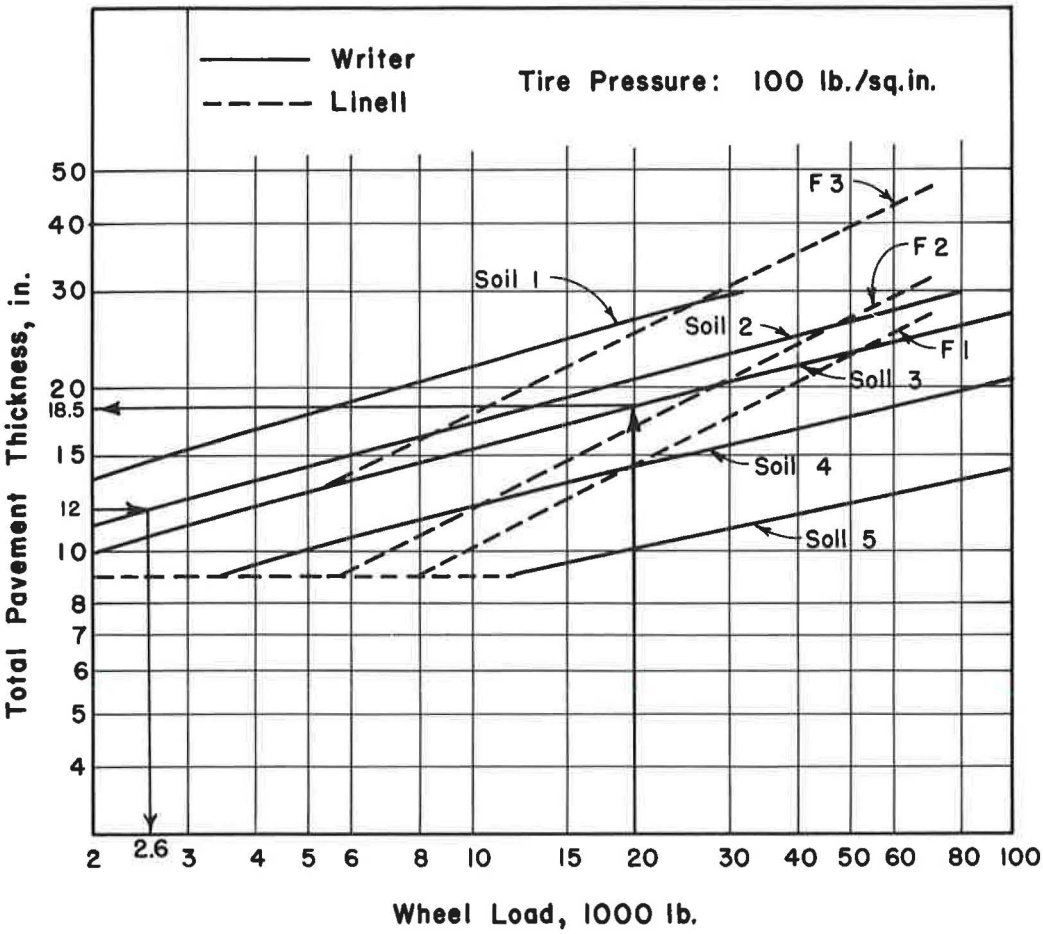

Figure 8. Ultimate bearing capacity of flexible pavements.

Figure 8 also shows the relationship between total thickness of the pavement and total capacity as proposed by Linell (2). It can be seen that the required thickness calculated by the method proposed by the author and by Linell yield approximately the same results. This general agreement indicates that the method proposed by the author yields reasonable results. However, the predicted combined thickness as calculated by the author's method is somewhat smaller for heavy wheel loads than that predicted by the method proposed by Linell. The opposite is true for low wheel loads. However, Linell's method was derived from observations of the behavior of flexible airfield pavements subjected to high wheel loads.

The relationships shown in Figures 6 through 9 are computed under the assumptions that the apparent angle of internal friction of the subgrade soil and the corresponding pore pressure coefficient A_f are known. Little is known about the value of the coefficient A_f for soils subjected to frost action. Comparisons between Soils 2 and 4 and between Soils 3 and 5 indicate that the coefficient A_f has a large effect on the bearing capacity of the soil. Therefore, it is possible that the relationships as shown in Figures 6 through 9 might change considerably as further knowledge is gained. However, the computed relationships might serve as an indication of the behavior of soils subjected to frost action.

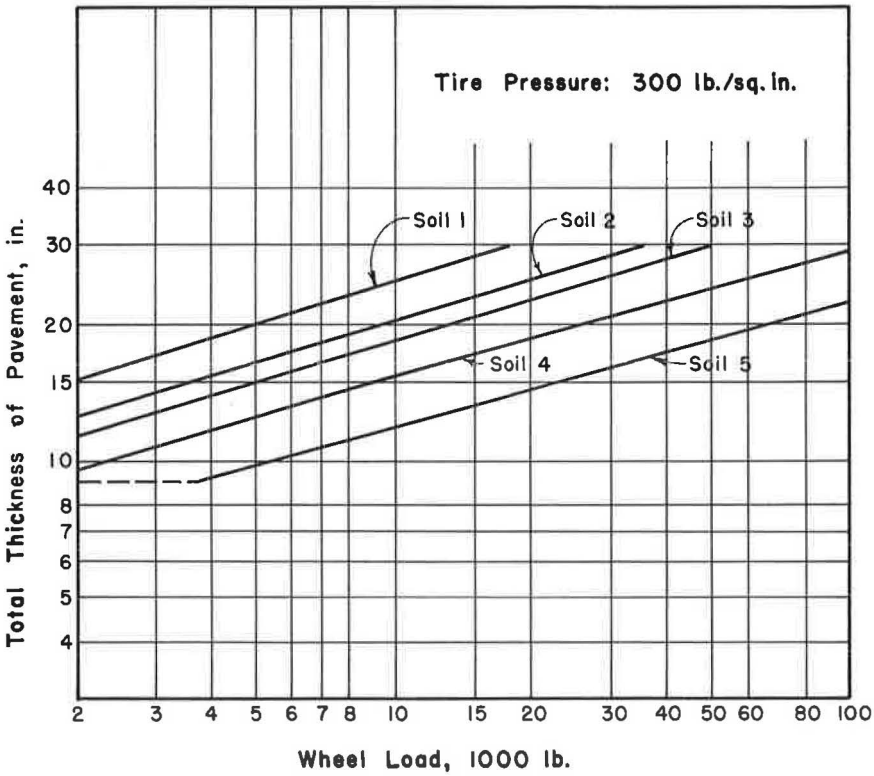

Figure 9. Ultimate bearing capacity of flexible pavements.

TABLE 1

ASSUMED VALUES OF APPARENT ANGLE OF INTERNAL FRICTION[1] ϕ_s AND OF PORE PRESSURE COEFFICIENT A

Soil	ϕ_s (deg.)	A_f	Soil Classification	
			Unified (23)	Army Uniform (2)
1	25	0.3	ML or MH	F4
2	30	0.1	SM or SC	F4
3	35	0.1	GM or GC	F3
4	30	-0.2	SW or SP	F2
5	35	-0.2	GW or GP	F1

[1]As measured by slow direct shear or triaxial test.

DESIGN AND LOAD RESTRICTIONS ON FLEXIBLE PAVEMENTS

Figures 8 and 9 might serve as a guide for the design of flexible pavements. These two figures show the ultimate bearing capacity of the pavement as a function of its thickness. If the indicated loads are placed on the pavements, failure will take place. To prevent damage, only a fraction of the ultimate load can be allowed. The reduction of the load depends on the number of load applications during the spring break-up period. It is estimated that the allowable load should be approximately one-half its ultimate value in order to prevent damage of the pavement if the pavement is only subjected to a few load applications, and one-third of its ultimate capacity if the pavement is subjected to a large number of load applications. For example, if the maximum

wheel load is equal to 10,000 lb and if the pavement is subjected to a few repetitions of load during the spring break-up period, the pavement should be designed for an ultimate load of 20,000 lb. For this total load, the required total thickness of the pavement is equal to 18.5 in. if the subsoil corresponds to Soil 3, and if the tire pressure is 100 psi. The corresponding required thickness according to Linell's method is 18.0 in.

Figures 8 and 9 can also be used to determine allowable wheel loads on airfield or highway pavements. If the total thickness of the wearing and base course is, for example, 12.0 in., and if the subsoil corresponds to Soil 2, then the ultimate capacity of the pavement is equal to 2,600 lb, as shown in Figure 8. With a limited amount of traffic during the spring break-up period, the allowable wheel load should be approximately 1,300 lb.

SUMMARY

A method has been presented by which the ultimate bearing capacity of pavements subjected to frost action can be calculated. It has been shown that the ultimate bearing capacity depends on the size and shape of the loaded area, the thickness of the flexible pavement, the location of the ground-water table, and the density of the subgrade material factors that are all known to influence the bearing capacity of pavements.

REFERENCES

1. Linell, K. A., and Haley, J. F., "Investigation of the Effect of Frost Action and Pavement Supporting Capacity." HRB Special Report 2, 295-325 (1952).
2. Linell, K. A., "Frost Design Criteria for Pavements." HRB Bull. 71, 18-32 (1953).
3. Terzaghi, K. V., "Erdbaumechanik." Denlicke, Leipzig (1925).
4. Tschebotarioff, G. P., "Soil Mechanics, Foundations and Earth Structures." McGraw-Hill (1951).
5. Bishop, A. W., "Test Requirements for Measuring the Coefficient of Earth Pressure at Rest." Brussels Conf. 58, on Earth Pressure Problems, 1:1-14 (1958).
6. Hansen, J. B., and Gibson, R. E., "Undrained Shear Strength of Anisotropically Consolidated Clays." Géotechnique, 1:189 (1949).
7. Skempton, A. W., and Bishop, A. W., "Soils." Ch. X, Building Materials, Their Elasticity and Inelasticity, North-Holland Pub. Co., Amsterdam (1954).
8. Skempton, A. W., "The Pore-Pressure Coefficients A and B." Géotechnique, 4:143-147 (1954).
9. Bishop, A. W., "The Use of Pore-Pressure Coefficients in Practice." Géotechnique, 4:148-152 (1954).
10. Skempton, A. W., "The $\phi = 0$ Analysis of Stability and Its Theoretical Basis." Proc., 2nd Internat. Conf. Soil Mechanics, Rotterdam, 1:72 (1948).
11. Bishop, A. W., and Eldin, G., "Undrained Triaxial Tests on Saturated Sands and Their Significance in the General Theory of Shear Strength." Géotechnique, 2:13-32 (1950).
12. Bishop, A. W., and Henkel, D. T., "The Measurement of Soil Properties in the Triaxial Test." Arnold, London (1957).
13. Hvorslev, M. J., "Uber die Festigkeitseigenshaften gestorter bindiger Boden." Ing., vid. skrifter, A 45, Kopenhagen (1937).
14. Leonards, G. A., "Foundation Engineering." McGraw-Hill (1962).
15. Beskow, G., "Soil Freezing and Frost Heaving." Swedish Geol. Survey, No. 375 (1935).
16. Taber, S. M., "The Mechanics of Frost Heaving." Jour. of Geology, 38:303-317 (1929).
17. Lundgren, H., and Hansen, J. B., "Geoteknik." Teknisk Forlag, Kopenhagen (1958).
18. Hough, B. K., "Basic Soils Engineering." Ronald Press (1957).
19. Prandtl, L., "Uber die Harte plastischer Korper." Nachr. Ges. Wiss. Gottingen (1920).

20. Terzaghi, K., "Theoretical Soil Mechanics." Wiley (1943).
21. Meyerhof, G. G., "The Ultimate Bearing Capacity of Foundations." Géotechnique 2:301 (1951).
22. Skempton, A. W., "The Bearing Capacity of Clays." Building Research Congress, pp. 180-189.
23. "The Unified Soil Classification System." Corps of Engineers, U. S. Army, Tech. Memo. 3-351 (1953).

Discussion

A. C. BENKELMAN, Altamonte Springs, Florida—The paper deals with an extremely important subject, one that should be given more consideration by research workers in the highway field. In the WASHO and the AASHO Road Tests a great deal more structural deterioration of the test sections occurred during the spring than during the summer and fall months. Considerable information was obtained regarding the condition of the subsurface components during these two periods. This information is of interest in connection with the subject matter of the paper.

Tables 2 and 3 summarize the data. For the embankment soil of the AASHO Road Test there was little difference in the percent saturation of the material in the spring and summer, 80.4 vs 78.8, and in both periods the material was well below complete saturation. However, there were appreciable differences in the indicated strength (CBR) and percent saturation of the base (high quality crushed stone) and of the subbase (uncrushed sandy gravel). This information strongly suggests that the weakness of the pavement in the spring (80 percent of the test sections failed in the two spring periods as against 6 percent in both summers) may have been due in large part to the adverse condition of the granular courses at this time.

The data for the WASHO Road Test (embankment soil only) show that only in areas that had failed completely or were about to fail was the percent saturation of the material greater in the spring (around 90 percent) than in the summer and fall (around 85 percent). The figures for unfailed areas that were sampled near the failed or about to fail areas actually show a lower level of saturation (around 83 percent) than in the summer and fall.

The embankment soil at both the AASHO and the WASHO Road Tests was a fine-grained material, an A-6 and an A-4-8, AASHO Classification. Complete data on their classification and physical characteristics are given in the published reports of the two tests.

TABLE 2

AASHO ROAD TEST MATERIALS, AVERAGE VALUES OF IN-PLACE TESTS

Time	Component	Density	M.C.	CBR	S (%)
Construction	Embankment	112.7	16.3	2.9	87.7
	Base	140.9	4.2	—	54.1
	Subbase	134.5	3.8	—	40.5
Spring	Embankment	113.5	14.6	4	80.4
	Base	143.8	4.3	87	62.5
	Subbase	136.5	5.5	24	63.4
Summer	Embankment	112.8	14.6	5.6	78.8
	Base	142.4	3.6	131	49.4
	Subbase	135.2	4.8	50	52.8

TABLE 3

WASHO ROAD TEST SEASONAL VARIATIONS IN CONDITION OF EMBANKMENT SOIL, AVERAGE VALUES OF IN-PLACE TESTS

Section	Construction Period 1952			November 1953			June 1954			Spring 1954												
										Failed Areas			About to Fail Areas			Unfailed Areas					
	M. C.	Density	S (%)	CBR	M. C.	Density	S (%)	CBR	M. C.	Density	S (%)	CBR	M. C.	Density	S (%)	CBR	M. C.	Density	S (%)	CBR	M. C.	Density	S (%)	CBR
All 22 in.	21	88	67	-	25	90	85	14	26	89	84	12												
All 18 in.	24	89	78	-	25	92	89	15	25	93	88	13												
All 14 in.	24	88	75	-	24	91	83	16	24	92	84	14												
All 10 in.	23	90	76	-	24	92	84	17	24	91	82	15	26	90	90	2	25	89	87	6	25	90	83	8
All 6 in.	24	89	77	-	22	94	81	25	23	92	80	18	24	96	91	4	22	98	90	10	22	95	82	14
Grand avg.	23	88	73	-	24	92	85	17	24	91	85	14												

Further, in the late 1940's and early 1950's a great amount of work was done by the northern States (New York included) in a study of the effect of frost action on the indicated ability of flexible pavements to support load. The work was sponsored by the Highway Research Board Committee on Load Supporting Capacity of Roads as Affected by Frost Action. It was found in the case of fine-grained soils that the reduction of plate load support values was consistently around 50 percent. In the case of sandy soils the reduction was considerably less. Because soils in most of the northern States vary in character from point to point, some of the States adopted the practice of reducing the permitted loads by 50 percent. Of course, load reduction on roads is generally limited to secondary roads or roads that are known to be weak.

At the present time a considerable number of States and all the Provinces of Canada are engaging in studies of the performance of flexible pavements in service and more work along this line is in prospect in connection with the application of the findings of the AASHO Road Test in practice. All factors (such as the condition and design of the pavement, materials, subgrade character, and traffic) are taken into consideration in these studies. Many of the States and all the Canadian Provinces are, in addition, running seasonal deflection tests of selected sections of the pavement, using the Benkelman beam. In Oklahoma and South Dakota and at the AASHO Road Test, good correlations were found between the results of beam and plate load tests. Of course, if the beam tests are a measure of the ability of a pavement to support load, a simple method of test is available for use in establishing limitation of load in the spring. In both the WASHO and AASHO Road Tests it was found that beam deflections were a fairly good predictor of pavement performance.

BENGT B. BROMS, Closure—Mr. Benkelman's discussion brought out that the degree of saturation for areas where failures have taken place at the WASHO Road Tests was higher than for areas where failures have not taken place. The degree of sat-

uration for the failed sections was approximately 90 percent as compared with 83 percent for the unfailed sections. These data indicate that the degree of saturation is an important parameter affecting the bearing capacity of flexible pavements.

In the method of calculation proposed by the author it has been assumed that the degree of saturation of the subgrade material is 100 percent and the data supplied by Mr. Benkelman suggest that the degree of saturation of the subgrade material may approach this value under unfavorable conditions. It is possible that the degree of saturation of the soil at the time of failure might have been higher than the measured values due to drainage of the soil between the time of failure and the time of sampling and that some small changes of the degree of saturation might have taken place during sampling and testing of the soil. The bearing capacity as calculated by the method proposed by the author should not be considered as the only bearing capacity of flexible pavements but as the lower limit that may be reached under unfavorable conditions, when the degree of saturation approaches 100 percent. It is an economic question if the design of flexible pavements should be based on the most unfavorable conditions or on some other more favorable condition; e.g., 90 percent saturation of the subgrade soil.

Mr. Benkelman also brought out that the bearing capacity of flexible pavement as affected by frost action has been evaluated by plate load tests. The bearing capacity determined in this manner when the load is applied relatively slowly and when very small excess pore pressures or none develop in the soil may be different from that governing the bearing capacity with respect to moving traffic loads when the loads are applied relatively rapidly and when high excess pore pressures may develop in the subgrade soil. The method proposed by the author takes these excess pore pressures in account and it has been shown that these excess pore pressures have a very large effect on the ultimate bearing capacity. It is possible that the results from the load tests cannot be used to predict under all conditions the bearing capacity of flexible pavement subject to rapidly applied loads such as moving traffic loads.